University of Southampton Research Repository

UNIVERSITY OF SOUTHAMPTON

FACULTY OF ENGINEERING AND PHYSICAL SCIENCES

INSTITUTE OF SOUND AND VIBRATION RESEARCH

THE INFLUENCE OF BASEPLATE FASTENING SYSTEMS ON RAILWAY ROLLING NOISE

by

Boniface Samwel Hima

Thesis for the degree of Engineering Doctorate in Sustainable Infrastructure Systems

July 2021

UNIVERSITY OF SOUTHAMPTON

ABSTRACT

FACULTY OF ENGINEERING AND PHYSICAL SCIENCES

INSTITUTE OF SOUND AND VIBRATION RESEARCH

Thesis for the degree of Engineering Doctorate

THE INFLUENCE OF BASEPLATE FASTENING SYSTEMS ON RAILWAY ROLLING NOISE

Boniface Samwel Hima

The focus of this study is placed on railway rolling noise that is in most situations the dominant source of railway airborne noise for conventional train speeds. This work aims to investigate and quantify the influence of the rail fastening system on the rolling noise. For this purpose, a commercial two-stage baseplate system mounted on a slab track is studied experimentally and numerically. The research aims to identify the key design parameters that affect the rolling noise, pointing the way towards controlling noise. These aims are addressed by using laboratory and field measurements of vibration and noise as well as prediction models.

Rail fastening systems perform an important role in distributing the train load to the sleepers or the slab, as well as in protecting them from excessive dynamic loading. Their types range from simple systems such as rubber rail pads, an elastic layer inserted between the rail and sleeper, held down by fastening clips, to more sophisticated ones that include fastening systems with baseplates and more than one rubber pad. The dynamic properties of the rail fastening system, such as its stiffness and damping, play a key role in the dynamic performance of the track and its noise emission. The dynamic stiffness affects the degree of coupling between the rail and the foundation as well as the vibration decay rate along the rail.

The dynamic stiffness of rail pads and rail fastening systems fitted on railway tracks has been measured in the laboratory. By definition, dynamic stiffness is the complex frequency-dependent ratio between the applied dynamic force and the deflection. An experimental procedure based on a standardised indirect method is applied for measuring the dynamic stiffness of rail pads and more complex rail fastening systems. The method allows the dynamic stiffness of resilient track elements to be obtained as a function of the excitation frequency for known loading conditions. The results are obtained in the frequency range 50 Hz - 1000 Hz.

The track decay rate (TDR) is the rate of vibration attenuation with distance along the track. It is usually determined for both the vertical and lateral waves propagating in the rail. It is a measurable quantity and it is closely related to the rolling noise performance of the track. For the purpose of this work, the TDR has been measured for four different configurations (rail pads) on a non-operational slab track section located at the National College for High-Speed Rail at Doncaster, UK.

The properties of rail pads and rail fastening systems in the context of noise and vibration are discussed using simple mass-spring models to explain features of the measured results. Initially, a model of a beam on an elastic foundation is used to calculate the TDR. This simple model does not provide a sufficient match with the measured TDR and thus a detailed 2.5D finite element (FE) model of the rail coupled with an FE model of the flexible fastening system (baseplate) is deployed. The 3D FE model for the baseplate and the 2.5D model for the rail are combined into a model of a discretely supported railway track using a receptance coupling technique. This model is used to predict the track mobilities and TDRs. The predicted results agree well with the measured ones for all the cases considered.

By using the baseplate response predicted from this model the sound radiation of the baseplate is estimated. Two models are used to calculate the baseplate sound radiation: an analytical model based on the Rayleigh integral and a more detailed boundary element (BE) model that can include the scattering effect of the rail. Although the BE model can account for more details, it is shown that adequate results are obtained using the analytical model. The predicted baseplate sound radiation is then compared with measured data obtained on a full-scale slab track section in the reverberation chamber. A good agreement is found for most configurations.

Finally, in order to predict the rolling noise from a slab track, the TWINS model is used with the results from the flexible baseplate model and the effect on the overall noise is determined. The results show that the contribution of the baseplate noise is 5 – 10 dB lower than that from the rail. If the thickness of the baseplate is increased, the rolling noise is reduced between 200 Hz and 1 kHz due to changes in the TDR, whereas the noise from the baseplate itself is increased. The change in the total noise is quite small. By comparing results for different stiffnesses of railpad it is found that the optimum stiffness of the railpad is around 500 MN/m.

Table of contents

ABSTRACT .... **i**

Table of contents .... **iii**

List of Figures .... **ix**

List of Tables .... **xxvii**

Declaration of Authorship .... **xxix**

Acknowledgements .... **xxxi**

List of Symbols .... **xxxiii**

Abbreviations .... **xxxv**

Chapter 1 Introduction **1**

1.1 Background and motivation 1

1.2 Introduction to track systems 4

1.2.1 Track structures 5

1.2.2 Static and dynamic stiffness of track resilient elements 8

1.2.3 Track decay rate 10

1.3 Aims and Objectives 10

1.4 Novel contributions of the thesis 12

1.5 Thesis layout 13

Chapter 2 Literature review **15**

2.1 Railway noise and pad stiffness 15

2.1.1 Slab tracks 18

2.2 Dynamic stiffness of railpads 19

2.3 Track decay rates 24

2.4 Track vibration modelling 26

2.5 Rail radiation 27

2.6 Sleeper radiation 29

2.7 Sound radiation efficiency measurements 31

Chapter 3 Experimental procedure for measurement of dynamic stiffness **33**

3.1 Introduction 33
3.2 Description of the experimental rig 33
3.3 The theoretical background of the experimental procedure 36
    3.3.1 2-DOF model representing the setup for standalone pad measurement 36
    3.3.2 3-DOF model representing the setup for double layer fastening system measurement 40
3.4 Effect of the bending of the lower block 45
3.5 Test procedure and data processing 47
3.6 Measured specimens 48
3.7 Measured results 50
    3.7.1 Standalone railpad results 50
    3.7.2 Results from the single-stage baseplate system 51
    3.7.3 The effect of clipping the rail and fixing the baseplate 54
    3.7.4 Results from the two-stage baseplate system 55
3.8 Comparison between measured and predicted dynamic stiffness 60
3.9 Summary 62

Chapter 4 Track vibration measurements 63

4.1 Introduction 63
4.2 Test track 63
4.3 Track decay rate 65
    4.3.1 TDR measurement procedure at the test track 66
    4.3.2 Processing of the measured data 69
4.4 Results and analysis 69
    4.4.1 Driving point mobility 69
    4.4.2 TDR results 74
    4.4.3 The effect of the temperature on the TDR results 75
    4.4.4 The effect of the fastener spacing on the TDR results 75
4.5 Laboratory measurement of baseplate vibration 77
    4.5.1 Measurement setup 77

4.5.2 Results from the vibration response measurement 80

4.6 In-situ vibration measurement of the baseplate.. 81

4.6.1 Measured driving point and transfer mobilities 82

4.7 Summary.. 84

Chapter 5 Slab track vibration modelling 87

5.1 Timoshenko beam model 87

5.2 Development of FE model of the baseplate 91

5.2.1 FE model 91

5.2.2 Measurements of free baseplate 92

5.2.3 Measurement setup for baseplate on lower pad 96

5.2.4 The effect of bolting torque 97

5.2.5 Comparisons of mode shapes and modal frequencies 98

5.2.6 Summary of the findings in section 5.2 101

5.3 Track model with flexible two-stage baseplate... 102

5.3.1 Introduction.. 102

5.3.2 Baseplate vibration response 103

5.3.3 Rail driving point mobility.. 104

5.3.4 TDR comparison... 106

5.3.5 Baseplate transmissibility 107

5.3.6 Summary of the findings 109

Chapter 6 Noise radiation from the baseplate 111

6.1 Modelling of the baseplate sound radiation 112

6.1.1 Baseplate sound radiation using the Rayleigh integral model 112

6.1.2 Sound radiation from three adjacent baseplates................................. 115

6.1.3 3D Boundary Element model of the baseplate 117

6.1.4 Baseplate sound radiation in the presence of the rail 120

6.1.5 Summary... 121

6.2 Sound radiation prediction for the two-stage baseplate coupled on 2.5D track model 121

6.2.1 Calculation of surface velocities 122

6.2.2 Rayleigh integral model results 124

6.2.3 Required number of baseplates 125

6.2.4 Comparison of the proposed model of the baseplate with the TWINS (bi-block) sleeper model 127

6.3 Measurements of sound radiation for the two-stage baseplate 130

6.3.1 Baseplate mobilities 131

6.3.2 Baseplate sound radiation 134

6.3.3 Rail vibration measured in the reverberation chamber 138

6.3.4 Rail sound radiation 142

6.3.5 Track radiated power 144

6.4 Summary 149

Chapter 7 Noise sensitivity analysis for the two-stage baseplate fastening system 151

7.1 The effect of the surface areas of the baseplate 151

7.1.1 Rolling noise predictions 153

7.2 The effect of the baseplate thickness 159

7.2.1 Vibration for different baseplate thickness 159

7.2.2 Radiated sound power comparisons for different baseplate thickness 162

7.2.3 Rolling noise predictions 163

7.3 The effect of railpad stiffness 164

7.3.1 The effect of railpad stiffness on track noise 164

7.3.2 Noise comparison 165

7.4 Summary 167

Chapter 8 Conclusions and recommendations 169

8.1 Conclusions 169

8.1.1 Dynamic stiffness measurements 169

8.1.2 Track vibration measurements 169
8.1.3 Vibration modelling of baseplates 170
8.1.4 Noise radiation from the baseplate 170
8.1.5 Noise sensitivity analysis for the two-stage baseplate 171

8.2 Recommendations for future research 171

Appendix A Dynamic stiffness of additional specimens 173

A.1 Additional measured specimens 173
A.2 Results from FCA fastening system 178
A.3 Results from China baseplate fastening system Type A 180
A.4 Results from China baseplate fastening system Type B 183

Appendix B The Vanguard fastener system 189

B.1 The Vanguard fastener system 189
B.2 Description of the experimental rig 189
B.3 Static stiffness measurement setup 190

B.3.1 Static stiffness results 191

B.4 Dynamic stiffness measurements 192

B.4.1 Vertical dynamic stiffness results 193

B.5 Measurement setup for lateral dynamic stiffness 194

B.5.1 Lateral dynamic stiffness results 195
B.5.2 Peak Identification 199

Appendix C Receptance coupling method 205
List of References 209

List of Figures

Figure 1-1 Illustration of the mechanism of generation of rolling noise [1]......................2

Figure 1-2 Schematic diagram of the rolling noise generation mechanism [1].................3

Figure 1-3 Typical predictions showing contributions of the wheel, rail and sleeper noise using TWINS model [1]...3

Figure 1-4 Two types of typical track construction showing the rails, railpads, fastener system, sleeper, ballast and slab **(a)** Ballasted track [23], **(b)** Slab track [24]. 5

Figure 1-5 Exploded view of a standalone fastener showing the rail, railpad, clips isolator and bracket placed on the sleeper [1]..5

Figure 1-6 Single-stage fasteners system (Pandrol FAST CLIP SFC baseplate) [25]. 6

Figure 1-7 Schematic view of the Pandrol two-stage baseplate (drawing courtesy of Pandrol, used with permission). 7

Figure 1-8 The Pandrol two-stage baseplate..7

Figure 1-9 Schematic view of Vanguard fastening system from Pandrol Ltd [25]. 8

Figure 1-10 A typical load-deflection curve for an elastomeric railpad [28].......................9

Figure 1-11 Illustration of the effect of the railpad stiffness on the coupling between rail and sleeper and on the damping of waves in the rail [1].....................................10

Figure 2-1 Measured effect of rail pad stiffness on track decay rates: same track fitted with three rail pads of different stiffnesses (approximately -125, ---270 and ···950 MN/m) [1]..16

Figure 2-2 Test rig for measuring the high-frequency dynamic stiffness of resilient elements redrawn from [55]. 20

Figure 2-3 Test rig and measurement setup used by Kari [59]..21

Figure 2-4 The direct method for elastic pad test rig set-up [61]....................................23

Figure 2-5 A schematic side view of the apparatus used by Morison et al. for driving point method [62]. 23

Figure 2-6 Embedded rail track [65]. 25

Figure 2-7 A beam on an elastic foundation showing waves generated by a point force [1]. 26

Figure 2-8 Models for track vibration: (a) continuously supported beam model; (b) periodically supported beam model; (c) continuously supported rail model including cross-section deformation [58]. 27

Figure 2-9 Radiation efficiencies of UIC 60 rail section modelled in 2D, – vertical motion, --- horizontal motion [80]. 29

Figure 2-10 Sleeper represented as a finite Timoshenko beam on an elastic foundation, excited by a point force at y = 0 showing the various waves that are generated [1]. .30

Figure 2-11 Illustration of reciprocity technique A: Exciter location, B: Response location [86]. 31

Figure 3-1 The test rig for measuring the dynamic stiffness at the UoS-HSL. 34

Figure 3-2 Schematic view of the experimental rig with two-stage baseplate installed..34

Figure 3-3 2-DOF model of the experimental rig. 37

Figure 3-4 Point and transfer receptances of the 2DOF system: (**a**) magnitude and (**b**) phase angle. 39

Figure 3-5 Predicted dynamic stiffness magnitude (**a**) and phase of complex stiffness (**b**) as well as the actual stiffness of a single layer resilient element. 40

Figure 3-6 3DOF model of the rig as a mass-spring system. 41

Figure 3-7 Point and transfer receptances of the 3DOF system: (**a**) magnitude and (**b**) phase angle. 42

Figure 3-8 Comparison of the stiffness magnitude for a single layer resilient element 2DOF model and a double layer resilient element 3DOF models, (**a**) magnitude, (**b**) phase angle of the complex stiffness. 42

Figure 3-9 Comparison of the stiffness for a single layer resilient element 2DOF model and a double layer resilient element 3DOF models for different values of the intermediate-mass. 43

Figure 3-10 2DOF model of the two-layer fastening system as a spring-mass-spring model (F_t is transmitted force)....43

Figure 3-11 Predicted direct and transfer stiffness magnitude (**a**) and phase of complex stiffness (**b**) of the two-stage baseplate from the 2DOF model. 45

Figure 3-12 (**a**) side view of the basic set-up measurement (**b**) top view shows the locations of the impact force and measured position. 46

Figure 3-13 Magnitude of the transfer accelerance of the lower steel block (distances from the edge of the block). 46

Figure 3-14 First bending mode shape of the steel block at 1250 Hz calculated in COMSOL. 47

Figure 3-15 Curve fitting of the magnitude for different preloads with a selecting the value at the frequency of 300 Hz for dynamic stiffness **(a)** and at a frequency of 360 Hz for damping loss factor **(b)**. 48

Figure 3-16 Railpad specimens (No1. No.2, No.3), and lower pads for the two-stage system No.6, No.7. 49

Figure 3-17 Dynamic stiffness magnitude plotted against frequency for different static preloads: (**a**) railpad No. 1; (**b**) railpad No. 2; (**c**) railpad No. 3; (**d**) railpad No. 4. 50

Figure 3-18 **(a)**Dynamic stiffness magnitude at 300 Hz, (**b**) loss factor at 360 Hz plotted against static preload for railpads No. 1-4. 51

Figure 3-19 Dynamic stiffness magnitude plotted against frequency for the single-stage fastener fitted with railpad No. 3 at different preloads. 52

Figure 3-20 Dynamic stiffness at 300 Hz of the single-stage fastener system fitted with different Pandrol railpads plotted against preload. 52

Figure 3-21 Loss factor of the single-stage fastener system fitted with different Pandrol railpads plotted against static preload. 53

Figure 3-22 Comparison of the dynamic stiffness magnitude at 300 Hz plotted against static preload for railpad No.3 as standalone and mounted in the single-stage fastener system. 54

Figure 3-23 Comparison of the loss factor plotted against static preload for railpad No.3 as standalone and mounted on the single-stage fastener system. 54

Figure 3-24 Dynamic stiffness with preload for clipped and bolted case compared with the unclipped, unbolted case that was shifted by 20 kN. 55

Figure 3-25 Dynamic stiffness magnitude for two-stage baseplate system fitted with type A lower pad and railpad No. 3 plotted against frequency. 56

Figure 3-26 Dynamic stiffness magnitude plotted against static preload for baseplate system, fitted with different lower pads and railpad No.2. 56

Figure 3-27 Dynamic stiffness magnitude plotted against static preload for baseplate system, fitted with different lower pads and railpad No.3. 57

Figure 3-28 Damping loss factor plotted against static preload for baseplate system, fitted with different lower pads and railpad No. 2. 57

Figure 3-29 Damping loss factor plotted against static preload for baseplate system, fitted with different lower pads and railpad No. 3. 58

Figure 3-30 Dynamic stiffness magnitude plotted against frequency for lower pad type A (No.6) fitted in the baseplate with no railpad. 59

Figure 3-31 Comparison of results for separate pads and combined two-stage baseplate assembly with railpad No. 3 and lower pad A; **(a)** dynamic stiffness magnitude, **(b)** Loss factor. 59

Figure 3-32 Comparison of results for railpad No.3 alone, mounted in single-stage baseplate No.5 and in two-stage baseplate with Type A lower pad; **(a)** dynamic stiffness magnitude, **(b)** Loss factor. 60

Figure 3-33 Comparison of results for railpad No.1 alone, mounted in single-stage baseplate No.6 and in two-stage baseplate with Types A and B lower pad: **(a)** dynamic stiffness magnitude, **(b)** Loss factor. 60

Figure 3-34 A comparison of the measured and the predicted for 2DOF model dynamic stiffness (**a-c**) railpad No.3, (**d-f**) railpad No.4 61

Figure 4-1 View of the section of the test slab track. The ballasted track can also be seen in the distance 64

Figure 4-2 Photographs of the fastening systems (**a**) Pandrol two-stage system, (**b**) Vossloh system 64

Figure 4-3 Schematic view of the test track's different sections with fastening system type for the slab track section. 64

Figure 4-4 Recommended positions for the accelerometers on the cross-section of the rail according to EN15461:2008 [94]. 66

Figure 4-5 Recommended grid positions of the excitation points relative to the fixed response point, according to EN15461:2008 [94] 66

Figure 4-6 Instrumented hammer and accelerometer position on the railhead. 67

Figure 4-7 TDR measurement in the lateral direction. 67

Figure 4-8 The equipment setup for the TDR measurements. 68

Figure 4-9 Measured (**a**) magnitude, (**b**) phase and (**c**) coherence of the vertical driving point mobility for Pandrol railpad No.1. 70

Figure 4-10 Measured (**a**) magnitude, (**b**) phase and (**c**) coherence of the vertical driving point mobility for Pandrol railpad No.2. 71

Figure 4-11 Measured (**a**) magnitude, (**b**) phase and (**c**) coherence of the vertical driving point mobility for Pandrol railpad No.4. 72

Figure 4-12 Measured (**a**) magnitude, (**b**) phase and (**c**) coherence of the vertical driving point mobility for Pandrol railpad No.8 73

Figure 4-13 Comparison of the measured vertical driving point mobility for all Pandrol railpads. 74

Figure 4-14 TDR measured in July 2018 **(a)** vertical, **(b)** lateral. 74

Figure 4-15 Comparison of the TDR for railpad No. 1 measured in December 2019 (5^0C) and July 2018 (26^0C) for **(a)** vertical, **(b)** lateral. 75

Figure 4-16 Comparison of the TDR measured in December 2019 for 0.65 m and 1.3 m fastener spacing **(a)** vertical, **(b)** lateral. 76

Figure 4-17 Wavenumber plotted against frequency (dispersion relation) for a Timoshenko beam showing the pinned-pinned frequencies corresponding to the fastener spacing of 1.3 m, 0.65 m, and 0.6 m. 76

Figure 4-18 Sensor locations: at the baseplate, (blue) next to the railpad, (red) at the bolting and (green) at the centre of the clipping area. 78

Figure 4-19 A schematic side view of the rig for vibration response measurement for the two-stage baseplate. 78

Figure 4-20 Side view showing the upper sensor and the lower sensor at baseplate bolting area. 79

Figure 4-21 Vibration ratios comparisons for all three measured areas of the baseplate. 80

Figure 4-22 View of the test setup for first baseplate vibration measurements. 81

Figure 4-23 View of the test setup for the second baseplate vibration measurements. 82

Figure 4-24 Measured mobilities for two sensors at baseplate and one at the railhead: (**a**) magnitude, (**b**) phase and (**c**) coherence. 83

Figure 4-25 Transmissibility ratio between the railhead and baseplate for the first baseplate. 83

Figure 4-26 Comparison between vibration ratio measured in Doncaster and the one measured in the laboratory: (**a**) next to the railpad area of the baseplate, (**b**) at the clipping ear of the baseplate. 84

Figure 5-1 Measured and predicted driving point mobility for track fitted with railpad No.1: **(a)** magnitude and **(b)** phase. 89

Figure 5-2 Measured and predicted driving point mobility for track fitted with railpad No.4: **(a)** magnitude and **(b)** phase. 89

Figure 5-3 (**a**)-(**d**) measured and predicted vertical TDR for four-track fitted with railpad No.1, No.2, No.4 and No.8, respectively. 90

Figure 5-4 Geometrical appearance of the FE model of the two-stage baseplate. 91

Figure 5-5 View of the laboratory vibration response measurement at the centre of the baseplate under the free boundary condition. 93

Figure 5-6 (**a**) Fine mesh for the FE model of the baseplate showing the impact and the response point (red circle), (**b**) comparison between the measured and the predicted accelerance at the centre of the baseplate. 93

Figure 5-7 View of the measuring setup for vibration responses of the free baseplate. The numbers 1-9 indicate the measured positions; the red mark indicates the impact point. 94

Figure 5-8 Comparisons of the first four modal frequencies and mode shapes identified experimentally and those predicted from the FE model of the baseplate. 95

Figure 5-9 View of the rig setup for the measurement setup of the two-stage baseplate.96

Figure 5-10 Schematic view of the rig setup for the measurements. 96

Figure 5-11 Top view of the two-stage baseplate showing the numbered locations for the excitation points. 97

Figure 5-12 Comparison of the measured driving point accelerance on the two-stage baseplate for different values of applied torque. 98

Figure 5-13 Top view of the excitation points (1-15 for vertical direction), purple arrows for lateral direction. Sensor locations for vertical and lateral directions are also shown. 98

Figure 5-14 Comparison of the first four modal frequencies and mode shapes between the measured and the FE model of the constrained two-stage baseplate with lower pad stiffness of 80 MN/m. 99

Figure 5-15 Comparison between the measured and predicted point accelerance for the two-stage baseplate at location 5 for stiffness of 80 MN/m. 100

Figure 5-16 Comparison between the measured and predicted point accelerance for the two-stage baseplate at location 5 for stiffness of 85, 75 and 65 MN/m for bolting torque of 400 Nm. 101

Figure 5-17 The combined structure of the two models; rail (2.5D FE model), railpads (discrete springs), baseplate and lower pad (3D FE model) and slab (assumed rigid). 102

Figure 5-18 Schematic view of the combination of the two models. 103

Figure 5-19 Schematic view for impact force and receiver locations. 104

Figure 5-20 Mobility magnitude and phase of the two-stage baseplate for force at location 5 and the response at positions 1, 2, 4 and 5 calculated using the FE model. 104

Figure 5-21 Comparison between measured and predicted driving point mobility excited above a fastener for Pandrol railpad No.1, No.2, No.4 and No.8. 105

Figure 5-22 Comparison between measured and predicted driving point mobility and phase of the two model (Timoshenko and 2.5D) excited above a fastener for Pandrol railpad No.1 and No.4. 106

Figure 5-23 Comparison between measured and predicted TDR for Pandrol railpad No.1, No.2, No.4, and No.8. 107

Figure 5-24 Measured locations on the first baseplate. 108

Figure 5-25 Baseplate transmissibility magnitude: **(a)** measured and **(b)** predicted. 109

Figure 5-26 Baseplate average of the three-point transmissibility magnitudes **(a)** first baseplate and **(b)** second baseplate (only three available measured locations: 2, 3 and 4); the force is applied above the baseplate. 109

Figure 6-1 Schematic view of a baffled surface representing the baseplate (not to scale).112

Figure 6-2 **(a)** Source locations on the baseplate surface ($\mathrm{d}x = \mathrm{d}y = 0.01\ \mathrm{m}$), **(b)** far-field receiver locations. 113

Figure 6-3 **(a)** Sound radiation ratio and **(b)** radiated sound power from a baffled surface area of the two-stage baseplate with different velocity allocation. 114

Figure 6-4 Radiation ratios for a baseplate with different dimensions and unit velocity.115

Figure 6-5 Schematic view of a baffled surface of the three adjacent two-stage baseplates. 116

Figure 6-6 **(a)** Source location segments ($\mathrm{d}x = \mathrm{d}y = 0.01\mathrm{m}$) **(b)** far-field receiver locations from the three baseplates. 116

Figure 6-7 Comparison of sound radiation ratios **(a)** and **(b)** sound radiated power from a baffled surface area for the single and the three baseplates....................117

Figure 6-8 An isometric view of the two-stage baseplate (image from Pandrol, used with permission). 117

Figure 6-9 (**a**) A simple 3D BE model of the baseplate, (**b**) mesh of the baseplate. 118

Figure 6-10 A comparison of **(a)** sound radiation ratio, **(b)** radiated sound power from a simple 3D BE model and analytical model of the baseplate. 118

Figure 6-11 A detailed 3D BE model of the two-stage baseplate. 119

Figure 6-12 A comparison of **(a)** sound radiation ratio and **(b)** radiated sound power from a detailed and simple BE model of the baseplate. 119

Figure 6-13 3D BE model of the simple baseplate with UIC60 rail attached. 120

Figure 6-14 Comparison of **(a)** sound radiation ratio, **(b)** sound radiated power predicted from the 3D BE model of the simple baseplate and from the model that includes scattering by the rail. 120

Figure 6-15 Schematic view of the force locations (railpad area in the green rectangle) and response points (blue circles) on the 3D baseplate model. 121

Figure 6-16 **(a)** Mobility magnitude and **(b)** phase with frequency for the outside response points due to force at the centre of the baseplate. 122

Figure 6-17 Forces at the railpad area due to a unit force on the railhead obtained from discretely supported track model using the properties of railpad No.1. 123

Figure 6-18 The calculated velocities at 300 Hz allocated to their respective areas on the baseplate surface (blue colour represents regions with velocity of zero (holes and railpad area). 124

Figure 6-19 **(a)** Velocity magnitude frequency spectra of the baseplate segments and **(b)** one-third octave band frequency spectrum of the average squared velocity, all for the baseplate below the excitation point. 125

Figure 6-20 **(a)** Sound radiation ratio spectrum and **(b)** one-third octave band frequency spectrum of the radiated sound power of a single baseplate with railpad No.1 for a unit force on the rail head. 125

Figure 6-21 Schematic view of the seven baseplates spaced 0.65 m apart. 126

Figure 6-22 Predictions using the different number of baseplates **(a)** sound radiation ratio and **(b)** one-third octave sound radiated power for railpad No.1 properties. 126

Figure 6-23 Average vibration of seven baseplates over the surface area outside the railpad region is determined using the bi-block sleeper model in TWINS (rigid) and using the combined 2.5D FE and COMSOL model (flexible) for railpad No.1 properties and unit roughness. 128

Figure 6-24 Comparison of sound power from the baseplate obtained from the bi-block model and the combined 2.5D FE and COMSOL model for railpad No.1, **(a)** for unit roughness, **(b)** for actual roughness spectrum. 128

Figure 6-25 A-weighted sound power for the rail, wheel and baseplates for railpad No.1 using the bi-block model. 129

Figure 6-26 A-weighted sound power for the rail, wheel and baseplates for railpad No.1 using the bi-block model for the rail and the combined 2.5D FE and COMSOL model for the baseplate. 129

Figure 6-27 Schematic view of the half-width slab track...130

Figure 6-28 View of a single slab unit with two sets of the two-stage baseplate installed.130

Figure 6-29 View of the 6 m half-width slab track assembled in the reverberation chamber for the measurements..131

Figure 6-30 Full schematic view of the measurement setup..131

Figure 6-31 Schematic view of FEM nodes location **(a)**, and **(b)** picture of the baseplate showing some of the measured points (red dots). 132

Figure 6-32 Comparison of the measured and the predicted driving point mobility of the baseplate with the impact at the centre of the baseplate **(a)** magnitude and **(b)** phase......132

Figure 6-33 Spectrum of the measured and predicted mean squared mobility of the baseplate: **(a)** narrowband, **(b)** one-third octave band. 133

Figure 6-34 Photographic view of the measurement setup, showing the sensor next to the baseplate and at the centre of the baseplate next to the impact force location. 134

Figure 6-35 Measured mobility magnitude measured at the driving point on the baseplate and the slab in **(a)** narrowband and **(b)** one-third octave band. 134

Figure 6-36 Setup for baseplate acoustic measurement. 135

Figure 6-37 Measured sound pressure level and background noise inside the reverberation chamber. 136

Figure 6-38 Measured acceleration with the accelerometer at the centre of the baseplate. Also shown is the background signal......137

Figure 6-39 Comparison between the measured and predicted **(a)** radiation ratio, **(b)** radiated power per unit mean square force for a single baseplate. 137

Figure 6-40 View of the rail damper contains steel mass and elastomer. 139

Figure 6-41 View of the setup showing the rail clip and isolator. 138

Figure 6-42 Transmissibility ratio between the baseplate and the rail **(a)** in narrowband, **(b)** in one-third octave band. 139

Figure 6-43 Impact locations: **black** circles along the railhead (32) and **red** circles along the railfoot (32). 140

Figure 6-44 Rail vibration measurements setup showing two attached accelerometers.140

Figure 6-45 Measured driving point mobility of the clipped rail with railpad No.1**:** **(a)** magnitude and **(b)** phase. 141

Figure 6-46 Measured mean squared rail mobility for the clipped case showing results for the two sensors: **(a)** narrowband and **(b)** one-third octave band. 141

Figure 6-47 Measured mean square mobility for the lifted and clipped cases, measured above baseplate. **(a)** In narrowband; **(b)** in one-third octave band. 142

Figure 6-48 Measured radiation ratio for the rail: **(a)** in narrowband and **(b)** in one-third octave bands. 142

Figure 6-49 Comparison of rail radiation ratio between the measurements and predictions from the 2D model for the same rail properties. **(a)** Measured result for lifted rail, predicted result above the ground and **(b)** measured result for rail resting on the pads, predicted result partially attached to the ground and partially above the ground...143

Figure 6-50 The predicted spatially averaged squared transfer mobilities for eight baseplates and the 6 m section of the rail, **(a)** in narrowband, **(b)** in one-third octave bands.146

Figure 6-51 The ratio of spatially averaged squared transfer mobilities for eight baseplates and 6 m of rail: **(a)** in narrowband and **(b)** in one-third octave bands................146

Figure 6-52 Comparison between the measured and predicted spatially-averaged squared transfer for eight baseplates and 6 m of rail in one-third octave. 147

Figure 6-53 Comparison ratio of spatially averaged squared transfer mobilities for eight baseplates and 6 m of rail in one-third octave bands. 147

Figure 6-54 Radiated sound power predicted for a unit force on the rail using the radiation ratio from [96] and of new developed model of the flexible baseplates. 148

Figure 6-55 Comparison of predicted sound power from the rail and the rail with addition of the baseplate contribution. 148

Figure 6-56 Comparison sound power of measured rail clipped and predicted from the total of the baseplate contribution for a unit force above the railhead...................149

Figure 7-1 View of the two-stage baseplate showing (**a**) the actual baseplate, (**b**) the nodes of the simplified model used in **Chapter 6**, (**c**) full vibrating surface, (**d**) vibrating surface with reduced sized holes. 152

Figure 7-2 Effect of changing baseplate surface area; results shown for three baseplates: (**a**) radiation ratio and (**b**) radiated power for a unit mean-square force on the rail. 153

Figure 7-3 Comparison of the rail mobilities between Timoshenko beam model and coupled 2.5D-FE model: (**a**) mobility magnitude (**b**) phase of the mobility. 155

Figure 7-4 Contact force for the interaction between rail and wheel for a unit roughness (a) narrowband and (b) third octave band. 156

Figure 7-5 Comparison of total radiated power from the track: (**a**) using the original representation of the baseplate with bigger holes, (**b**) the holes size reduce by increasing the vibrating the surface area by 46%, (**c**) the holes reduced in size, increasing the vibrating surface area by 92% and (**d**) comparison for baseplate power contribution with increase in area...157

Figure 7-6 A-weighted sound power for the rail, the wheel, the baseplate and the total.158

Figure 7-7 Comparison of the baseplate radiated power represented as a rigid mass and a flexible plate. 158

Figure 7-8 Baseplate FE model: (**a**) original baseplate, (**b**) thickness of the original baseplate is two times (2H) and (**c**) four times the original baseplate thickness (4H). 159

Figure 7-9 Comparison between the driving point mobilities predicted from 3D FEM of the baseplate for different thickness due to the impact at the centre of the baseplate: (**a**) magnitude and (**b**) phase: original, double (2H) and quadruple (4H). 160

Figure 7-10 Comparison between the spatially averaged baseplate squared mobilities for a unit force at the railhead above the baseplate for different thickness of the baseplate: (**a**) in narrowband and (**b**) third octave band: original, double (2H) and quadruple (4H). 160

Figure 7-11 TDR predicted from the 2.5D/3D FE model for railpad No.1 with different baseplate thicknesses: original, double (2H) and quadruple (4H). 161

Figure 7-12 Comparison of the mobility ratio between the baseplate and the rail: (**a**) in narrowband and (**b**) in one third-octave band: original, double (2H) and quadruple (4H). 161

Figure 7-13 Comparison between the radiation ratios for the baseplate with different thickness: original, double (2H) and quadruple (4H)..162

Figure 7-14 Comparison of the radiated power from 8 baseplates per unit mean square force on the rail for the baseplates with different thickness: original, double and quadruple. 162

Figure 7-15 Comparison of the predicted radiated power using different thickness of the baseplate for railpad No1: (**a**) rail, (**b**) baseplate and (**c**) total. 163

Figure 7-16 Comparison for the driving point mobilities from the coupled 2.5D-FE model for different railpad stiffness: (**a**) magnitude and (**b**) phase. 165

Figure 7-17 Comparison of the TDR predicted from the coupled 2.5D-FE model for different railpad stiffness. 165

Figure 7-18 Comparison of the predicted radiated sound power using different stiffnesses of the railpad: (**a**) rail, (**b**) baseplate and (**c**) total. 166

Figure 7-19 The overall predicted radiated power of the rail and baseplate against stiffness. 167

Figure A-1 (**1**) railpad specimens (No. A-13), (**2**) FCA fastener system No. A-23. 175

Figure A-2 Dynamic stiffness magnitude at 300 Hz plotted against static preload: (**a**) No.A1-A4 (Pandrol), (**b**) other available pads (No.A5-A7), (**c**) No. A8-A12 (SBB). 175

Figure A-3 Loss factor at 300 Hz plotted against static preload: (**a**) No.A1-A4 (Pandrol), (**b**) other available pads (No.A5-A7), (**c**) No. A8-A12 (SBB). 176

Figure A-4 (**a**) Dynamic stiffness magnitude and (**b**) loss factor at 300 Hz plotted against static preload for railpad No.A13. 176

Figure A-5 (**a**) Dynamic stiffness magnitude and (**b**) loss factor at 300 Hz plotted against static preload for lower pad No.A14 with railpad No.A3. 177

Figure A-6 (**a**) Dynamic stiffness magnitude and (**b**) loss factor at 300 Hz plotted against static preload for No.A15 single stage baseplate only. 177

Figure A-7 (**a**) Dynamic stiffness magnitude and (**b**) loss factor at 300 Hz plotted against static preload for No.A16 two-stage baseplate only with no pads. 178

Figure A-8 (**a**) Dynamic stiffness magnitude and (**b**) loss factor at 300 Hz plotted against static preload for two-stage baseplate with different lower pads (No.A17 – No.A22). 178

Figure A-9 FCA rail fastener system **(a)** top view, **(b)** bottom view No.A23. 179

Figure A-10 Dynamic stiffness magnitude plotted against frequency for FCA fastener system No.A23. 179

Figure A-11 **(a)** dynamic stiffness and **(b)** damping loss factor at 300 Hz plotted against static preload for FCA fastener system No.A23. 180

Figure A-12 China baseplate fastening system Type A **(a)** railpad only **(b)** Baseplate and railpad No. A-24. 180

Figure A-13 **(a)** Dynamic stiffness magnitude and (**b**) phase of the dynamic stiffness plotted against frequency, (**c**) dynamic stiffness and **(d)** damping loss factor at 160 Hz plotted against static preload for railpad only No.A-24. 181

Figure A-14 **(a)** Dynamic stiffness magnitude and (**b**) phase of the dynamic stiffness plotted against frequency, (**c**) dynamic stiffness and **(d)** damping loss factor at 160 Hz plotted against static preload for the baseplate and lower pad only No.A-25. 182

Figure A-15 **(a)** Dynamic stiffness magnitude and (**b**) phase of the dynamic stiffness plotted against frequency, (**c**) dynamic stiffness and **(d)** damping loss factor at 160 Hz plotted against static preload for the full system baseplate, lower pad and railpad No.A-26. 183

Figure A-16 China baseplate fastening system Type B **(a)** railpad only **(b)** Baseplate and railpad No. A-27. 184

Figure A-17 **(a)** Dynamic stiffness magnitude and (**b**) phase of the dynamic stiffness plotted against frequency, (**c**) dynamic stiffness and **(d)** damping loss factor at 160 Hz plotted against static preload for railpad only No.A-27. 185

Figure A-18 **(a)** Dynamic stiffness magnitude and (**b**) phase of the dynamic stiffness plotted against frequency, (**c**) dynamic stiffness and **(d)** damping loss factor at 160 Hz plotted against static preload for baseplate only No.A-28. 186

Figure A-19 **(a)** Dynamic stiffness magnitude and (**b**) phase of the dynamic stiffness plotted against frequency, (**c**) dynamic stiffness and **(d)** damping loss factor at 160 Hz plotted against static preload for the full system baseplate and railpad No.A-29. ...187

Figure B-20 Laboratory dynamic stiffness setup for the Vanguard system at the UoS HSL.190

Figure B-21 Schematic view for measured static stiffness for Vanguard system. 190

Figure B-22 **(a)** Load with left and right deflection, **(b)** static stiffness with preload. 191

Figure B-23 Comparison of measured load-deflection curves with the data provided by Pandrol. 192

Figure B-24 Top view of accelerometer placement for vertical dynamic stiffness measurement of Vanguard system 193

Figure B-25 **(a)** Magnitude and **(b)** phase of complex vertical stiffness with frequency for various preloads of the Vanguard system. 194

Figure B-26 Vertical stiffness **(a)** magnitude and **(b)** loss factor as a function of preload for the Vanguard system. 194

Figure B-27 View of the experimental setup for the lateral dynamic stiffness for the Vanguard system. 195

Figure B-28 Schematic view of the measurements for the lateral stiffness of the Vanguard system showing sensors and impact location. 196

Figure B-29 Vibration ratio with frequency between the railhead and lower block for the preload of 10 kN: **(a)** magnitude and **(b)** phase. 197

Figure B-30 Magnitude **(a)** and **(b)** phase of the lateral dynamic stiffnesses with frequency. 198

Figure B-31 **(a)** Magnitude and **(b)** damping loss factor of the lateral dynamic stiffness with preload. 198

Figure B-32 Schematic view of the measurements of the lateral stiffness with sensors at the rail foot of the Vanguard system. 199

Figure B-33 **(a)** Magnitude lateral dynamic stiffness and **(b)** loss factor with preload. ...199

Figure B-34 Mobility **(a)** magnitude and **(b)** phase with frequency (RH= railhead), (RF =rail foot). 200

Figure B-35 SolidWorks model of the rail and dog bone plate. 200

Figure B-36 Lateral stiffness for the Vanguard system; measured at the railhead (RH), measured at rail foot (RF) and predicted by the model. 202

Figure B-37 Mobility magnitude with frequency showing the mode identification.........203

Figure C-38 Source and receiver structure coupled at multiple connection points through resilient elements [36]. 205

List of Tables

Table 2-1 Measured noise reduction obtained from the various wheel and track treatments in Silent Freight and Silent Track project to nearest whole dB [42]. 17

Table 3-1 Experimental rig components 35

Table 3-2 Parameter values of the simple 2DOF model of the rig 39

Table 3-3 Assumed stiffness and loss factor values 45

Table 3-4 The details of the tested resilient elements 49

Table 3-5 Summary of measured railpad stiffness and loss factor 51

Table 3-6 Lower pads used in two-stage baseplate system 56

Table 4-1 Adopted TDR measurement positions..68

Table 4-2 Measurement equipment...69

Table 4-3 Measurement equipment used for baseplate vibration 81

Table 5-1 Track parameters used in the track model...88

Table 5-2 Parameters used in the FE model of the two-stage baseplate 91

Table 5-3 Comparison of the measured and predicted natural frequencies of the baseplate 93

Table 7-1 Track properties used in the models that represent the measured track in Doncaster 154

Table 7-2 Typical parameters used in TWINS 154

Table 7-3 Summary of predicted radiated power for the three thicknesses 164

Table 7-4 Summary of prediction radiated power for different stiffness 166

Table A-1 The details of extra the tested resilient elements..173

Table B-2 Moments of inertia and total mass 200

Table B-3 Peak frequencies obtained from mobility magnitude data..........................201

Declaration of Authorship

I, Boniface Hima, declare that this thesis entitled THE INFLUENCE OF BASEPLATE FASTENING SYSTEMS ON RAILWAY ROLLING NOISE and the work presented in it are my own and have been generated by me as the result of my own original research.

I confirm that:

1. This work was done wholly or mainly while in candidature for a research degree at this University;
2. No part of this thesis has previously been submitted for a degree or any other qualification at this University or any other institution;
3. Where I have consulted the published work of others, this is always clearly attributed;
4. Where I have quoted from the work of others, the source is always given. With the exception of such quotations, this thesis is entirely my own work;
5. I have acknowledged all main sources of help;
6. Where the thesis is based on work done by myself jointly with others, I have made clear exactly what was done by others and what I have contributed myself;
7. Parts of this work have been published as:

   B. Hima, D. Thompson, G. Squicciarini, E. Ntotsios D. Herron, Estimation of track decay rates and noise based on laboratory measurements on a baseplate fastening system, The 13th International Workshop on Railway Noise (IWRN13, September 2019), Notes of Numerical Fluid Mechanics and Multidisciplinary Design 150, 621-628, 2021.

Signed: ....

Date:...

Acknowledgements

Completing the EngD has been a challenging journey for me and COVID-19 has made it even more difficult. I would not have been able to complete the last four years of study in ISVR without the support from many people, and I would like to express my gratitude to them.

First and foremost, I would like to express my sincere gratitude to my main supervisor, Professor David Thompson, for the advice, insight, guidance, and support he has provided throughout my study. I learned from him the rigorous research attitude and English writing skills. Not only did I learn the academic knowledge but also life experiences; his hardworking attitude and his enthusiasm for this research area inspired me when I had a hard time. He has never given up on me, especially during the first 18 months where I struggled a lot in many things, including remembering meeting outcomes as well as insufficient writing skills as I was not aware of my specific learning difficulties. He supported me to get the right help I needed to continue with my research.

I am also tremendously indebted to my co-supervisors, Dr Giacomo Squicciarini and Dr Evangelos Ntotsios, for their help, advice, support, guidance and supervision in my research. They have helped with all my measurements during my study, from setting up the equipment to helping carry out the measurements and also taught me how to analyse results. A big thank you for their patience, especially when I had problems with programming and modelling, they were always there to help and explain everything in detail. They were also encouraging and motivating and inspired me in all areas of my research. Discussions with them were always useful and enjoyable.

I would like to thank Dr David Herron from Pandrol Limited who took the position of industrial supervisor for my project. Special thanks go to him for organising access to the site for in-situ measurements in Doncaster and the supply of the samples and equipment needed for the measurements. Also, for the advice and technical support during my research.

I would like to acknowledge the ISVR Consulting team for all support in the measurements, with special thanks to Phil Oxborrow. He was always there to provide technical support, advice and amend the rig; he did everything to make the measurements possible. I would also like to thank Dr Martin Toward, Dr Daniel Lurcock and Dr John Fithyan from ISVR Consulting for their advice, support and providing the acoustic measuring equipment for all my measurements.

Further appreciation goes to my dyslexia tutor, Dorota Wiatr; thank you for spending several hours teaching me the techniques to help me with my disability as well as guiding me in proofreading my thesis. Sorry, engineering is not your field, but you have done your upper best in bearing with me and reading with me all my chapters. Thank you.

Many thanks to my good friends and my colleagues in the Dynamics Group. This is a fantastic group, as a family. Dr Xianying Zhang (thank you for allowing me the access and use of your 2.5D Model), Dr Hongseok Jeong, Dr Jin Zhang, Dr Hui Li, Dr Xiaowan Liu, Davide Raffaele, Sorawit Limthongkul and Rahma Nassoro. I am very grateful to them for their moral support and help with measurements. The lunches and dinners we had together, the football matches we watched together during the World Cup, the office room where we studied together, the discussions with them were precious; the same PhD/EngD journey we had together are all valuable memories to me.

I gratefully acknowledge the financial support from the Engineering and Physical Sciences Research Council (EPSRC) and from industrial sponsor Network Rail in funding this project, without which I could not have achieved this success.

I would also like to express my gratitude to all those whom I did not mention explicitly.

Most of all, I am deeply grateful to my family and friends, particularly to my wife Siaeli Hima and my boys Benjamin and Barack Hima. The endless love and unconditional support from them were the vital power for me to finish this journey. The least I can do is to dedicate this work to them.

List of Symbols

A	Area
$A(x_\mathrm{n})$	Measured transfer frequency response (mobilities or accelerance)
$A(x_0)$	Measured point frequency response (mobilities or accelerance)
c_0	Speed of sound in air
DR	Decay rate
f	Frequency
F	Force
$[F]$	Force matrices
F_e	Harmonic force
f_i	Resonance frequency
F_t	Transfer force
$H_\mathrm{i,j}$	Transfer functions
I	Intensity
i	$\sqrt{-1}$
K	Dynamic stiffness
k_D	Direct stiffness
k_i	Resilient element stiffness
k_T	Transfer stiffness
$[m]$	Mass matrices
m_b	Mass of the baseplate
m_1	The upper mass
m_2	The lower mass
$\overline{p^2}$	Mean square pressure fluctuation
p_rms	Root-mean-square pressure
r	Distance
S	Surface area of vibration
$[V]$	Velocity matrices
$\overline{v^2}$	Mean square velocity
v_n	Surface normal velocity
W	Sound power
X_i	Harmonic displacement amplitude

List of Symbols

$\ddot{X}_{\mathrm{i}}$	Acceleration
Y	Mobility
$[Y_{i,\mathrm{j}}]$	Mobility matrices
Δ	Relative distance between adjacent points
$\int$	Integration
η	Loss factor
λ	Wavelength
ρ_0	Density of air
$\rho_0 c_0$	Specific acoustic impedance of air
σ	Radiation ratio
ω	Angular frequency

Abbreviations

BE	Boundary Element
BEM	Boundary Element Method
dB	Decibel
DOFs	Degrees of Freedom
EPSRC	Engineering and Physical Sciences Research Council
EVA	Ethylene-vinyl acetate
FE	Finite Element
FLOSS	Finite Line of Simple Sources
HSL	Heavy Structure Laboratory
ISVR	Institute of Sound and Vibration Research
MATLAB	A mathematical software package
NR	Natural rubber
SAFE	Semi-Analytical Finite Element
SPL	Sound Pressure Level
TDR	Track Decay Rate
TWINS	Track-Wheel Interaction Noise Software
UoS	University of Southampton
WANDS	Wave Number Domain Software
WFE	Waveguide Finite Element
2D	Two Dimensions
2.5D	Two and a half Dimensional
3D	Three Dimensions

Chapter 1 Introduction

1.1 Background and motivation

Railways are generally considered as an environmentally friendly means of transport, and their role has been expanded in recent years both for long-distance travel for passengers or freight carriage and short-distance metro systems in cities. The operation of railway transport results in considerably less pollution, energy use and CO_2 emissions per passenger-km than road or air transport [1]. However, a large proportion of the population worldwide is exposed to noise pollution caused by traffic, industrial and recreational activities, especially in urban areas, and this includes railways. Indicatively, around 20 per cent of inhabitants of Western Europe have been estimated to suffer from noise levels that scientists and health specialists consider to be unacceptable [2]. According to the World Health Organisation (WHO), train traffic noise is rated as the third most dangerous source of noise pollution in large cities while air traffic noise is second and road traffic noise is first [3]. The problem of noise and vibration along a railway route has increased significantly in recent years with the surge of more frequent, faster, heavier and longer train operations, especially with the introduction of high-speed trains. This has led the public and governments to increase the pressure on train operators to minimise the vibration and noise generated by trains. The reduction of vibration will also result in less degradation of the track superstructure and rolling stock; as an added advantage of these measures maintenance and the associated costs will also decrease.

By 2018, high-speed train operations (speeds of 200 km/h or above) covered around 60,000 km worldwide, of which 19,600 km were in Europe, and over 40,000 km in the rest of the world including 36,000 km in China [4]. However, in Europe, a further 3000 km were planned or under construction, and another 8,000 km under long-term planning, while in the rest of the world a further 20,000 km were intended or under construction, and 21,000 km under long-term planning (the majority of this in Asia, especially China) [5, 6]. Although the railway is regarded as a sustainable and environment-friendly means of transport in daily life, the opposition to new railway developments by local residents is often focussed on the impact of noise and vibration. As noise and vibration concerns have grown significantly, many countries have generated regulations for noise and vibration compliance. This includes the TSI (Technical Specifications for Interoperability) for Europe, which applies to all new rolling stock [7, 8].

Railway airborne noise is generated by two main mechanisms: structural vibration caused by wheel/rail interaction and aerodynamic noise due to the air flowing over solid objects. Aerodynamic noise is a dominant source of noise only for high-speed trains moving at speeds above about 350 km/h. For trains running below 300 km/h, the track and the wheels are the main sources of noise. For trains running along straight tracks, this occurs mostly in the form of rolling noise [1]. The surface roughness of the rails and the wheels causes a relative displacement at the wheel/rail interface, which makes the wheel and the track vibrate. The vibration of the wheel and track leads to sound radiation. **Figure 1-1** shows a visual representation of the mechanism of rolling noise caused by wheel and rail vibration induced at the wheel/rail contact area. The main wavelengths of roughness that are relevant to rolling noise are between about 5 and 500 mm. Rolling noise increases in level with $30\log_{10}(\mathrm{V})$, where V is the train speed, i.e. $+9\ \mathrm{dB}$ for a doubling of the speed [9].

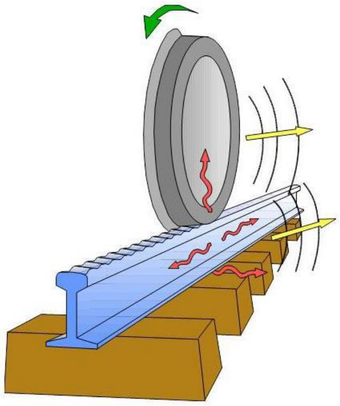

Figure 1-1 Illustration of the mechanism of generation of rolling noise [1].

Another type of noise and vibration phenomenon generated by trains is related to the propagation of waves in the soil beneath and beside the track. It is known as ground-borne vibration. The components that cause this phenomenon are the quasi-static excitation due to the moving axle loads, and the dynamic excitation, due to the wheel and track unevenness, a mechanism similar to the generation of rolling noise. This vibration is experienced in the surrounding buildings as feelable vibration, in the range 2 – 80 Hz, and as reradiated noise (ground-borne noise) in the range 30 – 250 Hz [1, 10-13].

Since the 1970s, research has been conducted to understand rolling noise. In [14-17], Remington summarised his work on theoretical modelling of rolling noise. His approach is divided into several steps, from the wheel and rail vibration to the inclusion of the contact stiffness and the ground effect on sound propagation to improve the modelling. Following Remington's work, a more comprehensive prediction model for rolling noise prediction was developed by Thompson et al. [18, 19], known as TWINS (Track-Wheel Interaction Noise Software). A schematic diagram of the rolling noise generation mechanism is shown in **Figure 1-2**. The software has been widely used in Europe and elsewhere as a tool for the prediction of railway noise and it has been verified by measurements.

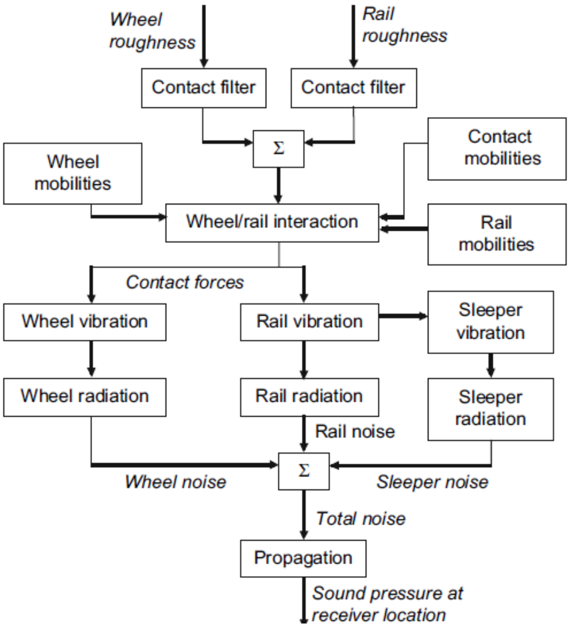

Figure 1-2 Schematic diagram of the rolling noise generation mechanism [1].

Figure 1-3 shows a typical prediction of the contribution of the rail, sleepers and wheel to total noise calculated with TWINS. The results are based on a freight vehicle travelling at 100 km/h on a ballast track with a relatively soft railpad (200 MN/m, dynamic stiffness) [18, 19]. From the predictions, it is shown that at low frequencies, below 500 Hz, the main contributor to the noise is the sleeper, in the mid-frequency range of 500 to 1600 Hz, the noise is mainly due to the rail, and at higher frequencies, it is caused by wheel vibration [1].

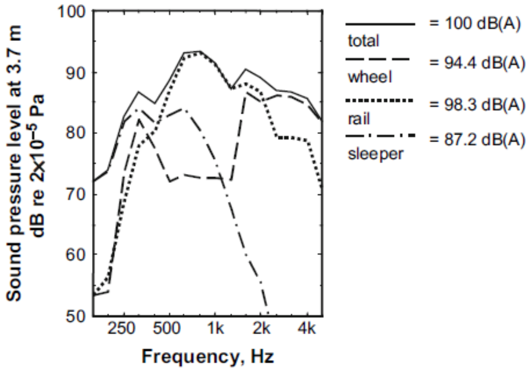

Figure 1-3 Typical predictions showing contributions of the wheel, rail and sleeper noise using TWINS model [1].

Both experimental, i.e. [20-22], and theoretical studies using models such as the TWINS model show that most often the track is the dominant source of noise from railways below 2 kHz. Therefore, the interest in controlling and reducing noise from the track has greatly increased. In order to achieve that, it is vital to understand the causes of noise and vibration from the railway to be able to provide the correct mitigation measures at the source. The dynamic behaviour of the rail fastening system has a significant influence on the noise and vibration phenomena in railways. For example, the use of a stiff railpad can result in the reduction of the rail component of rolling noise as the rails are more firmly coupled with the sleeper and therefore, they vibrate less. However, the use of a stiff pad can increase the sleeper or slab contribution as well as the vibration transmission to the ground. A soft pad will result in an increase in the rail vibration, with consequently increased noise radiation, but provides better isolation of ground vibration.

It is a great challenge to be able to reduce noise as well as vibration transmission at the same time. By modifying only the railpad stiffness, if one is reduced, the other one increases. The use of more complex resilient elements, such as two-stage rail fastening systems which contain a steel plate and two pads, could have the potential to control both rolling noise and ground vibration. The two pads of the two-stage fastening system are placed as follows; one is on top of the steel plate with the rail sitting on top of it, while the other one is inserted beneath the steel plate, between the plate and the sleeper or slab. The combination of different dynamic pad stiffnesses has the potential to reduce both rolling noise and ground-borne vibration.

As established above, the need for more trains, especially high-speed trains, will continue to grow, and one of the main challenges is the simultaneous reduction of radiated noise and ground vibration. Therefore, addressing the noise challenge by means of a track that is quieter and provides suitable vibration isolation is vital in obtaining future authorisation to build new railway lines. Hence the main reason to undertake this engineering doctorate research is to provide a solution that would reduce rolling noise from the track at the source. The focus is mainly on the baseplate fastening system with a double resilient layer commonly known as a two-stage baseplate fastening system. Such two-stage baseplates are suitable for installation on slab track for use with high-speed trains. However, the contribution of these baseplates to the noise radiation has not previously been studied. Therefore, this thesis will investigate the sound radiation from the track including the two-stage baseplate itself. The trade-off between noise and vibration is not studied here; this research is focused solely on the assessment of noise from the track. It is assumed that the transmission of vibration can be adequately controlled by using a baseplate system with a lower pad with suitable resilience.

1.2 Introduction to track systems

This section describes the most important components of the track and quantities that are adopted to describe its behaviour in this research.

1.2.1 Track structures

Two types of railway track structures and their components are shown in **Figure 1-4**. **Figure 1-4 (a)** presents a typical ballasted track, in which the rails are supported on railpads and attached with clips to the transverse sleepers, which may be made of concrete, wood or steel. The sleepers are supported by a layer of stones known as ballast. **Figure 1-4 (b)** shows a slab track with the rails supported on railpads and secured by clips, or by more advanced rail fastening systems with baseplates and either single- or double-layer pads. These are mounted on a concrete slab. The railpads are commonly made of natural or synthetic rubber (i.e., elastomeric rubber-like polymers such as ethylene-vinyl acetate rubber or EVA). **Figure 1-5** shows an exploded view of the rails, railpad, sleeper and fastening system, in this case for a system without a baseplate.

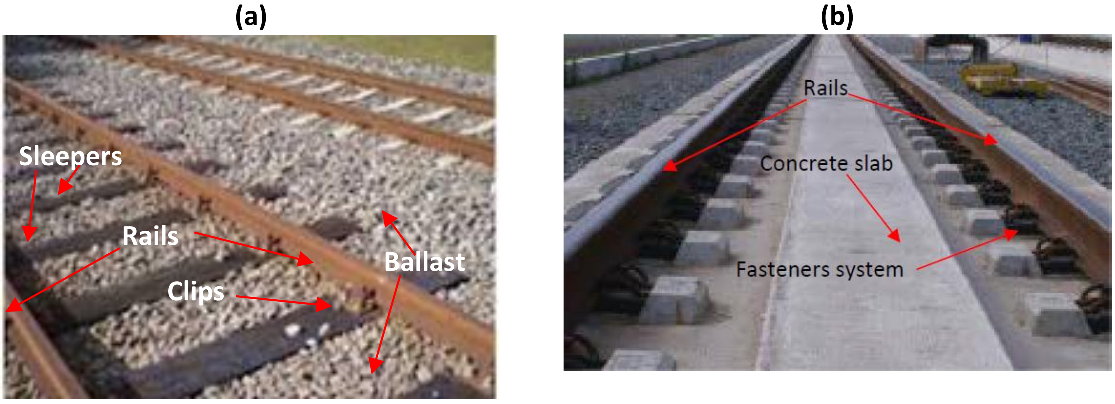

Figure 1-4 Two types of typical track construction showing the rails, railpads, fastener system, sleeper, ballast and slab **(a)** Ballasted track [23], **(b)** Slab track [24].

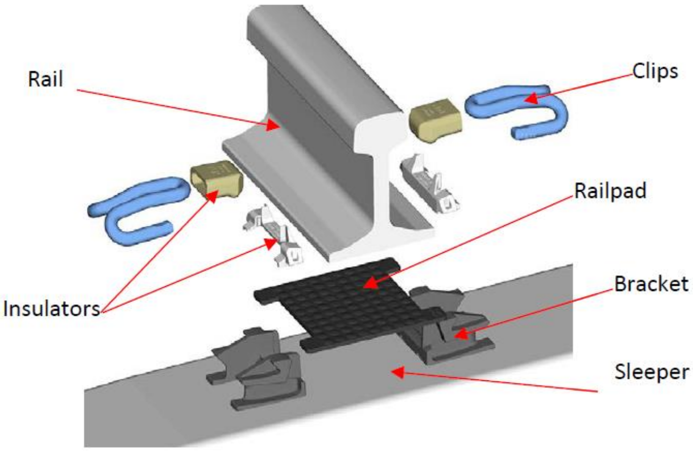

Figure 1-5 Exploded view of a standalone fastener showing the rail, railpad, clips isolator and bracket placed on the sleeper [1].

1.2.1.1 Single-stage baseplate system

The single-stage baseplate is a type of rail fastening system that secures the rail to a concrete sleeper, timber sleeper or slab track. It comprises a cast steel plate (baseplate) with shoulders to guide the rail horizontally and two elastic spring clips for applying a holding/downward force to the rail. Between the rail and the baseplate, there is the railpad and under the baseplate there is a stiff plastic layer designed for electrical isolation. **Figure 1-6** shows an example of a single-stage baseplate fastening system.

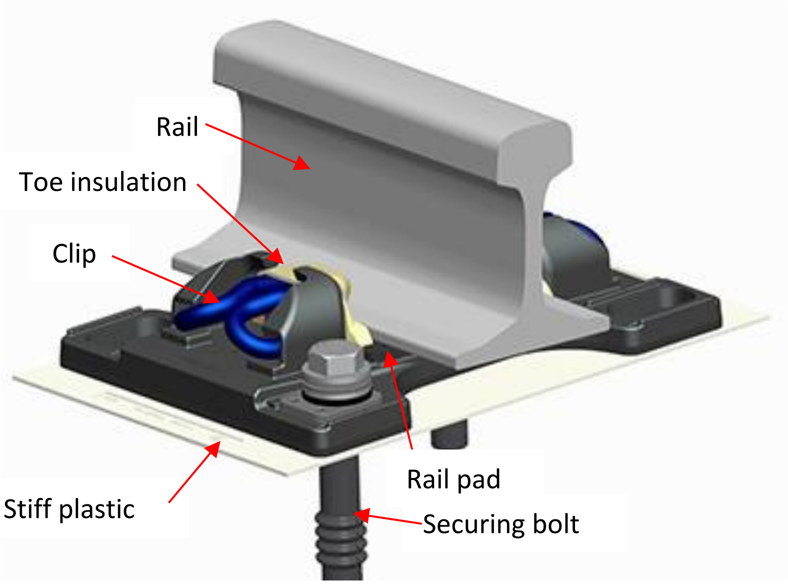

Figure 1-6 Single-stage fasteners system (Pandrol FAST CLIP SFC baseplate) [25].

1.2.1.2 Two-stage baseplate system

The two-stage baseplate is a type of rail fastening system, similar to the single-stage baseplate, but which contains two pads with different stiffness: an upper railpad, which is usually stiffer, and a lower pad, which is softer and is placed under the baseplate (replacing the stiff plastic electrical insulation used in the single-stage baseplate). **Figure 1-7** and **Figure 1-8** show a drawing and a photograph of a two-stage baseplate system. The two-stage baseplates are used as they introduce low dynamic stiffness. However to have low dynamic stiffness the baseplate has to be wider, as otherwise there would be excessive rail roll due to low torsional stiffness, which would cause gauge widening and potentially derailment. This research will also demonstrate that the uses of the two-stage baseplate allow a suitable choice of the combined stiffnesses of the two pads in series resulting in a low dynamic stiffness. The bolts and the spacer on the two-stage baseplate are used to hold the baseplate in position but also allow the lower pad to move freely in the vertical direction.

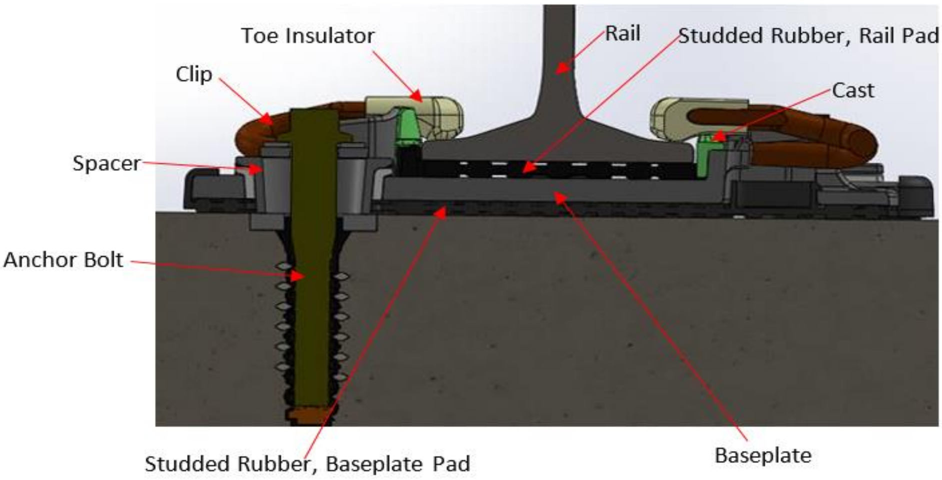

Figure 1-7 Schematic view of the Pandrol two-stage baseplate (drawing courtesy of Pandrol, used with permission).

Figure 1-8 The Pandrol two-stage baseplate.

1.2.1.3 Vanguard fastening system

The Vanguard System is a baseplate type of rail fastening system designed to support the rail by the web and to provide a very low vertical stiffness and hence a reduction in vibration transmission to the ground. With this design, the vertical stiffness can be very low while lateral stability is preserved by side shoulders. The Vanguard system consists of rubber wedges, a bump-stop pad and other supporting metal brackets, as seen in **Figure 1-9**. The rubber wedges support the rail with brackets and locking wedges. This system is suitable for use with concrete sleepers, timber sleepers and slab tracks on bridges, tunnels and viaducts [25]. Although this research focusses on conventional baseplate systems, the vertical dynamic stiffness of the Vanguard system has also been measured for comparison. Due to the time constraints, it was not possible to undertake a noise assessment of this system.

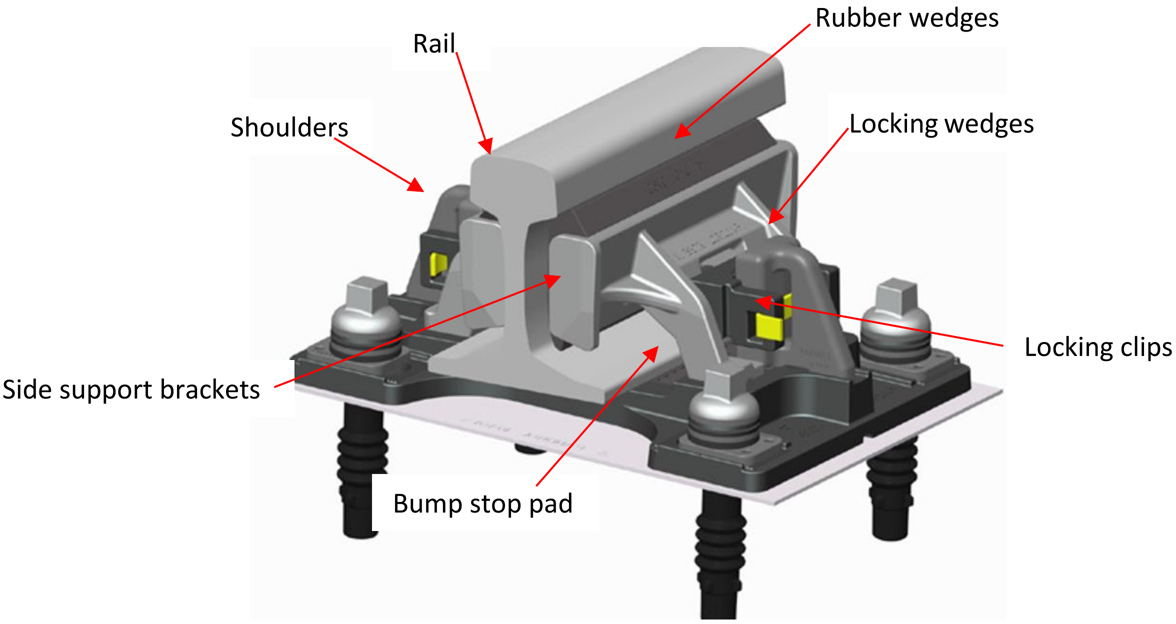

Figure 1-9 Schematic view of Vanguard fastening system from Pandrol Ltd [25].

1.2.2 Static and dynamic stiffness of track resilient elements

The static and dynamic stiffness of the resilient elements on the railway track play a key role in minimising the noise radiated by the track [1]. While the lateral stiffness and roll stiffness of the fastening system are of interest, it is usually the vertical stiffness that is the main consideration. Another importance of vertical stiffness is related to track deterioration and maintenance requirements [26].

Static stiffness

Static stiffness is defined as a ratio between the applied static force and the resulting static deflection. An elastomeric railpad has a non-linear load-deflection curve under a static loading condition. **Figure 1-10** shows a typical curve for an elastomeric pad; it can be seen that its stiffness increases with increasing load. Therefore, the static stiffness of the resilient fastening must be defined at a particular load, e.g. the wheel load of the train. The figure also shows the tangent and secant stiffness, which are two definitions of the static stiffness of a fastener. The secant stiffness is measured between 0 N and the wheel load. For small deflections around a mean load, the tangent stiffness can be used [27].

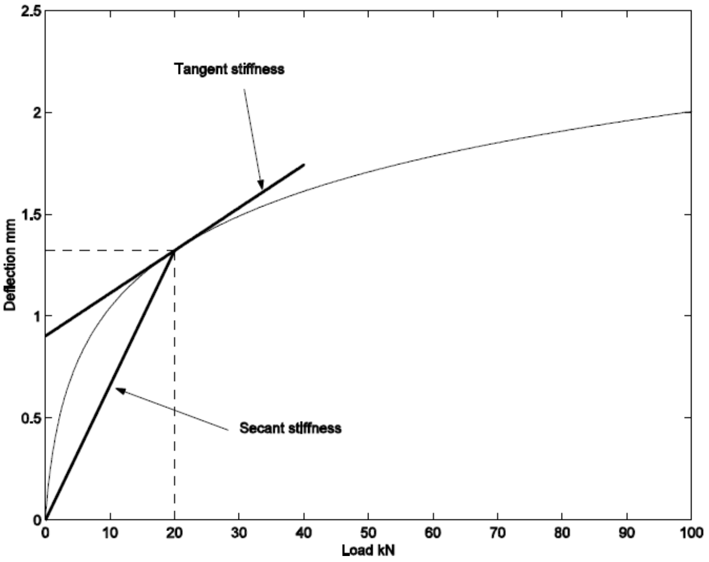

Figure 1-10 A typical load-deflection curve for an elastomeric railpad [28].

Dynamic stiffness

Dynamic stiffness is defined as the complex frequency-dependent ratio between the dynamic applied force and the resulting dynamic displacement. A rail fastening system contains elastomeric material exhibiting viscoelastic behaviour that changes with time when subject to stresses and strains.

Materials with viscoelastic properties produce lower deflections under dynamic loading in comparison to static loading. Therefore, the dynamic stiffness of these materials tends to be higher than the static stiffness. Besides, viscous effects cause lags in the deflection relative to the applied force. The dynamic stiffness of the material plays an important role in terms of noise and vibration attenuation on the track, i.e. for higher isolation, the fastening system is required to have a lower dynamic stiffness. Therefore, the optimisation of the dynamic stiffness of the resilient element is important in noise mitigation.

Dynamic stiffness can also be specified as low-frequency dynamic stiffness, normally performed at a frequency of 5 Hz, and high-frequency dynamic stiffness [29]. For the prediction of noise, it is the dynamic stiffness at higher frequencies with small strains that is needed [1, 30]. The dynamic stiffness of a material or resilient element can be measured in several ways, such as direct and indirect. In this research, the indirect method is adopted and measurements are performed up to 1 kHz [31].

The effect of stiffness on noise and vibration

The stiffness of resilient elements, such as railpads, affects the vibration of the rail and the degree of coupling between the sleeper and the rail. It results in changing the noise produced by the rail and the sleeper of the track. **Figure 1-11** shows the effect of pad stiffness on vibration propagation along the rail. For soft railpads, the sleepers are well isolated from the rail; this allows the vibration to propagate freely along the rail. However, for a stiff railpad, the transmission of vibration along the rail is restricted by the coupling between the sleeper and the rail. The vibration of the sleeper increases with a stiffer pad, which could result in a greater vibration transmission to the ground [1].

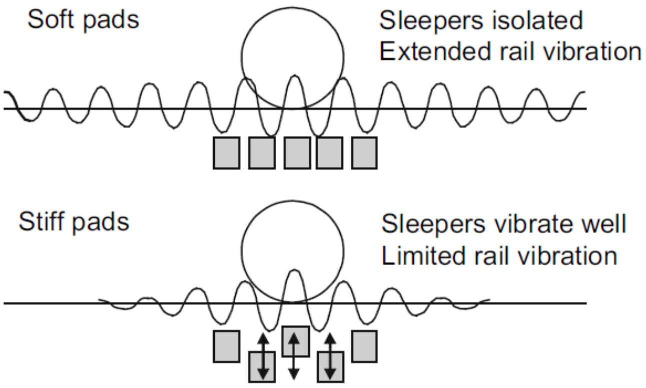

Figure 1-11 Illustration of the effect of the railpad stiffness on the coupling between rail and sleeper and on the damping of waves in the rail [1].

1.2.3 Track decay rate

When structural waves propagate along the track, they decrease in amplitude with distance from the excitation point. This is quantified by means of the Track Decay Rate (TDR) that expresses the amplitude decrease in dB/m [32]. It is usually represented in the form of one-third octave band spectra. It can be obtained using calculations, or it can be measured on track according to standards [33-35]. The TDR is also used in noise prediction models to evaluate the noise emission from the track.

1.3 Aims and Objectives

The main aim of this research is to establish the influence of baseplate fastening systems on the overall railway rolling noise. The research, therefore, aims to identify the key design parameters that affect the rolling noise. This knowledge will contribute to reducing rolling noise and controlling ground vibration. These aims are addressed by using laboratory and field measurements of vibration and noise as well as prediction models. It is assumed that vibration transmission can be adequately controlled by a suitable choice of resilient lower pad in the baseplate system.

To achieve these aims, the following steps have been accomplished:

a) Experimentally measure the dynamic stiffness of railpads and lower pads of the two-stage baseplate.
b) Measure TDRs of tracks equipped with two-stage baseplate systems.
c) Experimentally measure the sound radiation of the baseplate and the rail of a slab track.
d) Develop numerical models of track that account for the baseplates as a rigid or flexible body.
e) Develop a methodology that will enable the prediction of the sound radiation of the two-stage baseplate.

The main research objectives are as follows:

I. To determine what level of modelling detail is required for the baseplate fastening system to predict noise and vibration efficiently.

Laboratory measurements of the dynamic stiffness of different configurations of pads and baseplate systems are conducted. In situ track mobility and TDR measurements are taken for the same configurations. The predictions of TDR using the laboratory data and a simplified model of the track are obtained and compared with the measured decay rates. A finite element (FE) model of the baseplate is developed to calculate the mobilities at the interface between the baseplate and the rail, and it is used in a discretely supported track model based on a 2.5D FE model of the rail. This accounts for baseplate flexibility and enables the TDR to be calculated, which is then compared with the measurements.

II. To identify the significance of the sound radiation from the baseplate to the track noise.

Laboratory measurements of acoustic radiation are carried out on a 6 m half-section of slab track with a two-stage baseplate rail fastening system. Numerical predictions for the sound radiation from the baseplates are carried out using an analytical model based on the Rayleigh Integral method and the 3D boundary element (BE) method in COMSOL. The measurements and predicted results are compared.

III. To establish the effect of fastening system parameters on rolling noise.

Pad stiffness plays a vital role in the track design due to the coupling effect between rails and baseplates. For soft pads, the baseplates are well isolated from the rail, resulting in lower ground vibration but higher rolling noise, as the vibration can propagate more freely along the rail, and vice versa. A parametric study is conducted by changing the baseplate mass and pad stiffnesses to determine the effect on rolling noise.

IV. To establish how rail clips affect the vertical stiffness of the fastening systems.

The primary function of rail clips is to secure the rail in place when applying the train load. These clips can short-circuit the vibration isolation of the system and contribute to increases in dynamic stiffness in the track. Laboratory measurements of the dynamic stiffness of railpads and rail fastening systems with and without the rail clips are used to quantify this effect.

1.4 Novel contributions of the thesis

I. The level of detail required in the baseplate submodel used in predictions of rolling noise is identified.

In the current models for predicting rolling noise, such as TWINS, the baseplate is included as a rigid body. Moreover, the discrete rail fastening spacing is not considered. An FE model of the flexible baseplate is developed to calculate the mobilities at the interface between the baseplate and the rail and validated against measurements. This is then used in a discretely supported railway track model based on a 2.5D FE model for the rail using a receptance coupling approach, developed by Zhang et al. in [36]. By this approach, the discrete support model includes the flexibility of the baseplate and can be used to calculate the rail point mobility and track decay rate. Further study on the baseplate vibration has given more insight into the role of the baseplate in track vibration. Comparisons with measurements are used to validate the approach.

II. The contribution of the baseplate sound radiation to the rolling noise is quantified

The baseplates used on slab tracks may radiate significant noise contributions at low frequency due to their large area. A model that calculates the noise radiated by the baseplate when mounted in the track has been developed. Although similar procedures exist for the noise radiated by the sleepers, this has not previously been verified for baseplate systems. A full-scale section of a slab track is used to give additional laboratory data to validate the model predictions in terms of baseplate noise radiation.

III. A design sensitivity analysis of the baseplate is conducted in order to minimise rolling noise

In order to reduce the overall railway rolling noise and ground vibration, a design sensitivity study of key parameters of the baseplate fastening system is performed. A parametric study is conducted for sensitivity of the baseplate system in terms of its mass and the stiffnesses of the various layers of the resilient pads to identify how they affect the noise radiated from the whole track.

IV. The effect of rail clips on the vertical stiffness of the rail fastening system is established

The effect of rail clips on the vertical stiffness of the rail fasteners is shown to be negligible apart from their effect on the preload. This has been confirmed by taking laboratory measurements of the stiffness of the assembly with and without the clips under different preloads.

V. A database for vertical dynamic stiffness of railpads is produced

A large amount of data has been obtained in terms of the measured dynamic stiffness of railpads. These results are compiled in a database that stores the dynamic stiffness as a function of frequency and preload. The database is designed to allow researchers in the future to analyse and re-use the results obtained in this project and can constitute a reference set of results in this area of research. The data will be deposited in the University of Southampton ePrints system and registered with DOIs.

1.5 Thesis layout

The remainder of this thesis is organised as follows.

Chapter 2 presents a literature review of previous studies in this area of research. The main methodologies for measurements are covered and existing modelling approaches for vibration and sound radiation of the track are summarised.

The experimental procedure for dynamic stiffness is presented in Chapter 3 and it is supported by simple analytical modelling. Measurement results for two different types of baseplate as well as their component resilient elements are presented in this chapter. Appendix A lists measurement results for additional rail pads and Appendix B presents measurement results for the Vanguard fastening system.

Chapter 4 is focused on in-situ measurements of TDR and track mobility for a slab track equipped with two-stage baseplate fastening systems with different pads fitted.

In Chapter 5, models are developed for the vibration of a slab track fitted with two-stage baseplate systems. They account for the baseplate as a rigid mass or as a flexible plate. A detailed model of the two-stage baseplate is developed, and its vibration is studied and compared with measured data. Finally, the developed model is used to predict the TDR and track mobilities which are then compared with the measured data obtained in Chapter 4.

Chapter 6 presents the modelling of sound radiation from the baseplate with and without the presence of the rail. The results predicted from the models are then compared with laboratory measurements conducted on a 6 m long sample of a full-scale slab-track.

Chapter 7 analyses the sensitivity of the track noise to parameters of the baseplate. This chapter also identifies the parameters that need to be considered in the design of the baseplate for optimum reduction of rolling noise.

Finally, Chapter 8 presents a summary of the findings and gives an outline of the recommended future work.

Chapter 2 Literature review

Railway noise has been studied for several decades, especially the rolling noise associated with the track and wheel structural design. This chapter presents a summary of previous studies on rolling noise and methods for assessing the properties of the components of the track and its design. The effect of rail pad stiffness on railway noise is discussed in Section **2.1**, including the difference between slab tracks and ballasted tracks. Measurement methods for the dynamic stiffness of railpads are reviewed in Section **2.2**. Section **2.3** focuses on track decay rates and Section **2.4** on track vibration modelling. The sound radiation from the rail and sleeper are discussed in Sections **2.5** and **2.6**. Finally, Section **2.7** covers the measurement of the radiation ratio.

2.1 Railway noise and pad stiffness

Railpad stiffness is an important parameter that affects the rolling noise from the track. As mentioned in Section **1.2.2**, a stiff pad leads to high attenuation of rail vibration with distance along the track and an increase in the sleeper vibration. This will result in a reduction of the rail-radiated component of noise, but an increase of the sleeper component. On the other hand, a soft pad leads to a low sleeper noise component but greater rail noise, as the rail can vibrate over a greater length. When soft pads are used, they lead to reduced forces acting on the sleepers and consequently less damage to track components and reduced ground vibration. Thompson et al. [37] conducted measurements on a track fitted with three different types of railpads with different stiffness, installed on a dedicated 36 m long test track at the University of Southampton (see **Figure 2-1**).

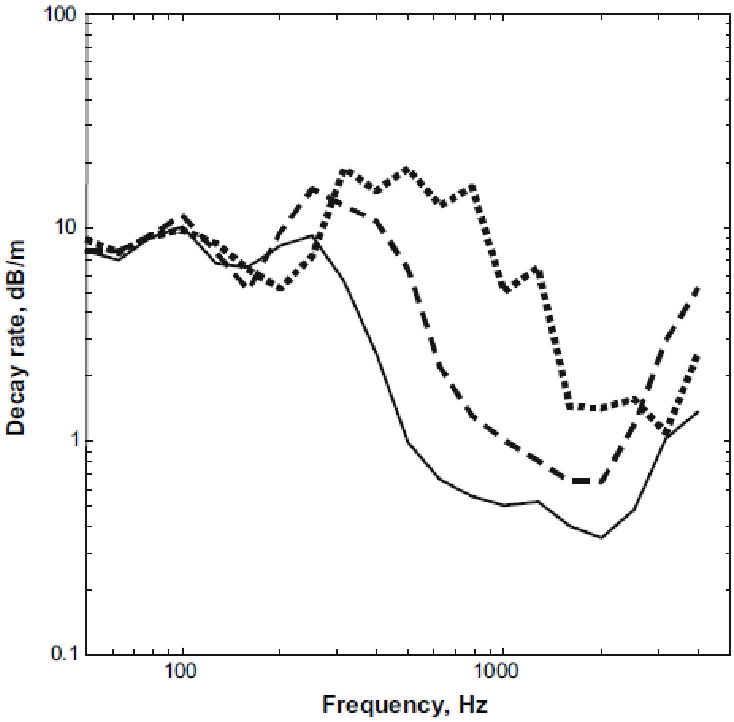

Figure 2-1 Measured effect of rail pad stiffness on track decay rates: same track fitted with three rail pads of different stiffnesses (approximately -125, ---270 and ···950 MN/m) [1].

The rail was excited by an impact hammer at several points along the railhead with the response measured at a fixed position. The results showed that up to 4 dB(A) of noise reduction from the rail could be achieved depending on the stiffness and damping properties of the railpad used. Moreover, it was shown that because of the high load dependency of the pad stiffness, neglect of the preloading effect could lead to a significant overprediction of the track noise component.

In this context, several theoretical and experimental studies dealing with the optimisation of the railpad stiffness to achieve noise reduction have been conducted. In one of the first studies, Vincent et al. in [38] conducted a study on the reduction of rolling noise from a ballasted track by optimising pad stiffness; they also considered introducing tuned dynamic absorbers (rail dampers) with 5 kg active mass at every 0.6 m (every sleeper bay). The study showed that the radiation of the track could be reduced by 2-6 dB(A) when optimising the rail pad and/or adopting rail dampers. Jones et al. [39] elaborate that the stiffness of the railpad is one of the most influential parameters of the track in relation to noise radiation. They showed that the optimisation of railpad stiffness could provide a reduction of 4-5 dB relative to a reference track.

Talotte et al. [40] presented a critical survey for the potential modelling and reduction of railway noise at the source. They explained alternative ways of reducing noise at the source and offered several methods of identification of noise sources from passing trains. They concluded that more attention is required on the modelling of various sources of noise in order to direct effort towards those measures with the most significant practical noise reductions. Oscarsson [41] showed the influence of the non-linear characteristics of the railpad on the vertical dynamic behaviour of railway track under a moving train. A numerical model was developed to investigate the vertical dynamic behaviour of the railway track. The results of laboratory and full-scale field measurements indicate the non-linear load-deflection behaviour of the railpad and the sleeper support. However, the difference in results for a weakly state-dependent railpad model has found to be negligible, compared with a linear model. Hemsworth et al. [42] presented a summary of the Silent Freight and Silent Track projects in which various noise reduction treatments of the track and wheels were studied. A summary of the reductions obtained is shown in **Table 2-1**. The results demonstrate that combinations of treatments on the wheel and track are required to achieve an overall noise reduction.

Table 2-1 Measured noise reduction obtained from the various wheel and track treatments in Silent Freight and Silent Track project to nearest whole dB [42].

	Track noise reduction	Perforated wheel with ring damper	Optimised wheel with shields	Optimised wheel with tuned absorbers
Wheel noise reduction	None	4	8	7
Stiffer pads	2	2	3	3
Reference track + absorbers	6	6	7	7
Stiffer pads + absorbers	5	4	5	6
New track	3	2	4	4
New track + absorbers	7	6	8	8

For those situations where the dominant source of noise is the structure below the track (e.g. bridges), a softer fastening system can result in a noise reduction. On the other hand, this can lead to an increase in the noise from the rail itself [1]. The coupling effect between the bridge and rails will depend on the stiffness of the rail fastener. For a stiffer rail fastener, the rail is more strongly coupled with the bridge, which allows the bridge to vibrate more and increases the noise. Using a softer fastener decouples the rail from the bridge resulting in less vibration of the bridge, and therefore lower noise [1]. Bewes [28] developed models for the calculation of noise and vibration on bridges and viaducts based on three types of track; some of them had double-layer fasteners installed. One of the tracks was fitted with the Vanguard system. The mobilities on each track were measured before and after the installation of the fasteners. The results show the reduction of overall structure-radiated sound power of around 13 dB, depending on the stiffness of the resilient element. In the case of the Vanguard system, the measured results were not sufficient to provide a good comparison. Wang et al. [43] measured the noise level on a bridge on the RSA line in Sydney with an originally fitted rigid baseplate on a timber bearer. The noise was found to be about 90 dB(A) at a distance of 5.5 m from the track centre. When a double layer resilient element (Pandrol VIPA) was fitted on the bridge, a total of 6 dB(A) noise reduction was obtained. The study concluded that under the right circumstances a significant noise reduction could be achieved using a double layer fastening system. Also, in [44], a resilient baseplate was implemented to reduce structure-borne sound on two bridges in Stockholm. A reduction of up to 10 dB(A) is achieved depending on the combination of stiffness used. Wettschureck et al. [45, 46] carried out field measurements for airborne noise before and after the installation of a softer and later stiffer resilient element on a steel bridge featuring a ballastless track. The noise results before and after the installation of rail fasteners were compared. The comparison showed that the installation of the softer rail fastener reduced the noise above 80 Hz by about 6 to 10 dB. The study concluded that it is important to have a very low ratio of the dynamic stiffness to the static stiffness of the fastening system pad for effective noise mitigation purposes.

2.1.1 **Slab tracks**

The majority of studies, e.g. [47-50], have indicated that slab tracks can be considered to be noisier than ballasted tracks. There are two important reasons for this: (i) the different degree of sound absorption and (ii) the difference in the TDRs that are usually lower on slab track. On slab tracks, the rails are supported above a concrete surface. This is highly reflective compared to the ballasted tracks which are partially absorptive. Therefore, slab tracks allow greater sound reflection compared with the ballasted tracks, leading to higher noise. However, this difference is usually considered to be around 1 dB. The second reason is the low TDR normally occurring on slab tracks. Since the slab tracks do not have the resilience of the ballast layer, softer fastening systems are used. The soft fastening system causes the rail to vibrate more, which results in higher noise levels.

The noise from each track type depends on many factors, especially the railpad stiffness [1]. Ballasted tracks are commonly used as they require lower capital investment. However, the use of slab tracks has recently increased, especially on high-speed lines. The main reason for this increase is that slab tracks require less maintenance, and have long durability and service life; they also provide good performance and stability and have high lateral track resistance [51].

In [52], an optimisation of vibro-acoustic performance for a slab track was conducted using UIC54 rails embedded in a stiff moulding material. The procedure shows that the optimum combination of properties for this slab track design could achieve a 4 to 6 dB(A) reduction in noise compared with a conventional ballasted track. More recently, Zhang et al. in [47] conducted a comparison study of the noise performance of slab and ballasted track designs. Two types of ballasted track were considered with different railpad stiffnesses, showing a difference of 4 dB. The study also demonstrated that the slab track considered is 3 dB noisier than the ballasted track with a stiffer pad of 800 MN/m, however, for a softer pad of 120 MN/m, the difference is only 0-1 dB. The results obtained in this study are sensitive to assumptions on the train speed, roughness, wheel design and location of the receiver. A theoretical study of ground vibration was conducted in [53], that showed that the performance of a ballasted track and a slab track are similar if an equivalent fastener stiffness is used. The slab track may produce 1-3 dB lower vibration for frequencies above about 16 Hz, but this is attributed mainly to the slab mass. However, as slab tracks are usually fitted with softer rail fasteners, further substantial reductions occur above 63 Hz.

A typical slab track rail fastening system comprises a baseplate and pads that secure the rail to the slab. There are several types of rail fasteners depending on the design and functionality. In most cases, they are designed as single-stage (single-layer) or two-stage (two-layer) systems. The single-stage system is a type of rail fastener that contains a single railpad on top of a steel plate, as shown in **Figure 1-6**. In contrast, a standalone rail fastening system is one that does not contain such baseplates, such as the one shown in **Figure 1-5**. The two-stage system is a type of fastener that contains two pads with different stiffness, an upper railpad and a lower pad with the steel baseplate between them (see **Figure 1-7**). The extra layer of resilience provides increased vibration isolation; however, in some cases, there are frequencies where the vibration is amplified around the resonances [45]. Therefore, using the fastener with a double layer could result in vibration reduction in the substructure.

In the Vanguard system, the railhead is supported by two rubber wedges that deform in shear rather than in compression as was shown in **Figure 1-9** . This allows a very low vertical stiffness to be achieved while retaining reasonable control of rail roll and track gauge. A static vertical stiffness of approximately 5 kN/mm is achieved when measured with the load required by the European standard for Metro track fastening systems [26, 54]. The design of this system allows vibration isolation by reducing the forces transmitted from the rail to the structure.

2.2 Dynamic stiffness of railpads

There are several methods of determining the stiffness and damping of resilient elements. These are based on two main approaches, known as the direct and the indirect measurement methods. Below, details of these two methods and examples of their application are presented.

The indirect method involves a test rig with two blocks of known mass; a resilient element can be inserted between them as shown in **Figure 2-2**. The lower mass is isolated from the ground. A hydraulic actuator applies a static preload. The hydraulic load is applied through soft rubber springs (isolators). These isolators filter out the high-frequency vibration/noise from other equipment in the laboratory or hydraulic fluid flow. The hydraulic force is continuously applied in a vertical direction to simulate the weight of the train on the upper block. The upper block is then excited dynamically with a shaker. The responses of the two blocks are measured using accelerometers. The frequency dependent complex dynamic stiffness of the resilient element can be obtained using the following equation [55]:

$$K = -m_2\omega^2\frac{\ddot{X}_2}{\ddot{X}_1} \;;\; \eta = \tan(\angle K) \tag{2-1}$$

where K is the complex transfer stiffness, η is the damping loss factor, m_2 is the mass of the lower block, $\ddot{X}_1$ is the complex acceleration amplitude of the upper block, $\ddot{X}_2$ is the complex acceleration amplitude of the lower block and ω is the circular frequency in rad/s.

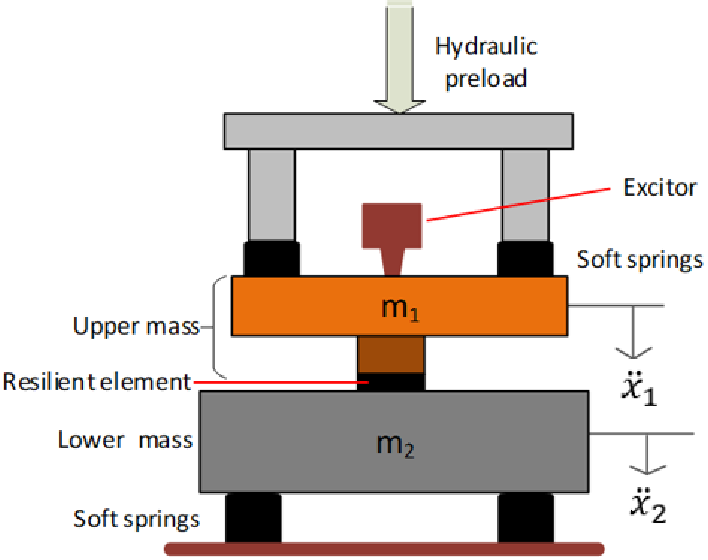

Figure 2-2 Test rig for measuring the high-frequency dynamic stiffness of resilient elements redrawn from [55].

Equation (**2-1**) is only valid when $|\ddot{X}_2| \ll |\ddot{X}_1|$ and the frequency range of valid measurements depends on the mass of the lower block and stiffness of the tested rail fastener system [55].

In [55, 56] Thompson and Verheiij conducted measurements for the stiffness of rail fasteners using this indirect method. It provides a reliable procedure for measuring the high-frequency transfer stiffness of resilient elements as a function of frequency. The indirect method has been included in the International Standard EN ISO 10846-3 [57].

The results in [55, 56] for the dynamic stiffness and the damping loss factor of the rail fasteners were presented in the frequency range of 100 to 1000 Hz. The results show that the stiffness of railpads is strongly dependent on preload. The results from laboratory measurements were compared with field measurements on track fitted with the same railpads and showed a good agreement. According to the findings, for frequencies above 1000 Hz, the test rig requires further modifications. Thompson and Vincent [58] discussed the effect of the clipping force on the rail fasteners. They stated that the clips provide an additional preload of about 20 kN on the resilient element, based on information provided by the suppliers.

In [59], Kari also used the indirect method to measure the dynamic transfer stiffness of vibration isolators in the audible frequency range, up to 1000 Hz. The study aimed to determine the attenuation of the isolators by measuring their dynamic stiffness. The test rig was set up as shown in **Figure 2-3**. The preload was decoupled from the rig frame to reduce flanking transmission.

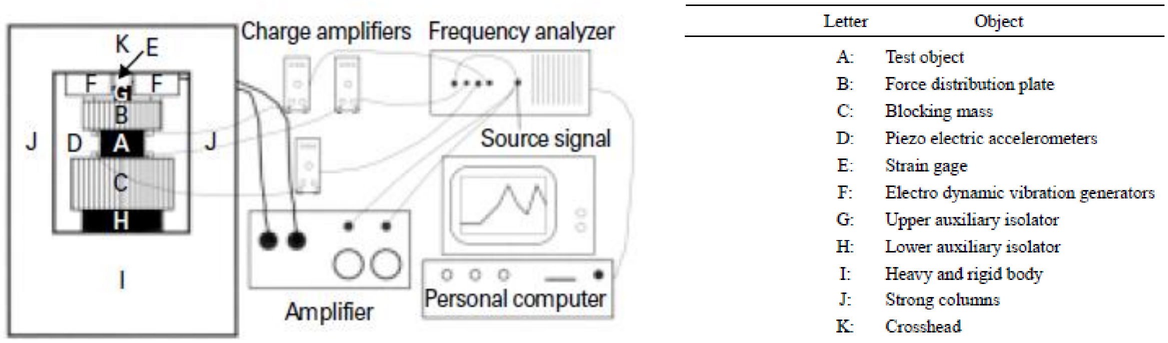

Letter	Object
A:	Test object
B:	Force distribution plate
C:	Blocking mass
D:	Piezo electric accelerometers
E:	Strain gage
F:	Electro dynamic vibration generators
G:	Upper auxiliary isolator
H:	Lower auxiliary isolator
I:	Heavy and rigid body
J:	Strong columns
K:	Crosshead

Figure 2-3 Test rig and measurement setup used by Kari [59].

Fenander [60] used the indirect method to determine the stiffness and damping loss factor of railpads. The study compared laboratory and field measurement data for the same railpad. The field data was taken from a newly built track in Sweden. The track consisted of concrete sleepers in ballast, UIC60 rails, and Pandrol 10 mm thick studded rubber railpads. Static preload on the track was applied by a special wagon owned by the Swedish National Rail Administration, which was stationary, with a maximum capacity of up to 150 kN. The load was applied by two servo-hydraulic cylinders acting vertically on the rails, with dynamic excitations up to 200 Hz. The laboratory measurements were from a static preload of 50 kN, 80 kN, and 100 kN with an excitation frequency range of 50 Hz to 1000 Hz. The comparison shows that the stiffness calculated using the field data was half the stiffness calculated using laboratory data for the preloads of 50 and 60 kN. However, for higher preloads, the difference was much smaller. The study concluded that the discrepancies in the results are due to the difficulties in calculating the correct level of preload in the field measurements. Also, the railpads in the track were secured on the sleepers using glue, while the railpads in the laboratory measurements were placed between two smooth surfaces and no adhesive was applied. Therefore, the adhesive could have filled in the gaps between the studs on the railpad, resulting in increasing the stiffness estimation from the field measurements. Also, the difference in measured stiffness could have been influenced by differences in temperature. Similar differences were found for the loss factor.

Maes et al. [61] carried out a study measuring the dynamic stiffness of small samples taken from railpads. They used a direct method for measuring stiffness and damping values between 20 Hz and 2500 Hz with variable preload. The test specimen (25 mm x 30 mm) was placed between two steel plates, where the top plate was fixed to a load cell, and the bottom plate was connected to an exciter (shaker). A steel frame supporting the experimental setup was used, and the whole rig was secured on a concrete mass, which was isolated from the ground, as shown in **Figure 2-4**. The dynamic stiffness and the loss factor were obtained using the following equations [61]:

$$k_{21}(f) = \frac{F_2}{u_1} = -(2\pi f)^2 \frac{F_2}{a_1} \tag{2-2}$$

$$\eta(f) = {Im\{k_{21}(f)\}}\Big/{Re\{k_{21}(f)\}} \tag{2-3}$$

where k_{21} is the dynamic transfer stiffness, η is the loss factor, f is the frequency, F_2 is the force measured at side 2, u_1 is the displacement at side 1 and a_1 is the corresponding acceleration.

The study showed that the direct method could be used to obtain the stiffness and loss factor up to higher frequencies if a smaller specimen is used. Moreover, it was shown that the determination of loss factor at higher frequencies is less accurate.

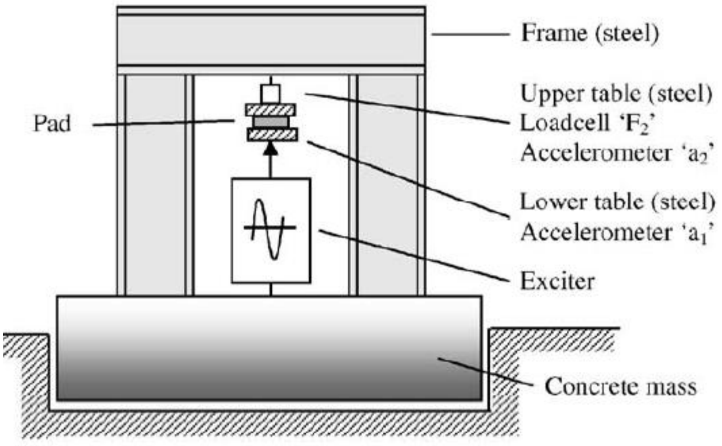

Figure 2-4 The direct method for elastic pad test rig set-up [61].

In [62], Morison et al. measured the dynamic stiffness of fasteners with low stiffness (the Vanguard system) using the driving point method [63]. The test rig is shown in **Figure 2-5**. The study described the limitation for obtaining the dynamic stiffness for low stiffness resilient elements due to the contribution of inertial forces at frequencies approaching and above the natural resonance of the system.

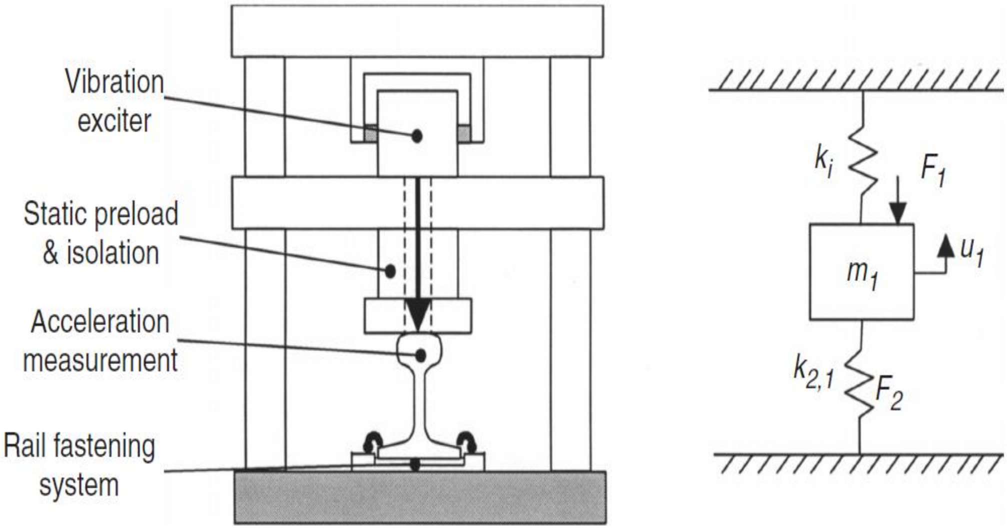

Figure 2-5 A schematic side view of the apparatus used by Morison et al. for driving point method [62].

The dynamic stiffness was obtained from the following:

$$k_{2,1}(\omega) \approx k_{1,1}(\omega) = \frac{F_1}{u_1} \tag{2-4}$$

where F_1 is the input side force, $k_{2,1}$ is dynamic transfer stiffness, which is assumed to be approximately equal to the dynamic point stiffness $k_{1,1}$.

The approximation in Equation (**2-4**) only holds at frequencies where the inertial force on the moving mass or the internal mass of the resilient element in the system remains well below the elastic forces, that is the measured point stiffness is only equal to the transfer stiffness at low frequency, where the inertial force is small. To apply an inertial correction, it was noted in [62] that

$$k_{1,1}(\omega) \approx k_{2,1}(\omega) - \omega^2 m_1 + k_{\mathrm{i}}(\omega) \tag{2-5}$$

where $k_{1,1}$ is the measured dynamic stiffness from Equation (**2-4**), $k_{2,1}$ is the actual dynamic transfer stiffness of the resilient element, $-\omega^2 m_1$is the dynamic stiffness of the moving mass of the system and k_{i} is the stiffness of the isolation spring. This can be used to determine $k_{2,1}$ from a measurement of $k_{1,1}$.

After applying the correction, the study achieved an increase in the upper limit of the measurement range from 30 Hz to 100 Hz and beyond. The results show that the dynamic stiffness of the Vanguard system is constant at low frequency from 5 Hz to 30 Hz, with a value of approximately 7.0 kN/mm with no preload and 14.5 kN/mm under a preload of 25 kN. The study concluded that using the driving point method with the correction allows the dynamic stiffness of the Vanguard system to be obtained accurately below the resonance of the system, which is 100 Hz under preload and 160 Hz without. The method can be applied to any resilient element with internal mass effects.

The indirect method provides the results for a range of frequencies depending on the inertia of the lower mass (the heavier the lower mass, the lower limit frequency can achieved).

2.3 Track decay rates

The decrease of the amplitude of the propagating waves along the track is quantified by means of the Track Decay Rate (TDR) that expresses the amplitude reduction in dB/m. They are usually represented in the form of one-third octave band spectra and they can be measured on track according to standards [1, 33, 35].

In [64] Thompson presented an experimental analysis of wave propagation in the rail. The forced responses for vertical and lateral excitation along the rail were measured, and the TDRs were obtained. The measured data were compared with the results from a model and showed a good agreement. Jones et al. [35] suggested a method of calculating the TDR from frequency response measurements obtained by applying an impact force (using an instrumented hammer) on the railhead and measuring the transfer mobility at different locations along the rail. The measured TDR results were compared with the predicted results from a simple beam track model and showed a good agreement.

Zhao et al. [65] developed a finite element (FE) model that can be used to predict the decay rate and vibration response of an embedded rail on a slab track. The model was then validated with measurement. A good agreement was found between the measured TDRs and the ones predicted from their models. Then they conducted an optimisation study on the embedded rail track shown in **Figure 2-6** using these models. They found that by optimising the cross-section of the gutter for the embedded rail, a reduction of noise radiation by up to 4 dB(A) can be achieved.

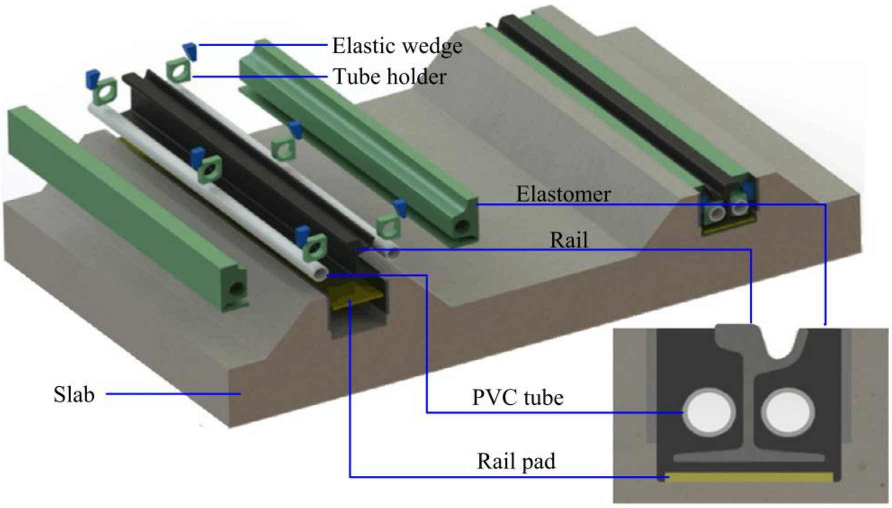

Figure 2-6 Embedded rail track [65].

Ryue et al. in [66, 67] used a numerical method called Wavenumber Finite Element (WFE) (also called 2.5D FE) method to predict the TDR of a rail on a continuous foundation up to a frequency of 80 kHz. The model was compared with a field measurement taken on an operational railway track, where the train-induced vibrations were acquired on the rail and compared with the results of the model. A good agreement was found between them. The study also found that, for frequencies above 20 kHz, the TDR of the wave that propagates the furthest is predominantly influenced by the material damping of the rail whereas at lower frequencies the stiffness and damping of the railpads had a bigger influence.

The stiffness of railpads has been found to play a critical role in the increase of the TDR along the rails (see **Figure 2-1**), which could result in low rolling noise by using stiff railpads [68]. The theoretical models for rolling noise such as TWINS [1] have shown that the vibration decay rate along the rail is linked to the noise performance of the track. Therefore, the TDR is a measurable parameter that can be used as input in noise prediction models. The TDR has been accepted in Europe as a criterion for track noise performance [1].

2.4 Track vibration modelling

The noise radiated by the track depends on the track vibration. This vibration is caused by the interaction between the wheel and the rail. In [69], Knothe and Grassie give a review of different modelling approaches for the track vibration. To understand the vibration of the track, a simple infinite model that represents the rail on an elastic foundation, as shown in **Figure 2-7**, has been used to obtain the dynamic behaviour of the rail.

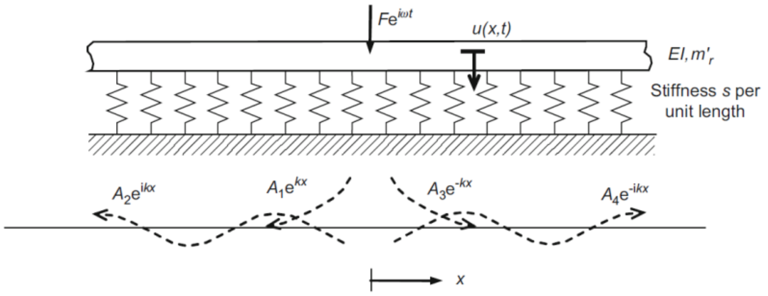

Figure 2-7 A beam on an elastic foundation showing waves generated by a point force [1].

The Euler-Bernoulli beam model assumes the section of the beam remains plane and perpendicular to the neutral axis and does not include shear deformation and rotational inertia. This assumption holds when the wavelength of the beam is longer than about six times its height [70, 71]. For a rail, the Euler-Bernoulli beam gives reliable results up to about 500 Hz [71]; for higher frequencies, the Timoshenko beam equations, which include these effects, are commonly used.

In [71], Grassie et al. developed a model for vertical vibration of a track based on an infinite Timoshenko beam and validated it with an experiment. They found that for vertical vibration the effects of discrete supports affect the frequency response only at certain frequencies. Clark et al. [72] developed a track model for vertical vibration, based on a finite length Timoshenko beam including the discrete nature of the rail supports, and used it to understand the response of the track to corrugated rails. From prediction and experiment analysis, it was found that the track with corrugated rails exhibits a dynamic response at the corrugation-passing frequency superimposed on the quasi-static response which would exist with smooth rails.

Thompson [73] developed a vibration model of an infinite rail supported on ballast, sleepers and railpads. The model is based on a finite element model of an arbitrary periodic length, see **Figure 2-8** (c). This model was compared with two others by Thompson and Vincent in [58], as shown in **Figure 2-8**. These models give an understanding of the dynamic behaviour of railway track in the frequency range 50-6000 Hz. The study demonstrates the advantages and disadvantages of each model. Vincent and Thompson [74] also carried out several experiments for the validation of the models. A good agreement between the models and the experiments has been found. It has also been noted that the decay rate could be more correctly predicted by the rail model that includes cross-section deformation.

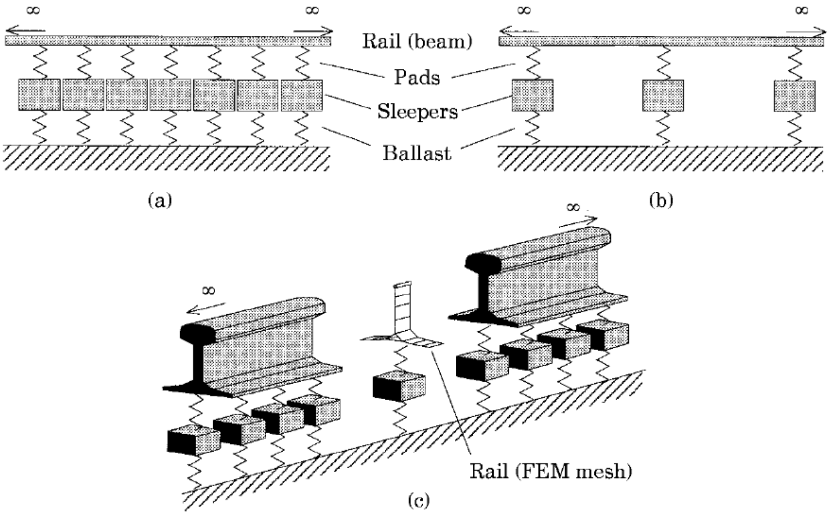

Figure 2-8 Models for track vibration: (a) continuously supported beam model; (b) periodically supported beam model; (c) continuously supported rail model including cross-section deformation [58].

A track model is presented by Zhang et al. [36] which uses a 2.5D FE representation for the rail. The 2.5D technique is also referred to as the Wavenumber Finite Element (WFE) [66, 67] or the Semi-Analytical FE (SAFE) method [75]. It represents a structure which is invariant in one direction by using a two-dimensional (2D), and which are invariant in the third direction. In [36] Zhang et al. coupled this 2.5D FE rail model to a finite number of sleepers to give a representation of a discretely supported track. Good agreement was found with measurements.

2.5 Rail radiation

The rail effectively has two-dimensional geometry, being infinite in the third direction, and the wavelengths in the rail are generally much longer than those of sound in air. The sound field can therefore be calculated efficiently using a two-dimensional boundary element (BE) model [1].

The sound field induced by a vibrating structure can be described as the distribution of sound pressure or in terms of sound power. The sound power produced is independent of receiver location, whereas the sound pressure varies from one location to another [76]. The sound power W radiated by a vibrating object is given by [76];

$$W = \rho_0 c_0 S \langle \overline{v^2} \rangle \sigma \tag{2-6}$$

where ρ_0 is the density of air, c_0 is the speed of sound in air, S is the surface area of the vibrating structure, σ is the radiation ratio or radiation efficiency and $\langle \overline{v^2} \rangle$ is the mean square velocity normal to the surface in the frequency band of interest averaged over the surface.

Bender and Remington [77] studied the influence of the rail on train rolling noise. The radiation efficiency of the rail (with mass 50 kg/m) was measured and compared with an analytical formulation for a cylinder. The cylinder diameter was set equal to the rail height to calculate the radiation efficiency for the horizontal forcing of the rail, whereas for the vertical forcing of the rail it was treated as two cylinders vibrating independently. There are several factors that were unknown during this study such as the directivity pattern of the radiation, the length of the rail that effectively radiates due to wheel excitation and the roughness spectra of the rail and wheel. Remington continued to conduct several studies to investigate the factors that were unknown and found that the prediction from the analytical model and measured data from the field agree well within the limitation of the model [15-17].

Thompson extended this engineering method of predicting rolling noise [78]. The model provides a way of predicting noise for a particular design of the track and wheel, also allowing the study of noise-reduction technologies. The model has been updated further and implemented in TWINS (Track-Wheel Interaction Noise Software) [18, 19]. Sound radiation in TWINS can be calculated in terms of sound power or average sound pressure during the passage of a train at specified positions at the trackside from various vibrating components of the track and wheel.

A three-dimensional model for sound radiation from a rail known as FLOSS (Finite Line of Simple Sources) was developed by Thompson et al. [79] to study the three-dimensional effects. Equally spaced monopole or dipole sources are placed along the axis of the rail. The distance between sources has to be small compared with the wavelength in the air and the wavelength in the structure. Also, the strengths of the source should be chosen to allow for the wavenumber and decay rate in the rail. It has been found that it is necessary to consider 3D radiation effects if the decay rate of the vibration along the rail becomes larger or the wavelength in the rail becomes small. However, in practice, the 2D approach has shown to give satisfactory noise prediction results for frequencies above 250 Hz in most practical situations and even where the 3D effects become important, simple correction terms can be used.

In [80], a 2D BE model for sound radiation from a railway track was presented. **Figure 2-9** shows the predicted radiation efficiencies of the UIC 60E1 rail section for uniform vertical and lateral motion. The result indicates that both radiation efficiencies follow a straight line with a slope of $30\log_{10}(f/f_0)$ up to approximately 800 Hz, where is f the frequency and is f_0 the frequency at which the line crosses 0 dB.

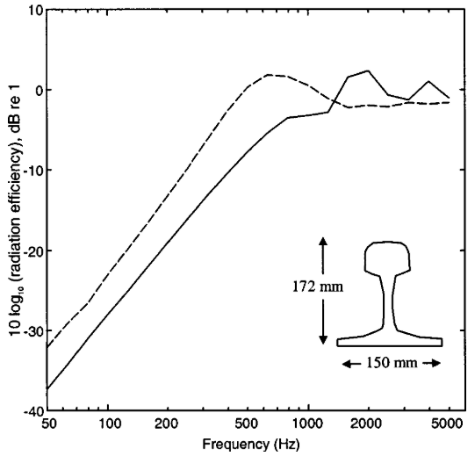

Figure 2-9 Radiation efficiencies of UIC 60 rail section modelled in 2D, – vertical motion, --- horizontal motion [80].

Kitagawa and Thompson [20] investigated the horizontal directivity of rail radiation using a similar model to FLOSS. It has been found that due to the wave propagation along the rail, the track forms an extended source of radiation, and the distribution of sound in the horizontal plane consists of sound propagation at a specific angle to the rail. This direction depends on the ratio of the wavenumbers in the rail and the air.

2.6 Sleeper radiation

Sleepers can be represented in the first instance as a mass layer under the rail beam. In [69], it was shown that using the sleeper model as a layer of mass, the dynamic response of the track to the forces at the railhead is represented well up to 1 kHz. This simplification, however, ignores the bending modes that monobloc sleepers have in the frequency range of interest [1]. In [81], Grassie described sleepers by using a simple Timoshenko beam model for a freely suspended sleeper. Also, in [82] Grassie and Cox studied the dynamic response of a railway track with flexible sleepers to high frequency vertical excitation; the sleeper was again modelled as a uniform Timoshenko beam. A quite reasonable agreement has been found with the measurements regarding natural frequencies, apart from the first mode, where the effect of the non-uniform profile is greatest.

The TWINS model [83] includes a model of the sleeper represented as a beam and also including the ballast beneath it. This model was based on a modal summation. Later, Thompson used a wave approach to develop a new model that can more readily account for the frequency-dependent ballast stiffness [1]. In all these models, the sleeper is represented as a finite beam on a continuous elastic foundation, in which the ballast is represented as an elastic layer (see **Figure 2-10**). The developed models have been verified by comparison with measurements from [84], and reasonable agreement has been found between the analytical prediction and the measurement results in terms of natural frequencies [1].

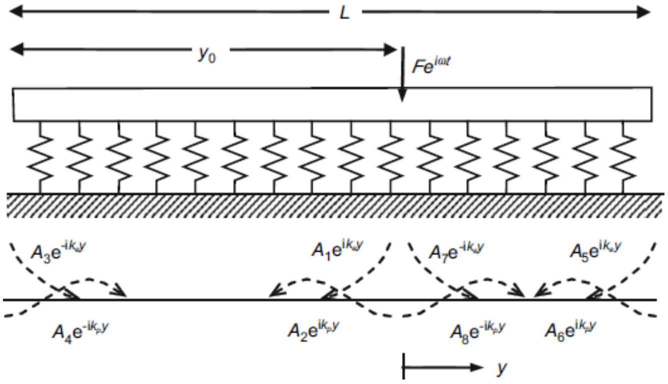

Figure 2-10 Sleeper represented as a finite Timoshenko beam on an elastic foundation, excited by a point force at y = 0 showing the various waves that are generated [1].

For an individual sleeper, the sound radiation can be considered as that from a rectangular surface located in a plane baffle. The lower surface of the sleeper is hidden under the ballast; therefore, it is neglected. A typical sleeper is 2.5 m long, and 0.2 m to 0.25 m wide. Sound radiation is explored numerically in terms of its radiation ratio in [1]. Using the Rayleigh integral method, the sound radiation of the sleeper is obtained for sleepers of various dimensions by assuming the sleeper vibration to be uniform. It is found that the radiation ratio depends on the sleeper width in the frequency range 300 to 800 Hz [1].

Vincent et al. [38] found that sleeper noise can be reduced in three ways: reducing the area of the upper side of the sleeper, increasing the sleeper mass and reducing the railpad stiffness. Nielsen [85] studied the acoustic optimization of sound radiation from railway sleepers (mono-bloc or bi-bloc). He used a mathematical model of vertical wheelset/track interaction, a finite element model of the sleeper vibration and a boundary element model for the radiation ratio. The model was used to investigate the influence of sleeper material properties, sleeper shape, ballast properties and railpads.

It was found that the sound power generated by the sleeper is strongly influenced by the ballast stiffness, damping and railpad stiffness. It is concluded that a bi-bloc sleeper with appropriate dimensions can lead to a reduction of 2-3 dB(A) in sound power compared to a reference mono-bloc sleeper.

2.7 Sound radiation efficiency measurements

The sound radiation from a vibrating structure can be defined in terms of its radiation efficiency, which is the sound power normalised by the surface area, the characteristic acoustic impedance of the medium and the spatially-averaged surface velocity, see equation **(2.6)** [57, 86-89]. The radiation ratio is measured using two separate steps: first the acoustic power radiated by the vibrating body is measured, and second the spatially-averaged mean-square normal velocity is measured. In [90] Zheng et al. use a reciprocity method to measure the sound pressure radiated by an internal combustion engine, where the surface of the engine was divided into discrete sub-areas and the vibration was measured in each sub-area due to a sound source located at the target receiver point. **Figure 2-11** demonstrates the reciprocity method [86].

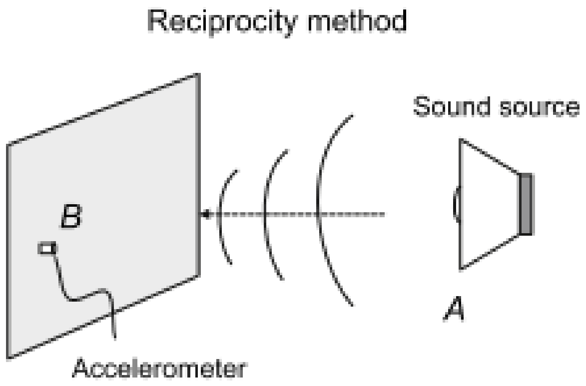

Figure 2-11 Illustration of reciprocity technique A: Exciter location, B: Response location [86].

Chapter 3 Experimental procedure for measurement of dynamic stiffness

3.1 Introduction

This chapter focuses on measurements of the vertical dynamic stiffness of resilient elements using a standardised indirect method that allows the values to be obtained as a function of excitation frequency for known loading conditions [56]. Measurements are presented for rail fasteners with both single and double stage baseplates as well as for the individual railpads and lower pads that are fitted in them. The effect of the force applied by rail clipping on the dynamic stiffness of railpads is demonstrated. The measured dynamic stiffness data are interpreted by using simple two degrees of freedom (2-DoF) and three degrees of freedom (3-DoF) models. The rig used for dynamic and static stiffness is described with the procedures adopted.

The purpose for measuring the dynamic stiffness of railpads and rail fasteners is to use the obtained data in noise assessment to understand the influence of dynamic stiffness on rolling noise. The reason for focusing on this type of fastener is due to its increased use on high-speed slab track, where the reduction of rolling noise will be essential for the further expansion of high-speed lines.

3.2 Description of the experimental rig

The measurements to determine the dynamic stiffness of the resilient elements of different fastening systems have been conducted at the University of Southampton (UoS) in the former Heavy Structures Laboratory (HSL) using the 100 kN Instron Schenck servo-hydraulic actuator rig. The main parts of the experimental rig setup comprise the servo-hydraulic actuator rig, a 2-tonne steel block, six bespoke isolators (used to isolate the rig from vibration of the floor and hydraulic system), a 0.6 m rail section and an inertial dynamic shaker. The setup of the rig is shown in **Figure 3-1**. A schematic view of the rig setup with a two-stage baseplate installed is shown in **Figure 3-2**. The details of the equipment used for assembling the rig and setting up the experimental procedure are reported in **Table 3-1**.

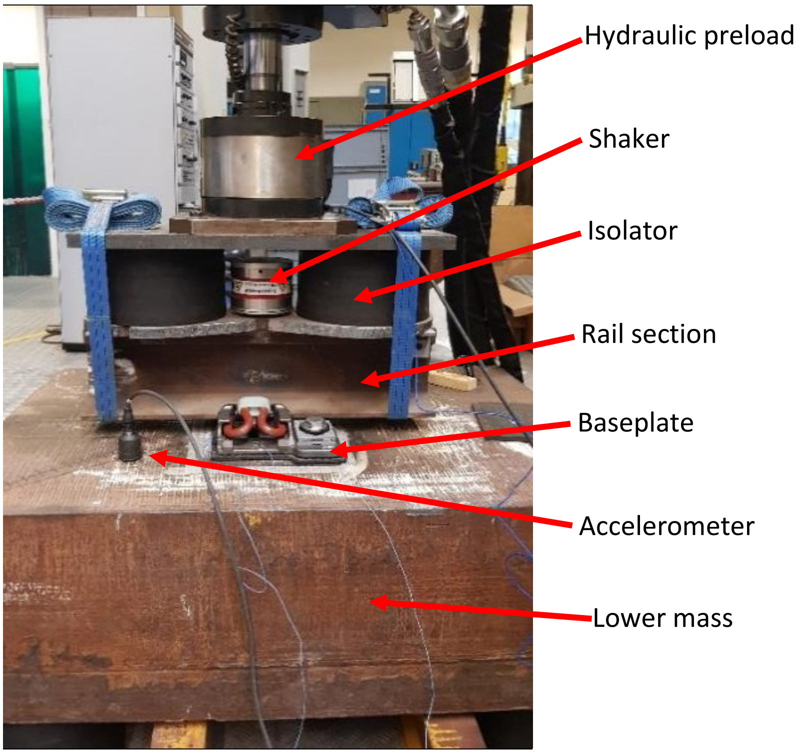

Figure 3-1 The test rig for measuring the dynamic stiffness at the UoS-HSL.

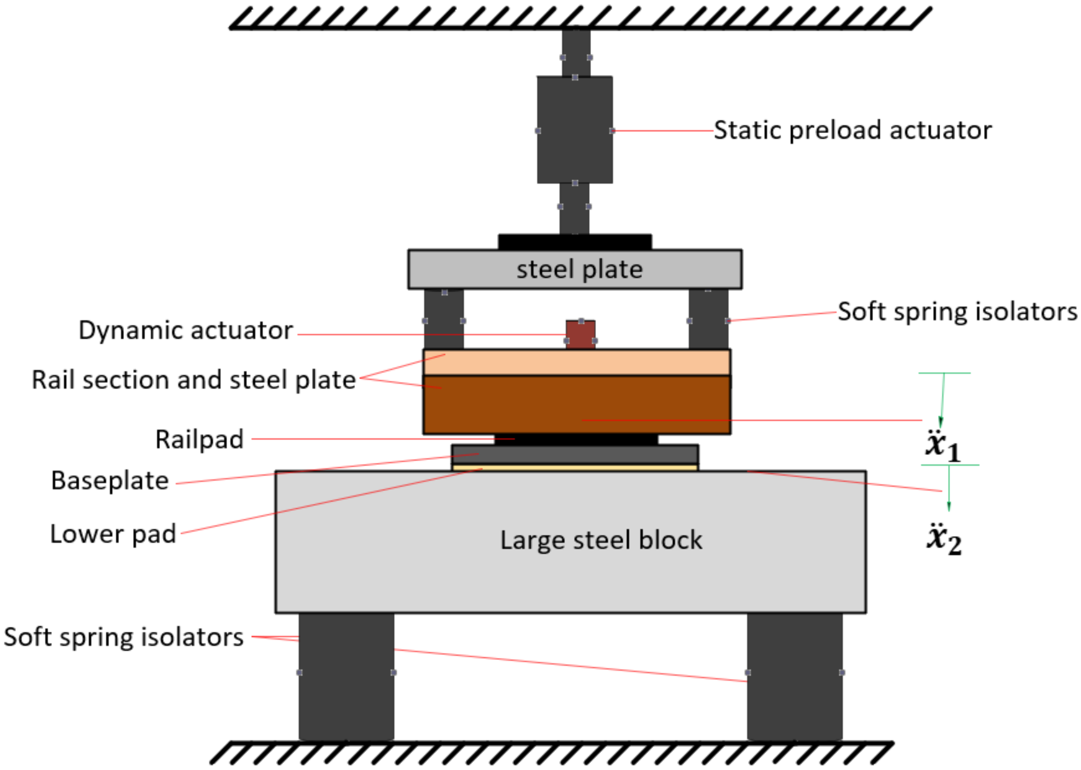

Figure 3-2 Schematic view of the experimental rig with two-stage baseplate installed.

Table 3-1 Experimental rig components

Equipment	Details
Instron Schenck actuator rig	100kN servo-hydraulic actuator mounted vertically on a steel frame.
Inertial shaker (dynamic actuator)	Data Physics, model IV45, S/N:13/A6P/30253, Mass 5 kg.
Accelerometers	PCB Piezotronics Shear Accelerometers Model: 352C34 with a sensitivity of 10mV/g and model 393B12 with a sensitivity of 10V/g.
Data analyser	Data Physics, Model: DP240.
Laptop computer	Dell Latitude E7470
Software	Data Physics SignalCalc 730 Dynamic Signal Analyser, MATLAB.
Large steel block	Weight 2050 kg (length 1040mm, width 740mm, height 350mm)
Rail and small steel plate (dog bone plate)	UIC60E1 rail with a length of 600 mm and a steel plate of 600×240×20 mm attached along the railhead to hold the shaker and the bespoke isolators with a combined mass of approximately 50 kg.
Six bespoke isolators	235 mm in diameter, 175 mm in height for the four at the bottom of the steel block mass. 135 mm in height for the two at the top of the railhead for the same diameter. They consist of layers of rubber separated by reinforcing plates with a critical load of 208 kN each.
Steel plate attached to the Instron hydraulic actuator	The plate has dimensions of 600 mm×300 mm×25 mm and holes drilled through to match the ones on the mounting of Instron; the plate is applying the actuator load on top of the two bespoke isolators.
Two load straps	The load straps help to keep the upper part of the equipment together when lifting it to install the test specimens (see **Figure 3-1**).

The experimental setup for this rig is designed to apply the indirect method [55] for evaluating the dynamic stiffness of the tested resilient elements, as discussed in Section **2.2**. The upper and lower soft springs are assumed to be grounded at each end and they are both sufficiently soft and the structure they rest on has a high impedance. These springs need to have low stiffness to minimize any effect on the impedance of the lower and upper blocks for the frequency range under consideration (the stiffnesses of the springs were evaluated in previous work by other researchers while designing this rig) [56]. To secure the rail section and the baseplate with bolts holes were drilled and tapped in the upper surface of the lower steel block (2-tonne block). The upper surface of the block was smooth to give a good interface with the bottom of the baseplate. The tested specimens are inserted between the foot of the rail section and the 2-tonne block. A static load that represents the loaded track conditions is applied through the two top isolators to the upper mass (which consists of a steel plate and the UIC60E1 rail section) by operating the Instron hydraulic actuator. The procedure for calculating the dynamic stiffness of the resilient element under test involves the measurement of the transmissibility between the upper (rail) and the lower (2-tonne block) mass. For this, the system is excited by the inertial shaker that is fixed on the upper mass and the acceleration of the two masses is measured. The transmissibility is obtained as a transfer function between the measured accelerations, $\ddot{x}_1$ of the upper mass (at the rail web as close as possible to the tested resilient element) and the accelerations $\ddot{x}_2$ of the lower mass. The excitation generated by the inertial shaker covers a wide frequency range. The shaker is attached at the top centre of the upper mass. The top two bespoke isolators isolate the vibration caused by three factors: the hydraulic fluid that operates the Instron actuator, the high-frequency resonances of the supporting frame and the actuator apparatus. The four isolators beneath the lower steel block isolate the rig from the vibration of the lab floor caused by other operations in the laboratory space and allow the lower block to act as an inertial reference.

3.3 The theoretical background of the experimental procedure

This section presents a simplified theoretical model consisting of a few degrees of freedom (DOFs) that can represent the experimental rig during the dynamic stiffness measurement for a standalone railpad (single layer) and a double layer fastening system.

3.3.1 **2-DOF model representing the setup for standalone pad measurement**

A mass-spring model of a 2DOF system is used here to describe the measurement rig setup. It is demonstrated how the dynamic stiffness of a resilient element can be evaluated indirectly from acceleration measurements. **Figure 3-3** shows a schematic view of the 2DOF model.

The model that represents the test rig consists of two blocks of known mass with a spring (the resilient element) mounted between them. The upper mass is used to distribute the load over the resilient element and the lower mass is resting on a second spring (the soft rubber mounts). A static preload can be applied to the resilient element by means of an external force (the actuator connected to the upper mass through soft rubber elements). The preload will affect the stiffness k_{u} of the resilient element; however, it is neglected in this theoretical formulation. To estimate the stiffness of the resilient element, an electrodynamic shaker is used to excite the upper mass while the acceleration of both masses is measured. The analytical model assumes rigid masses and allows only vertical displacements; in reality, the masses have their own flexibility and may rotate. Both these features have an impact on the measurements and will be addressed separately.

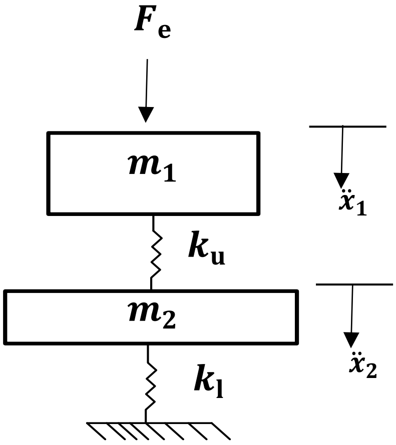

Figure 3-3 2-DOF model of the experimental rig.

Assuming harmonic excitation, the equations of motion of the system can be written as

$$\begin{bmatrix} m_1 & 0 \\ 0 & m_2 \end{bmatrix} \begin{Bmatrix} \ddot{x}_1 \\ \ddot{x}_2 \end{Bmatrix} + \begin{bmatrix} k_u & -k_u \\ -k_u & k_u + k_l \end{bmatrix} \begin{Bmatrix} x_1 \\ x_2 \end{Bmatrix} = \begin{Bmatrix} F_\text{e} \mathrm{e}^{i\omega t} \\ 0 \end{Bmatrix} \tag{3-1}$$

where m_1 is the upper mass, m_2 is the mass of the lower block, k_u is the stiffness of the resilient element, k_l is the stiffness of the bottom isolators, x_1 and x_2 are the displacements of the two masses and F_e is the amplitude of the applied force. The dot notation is used for differentiation. The quantity to be measured is k_u and in this formulation is representative of a single layer resilient element.

The solution of Equation (**3-1**) can be written as

$$\begin{Bmatrix} x_1 \\ x_2 \end{Bmatrix} = \begin{Bmatrix} X_1 \\ X_2 \end{Bmatrix} \mathrm{e}^{i\omega t} \tag{3-2}$$

and Equation (**3-1**) becomes

$$k_u X_1 - k_u X_2 - \omega^2 m_1 X_1 = F_e \tag{3-3}$$

$$k_u X_2 + k_l X_2 - k_u X_1 - \omega^2 m_2 X_2 = 0. \tag{3-4}$$

For free vibration, the natural frequencies of the 2DOF system can be obtained by solving Equation (**3-3**) and (**3-4**) with $F_e = 0$:

$$\begin{vmatrix} k_u X_1 - \omega^2 m_1 X_1 & -k_u X_2 \\ -k_u X_2 & k_u X_2 + k_l X_2 - \omega^2 m_2 X_2 \end{vmatrix} = 0 \tag{3-5}$$

This has two solutions for ω^2 from which the following approximate expressions for the natural frequencies can be found:

$$f_1 = \sqrt{\left(\frac{k_l}{m_1 + m_2}\right)} \Big/ 2\pi \tag{3-6}$$

$$f_2 = \sqrt{\left(\frac{k_u(m_1 + m_2)}{(m_1 m_2)}\right)} \Big/ 2\pi \tag{3-7}$$

The solution for the forced vibration problem can be found in Equations (**3-3**) and (**3-4**). From Equation (**3-4**), the ratio between the amplitudes of the two degrees of freedom is found to be

$$\frac{X_2}{X_1} = \frac{k_u}{k_u + k_l - \omega^2 m_2} \tag{3-8}$$

This is the transmissibility between the two masses that can be measured in the experiment and is used in determining the dynamic stiffness.

Equation (**3-8**) can be rearranged to give the stiffness k_u as follows:

$$k_u = (k_l - \omega^2 m_2)\left(\frac{X_2}{X_1 - X_2}\right) \tag{3-9}$$

The stiffness for the bottom isolator k_l is assumed to be small, therefore, negligible. As a result, the dynamic stiffness of the resilient element tested is expressed as

$$k_u = -\omega^2 m_2 \left(\frac{X_2}{X_1 - X_2}\right) \tag{3-10}$$

This can be rearranged as

$$k_u = -\omega^2 m_2 \left(\frac{1}{\left({}^{1}\!/_{H_{2,1}}\right) - 1}\right) \tag{3-11}$$

where $H_{2,1} = X_2/X_1$ is the transmissibility between the two degrees of freedom. Equation (**3-11**) can, therefore, be used to estimate the complex stiffness of the resilient element when m_2 is known.

The damping loss factor η can be determined from the phase angle of the estimated dynamic stiffness, see Equation (**2-3**).

Numerical example of the 2DOF model

Table 3-2 reports parameters of the 2DOF system representative of the experimental rig and the typical stiffness of a railway railpad. The corresponding receptances X_1/F_e and X_2/F_e are calculated according to the theory given above and are shown in **Figure 3-4**.

Table 3-2 Parameter values of the simple 2DOF model of the rig

Material	**Unit**
Top mass m_1	50 kg
Bottom mass m_2	2000 kg
Resilient element stiffness	120 MN/m
Bottom isolators stiffness	30 MN/m
Assumed damping loss factor for both stiffnesses	0.1

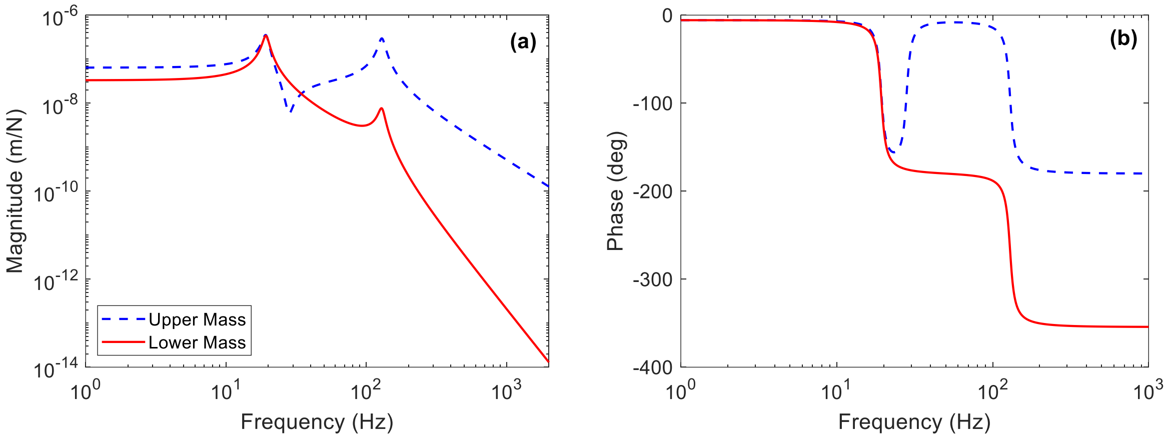

Figure 3-4 Point and transfer receptances of the 2DOF system: (**a**) magnitude and (**b**) phase angle.

From the predicted results in **Figure 3-4**, the first resonance frequency appears when the two masses bounce in phase on the lower isolator k_l; this frequency f_1 is at 19.3 Hz. The second resonance frequency occurs when the masses are bouncing out of phase, and the natural frequency is $f_2 = 249.6\text{ Hz}$. The anti-resonance dip is formed at a frequency $f_3 = 43.6\text{ Hz}$; this is equivalent to the resonance of the lower block bouncing between the two springs k_u and k_l when the upper mass is considered fixed. It can be seen from the predicted input and transfer receptances that the two masses are well-coupled up to slightly above the first resonance.

By using the indirect method (Equation (**3-10**)), the dynamic stiffness and loss factor of the resilient element inserted between the two masses can be obtained, as shown in **Figure 3-5** (**a**) and (**b**) respectively. From these results, it can be seen that the predicted value for the dynamic stiffness is the same as the actual value of stiffness for frequencies above about 60 Hz. The values below 60 Hz are affected by the first resonance (see **Figure 3-8 (a)**) of the system and do not provide the correct estimate for the stiffness. Therefore, the predicted dynamic stiffness values could be reliable for frequencies higher than about three times the first natural frequency. At lower frequencies Equation **(3.9)** should be used to allow for the stiffness of the lower spring.

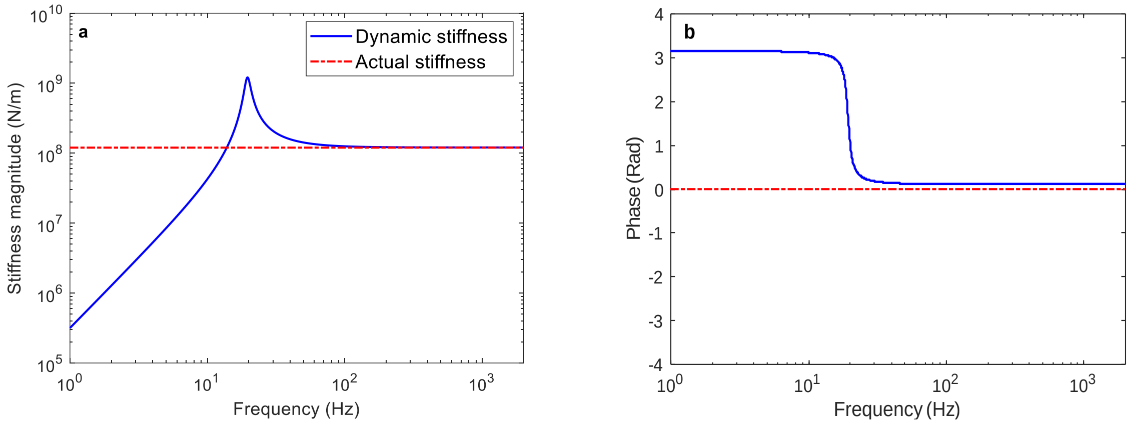

Figure 3-5 Predicted dynamic stiffness magnitude (**a**) and phase of complex stiffness (**b**) as well as the actual stiffness of a single layer resilient element.

3.3.2 3-DOF model representing the setup for double layer fastening system measurement

The model presented in Section **3.3.1** is valid for a single layer resilient element. In this section, the investigation is focussed on elements characterised by two layers. These elements are constructed with a metal baseplate inserted between two rubber pads. The indirect procedure can still be applied to measure the stiffness of the double-layer fastening system, but the presence of the baseplate mass can give internal resonances in the frequency range of interest. When a two-layer resilient element is mounted in the rig, it can be described as a 3-DOF system, as shown in **Figure 3-6**.

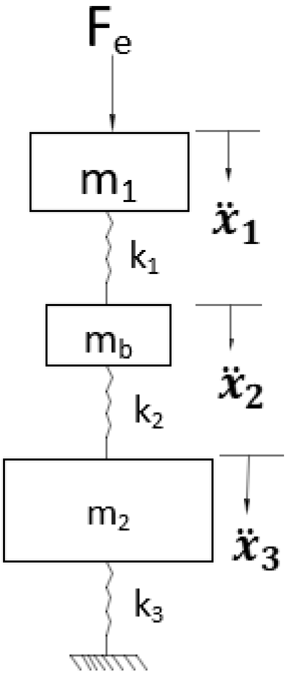

Figure 3-6 3DOF model of the rig as a mass-spring system.

Assuming harmonic excitation, the equations of motion of the system can be written as

$$\begin{bmatrix} m_1 & 0 & 0 \\ 0 & m_\mathrm{b} & 0 \\ 0 & 0 & m_2 \end{bmatrix} \begin{Bmatrix} \ddot{x}_1 \\ \ddot{x}_2 \\ \ddot{x}_3 \end{Bmatrix} + \begin{bmatrix} k_1 & -k_1 & 0 \\ -k_1 & k_1 + k_2 & -k_2 \\ 0 & -k_2 & k_2 + k_3 \end{bmatrix} \begin{Bmatrix} x_1 \\ x_2 \\ x_3 \end{Bmatrix} = \begin{Bmatrix} F_\mathrm{e} \mathrm{e}^{\mathrm{i}\omega t} \\ 0 \\ 0 \end{Bmatrix} \tag{3-12}$$

where $m_1$is the upper mass, m_2 is the mass of the lower block, m_b is the intermediate mass of the resilient element, k_1 is the stiffness of the upper pad of the resilient element (railpad), k_2 is the stiffness of the lower pad of the resilient element, k_3 is the stiffness of the bottom isolators, x_1, x_2 and x_3 are the displacements of the three masses respectively and F_e is the amplitude of the applied force. The quantity to be measured is the combined stiffness of k_1 and k_2.

From the 3DOF model, the corresponding receptances are calculated according to the theory given above with the values in **Table 3-2**. In addition, the mass of the baseplate is 6.2 kg and the lower pad stiffness of the baseplate is assumed to be 40 MN/m. The result is shown in **Figure 3-7**.

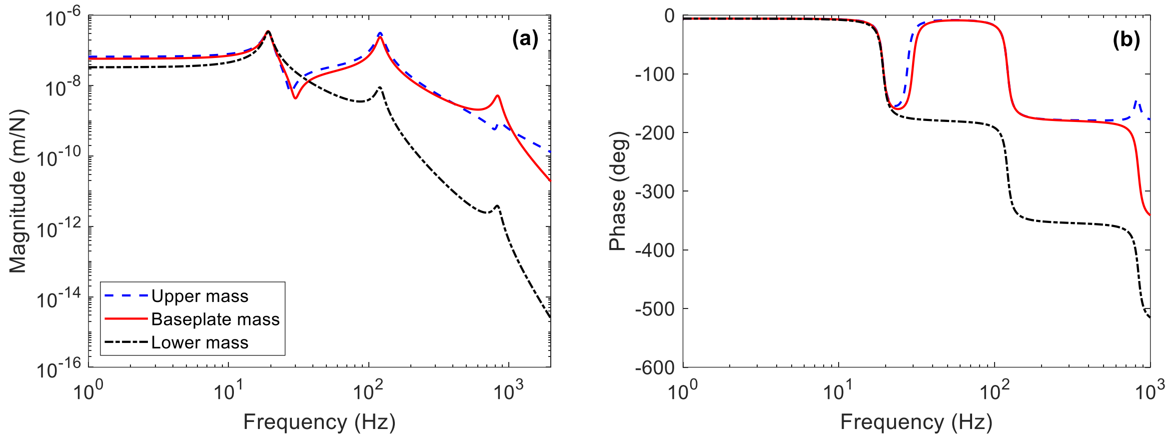

Figure 3-7 Point and transfer receptances of the 3DOF system: (**a**) magnitude and (**b**) phase angle.

The indirect method is applied to the 3DOF system to obtain the stiffness estimate of the resilient element. **Figure 3-8** shows a comparison of the 'measured' stiffness magnitude and loss factor obtained using Equation (**3-11**) between the 3DOF system (red dashed line) and a 2DOF system (solid black line) in which the baseplate mass is omitted and the two springs are added in series. Also, for comparison, the actual combined stiffness of the two pads (the upper pad (railpad) and the lower pad under the baseplate) added in series is shown as the blue dashed-dotted line. In this example, it can be seen that the internal resonance of the baseplate system can appear at frequencies below 1000 Hz.

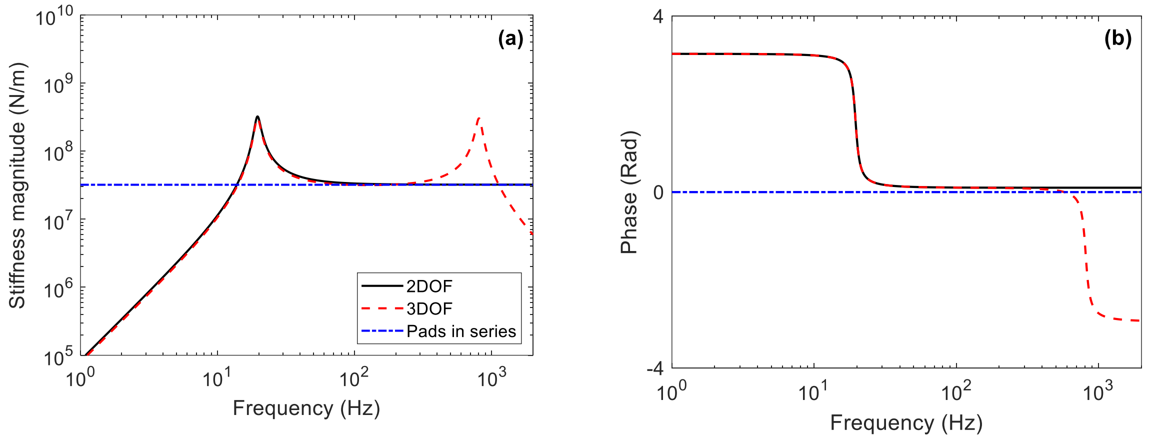

Figure 3-8 Comparison of the stiffness magnitude for a single layer resilient element 2DOF model and a double layer resilient element 3DOF models, (**a**) magnitude, (**b**) phase angle of the complex stiffness.

In **Figure 3-9**, the effect on the stiffness magnitude of varying the value of the intermediate mass (baseplate) is shown. As the mass increases, the internal resonance frequency is reduced.

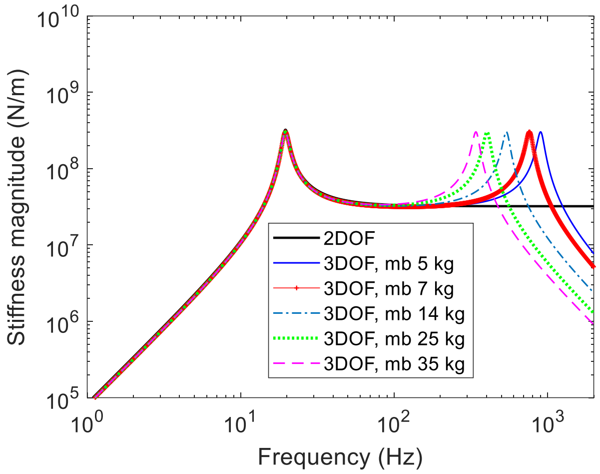

Figure 3-9 Comparison of the stiffness for a single layer resilient element 2DOF model and a double layer resilient element 3DOF models for different values of the intermediate-mass.

Model for direct and transfer stiffness for a two-layer fastening system

This section presents a simple model to obtain a formulation for the direct and transfer stiffness of a two-layer resilient element. The resilient element here is represented as shown in **Figure 3-10**. It is assumed that a displacement is applied to the top spring.

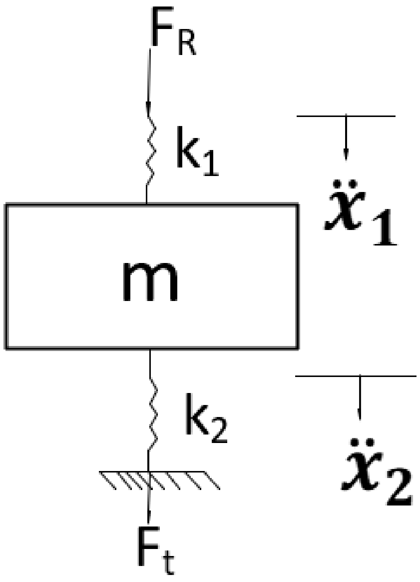

Figure 3-10 2DOF model of the two-layer fastening system as a spring-mass-spring model (F_t is transmitted force).

Experimental procedure for measurement of dynamic stiffness

In the spring-mass-spring model (**Figure 3-10**) of the two-layered resilient element, the springs (rubber pads) are considered to be massless with hysteretic damping resulting in complex stiffness of $k_j(1 + \mathrm{i}\eta)$ with j=1, 2.

The equation of motion of the system can be written as

$$\begin{bmatrix} 0 & 0 \\ 0 & m \end{bmatrix} \begin{Bmatrix} \ddot{x}_1 \\ \ddot{x}_2 \end{Bmatrix} + \begin{bmatrix} k_1 & -k_1 \\ -k_1 & k_1 + k_2 \end{bmatrix} \begin{Bmatrix} x_1 \\ x_2 \end{Bmatrix} = \begin{Bmatrix} F_\mathrm{R} \\ 0 \end{Bmatrix} \tag{3-13}$$

where m is the mass of the baseplate, k_1 is the stiffness of the upper pad, k_2 is the stiffness of the lower pad, while x_1 is the displacement of the mass m_1 and x_2 is the displacement of mass m of **Figure 3-10**, F_R represents the reaction force at the upper pad.

Assuming a harmonic displacement $x_1 = X_1 \mathrm{e}^{\mathrm{i}\omega t}$, the solution of the equation of motion can be found as

$$\frac{X_2}{X_1} = \frac{k_1}{(k_1 + k_2) - \omega^2 m} \tag{3-14}$$

The direct stiffness k_D can be obtained as

$$k_D = \frac{F_R}{X_1} = k_1 \left(1 - \frac{X_2}{X_1}\right) \tag{3-15}$$

and the transfer stiffness k_T is expressed as

$$k_T = \frac{F_t}{U_1} = k_2 \frac{X_2}{X_1} \tag{3-16}$$

By using the values from **Table 3-3** and a mass of 6.2 kg, the stiffness magnitude and loss factor of the direct and transfer stiffness is as shown in **Figure 3-11**. At low frequencies, both stiffnesses are equal and independent of frequency. The dip in the direct stiffness appears when the mass of the baseplate is bouncing on the lower spring k_2, which occurs at the frequency $f_1 = 355\ \mathrm{Hz}$. The peaks in both stiffness curves appear when the mass of the baseplate is bouncing on the combined stiffness of k_1 and k_2 with the top of the upper spring fixed, which occurs at the frequency $f_2 = 795\ \mathrm{Hz}$. Equations for these two frequencies are as follows

$$f_1 = \frac{1}{2\pi}\sqrt{k_2/m}\ ; \quad f_2 = \frac{1}{2\pi}\sqrt{(k_1 + k_2)/m} \tag{3-17}$$

Table 3-3 Assumed stiffness and loss factor values

	Upper pad	Lower pad
Stiffness (MN/m)	120	30
Damping loss factor	0.1	0.1

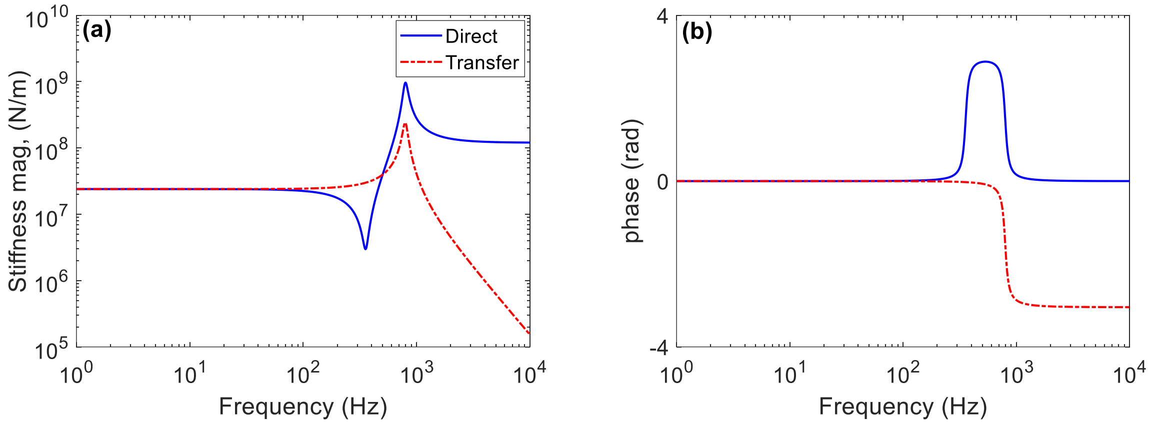

Figure 3-11 Predicted direct and transfer stiffness magnitude (**a**) and phase of complex stiffness (**b**) of the two-stage baseplate from the 2DOF model.

3.4 Effect of the bending of the lower block

It was identified that the 2-tonne steel block has vibration modes within the frequency range of interest that can that affect the measured data. Therefore, it is important to identify these vibration modes to allow positioning of the accelerometer at the nodal locations where the effect of the vibration modes is the least significant. To achieve this, an accelerometer was placed at the centre of the lower block and an impact force was applied using an instrumented hammer every 0.01 m along the centre line of the top surface of the block as shown in **Figure 3-12** (**a**) and (**b**). The acceleration was measured at the middle of the block where the test specimen is usually positioned as shown in **Figure 3-12** (**a**) and (**b**). By using reciprocity, the transfer function (accelerance) between the middle point and each point along the central line is determined. **Figure 3-13** shows the measured transfer functions for selected locations along the centre line. The results show a peak in the response at around 1250 Hz that is identified as the first bending mode of the block. The peak in the transfer function magnitude is smallest for excitation at the point that is located 0.25 m from the edge of the block.

In addition to these measured results, a simple FE model has been generated in COMSOL using the known geometry and material properties of the steel block. From the model, the vibration modes have been calculated for free boundary conditions. The model confirms that the first bending natural frequency of the steel mass is around 1250 Hz, with nodes located 0.25 m from the edge, as shown in **Figure 3-14**.

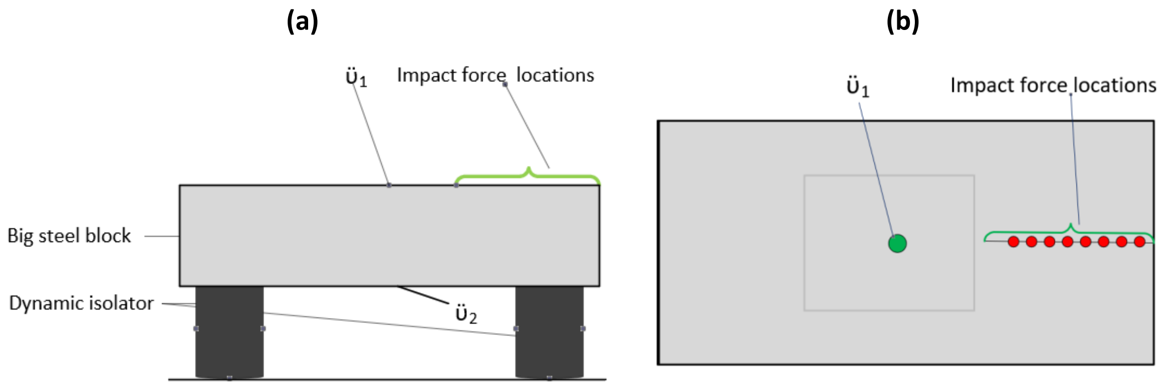

Figure 3-12 (**a**) side view of the basic set-up measurement (**b**) top view shows the locations of the impact force and measured position.

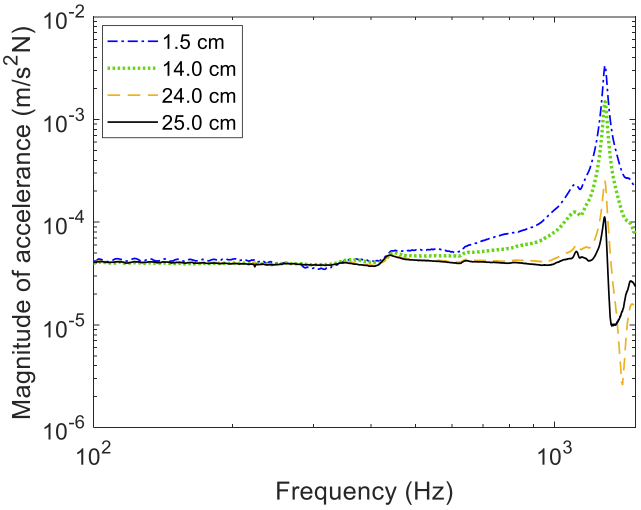

Figure 3-13 Magnitude of the transfer accelerance of the lower steel block (distances from the edge of the block).

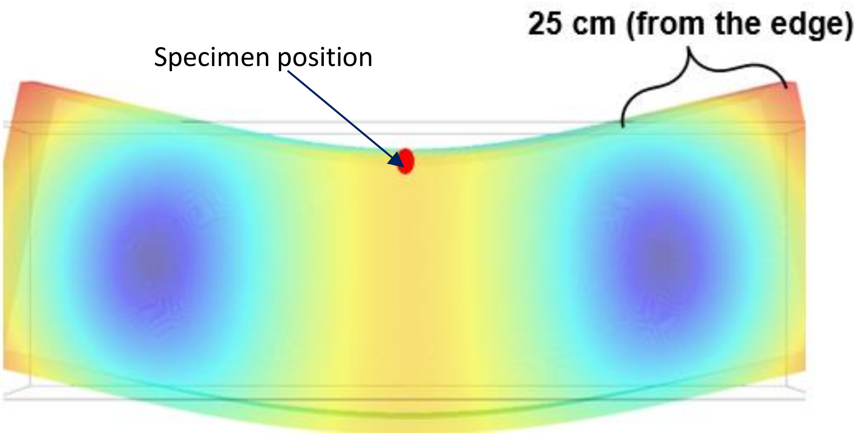

Figure 3-14 First bending mode shape of the steel block at 1250 Hz calculated in COMSOL.

Given these results, the sensor needs to be placed at this nodal point (0.25 m from the edge of the block) as this mode has the least effect there. The acceleration at this location can be related to the applied force by the inverse of the transfer accelerance, which is almost independent of frequency (and should be equal to the mass of the block).

3.5 Test procedure and data processing

Given the theoretical considerations in Section **3.3**, the test aims to determine the dynamic stiffness of the resilient element by measuring the transmissibility between the acceleration of the lower mass (steel block) and the acceleration of the upper mass (rail section). For the upper mass, it was found to be necessary to use the average of two accelerometers, one placed on either side of the rail web, to eliminate the effect of rotation of the rail. The resilient element is placed between the two masses, and a predefined value of hydraulic static preload is applied on the railhead through the two isolators (see **Figure 3-1** and **Figure 3-2**). The preload is allowed to settle for about 15 seconds before the dynamic excitation is applied, and the recording of the acceleration starts. The dynamic excitation is applied to the rail using the inertial shaker fed with a pseudo-random signal. The frequency range of interest is 1 Hz to 2 kHz, and a rectangular window is used. For each test, 60 frames (time windows) of the acceleration are captured using SignalCalc 730 Dynamic Signal Analyser, with a frequency span of 2.5 kHz and 1600 spectral lines. A Fast Fourier Transform (FFT) is applied to each frame, and the transfer function is calculated by the analyser using stable averaging. Next, the dynamic stiffness and damping loss factor are estimated as described in Section **3.3** from Equation (**3-11**).

In order to assign a single value for the dynamic stiffness and the damping loss factor from each measurement, the following procedure is followed. The magnitude of the dynamic stiffness is plotted against frequency for each preload (solid thin lines in **Figure 3-15** (**a**)). A straight line is fitted to the frequency dependent results on a double logarithmic scale within a certain frequency range (black dashed lines in **Figure 3-15** (**a**)). The selected frequency range is shown as the solid red lines in **Figure 3-15** (**a**)). From this fitted curve, a single value of dynamic stiffness is obtained at a chosen frequency, i.e. 300 Hz (a vertical black dashed-dotted line in **Figure 3-15** (**a**)). The resulting values of the dynamic stiffness magnitude can then be plotted against preload. The frequency of 300 Hz is chosen as it lies roughly in the middle of the frequency range of interest.

A similar process is followed for the damping loss factors, as shown in **Figure 3-15** (**b**). In this example, the damping loss is estimated from the fitted curve at 360 Hz. The frequency of 360 Hz is used rather than 300 Hz as the region used for fitting is more limited for the loss factor.

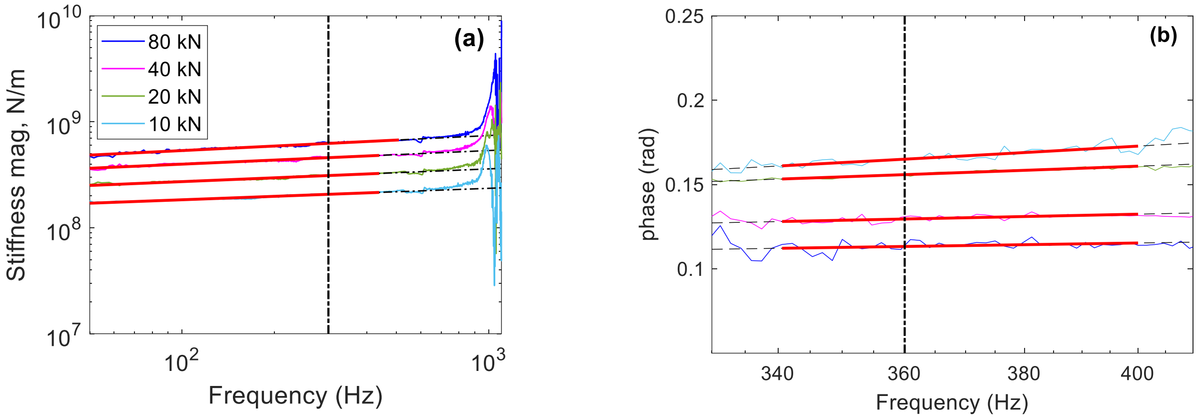

Figure 3-15 Curve fitting of the magnitude for different preloads with a selecting the value at the frequency of 300 Hz for dynamic stiffness **(a)** and at a frequency of 360 Hz for damping loss factor **(b)**.

3.6 Measured specimens

The dynamic stiffness and damping loss factor have been measured for a number of resilient elements, most of which were provided by Pandrol. These are: (a) eleven different railpads, four are presented in this chapter shown in **Table 3-4**, while the rest are presented in Appendix A, (b) a single-stage baseplate system, (c) a two-stage baseplate system, (d) the pads of the baseplate systems measured on their own and (e) a combined three-in-one system known as FCA system (a steel plate sandwiched between two layers of rubber) which is also presented in Appendix A. Indicatively, some of the samples are shown in **Figure 3-16**. The pads can be divided into two main categories regarding their material; those made of natural rubber (NR) and those made from Ethylene-Vinyl-Acetate (EVA). Natural rubber is usually softer than EVA. The surface of the pads is either studded, striped (the studs and strips have an effect on the stiffness of the pads as they tend to make the pad softer) or plain. In addition, the vertical and lateral dynamic stiffness of the Vanguard fastener system, as well as its static stiffness measurement, are presented in Appendix B.

Table 3-4 The details of the tested resilient elements

No.	Test specimen and material	Type (pad width)	Test details
1	EVA studded pad	Pandrol 9970 (150 mm)	On its own (and in single/two-stage fasteners)
2	EVA studded pad	Pandrol 21422 (150 mm)	On its own (and in single/two-stage fasteners)
3	NR Studded pad	Pandrol 21251 (150 mm)	On its own (and in single/two-stage fasteners)
4	NR Studded pad	Pandrol 8854 (150 mm)	On its own
5	Single-stage baseplate	Pandrol single layer (190 mm)	A single-stage system with Pandrol pad 21251 (No 3)
6	NR Lower pad for two-stage	Type A- This is a single stud pad	Two-stage system with no railpad
7	NR Lower pad for two-stage	Type B This is a double stud pad	Two-stage system with no railpad
8	Plain pad	Pandrol HDPE (150 mm)	Not tested for its dynamic stiffness
9	Two-stage baseplate	Lower pad Type A	With Pandrol railpad 21422 (No 2)
10	Two-stage baseplate	Lower pad Type B	With Pandrol railpad 21422 (No 2)

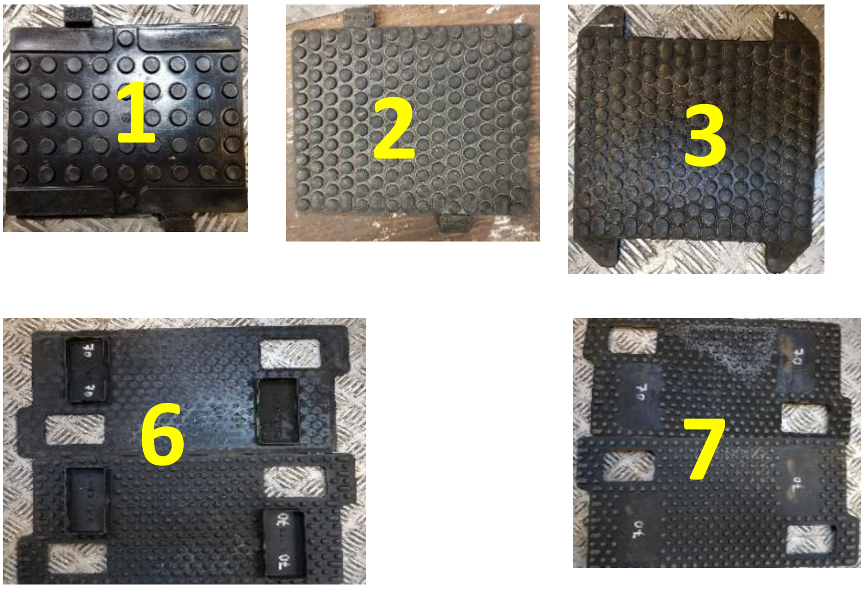

Figure 3-16 Railpad specimens (No1. No.2, No.3), and lower pads for the two-stage system No.6, No.7.

3.7 Measured results

3.7.1 Standalone railpad results

The dynamic stiffness and damping loss factor of several railpads are presented in this section. **Figure 3-17** shows the dynamic stiffness magnitude plotted against frequency under different static preloads for four different Pandrol pads.

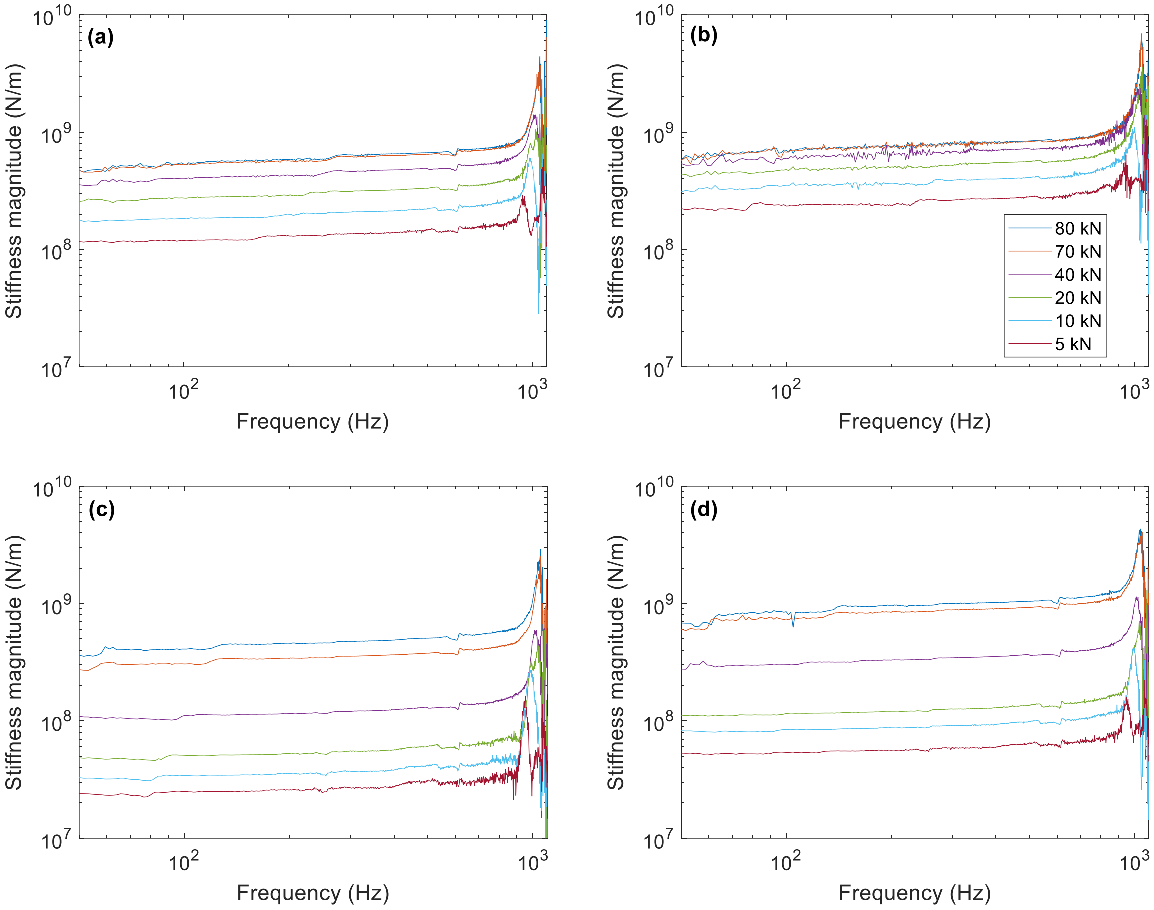

Figure 3-17 Dynamic stiffness magnitude plotted against frequency for different static preloads: (**a**) railpad No. 1; (**b**) railpad No. 2; (**c**) railpad No. 3; (**d**) railpad No. 4.

As described in Section **3.4**, the lower steel block has a bending mode at around 1.25 kHz. Therefore, the results around and above this frequency are affected and thus cannot be used. The frequency range of 50 Hz to 1 kHz has been selected to estimate the dynamic stiffness and loss factor of the tested railpads using the curve-fitting procedure described in Section **3.5**. **Figure 3-18** (**a**), shows the results for the dynamic stiffness magnitude at 300 Hz plotted against static preload for the different railpads tested, while **Figure 3-18** (**b**), shows the corresponding damping loss factors plotted against static preload.

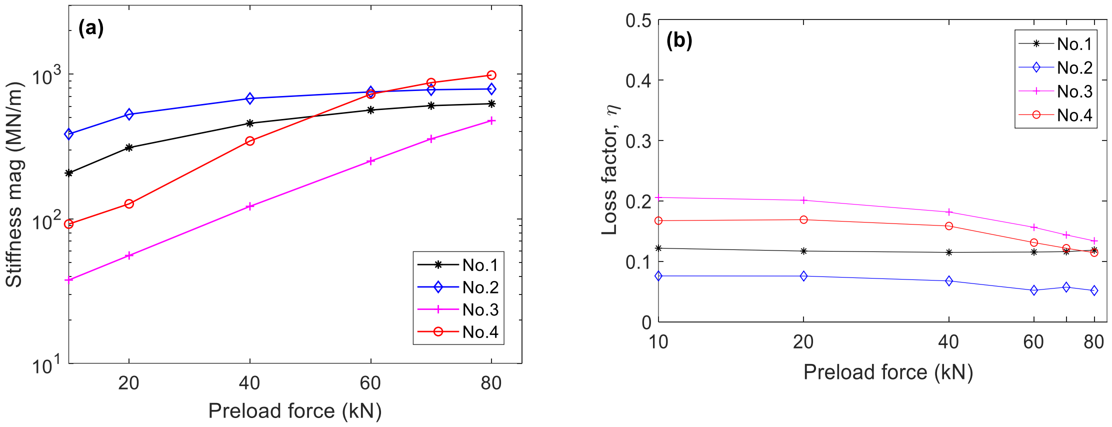

Figure 3-18 **(a)**Dynamic stiffness magnitude at 300 Hz, (**b**) loss factor at 360 Hz plotted against static preload for railpads No. 1-4.

As expected, the results show that the stiffness for all tested railpads increases with increasing static preload. Conversely, the increase of the preload generally results in a decrease in the loss factor. Similar trends are found for the other pads presented in Appendix A. **Table 3-5** provides a summary of stiffness and loss factor for the preload of 20 kN and 80 kN.

Table 3-5 Summary of measured railpad stiffness and loss factor

Railpads	**Stiffness (MN/m) at 300 Hz**		**Loss factor (η) at 360 Hz**	
	Preload of 20 kN	Preload of 80 kN	Preload of 20 kN	Preload of 80 kN
No.1	310	625	0.1	0.1
No.2	528	791	0.1	0.1
No.3	60	478	0.2	0.1
No.4	120	986	0.2	0.1

3.7.2 Results from the single-stage baseplate system

The single-stage baseplate system that has been tested (see **Figure 1-6**) is a Pandrol-manufactured rail fastener, Fastclip SFC, that consists of an 11 kg steel plate (404×206×19.4mm) which is commonly fitted with the soft NR studded railpad No. 3 (see **Table 3-4**). Usually, between the steel baseplate and the supporting track foundation (slab), a thin stiff plastic insert is used for electrical isolation to the ground. **Figure 3-19** shows the dynamic stiffness plotted against frequency of this configuration for different static preloads.

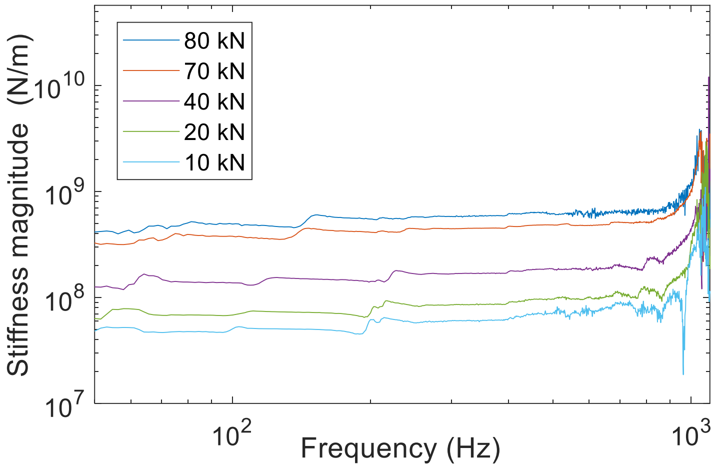

Figure 3-19 Dynamic stiffness magnitude plotted against frequency for the single-stage fastener fitted with railpad No. 3 at different preloads.

Two additional railpads (Pandrol No. 1 and No. 2) were mounted on the single-stage fastening system and the dynamic stiffness and loss factor were obtained. **Figure 3-20** presents the results at 300 Hz plotted against applied preload for the three different types of railpad mounted on the single-stage fastening system. As seen above, railpad No. 2 is the stiffer and railpad No. 3 is the softest of the three. **Figure 3-21** shows the corresponding loss factors.

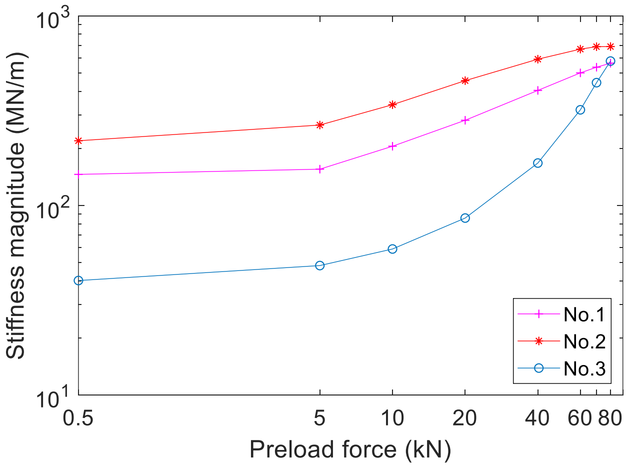

Figure 3-20 Dynamic stiffness at 300 Hz of the single-stage fastener system fitted with different Pandrol railpads plotted against preload.

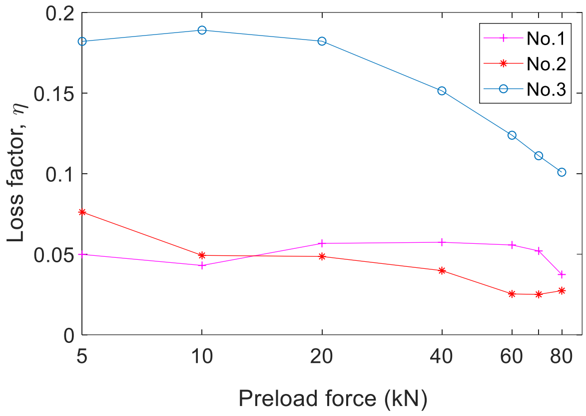

Figure 3-21 Loss factor of the single-stage fastener system fitted with different Pandrol railpads plotted against static preload.

The results in **Figure 3-20** and **Figure 3-21** are consistent with the standalone results for the same pads in **Figure 3-18 (a)** and **(b)** respectively. However, they are not exactly the same. For example, the results from the two measurements are compared for railpad No. 3 in **Figure 3-22** and **Figure 3-23**. It can be seen that when installed in the baseplate fastening system the dynamic stiffness is lower. Although the baseplate (steel) and the plastic isolator attached below the baseplate are very stiff, nevertheless adding an additional stiffness in series gives a lower total stiffness, as shown by the following equation:

$$k_{\mathrm{Tot}} = \frac{k_1 k_2}{k_2 + k_1} \tag{3-18}$$

where k_{Tot} is the total stiffness k_1 is the stiffness of the railpad, k_2 is the stiffness of the baseplate and the plastic isolator. On the other hand, the damping loss factor of the tested single-stage system tends to increase compared to the standalone pad, as shown in **Figure 3-23**. This could be due to friction at the various interfaces between the pad, baseplate, isolator and foundation.

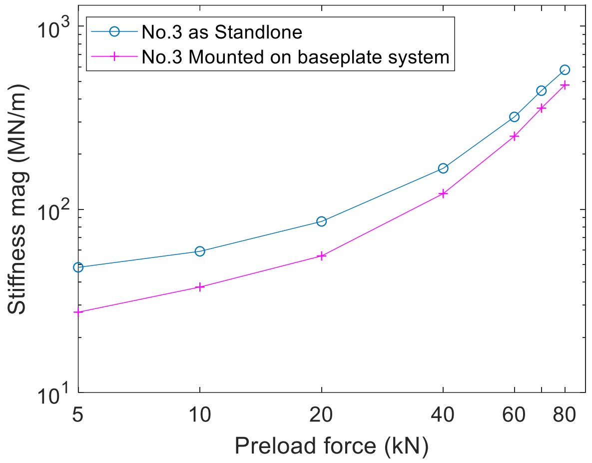

Figure 3-22 Comparison of the dynamic stiffness magnitude at 300 Hz plotted against static preload for railpad No.3 as standalone and mounted in the single-stage fastener system.

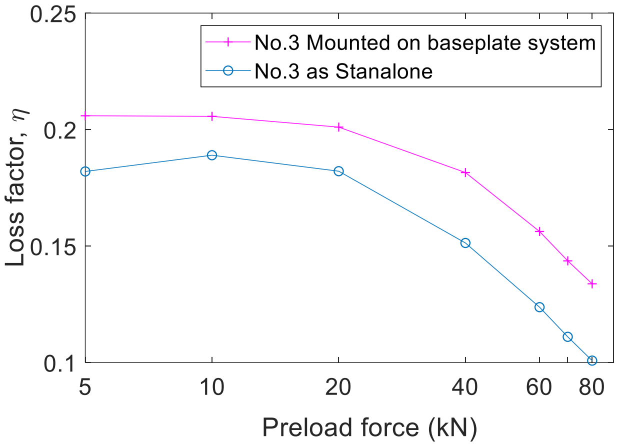

Figure 3-23 Comparison of the loss factor plotted against static preload for railpad No.3 as standalone and mounted on the single-stage fastener system.

3.7.3 The effect of clipping the rail and fixing the baseplate

In the initial measurements, the fastening system (baseplate) was not bolted on the steel block and the rail was not attached with clips. To investigate how bolting the baseplate and clipping the rail affects the measured stiffness, **Figure 3-24** presents a comparison between the clipped and bolted case and a free case for the baseplate fitted with railpad No.3. Since the clipping and the bolting forces could not be measured, the results in the unclipped and unbolted case have been shifted by adding an additional 20 kN preload to the value that was applied. It can be seen that by allowing for this force, the measured stiffness is close to the clipped and bolted case. Therefore, it can be assumed that the clipping force is equivalent to a 20 kN preload and no additional stiffness is introduced by the clips.

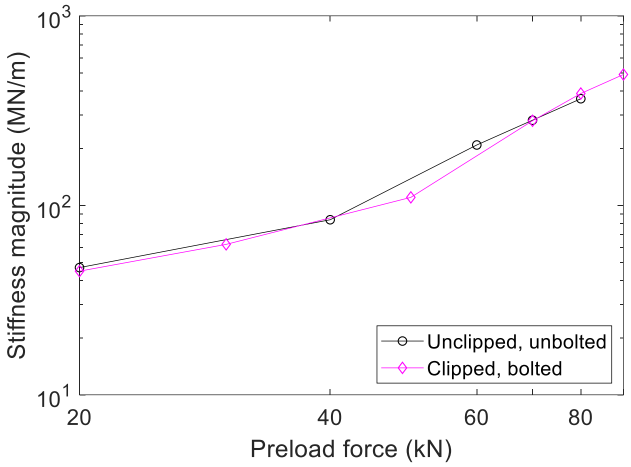

Figure 3-24 Dynamic stiffness with preload for clipped and bolted case compared with the unclipped, unbolted case that was shifted by 20 kN.

3.7.4 Results from the two-stage baseplate system

The two-stage baseplate system that was tested is also a Pandrol-manufactured type of rail fastener (see **Figure 1-7**) which consists of a 6.2 kg steel plate (404×206×15mm) with a combination of a stiffer upper railpad and a softer lower pad (between the baseplate and the slab foundation. The two-stage baseplate can be fitted with lower pads of different design; single-side studs, both-sides studs and with different hardness degrees (determined according to the International Rubber Hardness Degrees (IRHD) [91]). Hardness can be defined as a degree of deformation of the material that can be created by hand or with a hard, sharp object. It is also related to abrasion resistance and durability of rubber material [92]. Hardness can be used as an indicator of the stiffness of the material [93]. The IRHD values were measured by Pandrol prior to supply of the pads.

The baseplate fitted with the different types of lower pads are 'Type A' to 'Type F' baseplates as defined in **Table 3-6**. For the upper pad, railpad No. 2 or No. 3 is used. As an indication, the results of the frequency-dependent dynamic stiffness are shown in **Figure 3-25** for the type-A two-stage baseplate system fitted with Pandrol railpad No. 3. The variability shown around the frequency of 100 - 150 Hz appears to be an artefact of the test rig.

Table 3-6 Lower pads used in two-stage baseplate system

Lower pad types	Lower pad description	IRHD
Type A	Single studs	70
Type B	Double studs	62
Type C	Single studs	75
Type D	Double studs	64
Type E	Single studs	65
Type F	Double studs	60

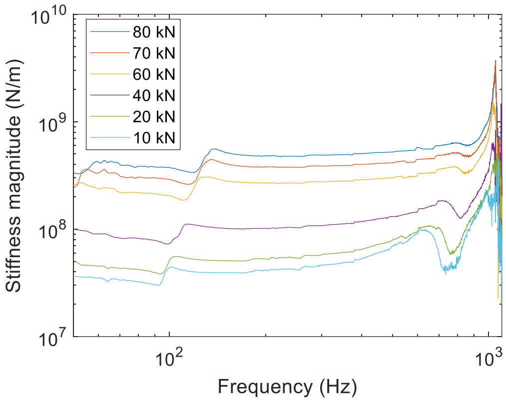

Figure 3-25 Dynamic stiffness magnitude for two-stage baseplate system fitted with type A lower pad and railpad No. 3 plotted against frequency.

Figure 3-26 and **Figure 3-27** shows the dynamic stiffness magnitude at 300 Hz plotted against preload for the two-stage baseplate system fitted with railpads No. 2 and No. 3 and mounted on the different lower pad types. It can be seen from the results that the stiffness increases with the value of IRHD, especially for higher preloads. The stiffness increases at higher preload as the studs on the pads deform.

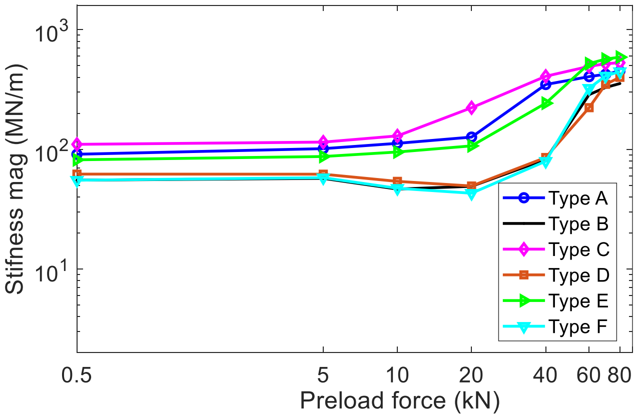

Figure 3-26 Dynamic stiffness magnitude plotted against static preload for baseplate system, fitted with different lower pads and railpad No.2.

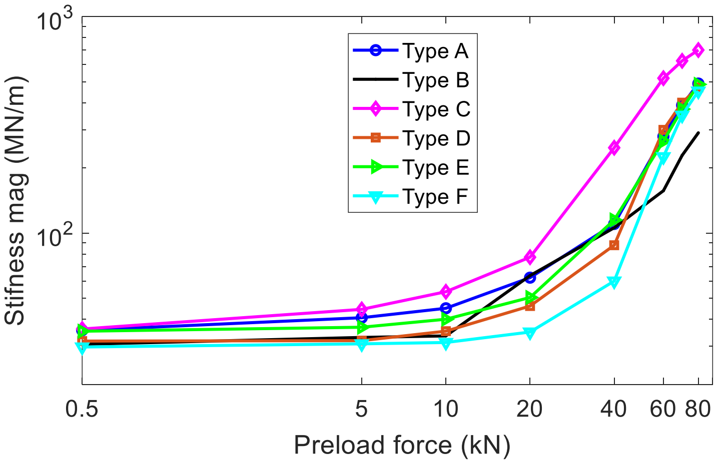

Figure 3-27 Dynamic stiffness magnitude plotted against static preload for baseplate system, fitted with different lower pads and railpad No.3.

Figure 3-28 and **Figure 3-29** shows the corresponding results for damping loss factor. The loss factor shows a smaller variation with the preload. For the case of railpad No.2, the loss factor tends to increase with preload, but above a certain value, depending on the IRHD value, it decreases again for high preload.

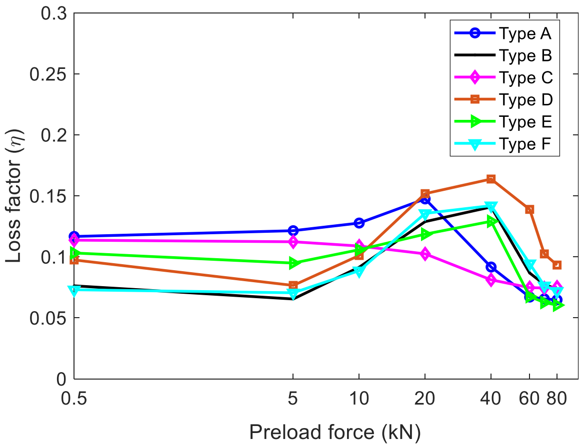

Figure 3-28 Damping loss factor plotted against static preload for baseplate system, fitted with different lower pads and railpad No. 2.

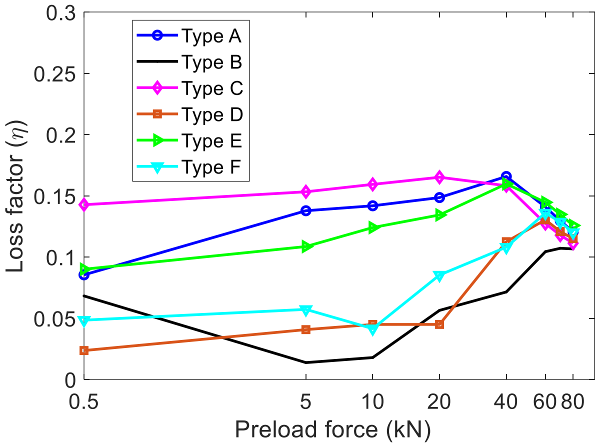

Figure 3-29 Damping loss factor plotted against static preload for baseplate system, fitted with different lower pads and railpad No. 3.

The lower pads of the two-stage baseplate are wider than the rail foot, which makes it difficult to measure their dynamic stiffness independently. In an attempt to measure their stiffness, they were installed below the baseplate and the rail was mounted on top with no railpad in place. Therefore, its dynamic stiffness is affected by the contribution of the bending of the baseplate. **Figure 3-30** presents the result for the dynamic stiffness plotted against frequency for the lower pad type A (No.6) when the baseplate is secured by the bolts on the lower mass and the rail is clipped. The bolting of the baseplate is not direct on the baseplate as shown in **Figure 1-7**; a metal spacer and plastic isolator are inserted between the baseplate and the bolts to avoid a rigid connection between the baseplate and the lower mass as well as to allow the baseplate to vibrate on the lower pad. It can be seen from the results that below 300 Hz many peaks and dips occur; this might be caused by either baseplate resonances or a contact stiffness effect between the rail and the baseplate. Nevertheless, it is possible using the curve fitting technique to extract a representative stiffness at 300 Hz.

Figure 3-31 compares the dynamic stiffness and loss factor as a function of preload for this lower pad, the railpad No.3 and the assembled baseplate containing these two elements. The results demonstrate that the lower pad is between 2 and 5 times stiffer than railpad No.3, so the assembled baseplate closely resembles the stiffness of the railpad.

A comparison of results is shown in **Figure 3-32** for railpad No.3 alone, fitted in the single-stage baseplate No.5 and in the two-stage baseplate No. 6 with Type A lower pad. With this railpad, each of the baseplates has a similar dynamic stiffness magnitude and loss factor. Larger differences are seen in **Figure 3-33** which shows results for railpad No.1 alone, fitted in the single-stage baseplate No.5 and in the two-stage baseplate with lower pad Types A and B. In this case, the railpad is much stiffer but using a softer lower pad (Type B) gives a much lower overall stiffness.

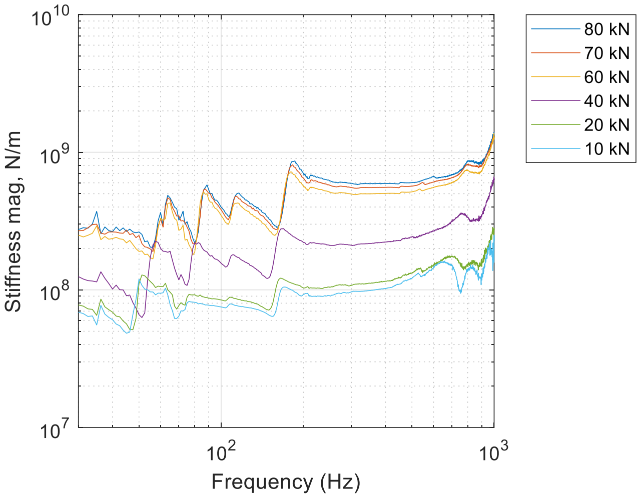

Figure 3-30 Dynamic stiffness magnitude plotted against frequency for lower pad type A (No.6) fitted in the baseplate with no railpad.

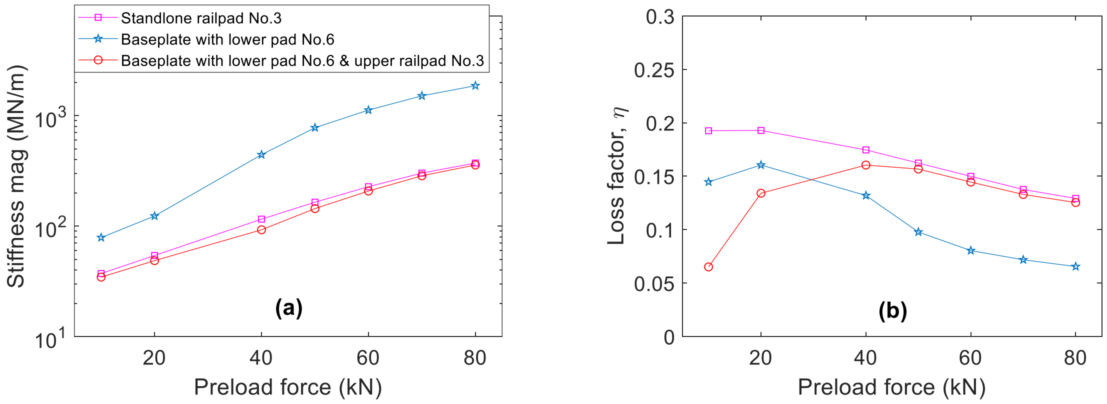

Figure 3-31 Comparison of results for separate pads and combined two-stage baseplate assembly with railpad No. 3 and lower pad A; **(a)** dynamic stiffness magnitude, **(b)** Loss factor.

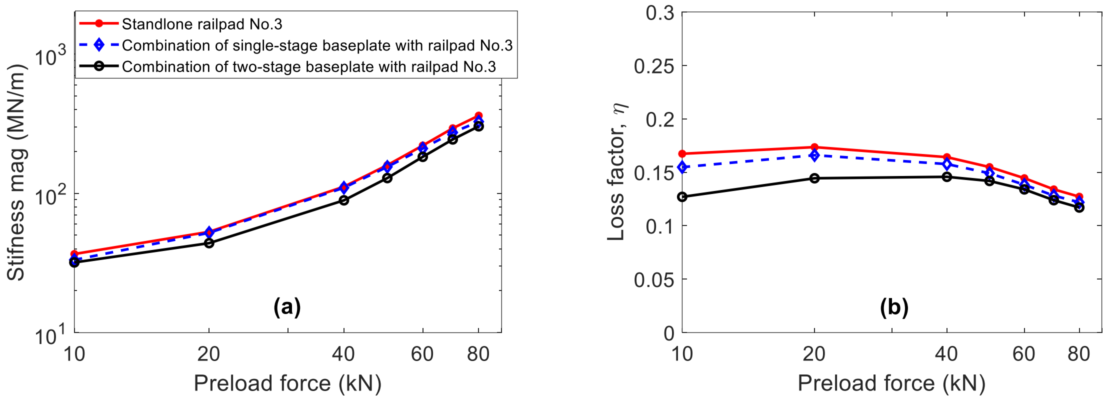

Figure 3-32 Comparison of results for railpad No.3 alone, mounted in single-stage baseplate No.5 and in two-stage baseplate with Type A lower pad; **(a)** dynamic stiffness magnitude, **(b)** Loss factor.

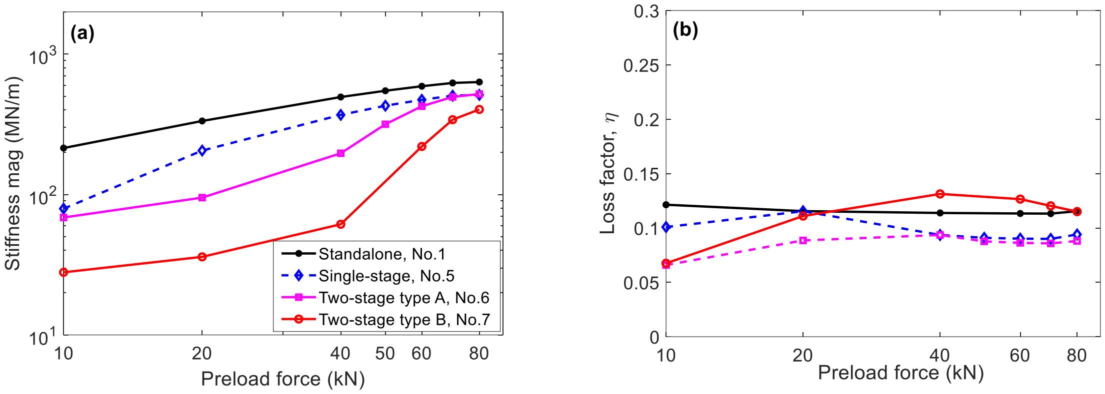

Figure 3-33 Comparison of results for railpad No.1 alone, mounted in single-stage baseplate No.6 and in two-stage baseplate with Types A and B lower pad: **(a)** dynamic stiffness magnitude, **(b)** Loss factor.

3.8 Comparison between measured and predicted dynamic stiffness

The 2DOF model of the baseplate described in Section **3.3** is used to predict the dynamic stiffness for an unclipped two-stage baseplate system. The results are compared with the measured dynamic stiffness for different preload conditions. The comparison is carried out in order to verify if the 2DOF system shown in **Figure 3-10** (**b**) is capable of describing the dynamic response of the two-stage baseplate system.

The calculation using the 2DOF system is based on the measured stiffness of the pads that have been determined by testing them individually. The single number values at 300 Hz are used in each case.

Note that the lower pad stiffness has been measured with the baseplate attached since it is wider than the rail foot and cannot be tested individually. The model calculates the combined transfer stiffness for the 2DOF system given by Equation (**3-16**). The predicted values are then compared with the measured dynamic stiffness determined by testing the whole two-stage system.

Figure 3-34, shows a comparison between the predicted and measured dynamic stiffness of the two-stage baseplate system. Results are shown for upper pads No. 3 and No. 4 and lower pad Type A (see **Table 3-6**). It should be noted that these results are for unclipped cases, so there is no preload from clipping. The values of the pad stiffness used for modelling are those presented in **Table 3-5** for the upper pad and a value of 80 MN/m is used for the lower pad which corresponds to a preload of 20 kN. The results show a generally good agreement in each case. At the higher preload of 80 kN, the predicted resonance frequency is higher than the measured frequency range. At this resonance, the rail upper mass and the baseplate mass move out of phase with one another. The sharp peak occurring at 1 kHz in all the results appears to be an artefact of the test rig, probably related to the lower mass bending mode.

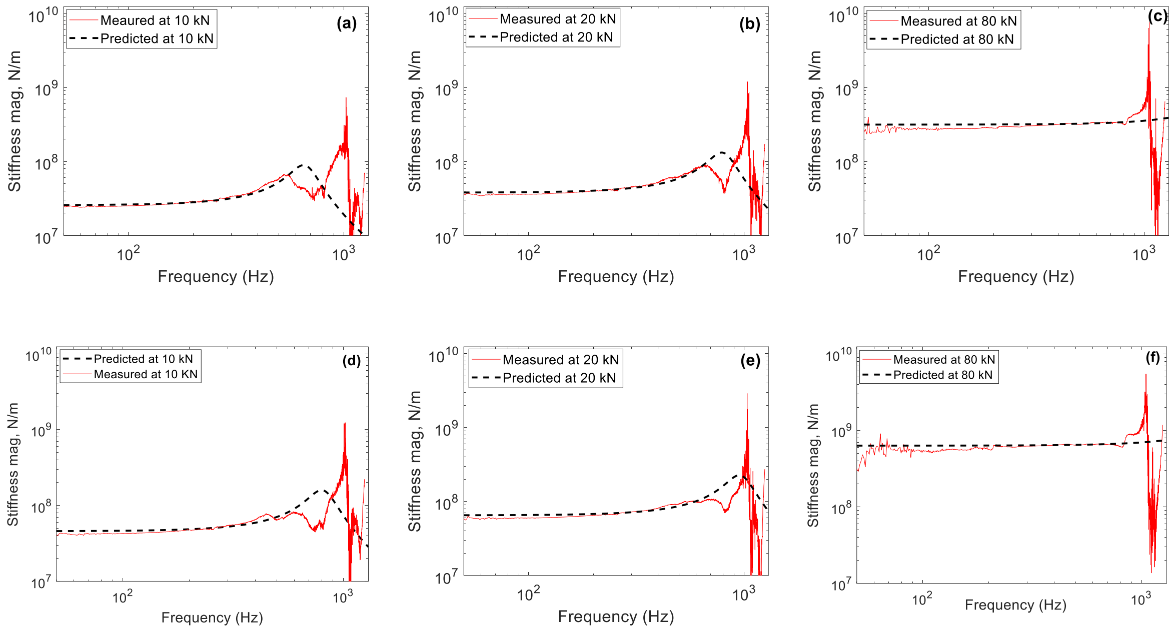

Figure 3-34 A comparison of the measured and the predicted for 2DOF model dynamic stiffness (**a-c**) railpad No.3, (**d-f**) railpad No.4.

3.9 Summary

The experimental setup for measuring the vertical dynamic stiffness of railpads and rail fastener systems (single and double stage) has been presented. The procedure for estimating the dynamic stiffness and damping loss factor from the measured transfer functions has been explained. The dynamic stiffness of several rail-fastening systems has been presented, and its dependence on frequency and preload has been discussed. Simple mass-spring models have been used to interpret the measured results and a good agreement is found between the measured data and these models. The effect of the force applied by rail clipping on the dynamic stiffness of railpads has been demonstrated. These results, in conjunction with in-situ measurements in **Chapter 4**, are used for model validation in **Chapter 5**, as well as in **Chapter 7** for noise assessment to understand the influence of dynamic stiffness on rolling noise. In addition, the vertical and lateral dynamic stiffness of the Vanguard fastener system, as well as its static stiffness are presented in Appendix B. These have been compared with other available data and good agreement is found. Moreover, the dynamic stiffness for a range of other railpads and for the FCA fastening system has been measured and results are presented in Appendix A. However, these other systems are not discussed further in the thesis.

Chapter 4 Track vibration measurements

4.1 Introduction

Measurements of TDRs were conducted on a demonstration slab track located at the National College for High-Speed Rail (now known as National College for Advanced Transport & Infrastructure) in Doncaster on the 30th and 31st of July 2018. The test track is fitted with 60E1 rails and consists of two 20 m long sections fitted with two different types of baseplate system: Pandrol and Vossloh. The measurements have been conducted mainly on the section containing the Pandrol two-stage system, and results have been obtained with the system fitted with four different types of railpad.

Additionally, to understand the vibrational behaviour of the two-stage baseplate system, measurements were conducted in the laboratory. In order to confirm the laboratory results, the test track was revisited, and additional measurements were conducted on the 5th of December 2019. Because of the different weather conditions between the two measurement dates, it was also possible to investigate the influence of temperature on the track and the fastening stiffness. For the December measurements, the vibration of baseplate fastening system has also been measured; however, only one type of railpad has been used. An additional TDR measurement was also conducted after removing the rail clips and railpads on every other rail fastener. The reason for this measurement was to validate and investigate further the results from the July TDR measurement.

The main aim for the measurements described in this Chapter has been to collect data that can be used to inform the vibration models developed in **Chapter 5.** These will in turn be used in **Chapter 6** and **Chapter 7** to assess the vibration and radiated noise of a slab track fitted with the two-stage baseplate design.

4.2 Test track

The demonstration track shown in **Figure 4-1** was constructed with the aim to train engineers on different aspects of servicing operations on high-speed lines. It accommodates rails with a total length of approximately 90 m (continuously welded), 40 m of which is on slab track while the rest is ballasted track. The fastener spacing is 0.65 m throughout the track.

Figure 4-1 View of the section of the test slab track. The ballasted track can also be seen in the distance.

The two types of rail fastening system are fitted on the slab track section, as shown in **Figure 4-2**. The Pandrol fasteners start at the transition from the ballasted track, and they are followed by the Vossloh system, which continues to the end of the test track. The overall layout can be seen in **Figure 4-3**. Track decay rates were only measured on the slab track sections.

(a) **(b)**

Figure 4-2 Photographs of the fastening systems (**a**) Pandrol two-stage system, (**b**) Vossloh system.

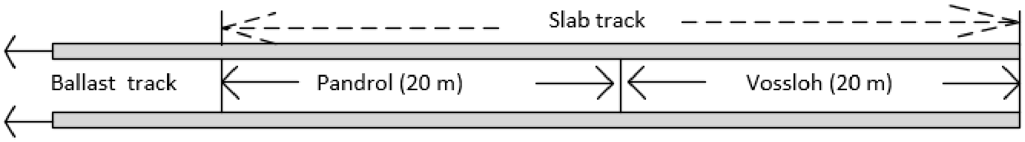

Figure 4-3 Schematic view of the test track's different sections with fastening system type for the slab track section.

For the Pandrol baseplates, measurements were taken with four different types of rail pad; the baseplate and lower pad were not changed. The dynamic stiffness of the four rail pad types has been previously measured in **Chapter 3,** Section **3.7**; these railpads have a dynamic stiffness range between 120 MN/m to 1200 MN/m.

4.3 Track decay rate

The interaction between the wheels of a train and the railway track during a train passage generates vibration of the wheels and track that radiates noise. The rail vibration consists of both vertical and lateral bending waves. The overall vibration of the whole vibrating length of the rail is directly affected by the rate of vibration amplitude decay along the rail as a function of distance, which is defined as a track decay rate. These decay rates are commonly represented as one-third-octave band spectra, expressed in decibels per metre (dB/m). Engineers use decay rates as an intermediate, measurable parameter that can be used to determine the noise performance of the track and as an input to noise models to improve their predictions [33-35].

TDRs are determined from a set of frequency response functions (FRF) of the rail. FRF measurements are taken at the force excitation point (driving point FRF) and at a certain number of distances from it (transfer FRFs) according to the EN15461:2008 standard [94]. The rail is excited by an instrumented hammer and the response is measured by an accelerometer fixed to the rail. **Figure 4-4** shows the standard recommended accelerometer positions and excitation positions. The accelerometer is mounted at a fixed position and the excitation is applied at different distances along the rail; in the vertical direction, these are on a longitudinal axis along the railhead and in the transverse direction they are along the outside face of the railhead. The excitation points are defined as a function of the sleeper spacing. A minimum test section of the rail that can be used for measuring the decay rate needs to be at least 20 m long with no expansion joints, with a minimum distance of 5 m from the driving point to any rail weld. However, the standard recommends that a full set of measuring positions for the track decay rates should extend over 66 sleeper spans, as shown in **Figure 4-5**. The results should be expressed in the form of a one-third octave spectrum covering frequency bands between 100 Hz and 5000 Hz [94]. Due to the limited length of the track available for these measurements, the standard positions are modified so that the last measuring position is at 15.3 m from the accelerometer to minimise any effects from the adjacent rail fasteners of different type and the reflections from the end of the rail.

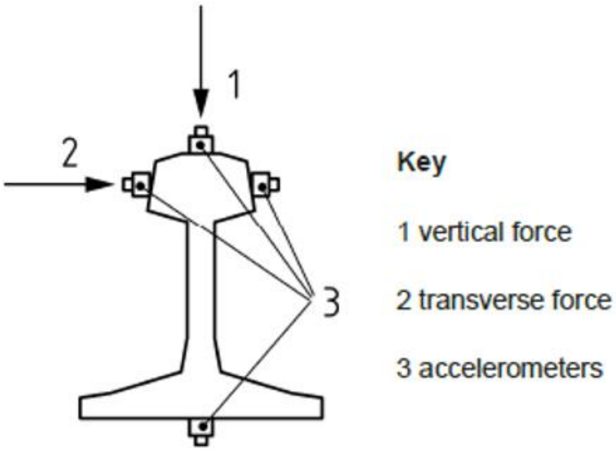

Figure 4-4 Recommended positions for the accelerometers on the cross-section of the rail according to EN15461:2008 [94].

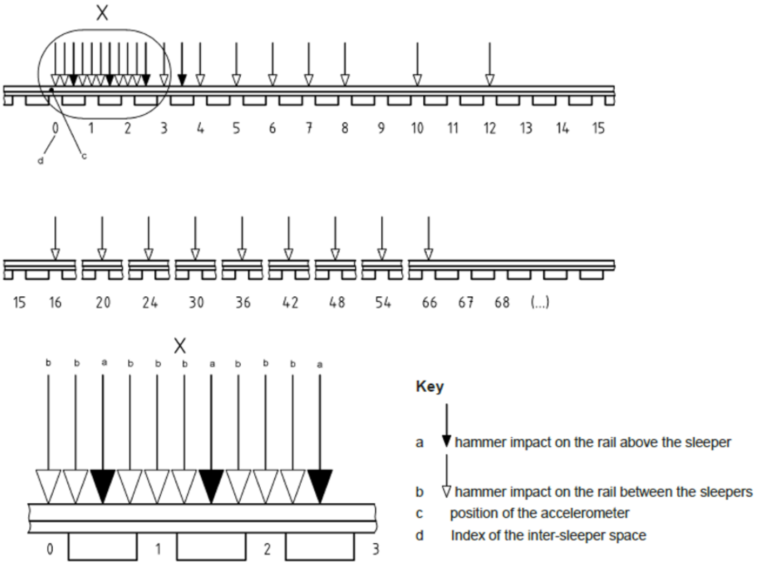

Figure 4-5 Recommended grid positions of the excitation points relative to the fixed response point, according to EN15461:2008 [94].

4.3.1 **TDR measurement procedure at the test track**

Figure 4-6 presents the excitation and accelerometer positions on the rail cross-section, and **Figure 4-7** shows a photograph for the lateral direction measurements.

The impact sequences were carried out for both vertical and lateral excitation, and the corresponding responses of the railhead were measured. **Table 4-1** presents the adopted measurement grid for the test. **Figure 4-8** shows a photograph of the equipment setup and marked measured positions. The atmospheric temperature was recorded during the measurement period. In July it was 26°C whereas in December it was 5°C.

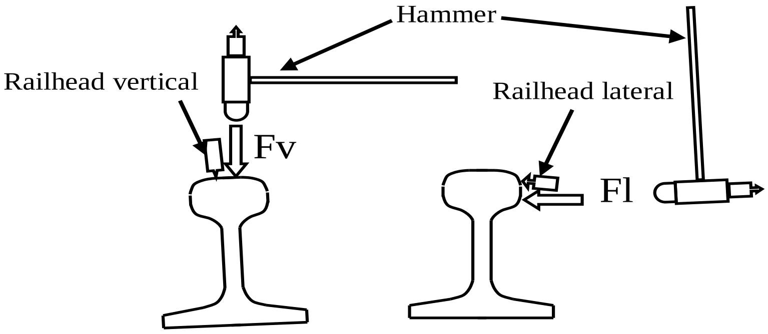

Figure 4-6 Instrumented hammer and accelerometer position on the railhead.

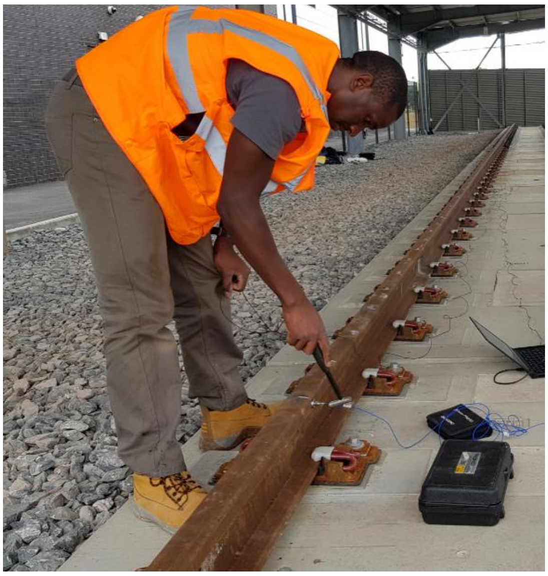

Figure 4-7 TDR measurement in the lateral direction.

Table 4-1 Adopted TDR measurement positions

Measurement number	Number of fasteners from the reference point	Distance from the reference point (m)	Comment
1	0	0	Above the fastener
2	0.5	0.325	Midspan
3	1	0.65	Above the fastener
4	1.5	0.975	Midspan
5	2	1.3	Above the fastener
6	2.5	1.625	Midspan
7	3	1.95	Above the fastener
8	3.5	2.275	Midspan
9	4	2.6	Above the fastener
10	4.5	2.925	Midspan
11	5	3.25	Above the fastener
12	6	3.75	Between fasteners
13	7	4.25	Between fasteners
14	7.5	4.875	Midspan
15	10	6.725	Between fasteners
16	11	7.4	Between fasteners
17	12	8	Between fasteners
18	13.5	8.775	Midspan
19	15	10	Between fasteners
20	17.5	11.375	Midspan
21	20.5	13.3	Midspan
22	23.5	15.3	Midspan

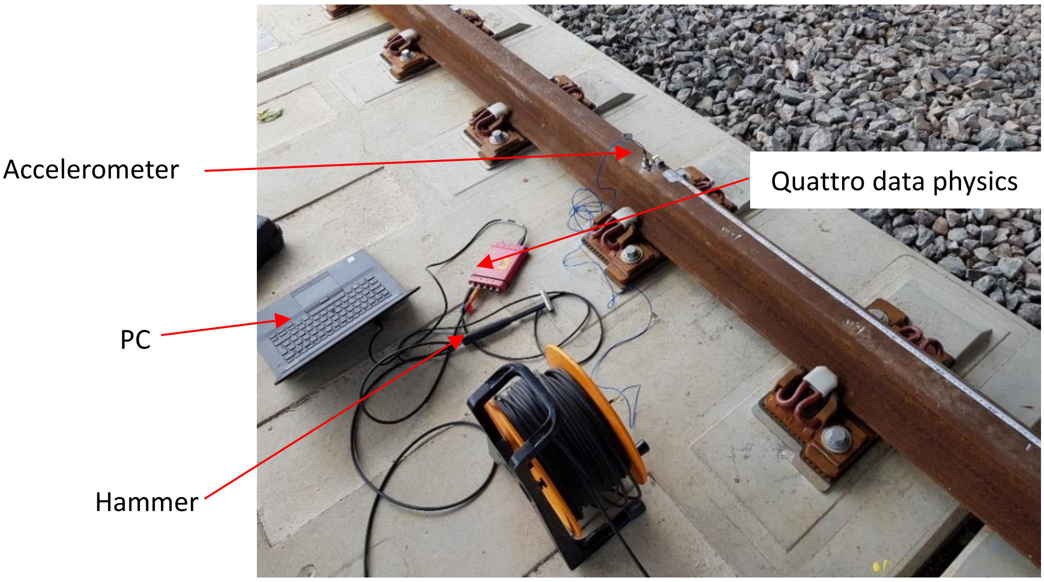

Figure 4-8 The equipment setup for the TDR measurements.

An overview of the equipment used for the tests is shown in **Table 4-2**.

Table 4-2 Measurement equipment

Equipment	Details
Accelerometers	PCB Piezotronics - Model: 352C34, sensitivity 104.0 mV/g
Impact hammer (150 g)	PCB Piezotronics-Model:086C02
Data analyser	Data Physics Corporation, Model: DP240, S/N: 20770
Laptop computer	Dell Latitude E7470
Software	Data Physics SignalCalc 730 Dynamic Signal Analyser, MATLAB

4.3.2 **Processing of the measured data**

From the available measured data in the form of FRFs (mobilities), the track decay rates DR are calculated in dB/m in accordance with EN15461:2008 [94] using the following formula:

$$DR \approx \frac{4.343}{\sum_{n=0}^{n_{max}} \frac{|A(x_n)|^2}{|A(x_0)|^2} \Delta x_n} \tag{4-1}$$

where $A(x_0)$ and $A(x_n)$ are the point and transfer FRFs respectively averaged in one third octave bands and Δx_n is the spacing between the adjacent n measurement positions.

4.4 Results and analysis

This section presents the results of the in-situ measurement for point mobility and TDR of the test track for the two measurement campaigns in July 2018 and in December 2019.

4.4.1 **Driving point mobility**

The magnitude and the phase angle of the vertical point mobility at the railhead for excitation above a fastener are shown in **Figure 4-9** to **Figure 4-12** for the cases when the test section was fitted with the four different Pandrol railpads. Two hammer tips were used to excite the rail, a soft tip for low frequencies up to 500 Hz and a hard tip for higher frequencies above 500 Hz. The impact test was repeated several times for each excitation location, and the final FRF is constructed by averaging the signals in the frequency domain. The associated coherence is also estimated by the acquisition system and is shown in **Figure 4-9** to **Figure 4-12** for the driving point mobilities. For the data acquisition, time samples of 320 ms were acquired with a rectangular window using the average of four samples in each case. The results in these figures demonstrate the importance of using the two types of tips; for the hard tip, the coherence is poor at the lower frequencies, while for the soft tip the coherence is poor at the higher frequencies. Therefore, for the TDR calculations, the soft tip results are used for frequencies up to 500 Hz and the hard tip for the frequencies above this.

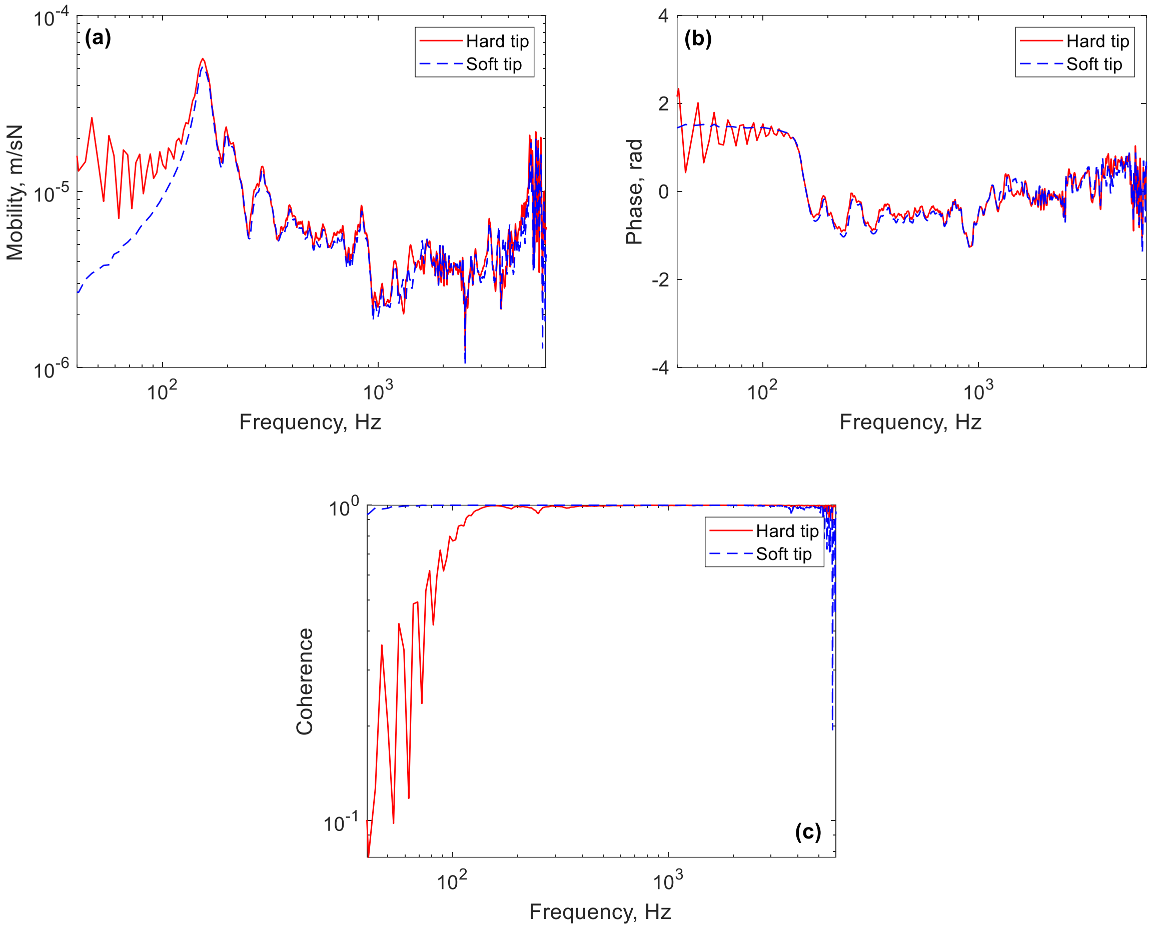

Figure 4-9 Measured (**a**) magnitude, (**b**) phase and (**c**) coherence of the vertical driving point mobility for Pandrol railpad No.1**.**

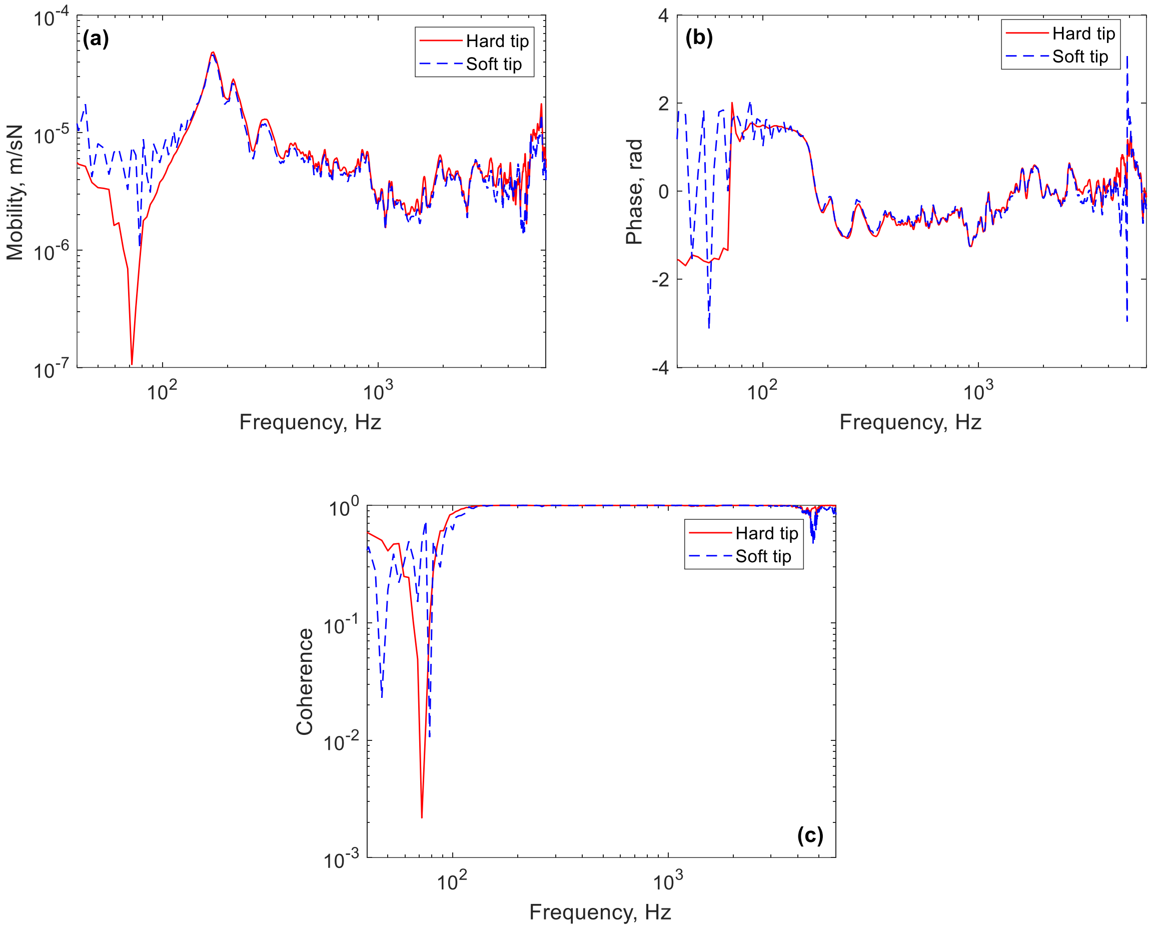

Figure 4-10 Measured (**a**) magnitude, (**b**) phase and (**c**) coherence of the vertical driving point mobility for Pandrol railpad No.2.

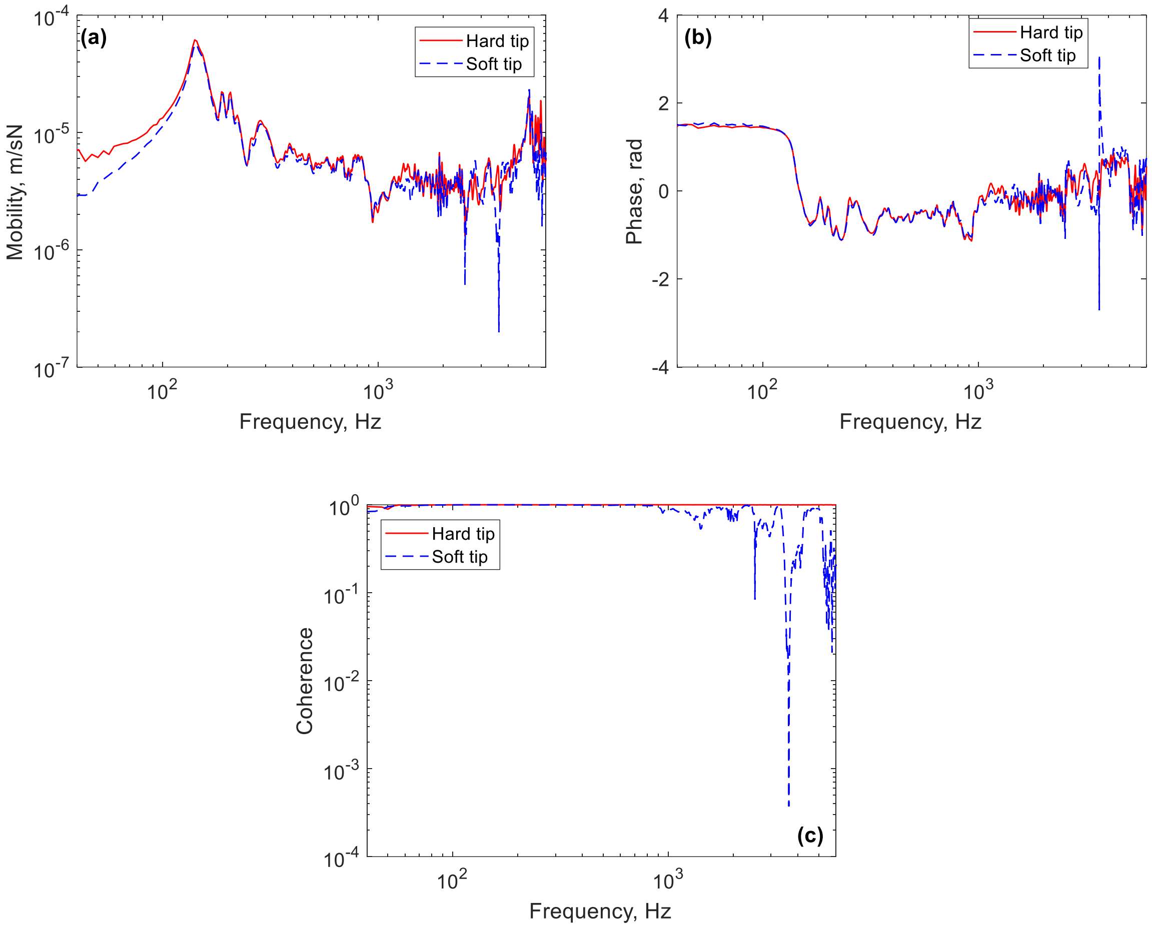

Figure 4-11 Measured (**a**) magnitude, (**b**) phase and (**c**) coherence of the vertical driving point mobility for Pandrol railpad No.4.

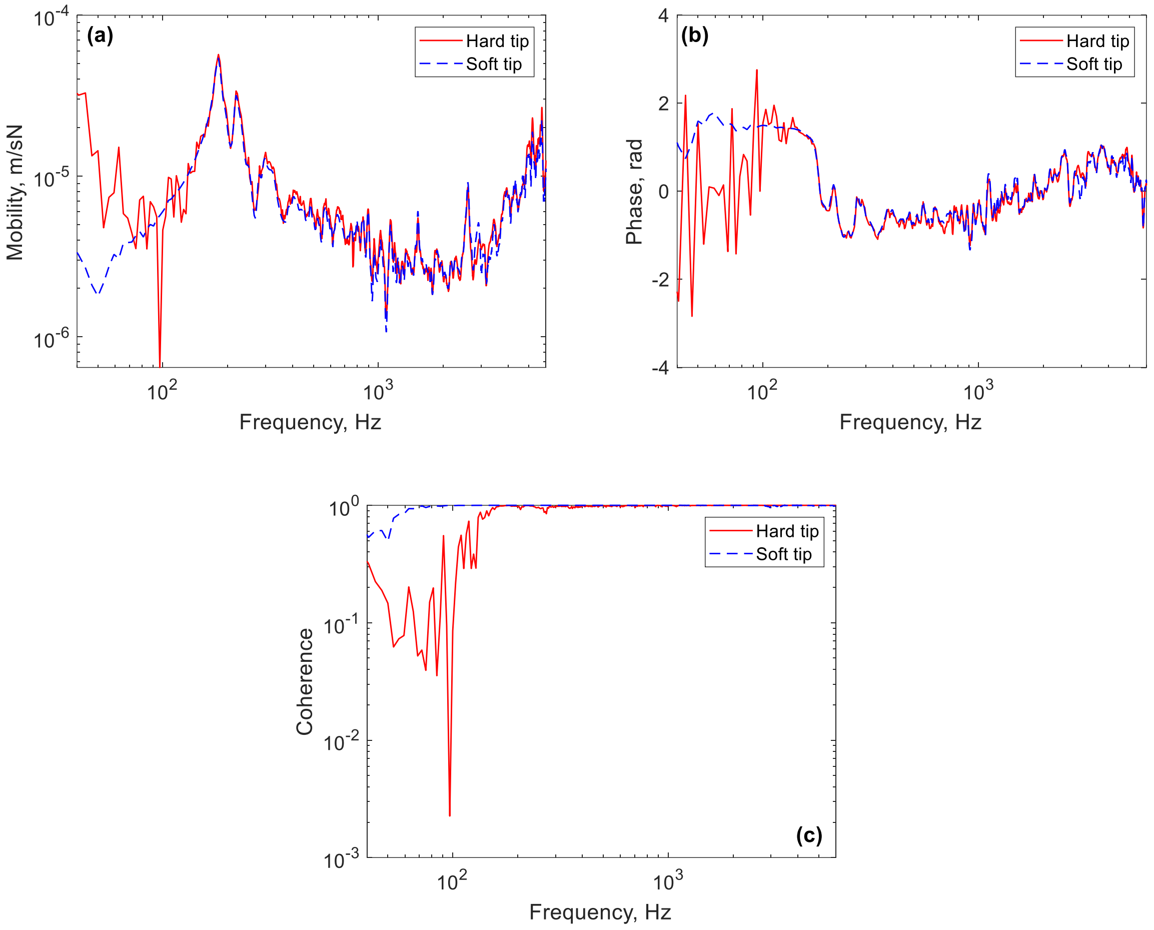

Figure 4-12 Measured (**a**) magnitude, (**b**) phase and (**c**) coherence of the vertical driving point mobility for Pandrol railpad No.8

Figure 4-13 compares the driving point mobilities for the track fitted with all the measured Pandrol railpads after combining the soft and hard tip measurements. These results are consistent with the stiffness measurement results given in **Chapter 3** showing that the rail's first natural frequency shifts to a higher frequency as the stiffness of the railpad increases. However, the shift is relatively small due to the presence of the lower pad.

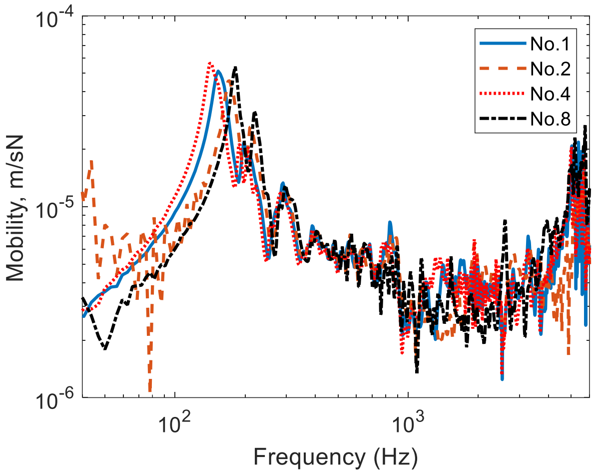

Figure 4-13 Comparison of the measured vertical driving point mobility for all Pandrol railpads.

4.4.2 **TDR results**

The vertical and lateral TDR measured in July 2018 are shown in **Figure 4-14**. Results are compared for the two types of fastening system on the test track, the Vossloh system and the Pandrol system. For the Pandrol system, results are given for the four different railpad types. In all cases the decay rate is high, close to 10 dB/m, at low frequency where the stiffness of the rail support causes the waves to be blocked [1]. The decay rate then falls to values around 1 dB/m at frequencies above the first resonance seen in the point mobility where the waves can propagate along the rail. It can be seen that as the stiffness of the pad increases, higher TDR values are achieved at low frequencies (below about 500 Hz) and even greater at high frequencies above 2 kHz. For a softer railpad, the rail is better isolated from the fastener system. Therefore, it is more free to vibrate and radiate noise, while for a stiffer railpad the rail is more strongly coupled to the foundation and for this reason, it will have a higher TDR.

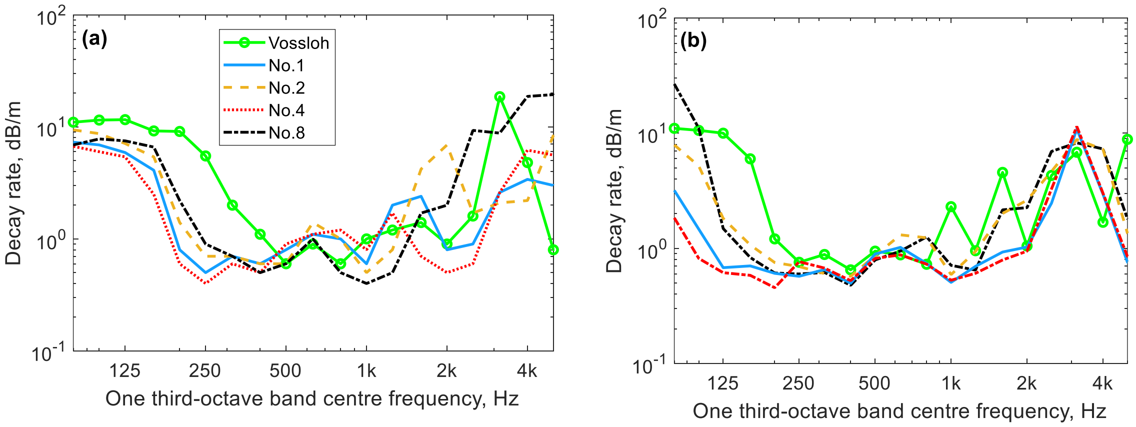

Figure 4-14 TDR measured in July 2018 **(a)** vertical, **(b)** lateral.

4.4.3 The effect of the temperature on the TDR results

Figure 4-15 shows the influence of temperature on the TDR by comparing results for the Pandrol system with railpad No. 1 measured in July 2018 and December 2019. For the July measurements, the railpad and the environmental temperature was measured at about 26°C whereas during the December measurements the temperature was 5^0C. A higher TDR is obtained from the December data for low frequencies up to 500 Hz and high frequencies above 1 kHz. For mid-frequencies (500 Hz to 1 kHz) the values are similar. The reason for the differences is due to the changes in the railpad stiffness. The stiffness of the railpad is expected to have increased at low temperature [95] and the results from December are more consistent with those for a stiffer pad (see **Figure 4-14**).

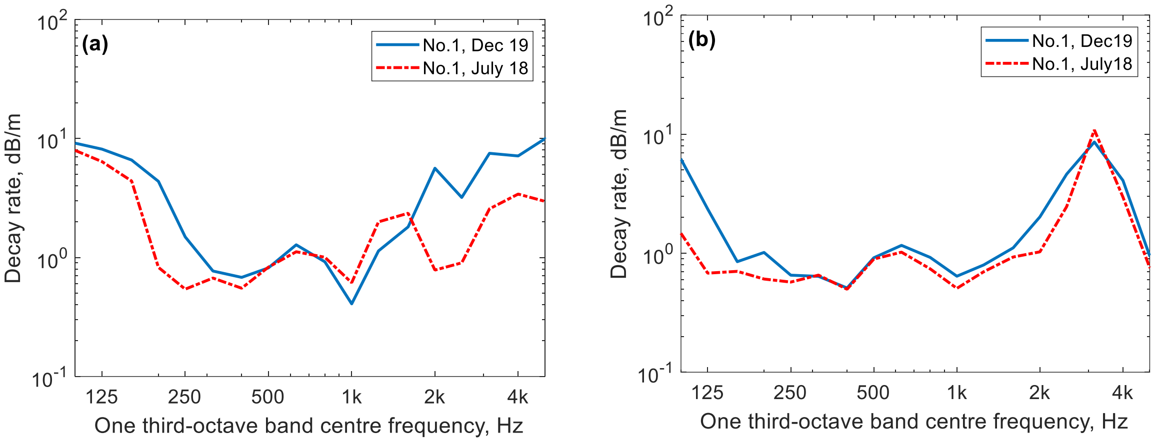

Figure 4-15 Comparison of the TDR for railpad No. 1 measured in December 2019 (5^0C) and July 2018 (26^0C) for **(a)** vertical, **(b)** lateral.

4.4.4 The effect of the fastener spacing on the TDR results

The effect of the rail fastener spacing on the measured TDR is investigated by removing the clips and railpads from every other fastener and repeating the TDR measurement for the Pandrol baseplates with railpad No.1. The reason for conducting this additional measurement was to investigate the peaks at 600 Hz and above 1 kHz and the dip at 1 kHz seen in **Figure 4-14** and **Figure 4-15**.

In **Figure 4-16 (a)** and **(b)** a comparison between the results for fastener spacings of 0.65 m and 1.3 m is shown for vertical and lateral TDR. It is expected that the pinned-pinned mode of the rail will be affected when the support spacing of the rail is increased from 0.65 m to 1.3 m. The pinned-pinned vibration mode occurs when a half wavelength in the rail corresponds to the supporting spacing. For example, for a UIC60 rail with a fastener spacing of 0.6 m, the vertical pinned-pinned mode occurs at a frequency of 1070 Hz [1]. From the calculation method detailed in [1] the vertical pinned-pinned vibration mode for a fastener spacing 1.3 m and 0.65 m occurs at 281 Hz and 942 Hz respectively (see **Figure 4-17**). In **Figure 4-13** the pinned-pinned mode can be seen as a peak in the mobility at about 900 Hz.

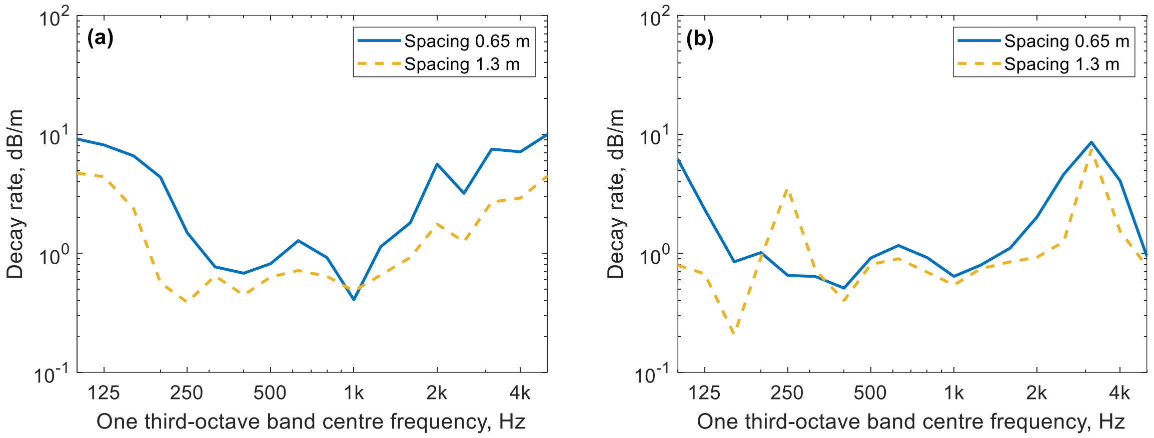

Figure 4-16 Comparison of the TDR measured in December 2019 for 0.65 m and 1.3 m fastener spacing **(a)** vertical, **(b)** lateral.

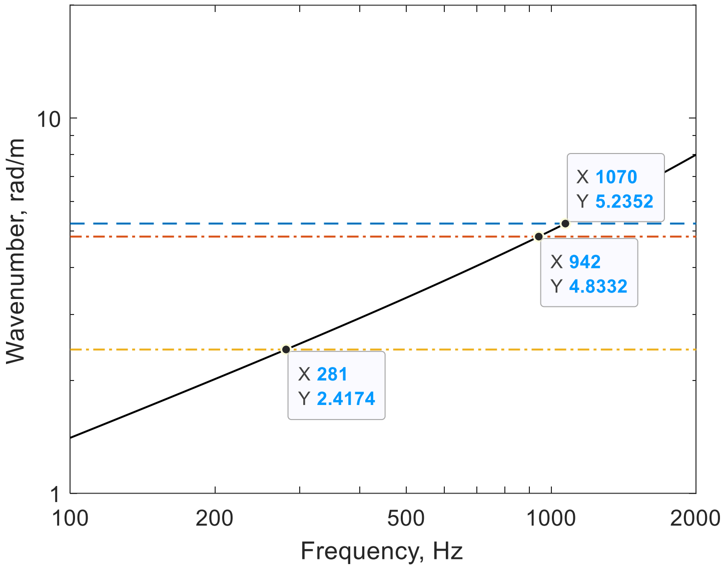

Figure 4-17 Wavenumber plotted against frequency (dispersion relation) for a Timoshenko beam showing the pinned-pinned frequencies corresponding to the fastener spacing of 1.3 m, 0.65 m, and 0.6 m.

In **Figure 4-16**, there is a dip at 1 kHz in the original TDR measurements that may be identified with the pinned-pinned mode. When the fastener spacing is increased, the peak at around 600 Hz has been smoothened, and the peaks above 1 kHz are not affected. The peak around 600 Hz is believed to be a bending mode of the fastening system; this is further investigated in Section **5.2.5**. These results also show that by doubling the fastener spacing, the TDR has been lowered across much of the frequency range. This occurs because the support stiffness (per unit length) has been halved.

4.5 Laboratory measurement of baseplate vibration

To understand the two-stage baseplate system's vibrational behaviour, measurements have been conducted in the laboratory using the rig setup for dynamic stiffness measurement described in **Chapter 3**. The baseplate system was placed between the two masses (a schematic view of the rig setup is shown in **Figure 3-2**). The vibration responses were measured at three locations on the baseplate to identify the distribution of vibration across the baseplate surface. For the current measurements, Pandrol rail pad No.2 was used.

4.5.1 **Measurement setup**

The two-stage baseplate was bolted on the 2-tonne steel block, and the Instron actuator applied a preload of 10 kN on top of the rail. The rail (upper mass) was not clipped on the baseplate for these tests. Two sensors were attached to the railhead, and two were placed in three different pairs of positions on the baseplate. Three sets of measurements were therefore performed to measure the vibration ratios between the top of the rail and the three regions on the baseplate shown in colour coding in **Figure 4-18**, namely:

- I: Near the bolting locations (red areas).
- II: Near the clipping area (green areas).
- III: Next to the railpad (blue areas).

The excitation was applied using the dynamic shaker as described in **Chapter 3**. A schematic side view of the rig setup is shown in **Figure 4-19**. The arrows in **Figure 4-19** indicate the sensors. A side view of the sensors on the rail and the bolting area of the baseplate is shown in **Figure 4-20**. There are four sensors in each measurement set up. In all three setups, two sensors (u_1 and u_2) were placed on the two sides of the railhead measuring acceleration in the vertical direction. The use of two sensors is to compensate for any rotation of the rail. The superscripts for variables u_3 and u_4 indicate the measured points. Therefore, for example, u_3^{I} indicates a measured point located on the left side of the baseplate measuring acceleration at the bolting area.

Data was collected using the Data Physics acquisition system and then processed using Matlab software.

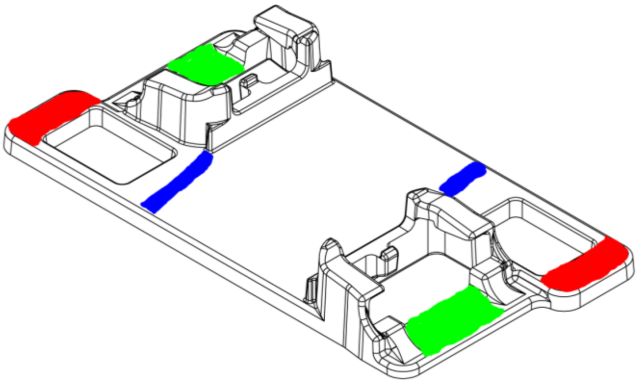

Figure 4-18 Sensor locations: at the baseplate, (blue) next to the railpad, (red) at the bolting and (green) at the centre of the clipping area.

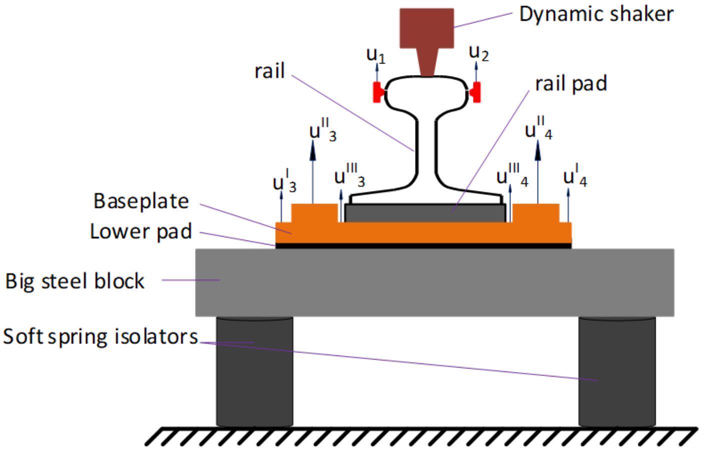

Figure 4-19 A schematic side view of the rig for vibration response measurement for the two-stage baseplate.

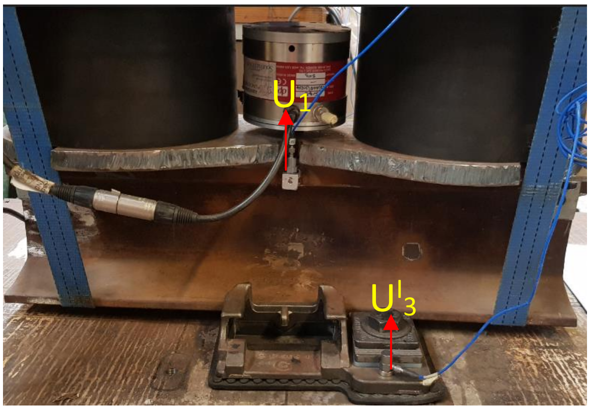

Figure 4-20 Side view showing the upper sensor and the lower sensor at baseplate bolting area.

Vibration response processing

The vibration ratio between the rail and the sensors placed on the left side of the baseplate is defined as:

$$V_{\mathrm{L}} = \frac{u_3^{\mathrm{i}}}{u_0} \tag{4-2}$$

where the subscript L indicates measurements taken on the left side of the baseplate, and the superscript i indicates the areas ($i = I, II, III$). The variable u_0 gives the vibration of the rail centre and is obtained as:

$$u_0 = \frac{u_1 + u_2}{2} \tag{4-3}$$

To obtain the ratio between the rail vibration in vertical direction and the vibration of the baseplate at the different areas, the signals are combined as:

$$V_{\mathrm{L}}^{\mathrm{i}} = \frac{2\dfrac{u_3^{\mathrm{i}}}{u_1}}{1 + \dfrac{u_2}{u_1}} = \frac{2H_{3,1}^{\mathrm{i}}}{1 + H_{2,1}} \tag{4-4}$$

$$V_{\mathrm{R}}^{\mathrm{i}} = \frac{2\dfrac{u_4^{\mathrm{i}}}{u_1}}{1 + \dfrac{u_2}{u_1}} = \frac{2H_{4,1}^{\mathrm{i}}}{1 + H_{2,1}} \tag{4-5}$$

with $H_{2,1}$, $H_{3,1}$ and $H_{4,1}$ representing the transfer functions between u_2, u_3 and u_4 and the reference signal u_1 as the Data Physics acquisition system exports them.

The formulas are used to obtain the vibration ratio between the excitation points at the rail and the vibration transmitted on the baseplate. The data acquisition system has four input channels, with one channel acting as a reference, and it produces transfer functions by Fourier Transforming the acceleration time histories.

4.5.2 Results from the vibration response measurement

The magnitude of the vibration ratios $V_{\mathrm{L}}^{\mathrm{i}}$ and $V_{\mathrm{R}}^{\mathrm{i}}$ (see Equations (**4-4**) and (**4-5**)) is shown in **Figure 4-21**. The vibration ratios shown are for the measurement locations near the bolting area, near the clipping area and next to the railpad. The results show that for each of the baseplate's measured positions, the vibration ratio is different, and thus the baseplate does not vibrate uniformly. At low frequencies the vibration is highest at the railpad area, whereas further from the rail the vibration is lower due to the constraint applied by the bolts. At around 700 Hz there is a peak for the vibration at the clipping area and at 900 Hz a peak in all the responses. Therefore, the different baseplate areas will radiate noise with different intensity. Moreover, the results show that higher vibration levels occur close to the railpad than at the other peripheral areas of the baseplate. Thus, it is expected that the peripheral areas will radiate less noise. In addition, the results show a similar trend of the measured vibration up to a frequency of 630 Hz. Above this frequency, the vibration of the baseplate starts to increase. The resonance of the baseplate may cause this increase. The baseplate sound radiation effect will be considered in **Chapter 6**.

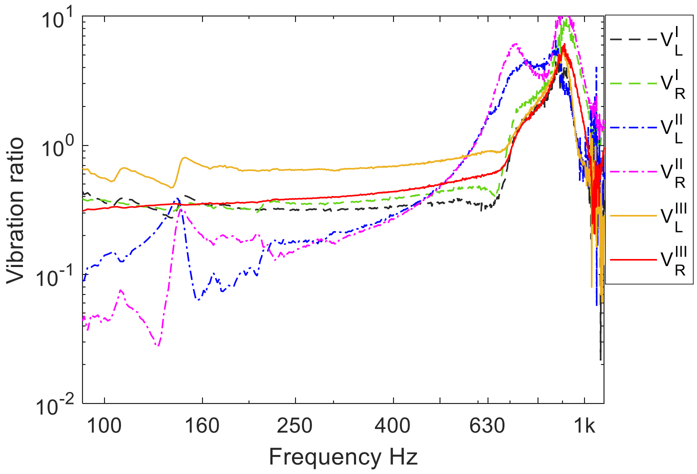

Figure 4-21 Vibration ratios comparisons for all three measured areas of the baseplate. $V_{\mathrm{L}}^{\mathrm{I}}$ and $V_{\mathrm{R}}^{\mathrm{I}}$: near the bolting locations; $V_{\mathrm{L}}^{\mathrm{II}}$ and $V_{\mathrm{R}}^{\mathrm{II}}$: near the clipping locations; $V_{\mathrm{L}}^{\mathrm{III}}$ and $V_{\mathrm{R}}^{\mathrm{III}}$: next to the rail pad.

4.6 In-situ vibration measurement of the baseplate

In addition to the measurements in the test rig described above, further vibration measurements were conducted on the test track at Doncaster during the December campaign to investigate the vibration behaviour of the baseplate. Accelerometers were placed on the rail and the baseplate, as shown in **Figure 4-22**. Excitation was applied vertically at the railhead using the small hand-held instrumented impact hammer with the hard tip. The full details of the equipment used for these measurements are given in **Table 4-3**. Different measurement locations on the baseplate were selected; setup examples are shown in **Figure 4-22** and **Figure 4-23**. The vibration of five consecutive baseplates was measured by moving the sensors at the rail and at the baseplate for each baseplate measurement. For all the measurements, railpad No.1 was fitted, and the excitation location was always at the railhead above the first baseplate.

Table 4-3 Measurement equipment used for baseplate vibration

Equipment	Details
Accelerometer	PCB Piezotronics - Model: 352C34, sensitivity 104.0 mV/g
Accelerometer	B&K - Model: DeltaTron: 4514 - 001, sensitivity 98.23 mV/g
Impact hammer (150 g)	PCB Piezotronics-Model:086C02
Data analyser	Data Physics Corporation, Model: DP240, S/N: 20770
Laptop computer	Dell Latitude E7470
Software	Data Physics SignalCalc 730 Dynamic Signal Analyser, MATLAB

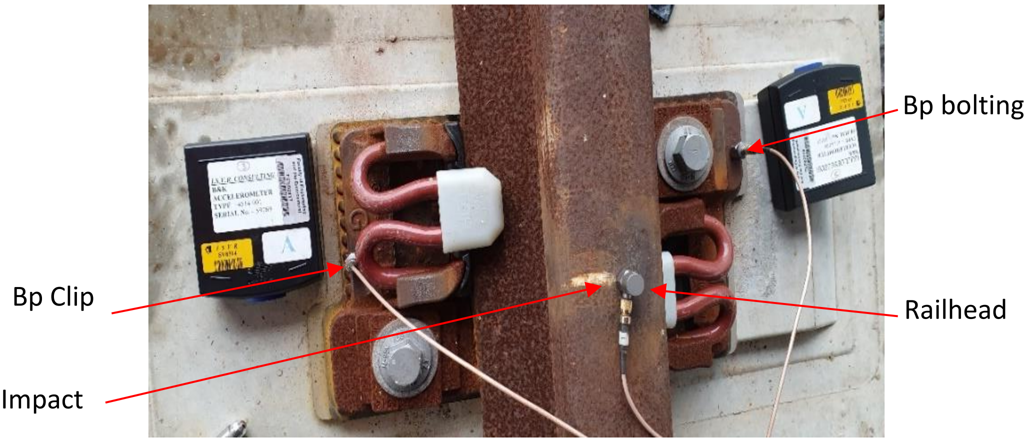

Figure 4-22 View of the test setup for first baseplate vibration measurements.

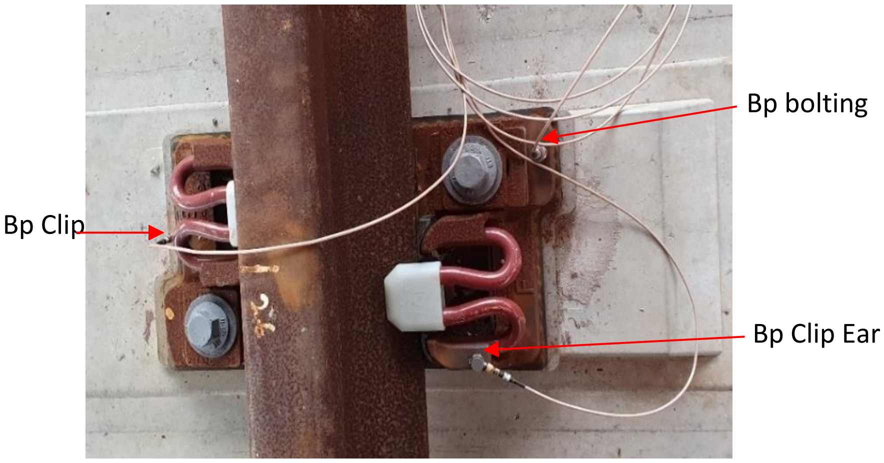

Figure 4-23 View of the test setup for the second baseplate vibration measurements.

4.6.1 Measured driving point and transfer mobilities

Figure 4-24 presents the mobilities measured on the baseplate with the impact at the railhead according to the setup shown in **Figure 4-22**. The magnitude and the phase of the mobility are shown along with the signal coherence. The results show the driving point mobility at the railhead and the transfer mobilities on the baseplate. It can be seen from the measurements that the magnitude of the transfer mobility at the baseplate near the clip for the frequencies 400 - 900 Hz and 1100 - 1400 Hz is higher than the rail mobility. At these frequencies, the baseplate and rail are strongly coupled (vibrating in-phase) resulting in the increased baseplate vibration. Also, below 400 Hz, the rail vibration propagates through the baseplate's clipping area; therefore, similar vibration levels are obtained. At 600 Hz and 1350 Hz, local modes of the baseplate can be observed. However, the baseplate vibration close to the railpad has a lower amplitude. This is demonstrated in **Figure 4-25** where the transmissibility ratio between the railhead and the baseplate is shown and that at the baseplate vibration at the railpad area is below 1.

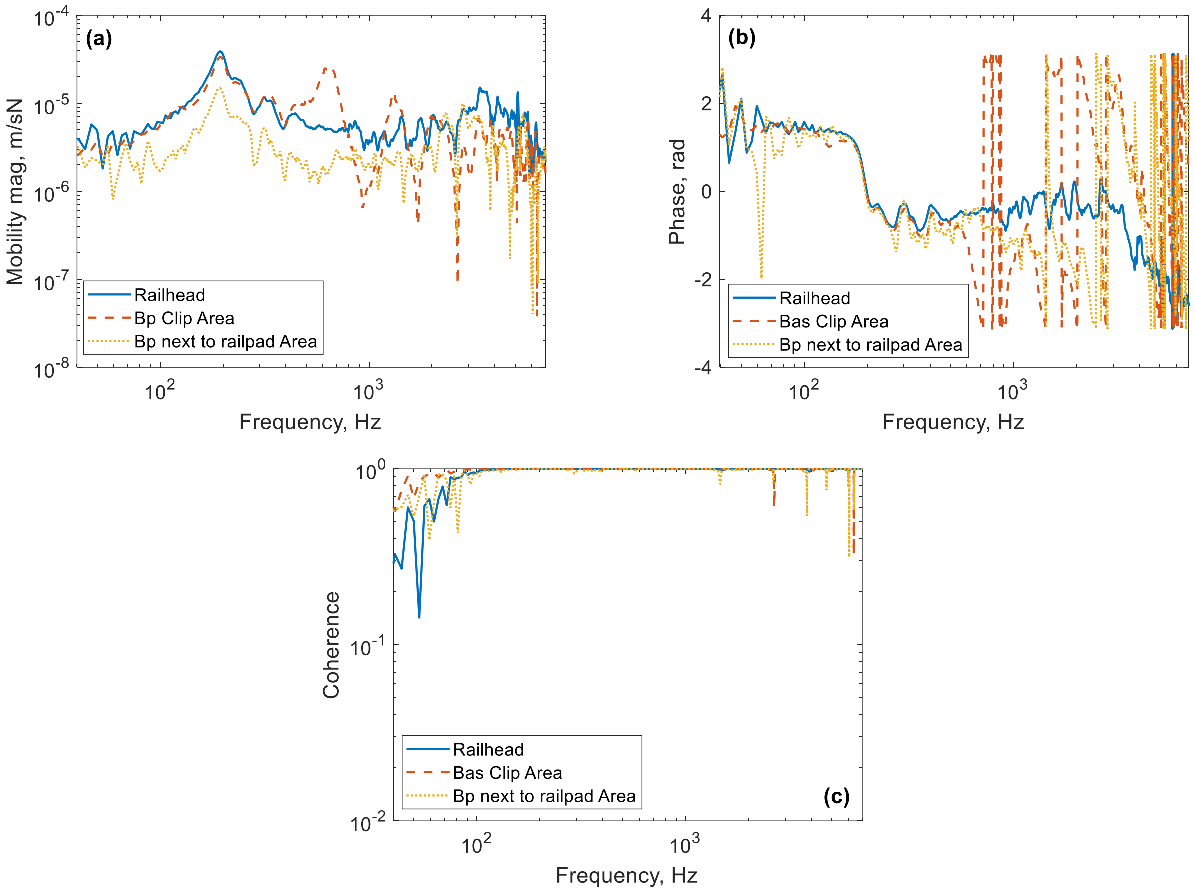

Figure 4-24 Measured mobilities for two sensors at baseplate and one at the railhead: (**a**) magnitude, (**b**) phase and (**c**) coherence.

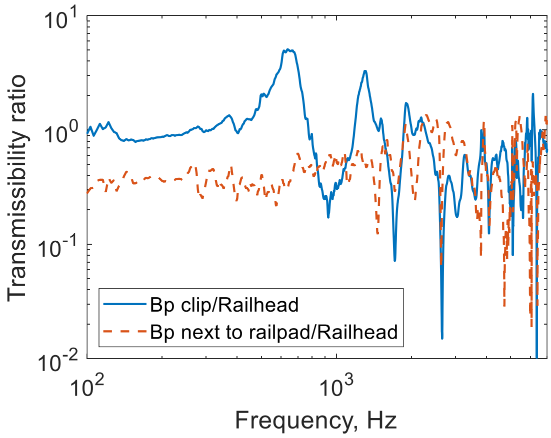

Figure 4-25 Transmissibility ratio between the railhead and baseplate for the first baseplate.

Figure 4-26 compares the vibration ratio measured on the track at Doncaster with the one measured in the laboratory. Note that the railpad used was not the same: for the track at Doncaster, it was railpad No.1 while in the laboratory it was railpad No.2 which is stiffer (see **Table 3-5**). Moreover, the temperature was much lower for the Doncaster measurements. The results at the railpad area are similar in each case for frequencies below 400 Hz. Above this frequency, the laboratory data have higher vibration ratios. For the baseplate clipping area, the Doncaster data has higher values up to 700 Hz whereas again the laboratory data have higher vibration ratios above this frequency. The difference in the results could be due to the following reasons: (i) for the Doncaster measurements a stiffer railpad was used; (ii) the torque applied at Doncaster and in the laboratory could be different as it was not measured; (iii) for the Doncaster measurement the temperature was very low which increases the stiffness of the baseplate pad and railpad.

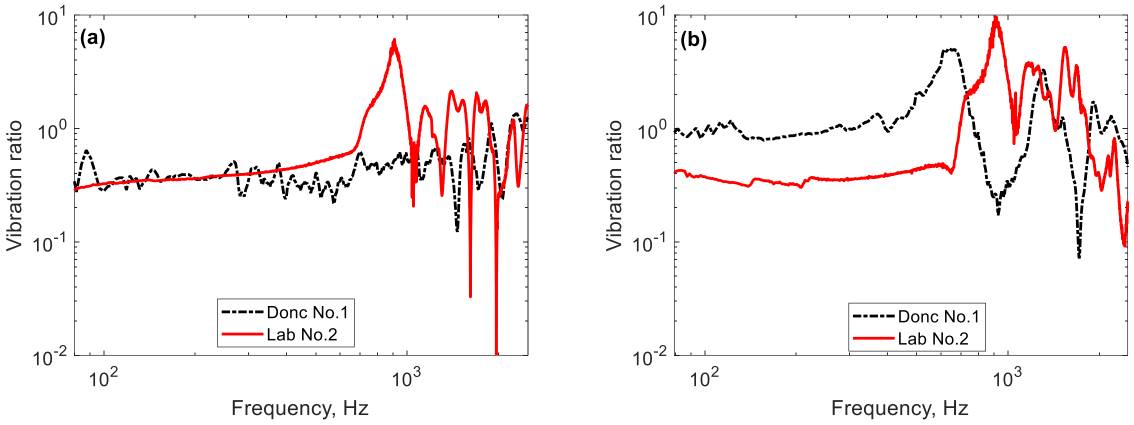

Figure 4-26 Comparison between vibration ratio measured in Doncaster and the one measured in the laboratory: (**a**) next to the railpad area of the baseplate, (**b**) at the clipping ear of the baseplate.

4.7 Summary

This chapter has presented the in-situ measured data collected at the Doncaster test track during two measurement campaigns and additional vibration tests on the baseplate undertaken in the laboratory.

The features and characteristics of the track in the presence of the flexible fastening system fitted with different railpads have been determined including the point mobilities and track decay rates. The results have shown that the stiffness of the railpad has a significant effect on the track decay rates. Measurements at different temperatures have demonstrated that the railpad stiffness increases considerably at lower temperatures.

The vibration response of the baseplate has been investigated using in-situ and laboratory measurements. The results have shown that the baseplate is not vibrating uniformly, and a higher vibration response occurs near the railpad compared with other peripheral locations of the baseplate.

Therefore, the noise from the baseplate will not be radiate uniformly. The information collected in this Chapter is used in **Chapter 5** to validate the developed model FE model of the baseplate in situ. These results will also be used in **Chapter 7** for the rolling noise assessment.

Chapter 5 Slab track vibration modelling

The dynamic behaviour of the railway track plays a key role in the generation of rolling noise [1]. The railway track consists of many components that support the rail and they all contribute to the overall track vibration and noise. Many authors have developed track models with either continuous or discrete supports. For slab tracks equipped with two-stage fastening systems, the most common approach is to model the baseplate as a rigid body, to use Timoshenko or Euler-Bernoulli beam theory for the rail and an equivalent continuous rail support [1, 58, 69, 96].

In the current chapter, two different track models are studied, focusing on the differences between continuous and discrete rail support and the differences caused by introducing a flexible model of the baseplate. Comparisons are given with the measured results presented in the previous Chapter.

The aim of modelling the two-stage baseplate as a flexible plate is to answer the following questions: (i) Does a flexible baseplate model give an improvement over a rigid mass? (ii) Does a discrete support model give an improvement over a continuous support model? (iii) Is there any misrepresentation of the baseplate if modelled as a rigid mass?

5.1 Timoshenko beam model

In this section, the track is modelled using a Timoshenko beam supported on a continuous double elastic foundation layer in which the baseplate is treated as a rigid mass layer between the two elastic layers. This model is available as part of the TWINS model [1, 35]. It is used here to predict the driving point mobility and track decay rate based on the properties given in **Table 5-1**. The results are compared with the measured data from **Chapter 4** for the test track in Doncaster installed with the two-stage baseplate system.

The track decay rate is obtained from the imaginary part of the wavenumber of the propagating structural wave. The complex structural wavenumber k generically is in the form:

$$k = k_{\mathrm{r}} + \mathrm{i}k_i \tag{5-1}$$

where k_i is a negative real number. The wave amplitude reduces by a factor of $\exp(k_i)$ over a distance of 1 m. Therefore, the decay rate in dB/m is given by [1]:

$$TDR = -20\log_{10}(\exp(k_i)) = -8.686k_i \tag{5-2}$$

It is shown in [1] that the sound power radiated by the rail is related to the decay rate according to

$$L_w \approx 10\log_{10}\left(4.343\rho_0 c_0 P\frac{v_{\text{ref}}^2}{W_{\text{ref}}}\right) + 10\log_{10}\sigma + 10\log_{10}\left(\frac{|v(0)|^2}{2v_{\text{ref}}^2}\right) - 10\log_{10}DR \qquad (5\text{-}3)$$

where L_{w} is sound power level in decibels, $\rho_0 c_0$ is the characteristic acoustic impedance of air with ρ_0 the density and c_0 the speed of sound and P is the perimeter length of the rail cross-section of which only the part that is projected onto a plane perpendicular to the motion is considered. $v(0)$ is the velocity amplitude of the rail at the excitation point. W_{ref} is the reference value used for the definition of sound power level, v_{ref} is the corresponding reference value for velocity and σ is the radiation ratio which depends on the frequency [1]. From this, it can be seen that the decay rate influences the sound power according to:

$$L_w = -10\log_{10}TDR + \text{const} \qquad (5\text{-}4)$$

Table 5-1 Track parameters used in the track model

Parameters	Details
Rail type	60E1
Rail vertical bending stiffness	6.42 MNm^2
Rail vertical loss factor	0.02
Baseplate mass	6.2 kg
Lower pad stiffness	32 MN/m
Lower pad loss factor	0.2
Upper pad (rail pad)	See **Table 3-5**, for the preload of 20kN

The measured dynamic stiffness and loss factor of the railpads presented in **Chapter 3** are used in the model. **Figure 5-1** and **Figure 5-2** show the comparison for the vertical driving point mobility magnitude and phase for the cases of railpads No.1 and No.4 respectively. Railpads No.1 and No.4 have been chosen here as they are commonly used when these baseplates are installed.

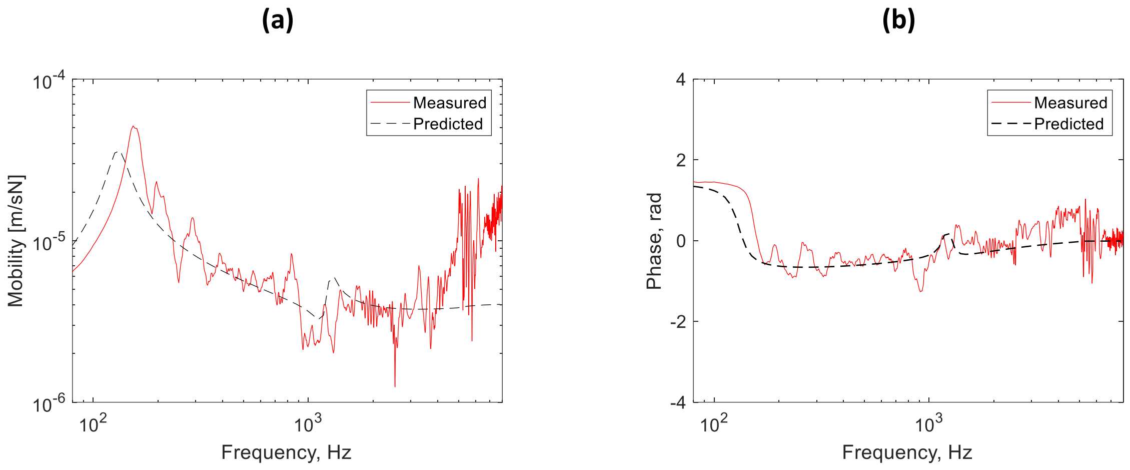

Figure 5-1 Measured and predicted driving point mobility for track fitted with railpad No.1: **(a)** magnitude and **(b)** phase.

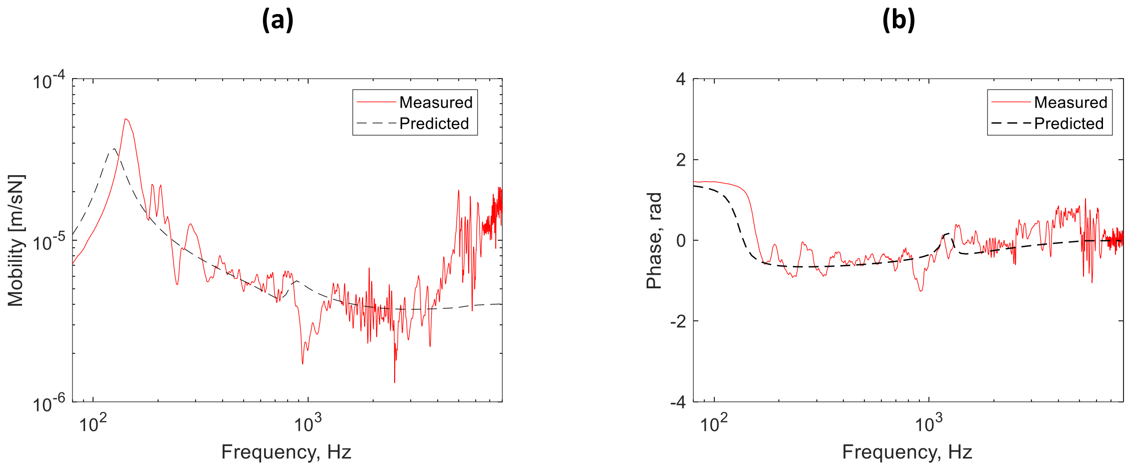

Figure 5-2 Measured and predicted driving point mobility for track fitted with railpad No.4: **(a)** magnitude and **(b)** phase.

The comparison between the measured and the predicted driving point mobilities shows reasonable agreement in the frequency range 200 Hz to 2 kHz for both railpad cases. The multiple peaks in the measured mobility between 200 and 1000 Hz will be introduced by reflections from the end of the finite rail, not present in the model. For both pads, the first peak in the predicted mobility has a lower amplitude and appears at a lower frequency than in the measurements. At this peak, the mass of the rail and the baseplate bounce on the stiffness of the lower pad. Its damping loss factor controls the bandwidth. A second peak occurs in the predicted mobility at around 1 kHz at which the baseplate mass vibrates out of phase with the rail. This is not clearly evident in the measurements. Furthermore, the measured mobility rises at frequencies above about 3 kHz due to the cross-section deformation of the rail [1].

Figure 5-3 show the vertical TDR results for all four railpads used on the test track (No. 1, No.2, No 4 and No. 8). Reasonable agreement is again found for all railpad cases. At low frequencies, the decay rate falls at a frequency that corresponds to the peak in mobility (the cut-on frequency of waves in the rail) [1]. This cut-on frequency is a little lower in the predictions than in the measurements in each case. A strong peak occurs in the predicted decay rates between 800 and 2000 Hz, depending on the pad stiffness. This corresponds to the second peak in the mobility. This peak in the TDR is not seen clearly in the measurements whereas there are also peaks appearing at other frequencies. This suggests that representing the baseplate as a mass is insufficient.

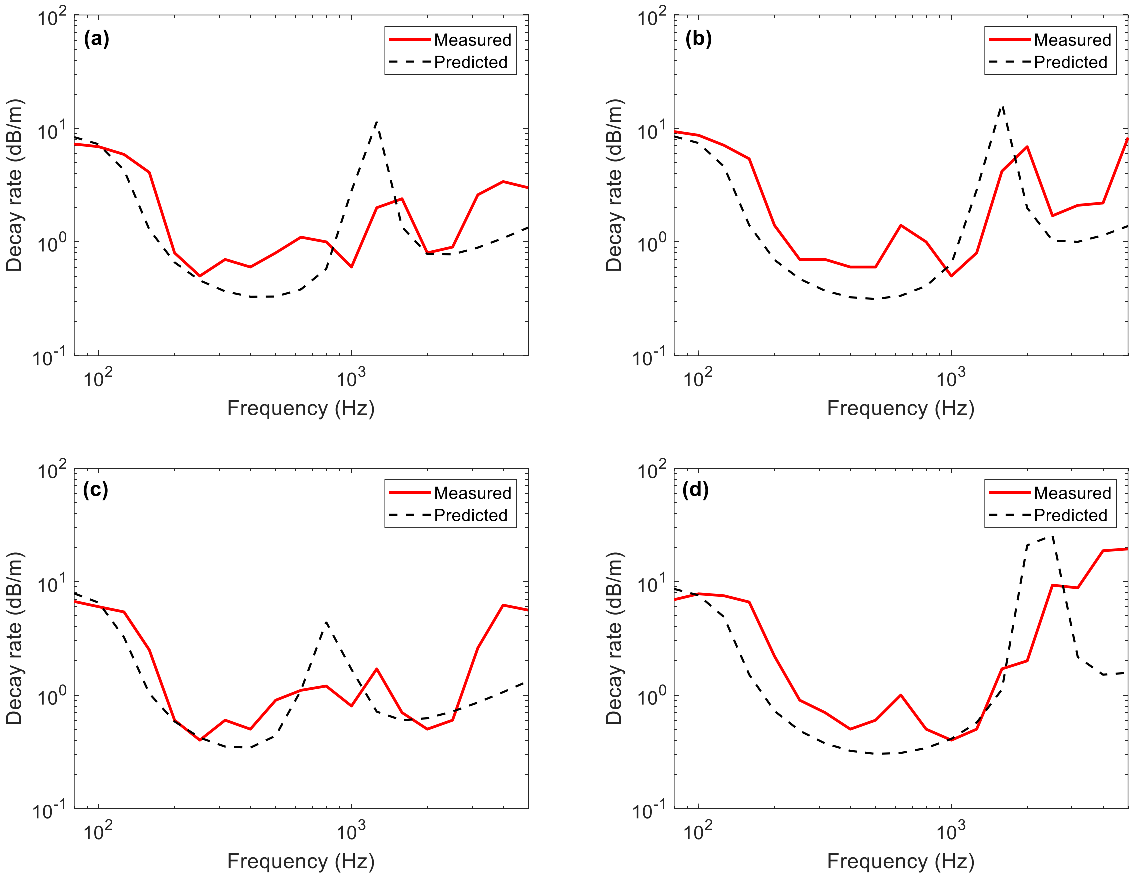

Figure 5-3 (**a**)-(**d**) measured and predicted vertical TDR for four-track fitted with railpad No.1, No.2, No.4 and No.8, respectively.

The measured vibration response of the two-stage baseplate system presented in **Chapter 4** showed that the baseplate does not vibrate uniformly. This flexible motion of the baseplate is likely to affect the agreement between the measured and predicted results. A track model that considers the baseplate as a flexible plate could improve the agreement with the measurements. This model can then be used for rolling noise predictions to account for the influence on the mobility, TDR and the vibration of the baseplate and hence its noise radiation.

For the above reasons and to further understand the vibrational behaviour of the two-stage baseplate, a Finite Element (FE) model of the two-stage baseplate is developed, and its modal properties and vibration predictions are investigated.

5.2 Development of FE model of the baseplate

5.2.1 FE model

COMSOL software is used to create the FE model of the baseplate of the Pandrol two-stage fastening system using its actual dimensions. **Figure 5-4** shows the geometry of the developed model. The baseplate has a length of 0.404 m, width 0.206 m and a basic thickness of 0.015 m; however, it has a more complex geometry than a simple rectangular plate. The geometry of the model contains the basic features of the actual baseplate that were considered appropriate for the needs and the frequency range of this study. The exact material properties for the supplied baseplate were not available. Therefore, reference material properties for cast iron are selected, as listed in **Table 5-2**.

Table 5-2 Parameters used in the FE model of the two-stage baseplate

Mass	6.2 kg
Density	6926 kg/m^3
Young's modulus	191 GPa
Poisson's ratio	0.26
Damping loss factor	0.005
Structure volume	9.453×10^{-4} m^3

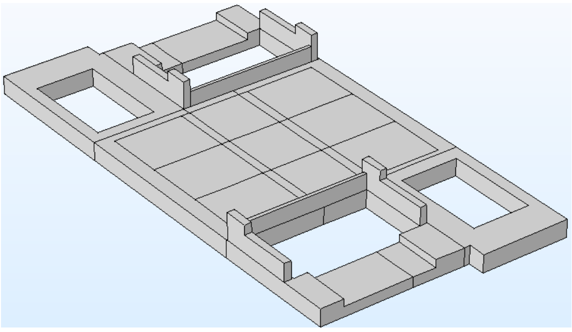

Figure 5-4 Geometrical appearance of the FE model of the two-stage baseplate.

5.2.2 Measurements of free baseplate

To assist in verification of the model, initially, the vibration response of the baseplate under free boundary conditions was measured in the laboratory. This was achieved by hanging the baseplate by a string, as indicated in **Figure 5-5**. An instrumented impact hammer was used to excite the baseplate at the centre of the rear side of the plate and the response was measured by an accelerometer attached at the centre of the front side, as shown in **Figure 5-5**. The measured accelerance is then compared with the prediction from the FE model with the same boundary conditions. A fine mesh of triangular elements with a maximum element size of 24mm is chosen for the FE model. A point force is applied at the centre of the FE model and its vibration response is predicted at the same location, as shown in **Figure 5-6** (**a**) (a red circle). The measured and predicted accelerances are compared in **Figure 5-6** (**b**). The agreement is good for most frequencies, although the measured peaks are sharper indicating the damping is smaller than assumed in the model by around a factor of 10. This will be less important once the baseplate is attached to the lower pad. The values of the measured and predicted modal frequencies are given in **Table 5-3**. The natural frequency of the first mode agrees well but, for the second and fourth modes, the natural frequencies of the FE model are occurred at higher frequencies by 11% and 2.6% respectively, while the third mode of the FE occurred at lower frequency by 3.3 %. The first mode is a bending mode in which the edges vibrate out of phase with the rail seat. The second and third modes are torsion modes and the fourth is another bending mode. The third and fourth modes have minimal response at the centre of the rail seat as their modeshapes are anti-symmetric. Between each pair of resonances there is an antiresonance, which is characteristic of a point FRF. The antiresonance around 350 Hz occurs between the first bending resonance at 485 Hz and the rigid body modes which occur at 0 Hz. The accelerance from the FE model tends to a value at a low frequency that is 4% higher than the measured accelerance (the position of the dip will affect the results at higher frequencies). This result corresponds to the inverse of the mass which suggests that the density is slightly too low.

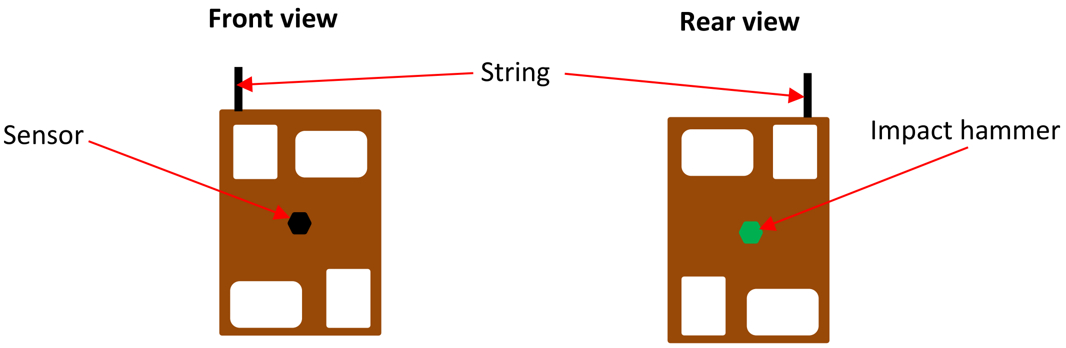

Figure 5-5 View of the laboratory vibration response measurement at the centre of the baseplate under the free boundary condition.

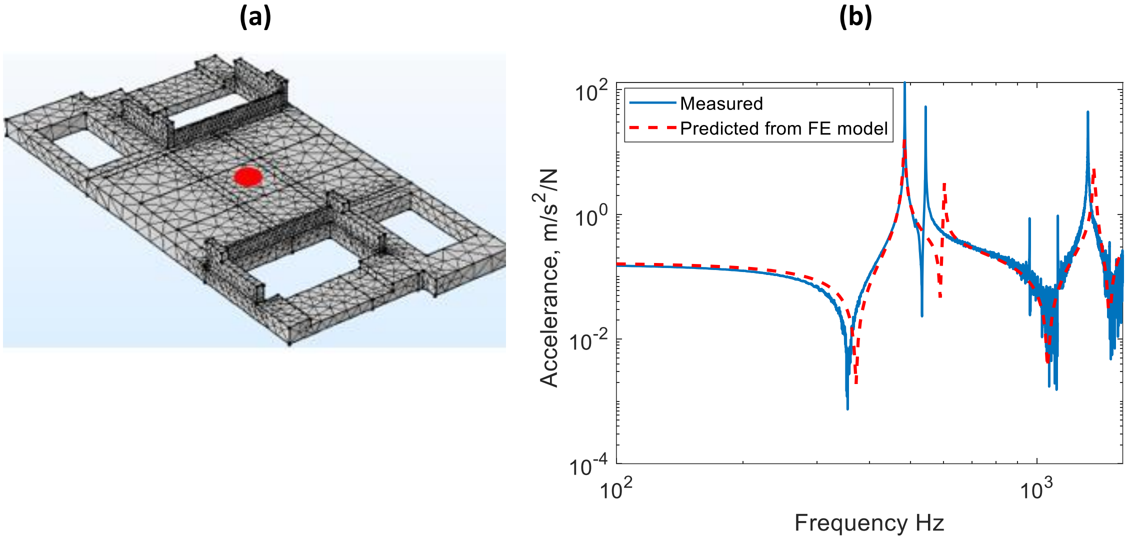

Figure 5-6 (**a**) Fine mesh for the FE model of the baseplate showing the impact and the response point (red circle), (**b**) comparison between the measured and the predicted accelerance at the centre of the baseplate.

Table 5-3 Comparison of the measured and predicted natural frequencies of the baseplate

Main Modes peaks	Mode shape	Measured (Hz)	Predicted (Hz)	Difference in (%)
1	Bending	485	485	0
2	Torsion	544	603	11
3	Second torsion	961	929	-3.3
4	Second bending	1122	1152	2.6

Further measurements were conducted on the free baseplate to estimate the mode shapes. Nine measured locations (1-9) were marked on the baseplate (see **Figure 5-7**), and the sensors were attached to each point for accelerance measurements. The impact hammer was used to excite the baseplate at one of the locations, identified by the red circle in **Figure 5-7**. The data was collected using the Data Physics Acquisition System and then processed using Matlab software. The modal identification technique from Ntotsios [97] is used here to extract the modal parameters from the measurements. The procedure is based on the minimization of the difference between the measured FRFs and a modal model of the structure (baseplate). The results for the modal frequencies and mode shapes are then compared with the ones predicted by the FE model of the baseplate. These are presented in **Figure 5-8** for the first four modal frequencies and mode shapes, occurring below 1.2 kHz.

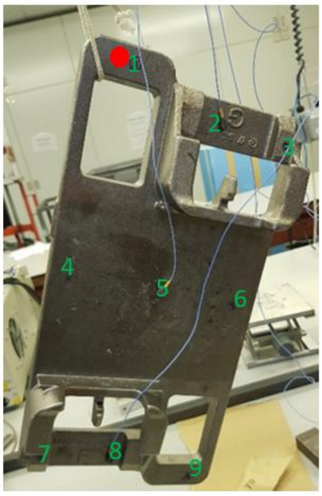

Figure 5-7 View of the measuring setup for vibration responses of the free baseplate. The numbers 1-9 indicate the measured positions; the red mark indicates the impact point.

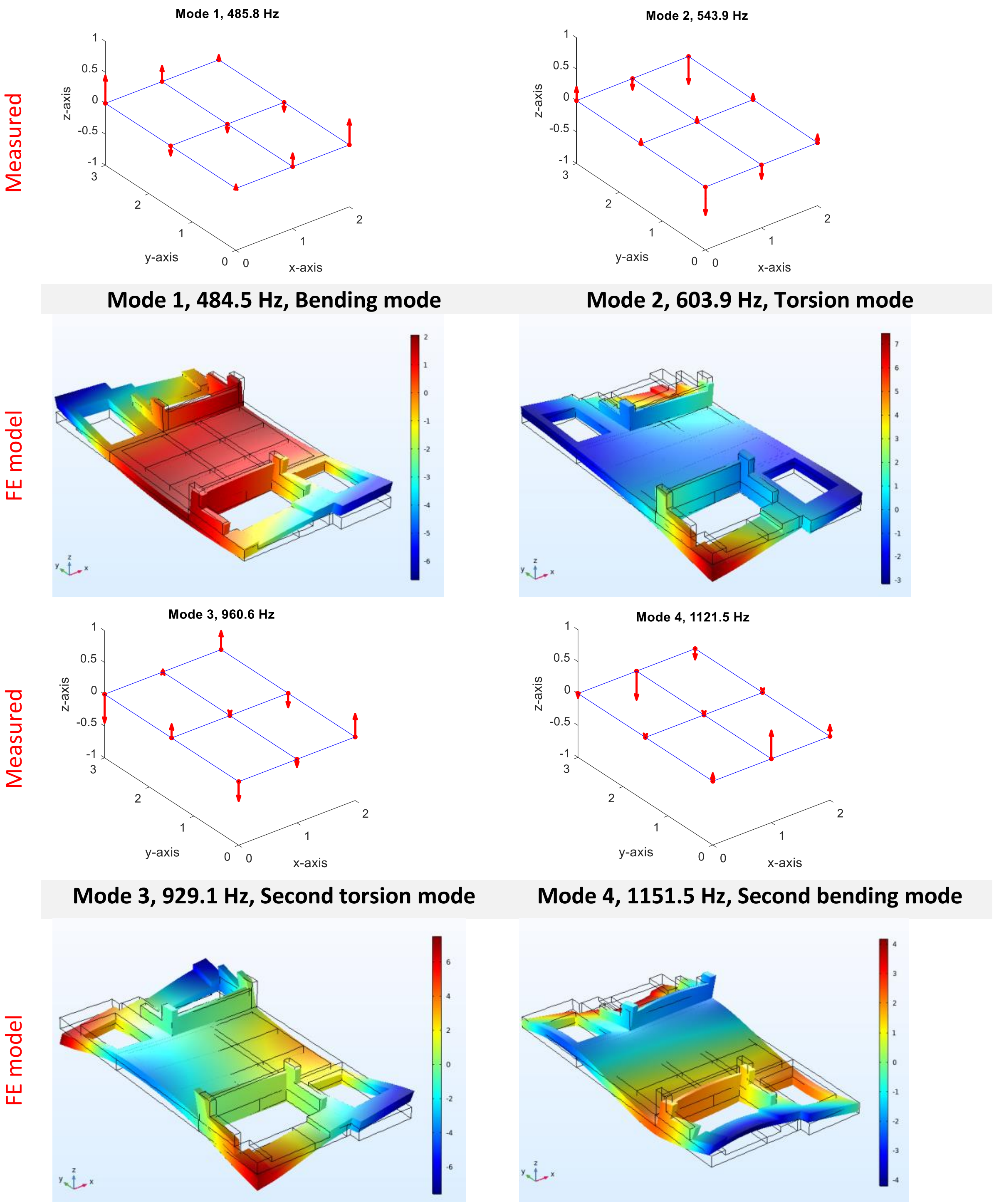

Figure 5-8 Comparisons of the first four modal frequencies and mode shapes identified experimentally and those predicted from the FE model of the baseplate.

A close match is seen in the comparison shown in **Figure 5-8** for both modal frequencies and mode shapes. The small difference in some modes is probably due to the complex geometric shape of the baseplate, which makes it difficult to model it accurately. These comparisons demonstrate a good agreement for free boundary conditions. However, when installed in the track, the two-stage baseplate is mounted via an elastic pad onto the slab. To simulate the in-situ condition, the FE model of the baseplate has next been modified to account for the lower pad attached at its lower surface. This is then compared with measured data obtained under the same conditions. The reason for this is to identify the effect of the lower pad and the constraint conditions on the baseplate modal properties.

5.2.3 Measurement setup for baseplate on lower pad

The two-stage baseplate with a lower pad No.6, Type A, was bolted on the steel block that was used for the dynamic stiffness measurements in **Chapter 3**, as shown in **Figure 5-9**. The solid block is isolated from the floor with springs with a resonance frequency of 19 Hz. A schematic side view of the rig setup is shown in **Figure 5-10**. An impact hammer was used to excite the baseplate and the accelerance was measured.

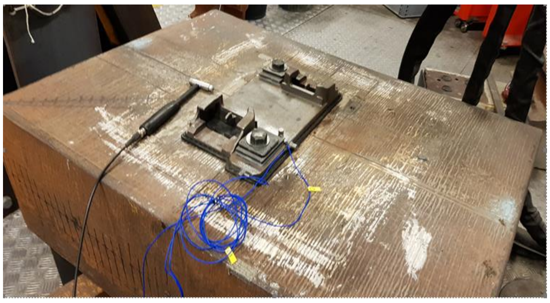

Figure 5-9 View of the rig setup for the measurement setup of the two-stage baseplate.

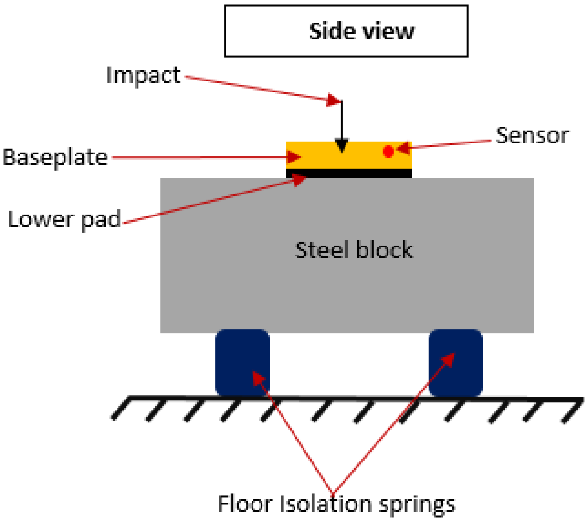

Figure 5-10 Schematic view of the rig setup for the measurements.

The initial results showed some variation when the baseplate was removed and re-bolted on the rig. This effect might be caused by the application of different bolting torque when installed. Therefore, the effect of torque is investigated first.

5.2.4 The effect of bolting torque

The vibration of the baseplate with different torque applied on the bolts in the range 100 Nm to 400 Nm was measured using the setup shown in **Figure 5-9** and **Figure 5-10**. The excitation was applied at the centre of the baseplate with the impact hammer and the response is measured with an accelerometer attached on the baseplate next to the impact point, identified as location 5 in **Figure 5-11**. The measured point accelerance at location 5 for different values of torque is shown in **Figure 5-12**. As the torque increases, the peaks shift to a higher frequency; the first peak shifts from 380 Hz at 100 Nm to 540 Hz at 400 Nm. This mode is considered to be the bouncing mode of the baseplate on the pad stiffness. As expected, by increasing the applied torque, the stiffness of the compressed lower pad increases, and this results in a shift of the baseplate modes to higher frequencies.

These results confirm that the applied torque plays an important role in the supporting stiffness of the two-stage baseplate and consequently for its vibration. At the highest applied torque of 400 Nm, the spacer is in contact with the steel block (see **Figure 1-7**), which shifts the peak considerably (see **Figure 5-12**). Due to the importance of the torque, it is essential to apply the correct torque in accordance with in-situ conditions. The manufacturer, Pandrol Ltd, has confirmed that when installed in situ a torque of 400 Nm should be applied. Therefore, all the subsequent measured responses are based on this torque.

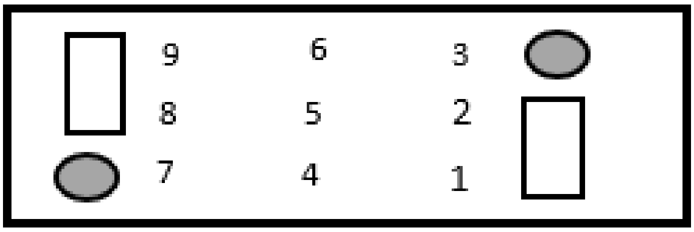

Figure 5-11 Top view of the two-stage baseplate showing the numbered locations for the excitation points.

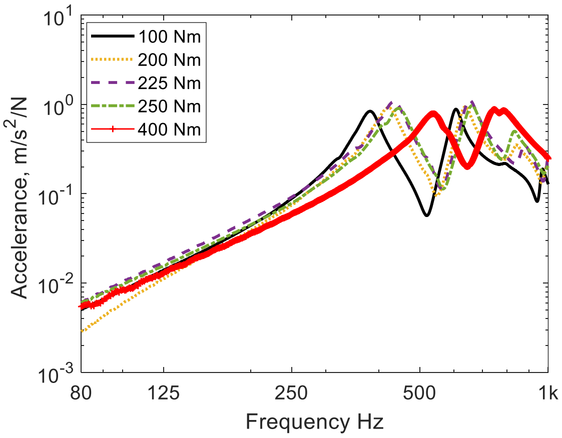

Figure 5-12 Comparison of the measured driving point accelerance on the two-stage baseplate for different values of applied torque.

5.2.5 Comparisons of mode shapes and modal frequencies

An impact hammer was used to excite the baseplate at 15 different positions vertically and two in lateral directions, as shown in the top view in **Figure 5-13**. The accelerometer was fixed at position 4 for the vertical direction and at two positions on the edge for the lateral directions. The same modal identification technique [97] that was used in Section **5.2.2** is applied here to estimate the modal frequencies and mode shapes from the measured vibration data. These are then compared with the predicted results from the FE model of the baseplate mounted on the lower pad. In the FE model, the stiffness of the uniformly distributed area support was manually adjusted to match the measured data. Only the first four modes (below 1.2 kHz) are used for tuning the FE model. The procedure shows a good match between predicted and measured results for an overall vertical stiffness of 80 MN/m and lateral stiffness of 61 MN/m, with a damping loss factor of 0.05. The measured and predicted modal frequencies and mode shape results are shown in **Figure 5-14**. It can be seen that for the selected stiffness values, the mode shapes are quite similar, and the natural frequencies are very close.

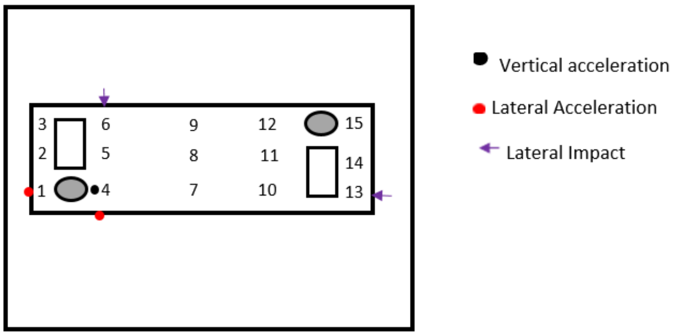

Figure 5-13 Top view of the excitation points (1-15 for vertical direction), purple arrows for lateral direction. Sensor locations for vertical and lateral directions are also shown.

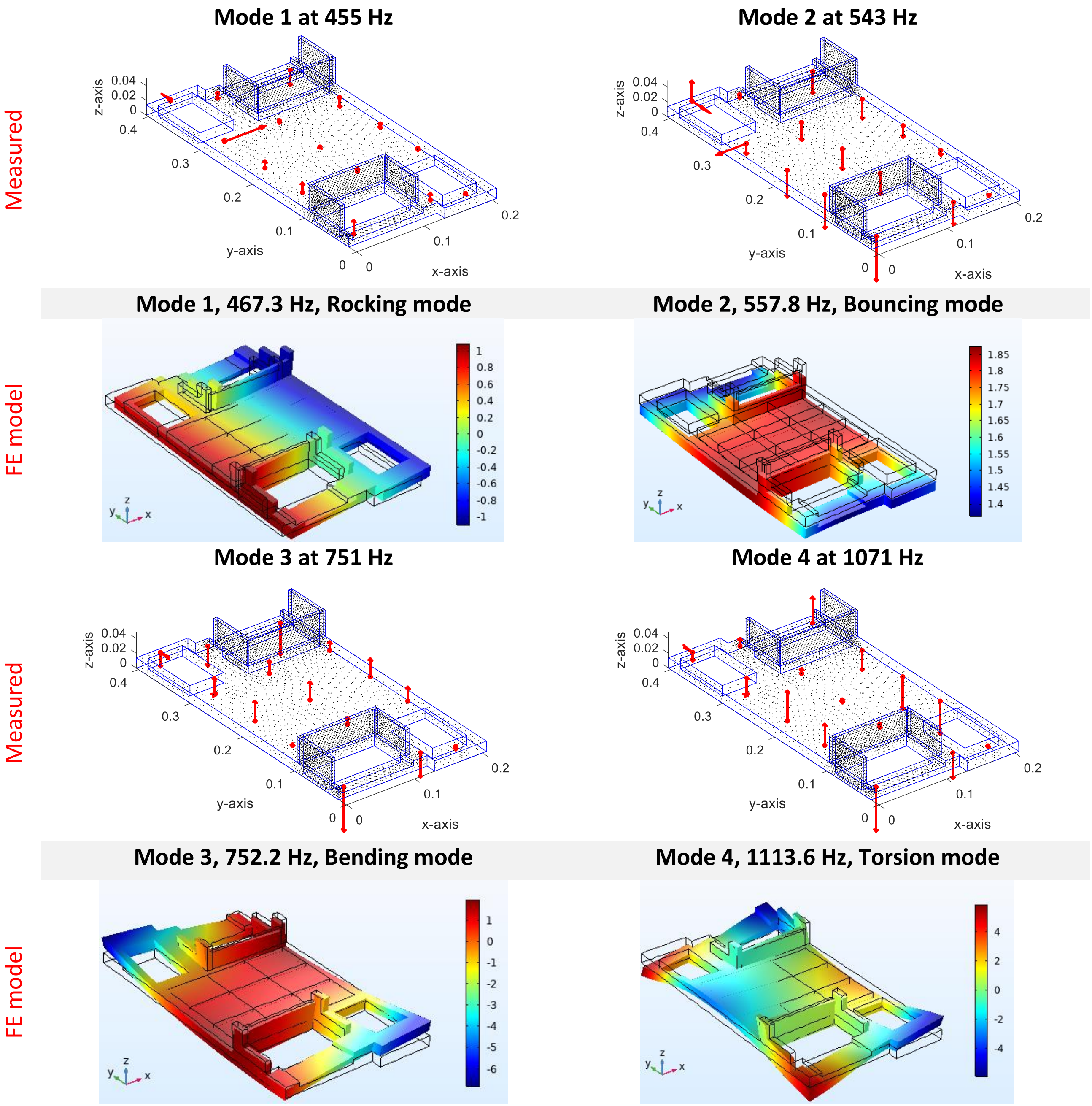

Figure 5-14 Comparison of the first four modal frequencies and mode shapes between the measured and the FE model of the constrained two-stage baseplate with lower pad stiffness of 80 MN/m.

Figure 5-15 shows a comparison between the measured driving point accelerance at the centre of the baseplate (location 5) and the corresponding FE model predictions. The vertical spring stiffness of the lower pad is set as 80 MN/m, with a damping loss factor of 0.02, and is uniformly distributed on the baseplate-lower pad interaction area. It can be seen that a good agreement is found for frequencies up to the first peak. For the second resonance peak, the trend of the response is similar, but the amplitude from the FE model is lower.

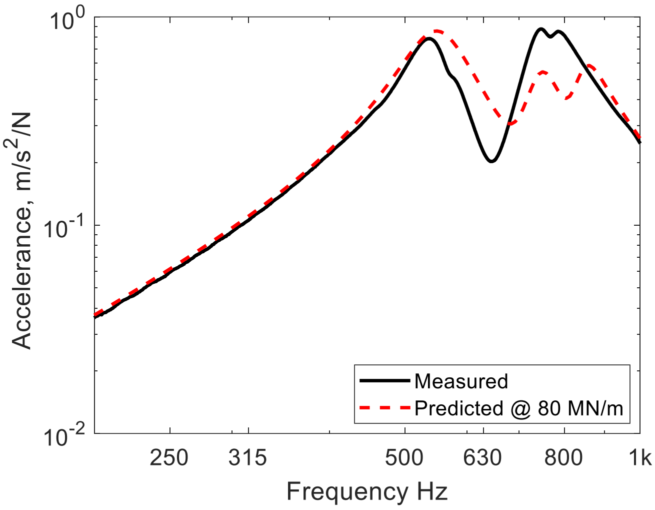

Figure 5-15 Comparison between the measured and predicted point accelerance for the two-stage baseplate at location 5 for stiffness of 80 MN/m.

Additional results are shown in **Figure 5-16** for stiffnesses of 65, 75 and 85 MN/m. This shows how the peak shifts with increasing stiffness, from 530 Hz to 590 Hz. Using the stiffness of 65 MN/m the trend of the accelerance is similar to the measured data, but the accelerance from the FE model is about 10% higher than the measured response. For the stiffness of 85 MN/m, a good agreement is found at the lower frequencies, but the resonance peak from the FE model appears at a higher frequency than in the measured response. The stiffness of 80 MN/m is a good compromise. Therefore, the FE model with the stiffness of 80 MN/m for the lower pad can be used for future assessment of noise properties of the two-stage baseplate system.

With the current procedure, the vertical stiffness of the lower pad is found to have a different value from the results of the indirect stiffness measurement method reported in **Section 3.7.4**. The tests in **Section 3.7.4** resulted in a value of around 90 MN/m for the preload of 10 kN, while the results of the current impact test are consistent with the stiffness of around 75-80 MN/m. The difference between these values might be due to differences in the bolting torque, as discussed in the previous section, as this was not controlled during the measurements in **Section 3.7.4**.

Due to the force applied by the bolts, the stiffness of the pad may be higher in the region of the bolts than elsewhere. However, attempts to use different stiffnesses in different regions did not lead to any significant improvement in the agreement.

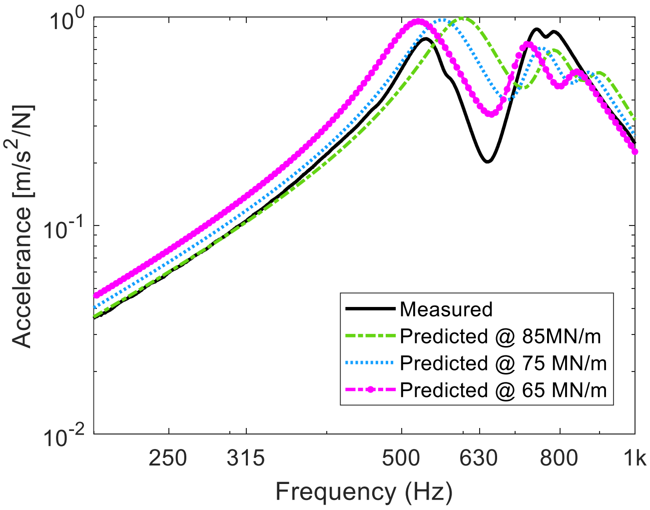

Figure 5-16 Comparison between the measured and predicted point accelerance for the two-stage baseplate at location 5 for stiffness of 85, 75 and 65 MN/m for bolting torque of 400 Nm.

5.2.6 Summary of the findings in section 5.2

For the unconstrained baseplate, a good agreement is found between the measured response and the predicted response from the FE model apart from the second resonance, which occurs at a higher frequency in the FE model than in the measured results.

Considering the two-stage baseplate attached on the lower pad of Type A, the accelerance depends on the stiffness value of the lower pad. A stiffness value of 80 MN/m distributed evenly over the base gives a reasonable agreement with the measured accelerance. However, this value of stiffness differs from the results obtained from the stiffness measurements in **Chapter 3**. The indirect method produced a value of around 90 MN/m for a preload of 10 kN although the torque was not controlled in those experiments.

The results obtained with the vertical stiffness of 80 MN/m and lateral stiffness of 60 MN/m from the FE model could be accepted as a good compromise. This FE model of the baseplate fastening system will be incorporated into a model of the whole track in the next section.

5.3 Track model with flexible two-stage baseplate

5.3.1 **Introduction**

An efficient model is used to represent the vibration of the track, including the baseplate as a flexible plate, by combining two models:

(i) The FE model of the flexible baseplate developed in the previous section using COMSOL software.

(ii) The model of a discretely supported railway track based on a 2.5D FE model of the rail developed by Zhang et al. [36].

The model of Zhang et al. [36] was developed to represent a ballasted track but is here adapted to represent a slab track including a detailed model of the baseplate.

The general procedure for combining the two models is presented in a pictorial view in **Figure 5-17**. The developed model is a more realistic representation of the track with the flexible two-stage baseplate compared with the model in Section **5.1** that accounts for the baseplate as only a rigid mass. The detailed modelling approach for the combined track vibration model is presented in [36]. It uses a 2.5D FE frequency-domain representation for a free rail. The 2.5D technique is a numerical method (also referred to as the Semi-Analytical FE (SAFE) method) which can represent structures with a two-dimensional (2D) geometry that is invariant in the third direction. It can therefore represent an infinite rail. This 2.5D model of the free rail was coupled in [36] with a finite number of discrete supports which represented railpads and sleepers. The model from [36] has been modified to include the FE model of the flexible baseplate in place of the sleepers.

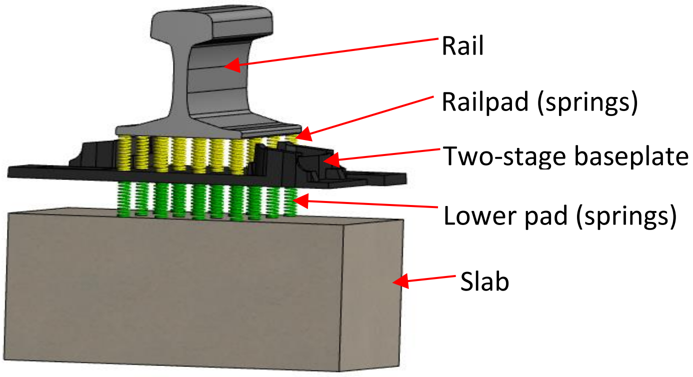

Figure 5-17 The combined structure of the two models; rail (2.5D FE model), railpads (discrete springs), baseplate and lower pad (3D FE model) and slab (assumed rigid).

The interface between the rail and each railpad is defined by a 3×3 array of points. The 2.5D model of the rail is used to calculate the transfer receptances between these nine points in the railpad area for multiple fastener locations. Transfer receptances from the railhead to each of these positions are also determined. A receptance coupling method is then used to find the response of the coupled system to a vertical force on the railhead [36]. Details of this method are given in **Appendix** C.

The FE model of the baseplate is used to obtain a 9×9 receptance matrix for excitation forces acting on each of the nine locations in the railpad area (see **Figure 5-11**). The receptances obtained are then implemented into the coupled model. The railpad itself is represented by nine independent springs. A schematic view of the combination of the two models and the analysis of the results is presented in **Figure 5-18**.

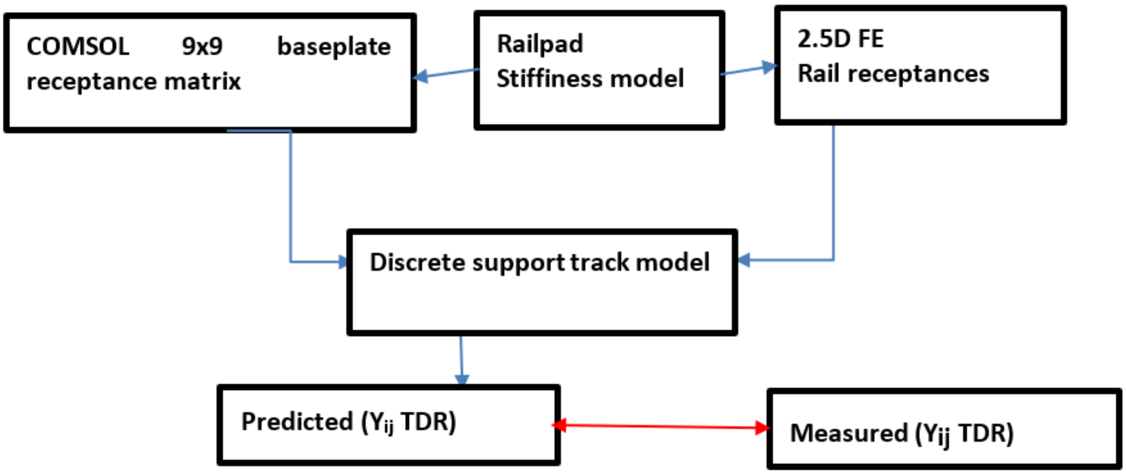

Figure 5-18 Schematic view of the combination of the two models.

5.3.2 Baseplate vibration response

To find the receptance matrix of the baseplate, a unit force is applied at each of the nine locations in the railpad area of the baseplate, and the nine responses are calculated for each applied force. A schematic view of these locations is shown in **Figure 5-19**. Example FE predictions for excitation at the centre of the baseplate (at location 5) and the receptances at positions 1, 2, 4 and 5 are shown in **Figure 5-20** as mobility magnitude and phase. In these results, the responses at the first resonance are all in phase and a series of other resonances occur at higher frequencies.

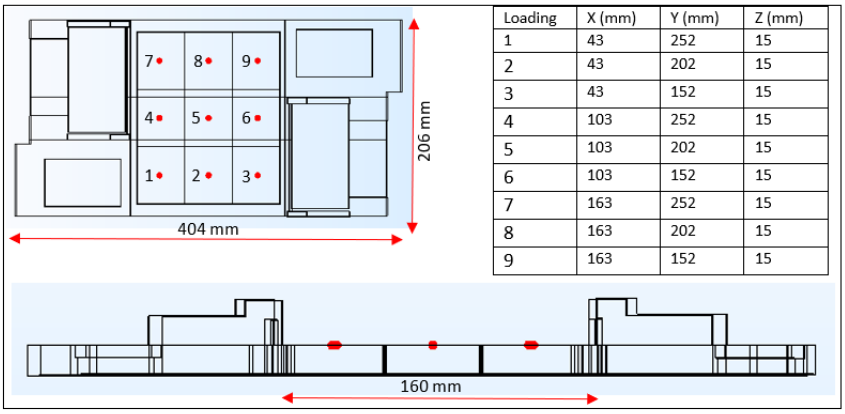

Loading	X (mm)	Y (mm)	Z (mm)
1	43	252	15
2	43	202	15
3	43	152	15
4	103	252	15
5	103	202	15
6	103	152	15
7	163	252	15
8	163	202	15
9	163	152	15

Figure 5-19 Schematic view for impact force and receiver locations.

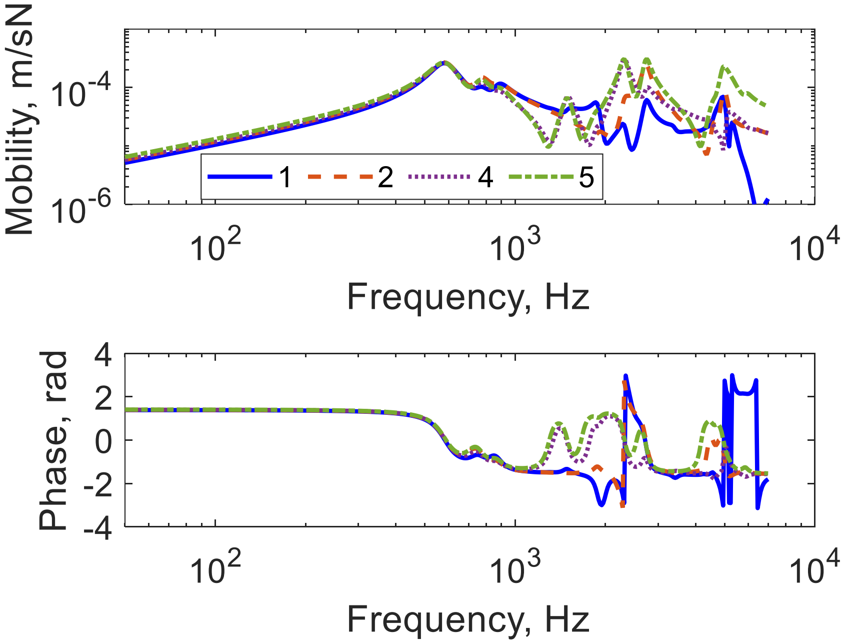

Figure 5-20 Mobility magnitude and phase of the two-stage baseplate for force at location 5 and the response at positions 1, 2, 4 and 5 calculated using the FE model.

5.3.3 Rail driving point mobility

The combined model is used to predict the vertical rail mobility and track decay rate with the excitation at the railhead above a fastener for four types of railpad: No.1, No.2, No.4 and No.8 (see **Table 3-4**) with stiffnesses and loss factor values measured in the laboratory for the preload of 20 kN (see **Table 3-5**). For the lower pad the stiffness of 80 MN/m and loss factor of 0.2 is used. The results are shown in **Figure 5-21** and compared with the measured data from **Section 4.3.2**. The predicted mobility agrees well with the measured one in all cases. These results using the developed 2.5D model including the baseplate as a flexible plate give much better agreement than the model presented in

Section 5.1, **Figure 5-1** and **Figure 5-2**, where the baseplate was considered as a rigid mass. **Figure 5-22** shows the direct comparison between the two models and the measured results.

The developed model has replicated most of the features found in the measured data. The oscillations seen in the measured mobility are due to reflections from the end of the finite rail. For the case with the softer railpad, i.e., railpad No.4, the first peak in the prediction has a slightly lower amplitude and it appears at a higher frequency than the measured results. The stiffness of the railpad shifts the peak occurring at around 170 Hz which corresponds to the rail mass bouncing on the stiffness of the fastener. With the softer pads (No. 1 and No. 4) the rail is better isolated from the baseplate whereas with the stiffer ones (No. 2 and No. 8) it is more strongly coupled with the baseplate. Consequently, it appears that the higher frequency baseplate modes can affect the rail mobility for these stiffer pads.

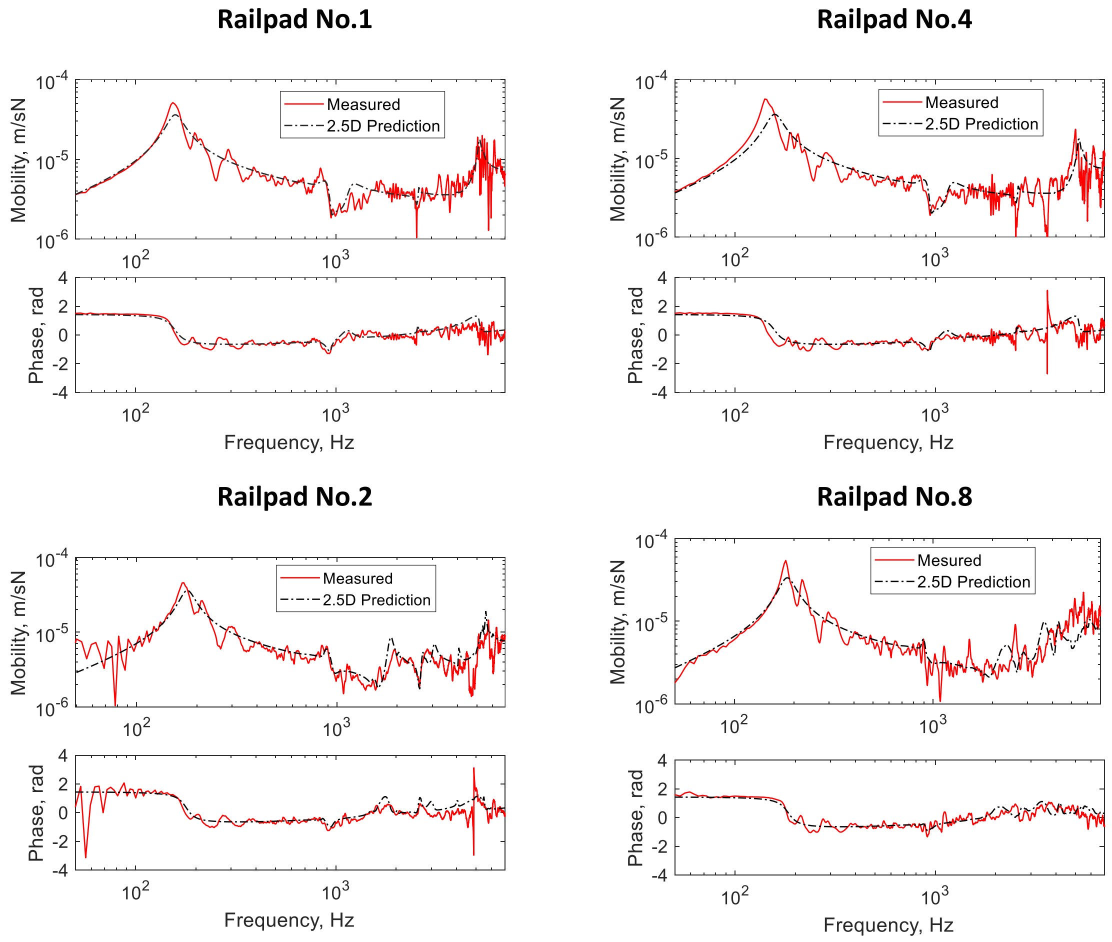
Railpad No.1

Railpad No.4

Railpad No.2

Railpad No.8

Figure 5-21 Comparison between measured and predicted driving point mobility excited above a fastener for Pandrol railpad No.1, No.2, No.4 and No.8.

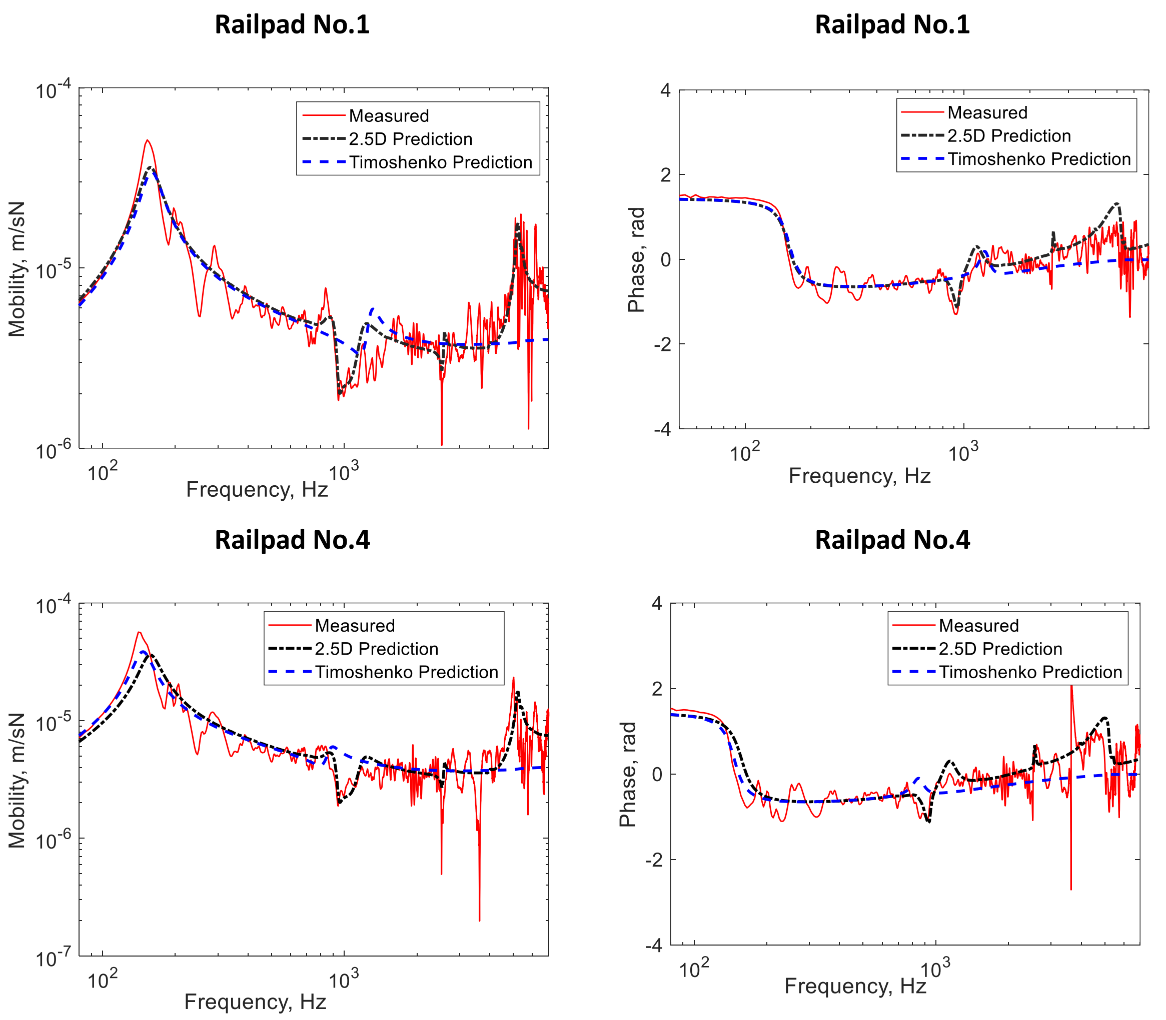

Figure 5-22 Comparison between measured and predicted driving point mobility and phase of the two model (Timoshenko and 2.5D) excited above a fastener for Pandrol railpad No.1 and No.4.

5.3.4 TDR comparison

The TDR has been predicted from the model by calculating the transfer mobility of the track to different distances and applying the procedure from EN15461:2008 [94] to the computed results. Results are again presented for the four different types of railpad. These are compared in **Figure 5-23** with the measured TDRs that were obtained in **Chapter 4**. The agreement is much better than found in section **5.1**, **Figure 5-3** (**a**)-(**d**), where the simple beam model was used with the baseplate represented as a rigid mass.

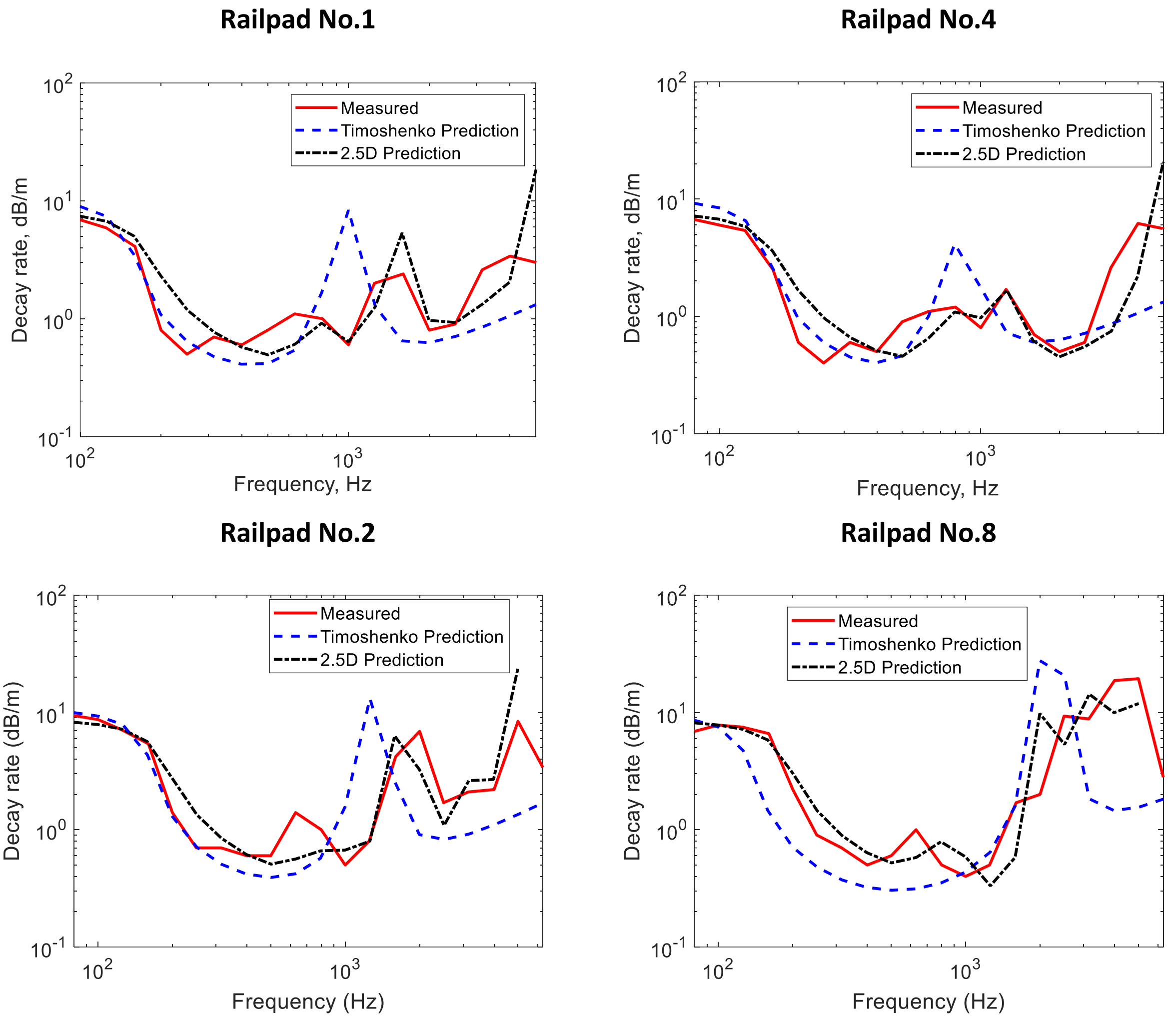

Figure 5-23 Comparison between measured and predicted TDR for Pandrol railpad No.1, No.2, No.4, and No.8.

5.3.5 Baseplate transmissibility

This section presents comparisons between the measured transmissibility on the baseplate measured at the test slab track in Doncaster and the one predicted from the model presented above. The results are presented as transmissibilities to identify the vibration transmitted to the baseplate due to an impact force at the railhead above the baseplate. Six positions were measured to identify the significant vibration at each location on the baseplate. Results from three positions chosen randomly are presented as an example to demonstrate the comparison. **Figure 5-24** illustrates the measuring locations where the sensors are placed at the baseplate and the railhead. The excitation is applied at the railhead at the location marked with a red dot.

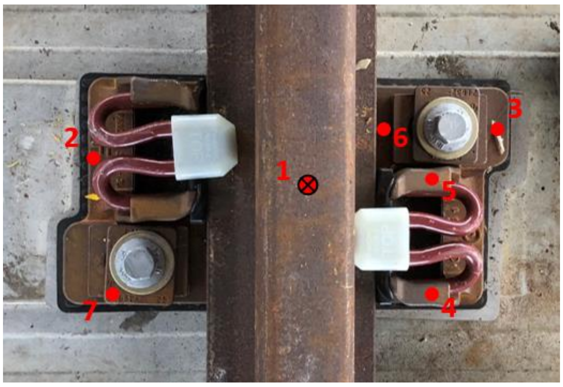

Figure 5-24 Measured locations on the first baseplate.

Figure 5-25 presents the measured and predicted baseplate transmissibility (from the acceleration of the railhead adjacent to the force location to the acceleration measured on the baseplate) in narrowband form. Both sets of curves contain similar trends, with a transmissibility between 0.1 and 0.5 at low frequency, rising to a series of peaks above 600 Hz before falling slightly at high frequency. There are several differences in the details of the curves, however. The measured results show larger variations between the different positions at low frequency. Moreover, in the measurements, a strong peak is found at 650 Hz at position 3 whereas in the predictions there are peaks at 700 Hz for all positions and 900 Hz for positions 2 and 3. Finally, at high frequency the predicted transmissibility rolls off more steeply than the measured one, possibly due to omission of frequency dependent stiffness effects for the pads.

The baseplate transmissibilities at three measured points (at clipping ear, bolting area and next to railpad area) are averaged and this is compared with the predicted values calculated as the corresponding locations in **Figure 5-26** in narrowband form. **Figure 5-26** (**a**) is for the first baseplate (directly below the excitation location) and (**b**) is for the second one. For both the cases shown, the impact is applied at the railhead directly above the baseplate and rail acceleration is measured above the first and second baseplate. This confirms the above conclusions that the two sets of results show similar trends, with the predicted results dropping more sharply than the measured ones above 3 kHz.

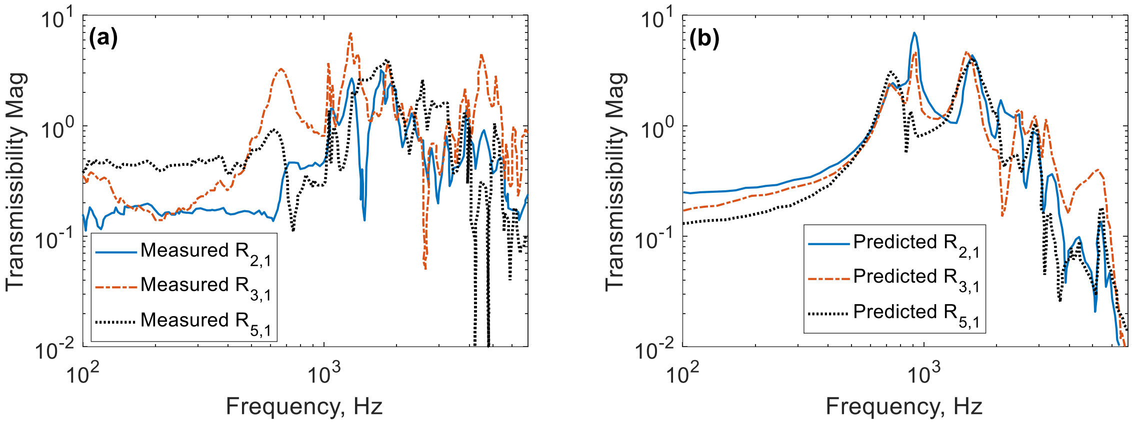

Figure 5-25 Baseplate transmissibility magnitude: **(a)** measured and **(b)** predicted.

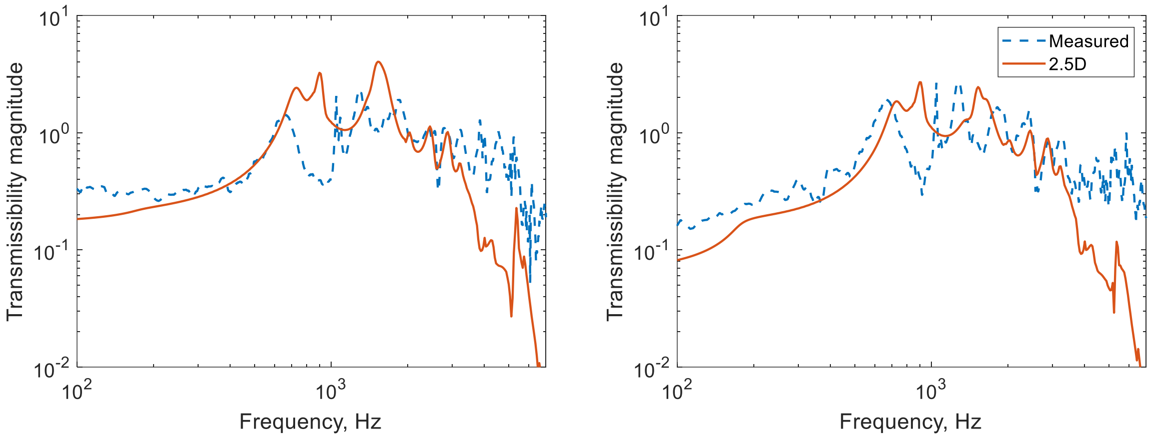
(a) **(b)**

Figure 5-26 Average of the baseplate transmissibility magnitudes over the measured positions **(a)** first baseplate and **(b)** second baseplate (only three available measured locations: 2, 3 and 4); the force is applied above the corresponding baseplate.

5.3.6 Summary of the findings

The track model based on a 2.5D FE model of the rail coupled with the detailed 3D FE model of the baseplate developed here gives a much better representation of the vibration behaviour of the track than the model that accounts for the baseplate as a rigid mass. A good agreement is found between predicted and measured results for both mobility and TDR and most of the features in the measured data such as peaks/dips are well replicated in the new model. Therefore, the vibration results from this model can be further used for the analysis of the track noise performance. The coupled model of the track and the FE submodel of the baseplate are used in **Chapter 6** to study the influence of the flexible baseplate on the sound radiation of the track.

Chapter 6 Noise radiation from the baseplate

The current chapter studies the sound radiation from the two-stage baseplate system. This will be examined for the baseplate alone as well as in the presence of the rail. Calculations are performed using the Rayleigh integral method and using a 3D BE model in COMSOL. The vibration from the coupled 2.5D FE model described in **Chapter 5** is used to study the radiation from multiple baseplates when installed in the track. To evaluate the importance of analysing the baseplate as a flexible body, the results from the current approach are compared with those from an existing model in TWINS that accounts for the baseplate as a rigid body.

Measurements of the sound radiation from a full-scale section of slab track, fitted with the rail and the baseplates, are conducted in the reverberation chamber at the University of Southampton. These measurements are used to validate the approach adopted for modelling the sound radiation of the baseplate.

The chapter starts by looking at the prediction of sound radiation from a simple plain plate with similar dimensions to the baseplate using the Rayleigh integral method. The number of baseplates required to represent sound radiation from the baseplates is investigated. To investigate the limitations of the Rayleigh integral method a 3D BE model is then used to study the sound radiation of a more detailed model of the baseplate and the result is compared with the one from the simple plate model. The effect of the presence of the rail on the radiation of the baseplate is also investigated using a 3D BE model.

The track vibration model described in **Chapter 5** is used to obtain the vibration of each baseplate for a complete track due to a force at the railhead. This vibration is then used in the Rayleigh integral approximation for the calculation of sound radiation. The results with the flexible baseplate model are compared with the existing TWINS model that treats the baseplate as a rigid mass.

Finally, noise and vibration measurements are conducted on the baseplates and the rail to determine their sound radiation. For this, a sample of half-width slab track (6 m length) including the baseplates, railpad, and lower pad is used.

6.1 Modelling of the baseplate sound radiation

6.1.1 Baseplate sound radiation using the Rayleigh integral model

The Rayleigh integral approach [76] allows the sound radiation to be determined from vibrating flat surfaces mounted in an infinite baffle. Although this neglects some of the detail of the geometry it is much more efficient than a full BE approach. It is therefore adopted first for the baseplate before considering the BE method. To evaluate the sound radiation using the Rayleigh integral, a baffled surface (**Figure 6-1**) with the same size as the top surface of the baseplate is initially considered.

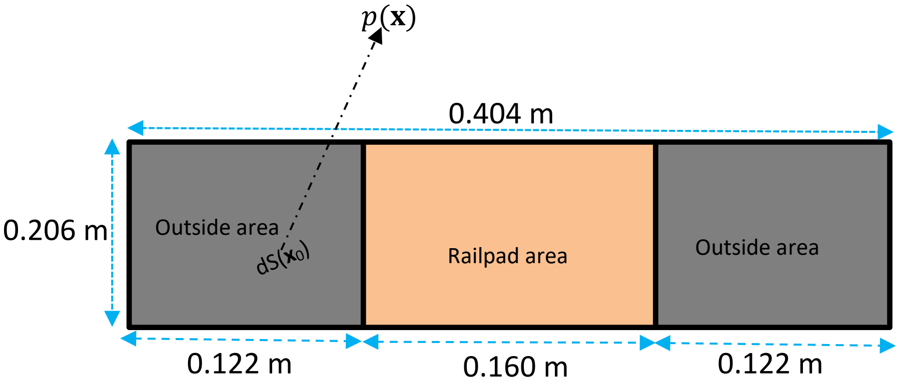

Figure 6-1 Schematic view of a baffled surface representing the baseplate (not to scale).

The pressure $p(\mathbf{x})$ at far-field point $\mathbf{x}$ can be calculated as:

$$p(\mathbf{x}) = \mathrm{i}\rho_0\omega \int_S v_n(\mathbf{x}_0) \frac{\mathrm{e}^{-\mathrm{i}k_0 r}}{2\pi r} \mathrm{d}S \tag{6-1}$$

where ρ_0 is the density of air, ω is the angular frequency, v_n is the normal velocity at $\mathbf{x}_0$ of the baffled surface of total area S, k_0 is the acoustic wavenumber and $r = |\mathbf{x} - \mathbf{x}_0|$ is the distance between the surface element at $\mathbf{x}_0$ to the far-field point $\mathbf{x}$. Equation (**6-1**) can be approximated by a discrete summation.

The sound power in the far field is calculated by integrating the sound intensity around a hemisphere with radius r:

$$W = \int_A \mathbf{I}.\mathbf{n}\, \mathrm{d}A \tag{6-2}$$

where $\mathbf{I}$ is the time-averaged intensity, A is a closed surface, $\mathbf{n}$ is the unit normal vector pointing outwards from A. In the far field, the intensity is approximately equal to $|p|^2/2\rho_0 c_0$ and the sound power can be written as

$$W = \int_0^{\pi/2} \int_0^{2\pi} \frac{|p(\mathbf{r})|^2}{2\rho_0 c_0} r^2 \sin\theta \, \mathrm{d}\theta \, \mathrm{d}\varphi \tag{6-3}$$

where ρ_0 is the density of air, c_0 is the speed of sound in air, r is the radius of the hemisphere, θ and φ are the angles of the vector from the centre of the source area to the receiver at position $\mathbf{r}$.

The integral in Equation (**6-3**) can be approximated by discrete summation over the hemisphere

$$W = \sum_{i=1}^{N} \frac{|p(\mathbf{r}_i)|^2}{2\rho_0 c_0} r^2 \sin\theta_i \, d\theta_i \, d\varphi_i \tag{6-4}$$

Once the sound power is calculated, the radiation ratio or radiation efficiency can be evaluated as

$$\sigma_{\mathrm{rad}} = \frac{W}{\rho_0 c_0 S \, \langle \overline{v^2} \rangle} \tag{6-5}$$

where $\langle \overline{v^2} \rangle = \frac{1}{2S} \int_S |v_n|^2 \, \mathrm{d}S$ is the surface-averaged mean-square velocity of the vibrating surface S. The source locations on the baseplate surface are chosen with a spacing of $\mathrm{d}x = \mathrm{d}y = 0.01$ m as shown in **Figure 6-2 (a)**. The far-field points are chosen on a hemisphere of radius 10 m as shown in **Figure 6-2 (b)**. Using symmetry, only half of the hemisphere is evaluated.

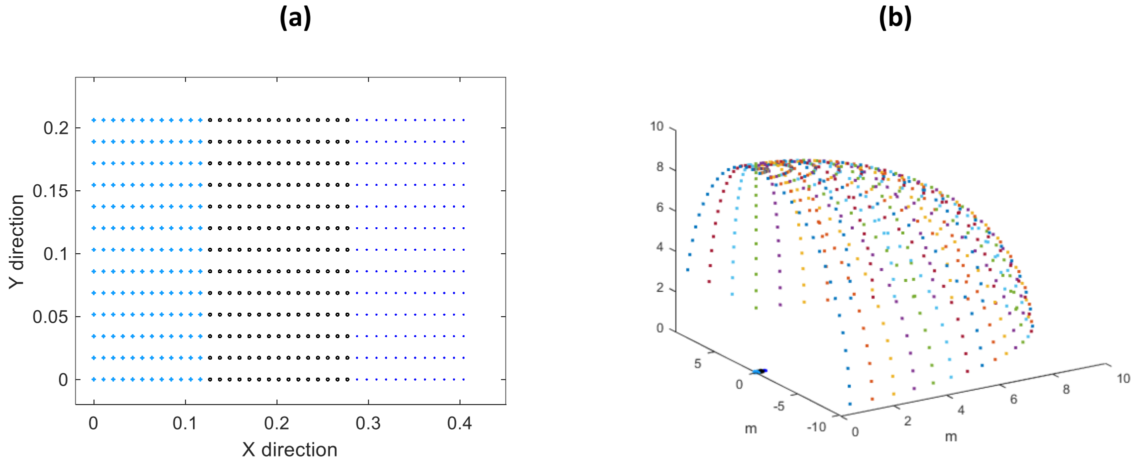

Figure 6-2 **(a)** Source locations on the baseplate surface ($\mathrm{d}x = \mathrm{d}y = 0.01$ m), **(b)** far-field receiver locations.

Noise radiation from the baseplate

The baseplate sound radiation is studied by dividing the baseplate surface into three separate regions, the central railpad area and the two adjacent outer areas (clipping and bolting areas), where different surface velocities are applied (see **Figure 6-1** and **Figure 6-2 (a)**). Initially, for the railpad area at the centre of the baseplate, the velocity is selected as zero, whereas for both the outer areas, the velocity amplitude is set to 1 m/s. The railpad area is given a velocity of zero as the railpad and rail cover it and no sound can be radiated. A second case is considered in which the whole surface area has a velocity of 1 m/s. In both cases, all points are assumed to vibrate in phase with one another.

Figure 6-3 (a) and **(b)** show the calculated results for the sound radiation ratio and the radiated power, respectively. At low frequencies the radiation ratio from this simple baseplate model increases in proportion to the square of the frequency, consistent with a monopole source. Above about 1 kHz it tends to unity. The radiated power follows a similar trend. The radiation ratio for a sphere of radius a representing a point monopole is given by [34].

$$\sigma_{\text{rad}} = \frac{(ka)^2}{1+(ka)^2} \tag{6-6}$$

where a is the radius of the sphere and k is the acoustic wavenumber, $k = \omega/c_0$. At lower frequency $\sigma_{\text{rad}} \approx (ka)^2$ which is proportional to f^2, where f is the frequency, i.e., the radiation index increases at a rate of 20 dB/decade of frequency. The figure also shows that, by having a unit velocity (1 m/s) on all the three areas of the plate, a higher radiation ratio occurs up to 1 kHz than when the velocity at the centre of the plate (railpad area) is set to 0.

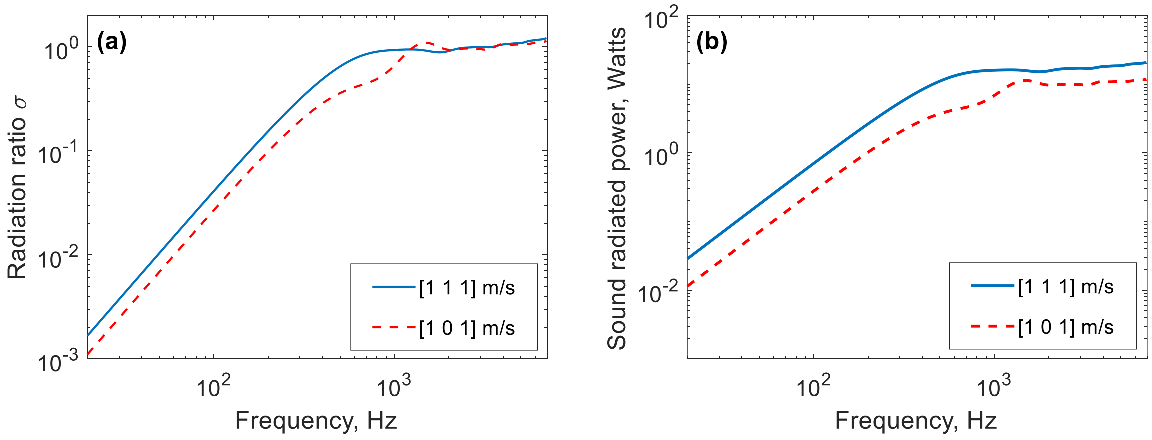

Figure 6-3 **(a)** Sound radiation ratio and **(b)** radiated sound power from a baffled surface area of the two-stage baseplate with different velocity allocation.

The effect of baseplate size on the radiation ratio is shown in **Figure 6-4** which compares results for lengths of 101 mm, 202 mm, 404 mm; the width is fixed at 206 mm and a uniform velocity of 1 m/s is used. It can be seen that the radiation ratio for different baseplate dimensions tends to unity above about 1 kHz, whereas below this frequency, the radiation ratio increases with the increase of the baseplate length.

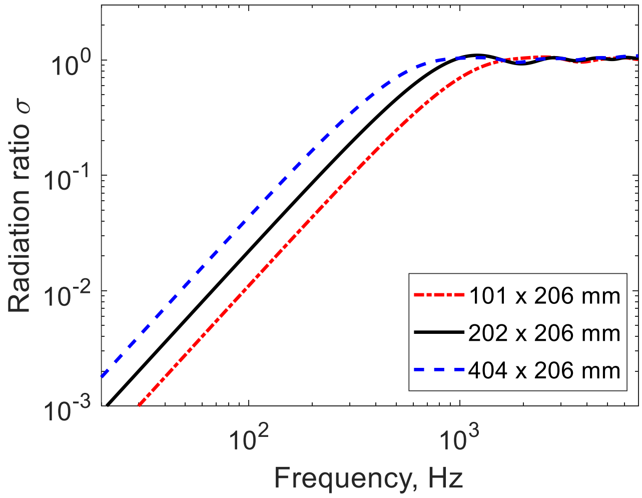

Figure 6-4 Radiation ratios for a baseplate with different dimensions and unit velocity.

6.1.2 Sound radiation from three adjacent baseplates

It has been shown by Zhang et al. [98] that the number of sleepers used to calculate the sound radiation will affect the radiation ratio. As all the sleepers are connected to the rail, they vibrate with an amplitude that depends on the rail vibration at the same position. Also, when the distance between sleepers is small or comparable with the acoustic wavelength, the sleepers can acoustically interact with each other, and it is not sufficient to include only a single sleeper in the calculation of the radiation ratio. The same is expected to be true of baseplates.

Three adjacent baseplates spaced 0.65 m apart are considered, as shown in **Figure 6-5**. The baseplates are each divided into three segments: the middle part (railpad area 160 mm by 206 mm) and the outer parts left and right (each area is 122 mm by 206 mm). The source positions and the far-field receiver positions are presented in **Figure 6-6 (a)** and **(b)**, respectively.

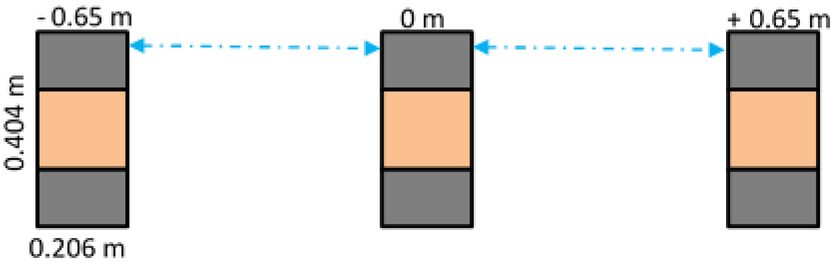

Figure 6-5 Schematic view of a baffled surface of the three adjacent two-stage baseplates.

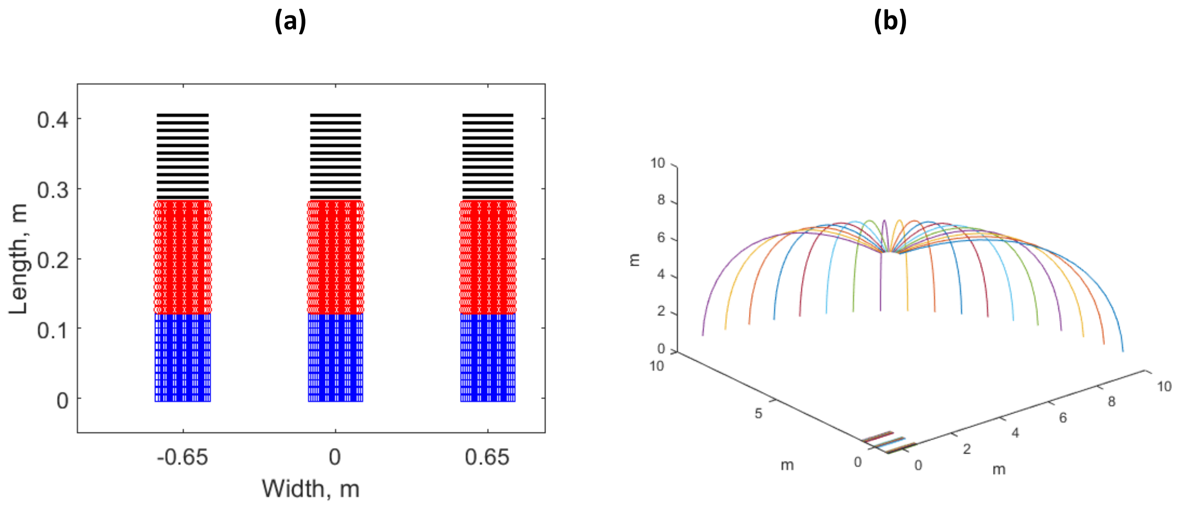

Figure 6-6 **(a)** Source location segments ($\mathrm{d}x = \mathrm{d}y = 0.01\mathrm{m}$) **(b)** far-field receiver locations from the three baseplates.

A velocity amplitude of 0.5 m/s is allocated to the outer areas of each baseplate, and 0 m/s at the railpad area. The results are presented in **Figure 6-7 (a)** and **(b)** for sound radiation ratio and radiated power, respectively, and compared with the results for a single baseplate with a similar velocity amplitude. The radiation ratio for the three adjacent baseplates is higher than for a single baseplate for frequencies below 300 Hz, similar to the conclusions of Zhang et al. [98]. In section **6.2.2**, the minimum number of baseplates required for the track sound radiation calculation is investigated further.

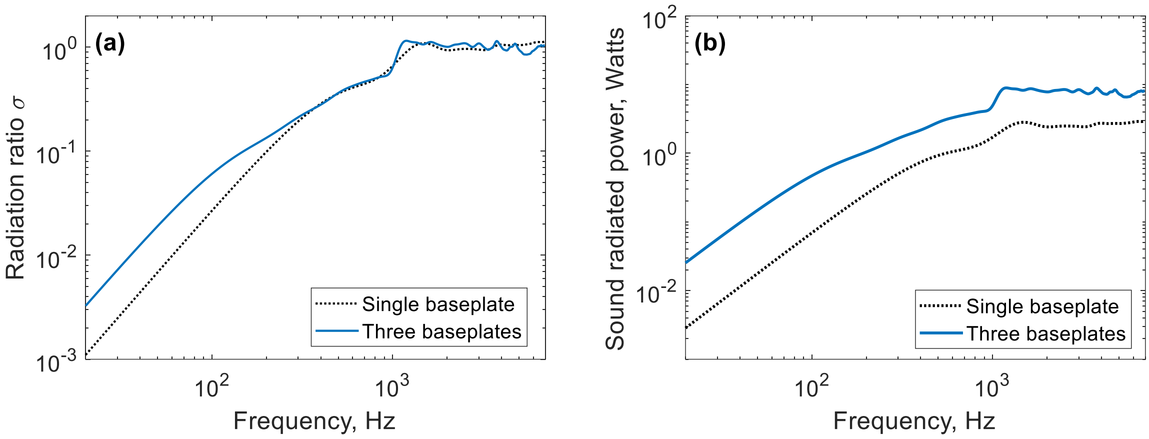

Figure 6-7 Comparison of sound radiation ratios **(a)** and **(b)** sound radiated power from a baffled surface area for the single and the three baseplates.

6.1.3 **3D Boundary Element model of the baseplate**

COMSOL Multiphysics software is used with the Pressure Acoustics Boundary Elements method to investigate the sound radiation from the baseplate alone as well as with a section of UIC60 rail attached. The actual two-stage baseplate has an intricate structure as shown in **Figure 6-8**; modelling the actual structure in COMSOL Multiphysics can result in large computation times. Therefore, as an initial step, a simpler baseplate model is used (**Figure 6-9**); it only accounts for the actual length, width, and height. The other parts, such as clipping, bolting and holes, are not included in the model. The effect of these is studied later, and the results compared with those of the simple model. The baseplate is assumed to be installed on an infinite rigid ground plane.

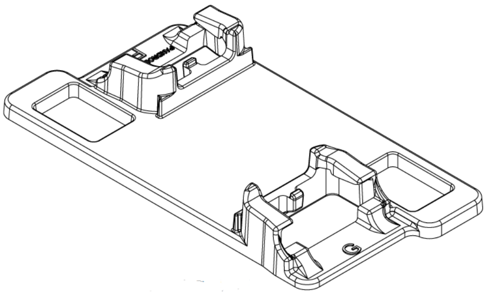

Figure 6-8 An isometric view of the two-stage baseplate (image from Pandrol, used with permission).

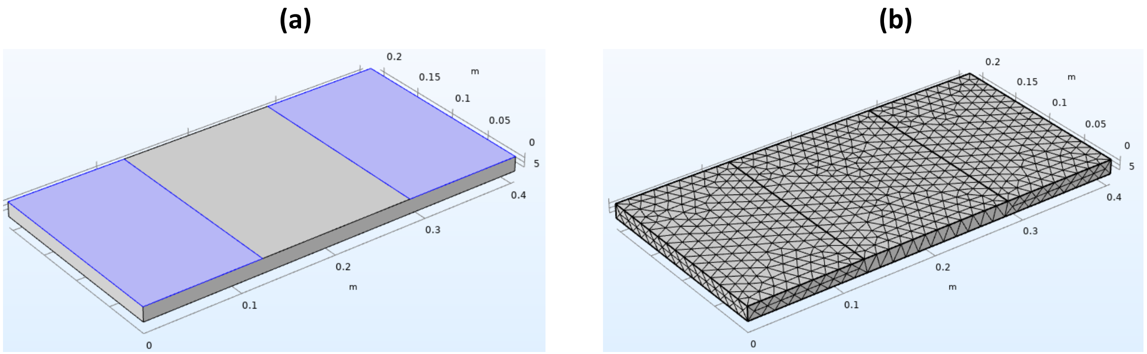

Figure 6-9 (**a**) A simple 3D BE model of the baseplate, (**b**) mesh of the baseplate.

For the sound radiation studies, an average element size of 12 mm is used, as shown in **Figure 6-9** (**b**). An infinite hard boundary is applied at the bottom surface of the baseplate. The amplitude of 0.7 m/s is used at each side (representing clipping and bolting areas) of the baseplate shown in blue colour in **Figure 6-9** (**a**). For the middle part (railpad area), a zero velocity condition is applied.

The results from the 3D BE model are compared with those from the Rayleigh integral approach for the single plate. Note that the Rayleigh integral approach does not include the thickness of the baseplate. However, the same dimensions and velocity allocation are applied. The results are shown in **Figure 6-10** and show a very good agreement between the two methods.

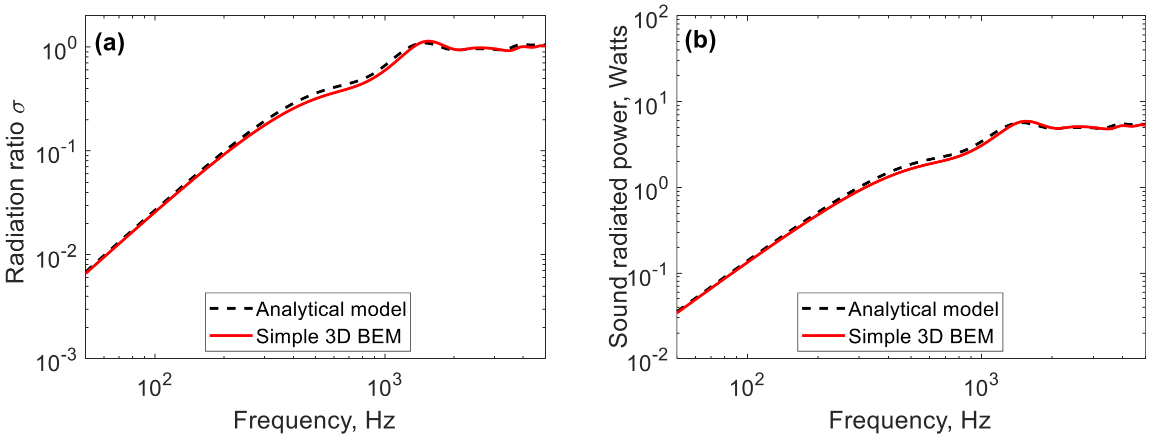

Figure 6-10 A comparison of **(a)** sound radiation ratio, **(b)** radiated sound power from a simple 3D BE model and analytical model of the baseplate.

A more detailed model of the baseplate is developed next, as shown in **Figure 6-11**. The same velocity distribution used in the simpler model is applied to the detailed model; the regions highlighted in blue in **Figure 6-11** are given the same velocity as the simple model. An infinite hard boundary is again applied at the bottom surface of the baseplate. The results are compared with those from the simple BE model in **Figure 6-12**.

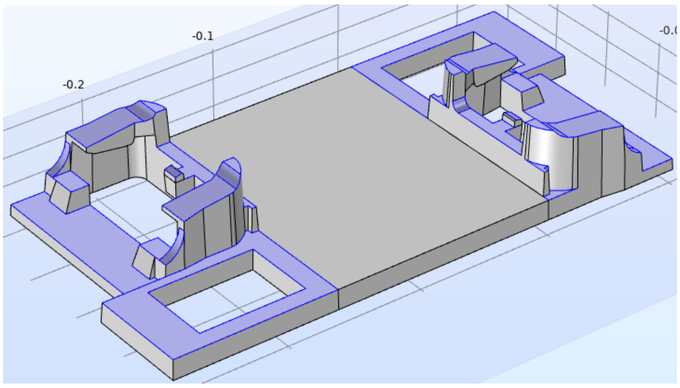

Figure 6-11 A detailed 3D BE model of the two-stage baseplate.

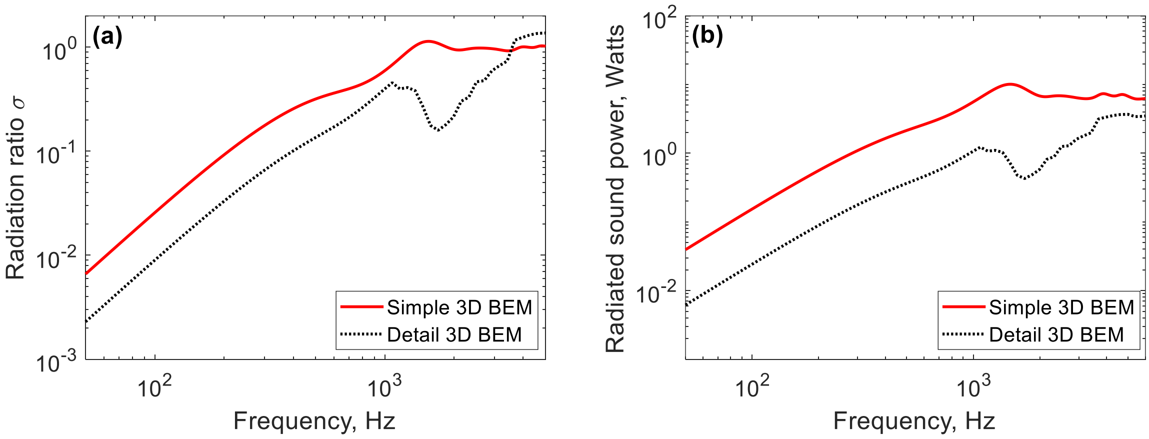

Figure 6-12 A comparison of **(a)** sound radiation ratio and **(b)** radiated sound power from a detailed and simple BE model of the baseplate.

The comparison in **Figure 6-12** demonstrates that the detailed model has lower radiation ratio than the simplified model up to 4 kHz. In the frequency range up to 1 kHz, the difference in radiation ratio is almost constant at 6 dB and the difference is even greater for the sound power as there is a smaller area. The main reason for this lower sound radiation is due to the holes introduced in the baseplate surface. The dip found for the detailed BE model at around 2 kHz might be caused by the interactions between the different radiating parts of the complex structure. In general, the comparison demonstrates that a lower radiation ratio is obtained at low frequencies for the smaller surface area due to the introduction of holes (see **Chapter 7** for further discussion of the effect of the holes). However, the computation time for the complex model has increased significantly.

6.1.4 Baseplate sound radiation in the presence of the rail

The effect of the presence of the rail on the sound radiation of the baseplate is also investigated. A section of the UIC60 rail is included in the simple BE model of the baseplate used in the previous section, as shown in **Figure 6-13**. The rail is assumed not to be vibrating; it is included to study any scattering effect it has on the radiation from the baseplate. The rail length is 1.2 m, and a solid plate representing the railpad is added between the rail and the baseplate to cover the gap between the baseplate and the rail. An infinite hard boundary is applied at the bottom surface of the baseplate. The amplitude of 0.7 m/s is applied at each side of the baseplate shown in blue colour (**Figure 6-13**), and the velocity of 0 m/s is applied at the railpad area (the centre of the baseplate) as well as on the rail.

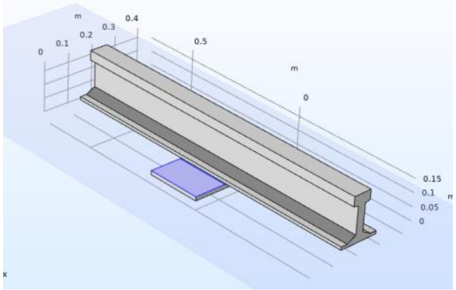

Figure 6-13 3D BE model of the simple baseplate with UIC60 rail attached.

The predicted sound radiation ratio and radiated power are presented in **Figure 6-14**. These are compared with the results obtained from the same 3D BE model without the rail. The comparison shows that the presence of the rail has a negligible effect on the radiated sound of the baseplate.

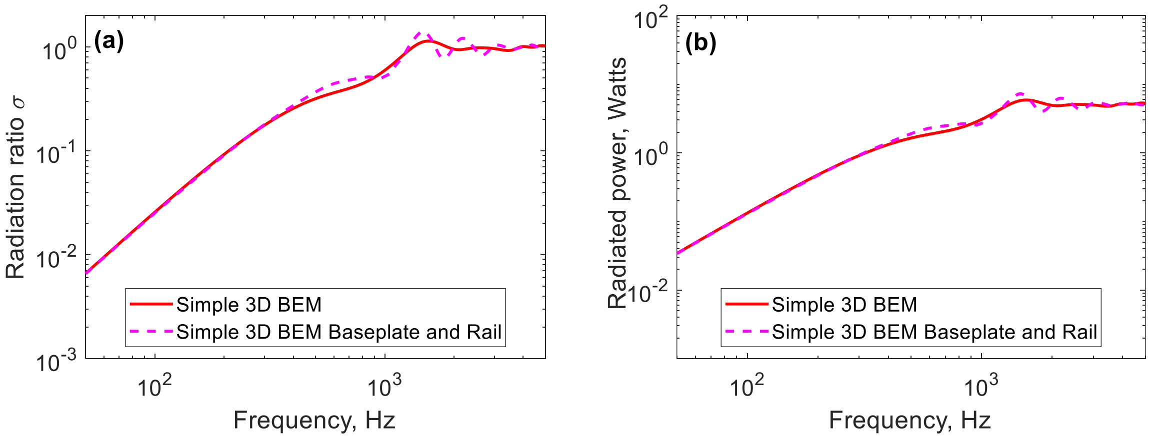

Figure 6-14 Comparison of **(a)** sound radiation ratio, **(b)** sound radiated power predicted from the 3D BE model of the simple baseplate and from the model that includes scattering by the rail.

6.1.5 Summary

The Rayleigh integral and BE methods give similar results for the sound radiation of the baseplate. For radiation ratio calculations, more than one baseplate is required. The model demonstrates that the holes in the baseplate should be taken into account. The sound radiation from the bolt-heads and the baseplate clips has not been assessed. These are quite small areas; however, these areas could contribute to a slight increase in total radiation ratio. The effect of the size of the holes is investigated further in **Chapter 7.**

6.2 Sound radiation prediction for the two-stage baseplate coupled on 2.5D track model

The track model based on the 2.5D FE model of the rail and the mobilities from the 3D FE model of the baseplate described in **Chapter 5** is used to obtain the vibration of each baseplate for a complete track due to a force at the railhead. This vibration is then used in the Rayleigh integral approximation for the calculation of sound radiation of the track. The 3D FE model of the baseplate is used to obtain the transfer mobility response of eight points in the outer region due to excitation forces applied at nine points in the railpad region, as shown in **Figure 6-15**. These form an 8×9 matrix for each excitation frequency. The transfer mobility magnitude and phase of selected locations at the outside section of the baseplate for a force at the centre of the baseplate are shown in **Figure 6-16**. It can be seen that the vibration response shows a consistent trend for most locations. However, for location 4 (not shown in the figure) which corresponds to location 5 on the other side, the response is lower for frequencies below 500 Hz.

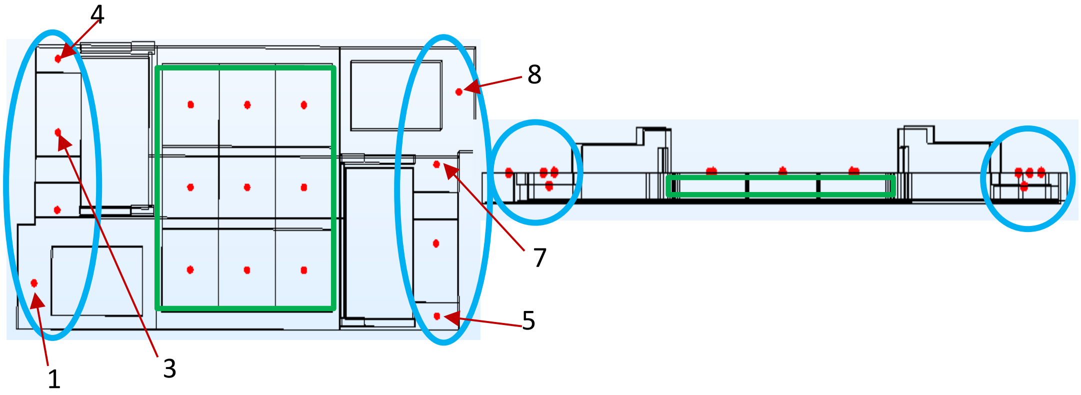

Figure 6-15 Schematic view of the force locations (railpad area in the green rectangle) and response points (blue circles) on the 3D baseplate model.

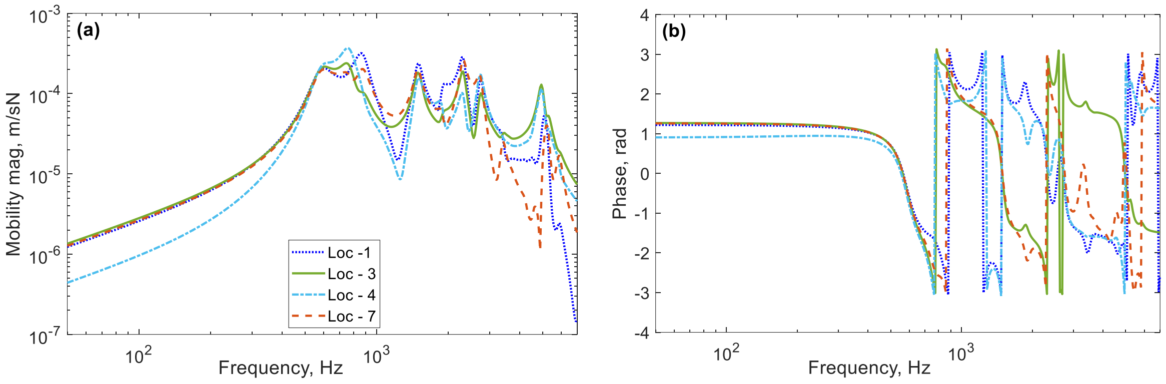

Figure 6-16 **(a)** Mobility magnitude and **(b)** phase with frequency for the outside response points due to force at the centre of the baseplate.

The coupled 2.5D FE track model is used to obtain the nine interaction forces acting on the baseplate after applying a unit point force at the railhead. The 8×9 matrix of the transfer mobilities from the 3D FE model of the baseplate and the $9 \times n$ array (where n is the number of the baseplates (121) given in the output) that contains the interaction forces acting on the baseplate are multiplied for each frequency to obtain the velocities of each of the response points. The velocity response at each point is then used in the Rayleigh integral model to predict the radiation ratio and sound power. To achieve this, the obtained velocities are allocated to a corresponding area on the baseplate surface. The area used in the approach does not include the areas that contain the holes in the actual baseplate design. The procedure is explained in more detail below.

6.2.1 Calculation of surface velocities

The transfer mobilities from the nine force points in the railpad region to the eight locations on the outer part of the baseplate (see **Figure 6-15**) are written as an 8×9 mobility matrix $\mathbf{Y}_{\mathrm{bp}}$:

$$\mathbf{Y}_{\mathrm{bp}} = \begin{bmatrix} Y_{11} & \cdots & Y_{19} \\ \vdots & \ddots & \vdots \\ Y_{81} & \cdots & Y_{89} \end{bmatrix} \qquad (6\text{-}7)$$

where Y_{ij} is the measured velocity at the i-th output location due to unit excitation at the j-th force location.

The coupled track model including the two-stage flexible baseplate FE model is used to calculate the interaction forces in each railpad spring element. These are intermediate results required in the track model. A vertical unit force is applied at the railhead above a fastener. The model gives the interaction forces for all the baseplates considered. For each frequency, the forces are gathered to form a 9×1 vector for each baseplate:

$$\mathbf{F}_\mathrm{c} = \begin{bmatrix} Ft_1 \\ \vdots \\ Ft_9 \end{bmatrix} \tag{6-8}$$

where $\mathbf{F}_\mathrm{c}$ is a vector of force transmissibilities, Ft_k is the force at the k-th location due to the unit force at the railhead. Examples of these interaction forces for the baseplate directly below the excitation point on the rail head are shown in **Figure 6-17** for railpad No.1. A peak occurs at around 170 Hz corresponding to the rail bouncing on the stiffness of the fastener, while the second peak at 1 kHz is the pinned-pinned mode of the rail.

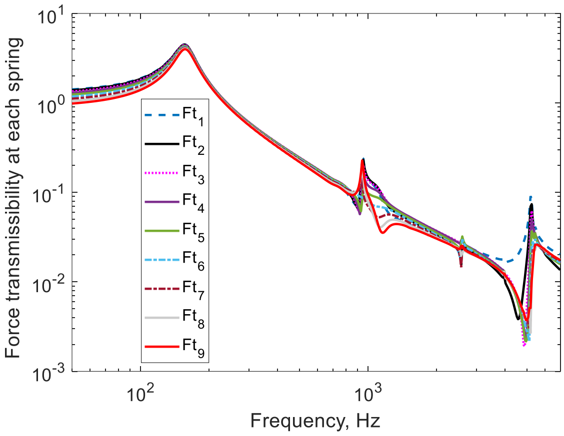

Figure 6-17 Forces at the railpad area due to a unit force on the railhead obtained from discretely supported track model using the properties of railpad No.1.

Based on the transfer mobility matrix in Equation (**6-7**) and the force vector in Equation (**6-8**), the velocities of the baseplate are determined as:

$$\mathbf{V}_\mathrm{bp} = \mathbf{Y}_\mathrm{bp}\mathbf{F}_\mathrm{c} \tag{6-9}$$

Figure 6-18 presents how the velocities contained in the $9 \times n$ vector $\mathbf{V}_\mathrm{bp}$ are located on the surface of the baseplate to be used in the Rayleigh integral approach. This figure illustrates that the allocated velocities are set to be constant in each section on the outer part of the baseplate.

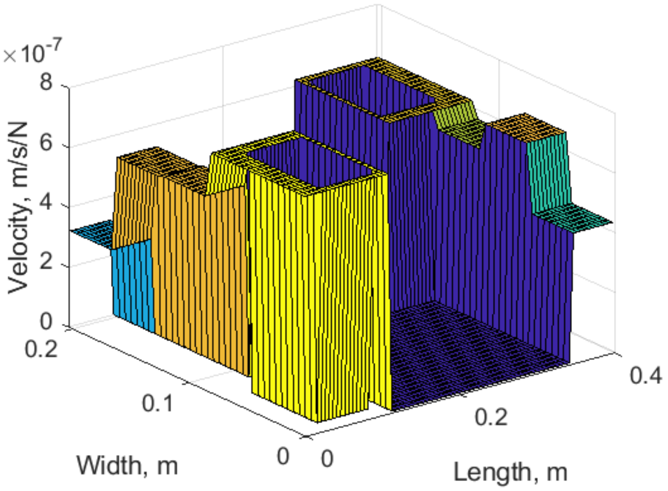

Figure 6-18 The calculated velocities at 300 Hz allocated to their respective areas on the baseplate surface (blue colour represents regions with velocity of zero (holes and railpad area).

6.2.2 Rayleigh integral model results

As explained above, the velocity values for each of the baseplate's eight response points are applied on the corresponding baseplate segment. The Rayleigh integral approach is then used to obtain the radiated sound power W_{rad}. The radiation ratio is determined as

$$\sigma_{\mathrm{rad}} = \frac{W_{\mathrm{rad}}}{\rho_0 c_0 S_{\mathrm{tt}}\,(|v_{\mathrm{b}}|^2/2)} \qquad (6\text{-}10)$$

where v_{b} is the average squared velocity amplitude obtained as follows:

$$|v_{\mathrm{b}}|^2 = \frac{v_1^2 S_1 + v_2^2 S_2 + \cdots v_8^2 S_8}{S_{\mathrm{tt}}} \qquad (6\text{-}11)$$

where v_i is velocity allocated to the i-th baseplate segment (contained in the $\mathbf{V}_{\mathrm{bp}}$ vector), S_i is the surface area of the segment and S_{tt} is the total area of the eight segments used in the calculation (for more than one baseplate S_{tt} becomes $n \times S_{\mathrm{tt}}$ where n is the number of baseplates included and more terms are included in $|v_{\mathrm{b}}|^2$).

Figure 6-19 (a) shows the spectrum of the velocity magnitude for each baseplate area, while **Figure 6-19 (b)** presents the average squared velocity for a single baseplate. At this initial stage, only the baseplate directly below the excitation location is used for the radiation prediction for a unit force on the rail. These results are for railpad No.1 and lower pad No.6, type A. The first peak at 160 Hz corresponds to the peak seen in the force spectra in **Figure 6-17**.

Figure 6-20 (a) and **(b)** show the predicted radiation ratio and sound power spectra for this single baseplate. The radiation ratio has a similar form to the results obtained using the detailed BE model in **Figure 6-12**, indicating that the inclusion of the holes has more effect than other aspects of the shape of velocity distribution.

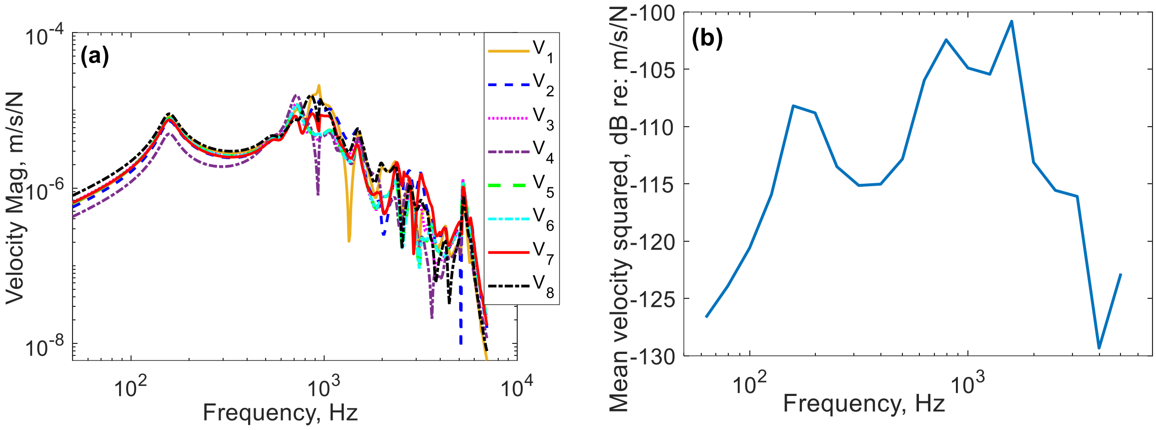

Figure 6-19 **(a)** Velocity magnitude frequency spectra of the baseplate segments and **(b)** one-third octave band frequency spectrum of the average squared velocity, all for the baseplate below the excitation point.

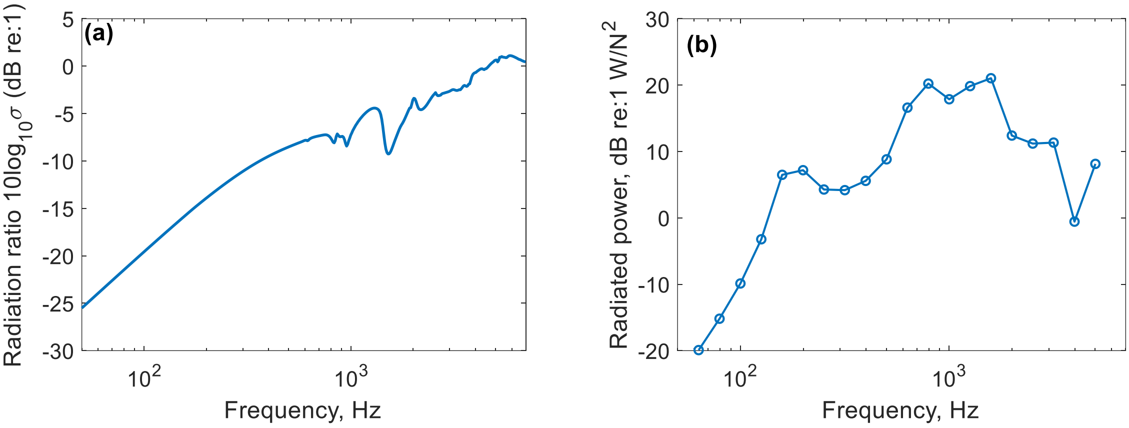

Figure 6-20 **(a)** Sound radiation ratio spectrum and **(b)** one-third octave band frequency spectrum of the radiated sound power of a single baseplate with railpad No.1 for a unit force on the rail head.

6.2.3 **Required number of baseplates**

In this section a study is conducted to identify the number of discrete baseplates that are required for the prediction of the radiation ratio. The number of baseplates is increased, and the results are compared until no further changes occur in the radiation ratio. Calculations are performed for 1, 3, 5 and 7 baseplates spaced at 0.65 m apart for railpad No.1 and lower pad No.6, Type A. **Figure 6-21** presents a schematic view of the seven baseplates. In each case the rail is excited above the central baseplate, and the vibration model contains 121 baseplates. The radiation ratios are presented in **Figure 6-22 (a)** which shows that using three baseplates is adequate to describe the radiation ratio, as also found by Zhang et al. [98] for the sleepers in a ballasted track. **Figure 6-22 (b)** presents the one-third octave band spectrum of the calculated sound power for the different numbers of baseplates. The results show that, although at higher frequencies the radiation ratio is independent of the number of the baseplates used, the sound power still depends on the number of baseplates because of the transmission of vibration along the rail.

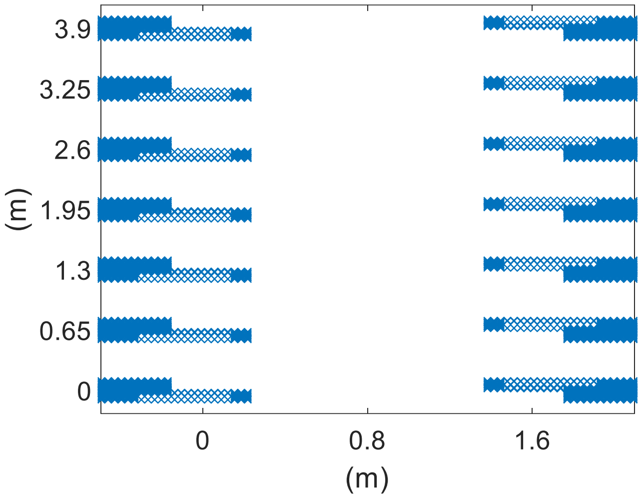

Figure 6-21 Schematic view of the seven baseplates spaced 0.65 m apart.

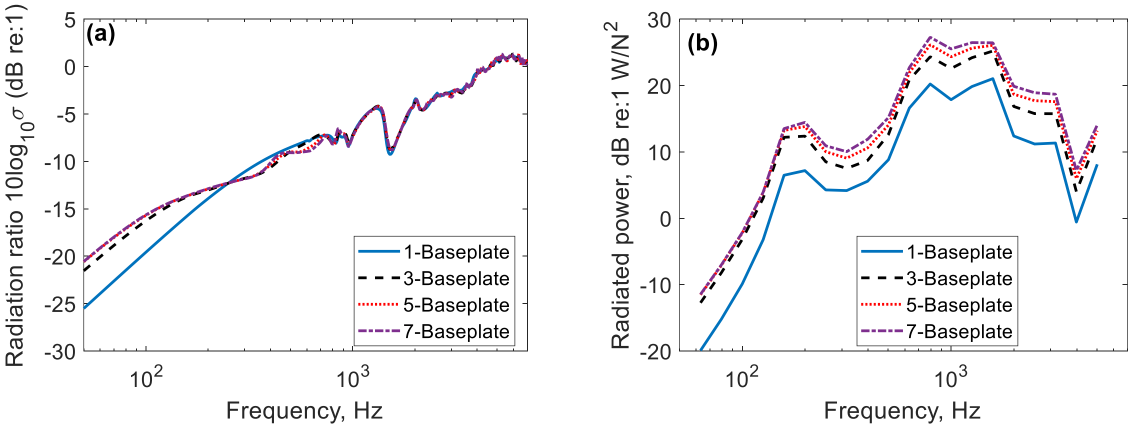

Figure 6-22 Predictions using the different number of baseplates **(a)** sound radiation ratio and **(b)** one-third octave sound radiated power for railpad No.1 properties.

6.2.4 Comparison of the proposed model of the baseplate with the TWINS (bi-block) sleeper model

In this section a comparison is made between a rolling noise prediction in TWINS using the bi-block sleeper model to represent the baseplate as a rigid mass and the results from the model developed in this chapter. Note for TWINS calculations the results are for an integration length of one train length which is 20 m that is equivalent to about 31 baseplates spans (20/0.65 m). Railpad No.1 is used in the baseplate. In the TWINS model, the baseplate is represented by its mass and the whole surface area is included in the prediction of sound radiation. The wheel is from a UK class 378, typical of a modern multiple unit train, with a diameter of 0.84 m and a straight web. The train speed is 120 km/h and measured roughness data is used from an actual (typical of UK) ballasted track at Fishbourne, UK in 2013 [36, 47]. To calculate the baseplate noise using the model proposed in this chapter, the wheel/rail interaction force (contact force) per unit roughness is extracted from the TWINS model of the slab track and applied to the 2.5D track model (this is interpolated to the frequencies used in the track model).

The results are compared in terms of the average vibration of seven baseplates (per unit roughness) in **Figure 6-23**. For frequencies between 200 Hz and 1.6 kHz, the average vibration predicted by the flexible baseplate model is around 20 dB less than that predicted by the rigid mass model, whereas above 2 kHz the results of the two models are similar. The difference is even greater below 160 Hz.

The sound power for a unit roughness (i.e. a roughness of amplitude 1 at each frequency, which yields a transfer function from roughness-squared to sound power) for the track with 121 baseplates is shown in **Figure 6-24** (a), and in **Figure 6-24** (b) the same results are shown after adding the roughness spectrum. The results demonstrate that the flexible baseplate has much lower levels of sound power at frequencies below 2000 Hz.

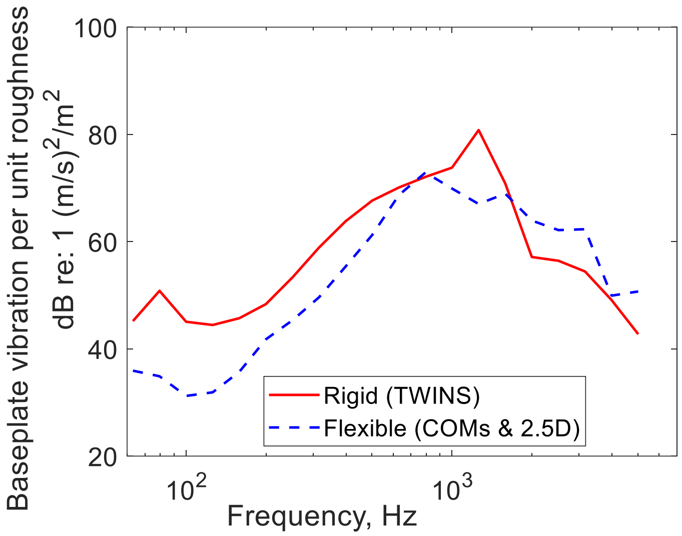

Figure 6-23 Average vibration of seven baseplates over the surface area outside the railpad region is determined using the bi-block sleeper model in TWINS (rigid) and using the combined 2.5D FE and COMSOL model (flexible) for railpad No.1 properties and unit roughness.

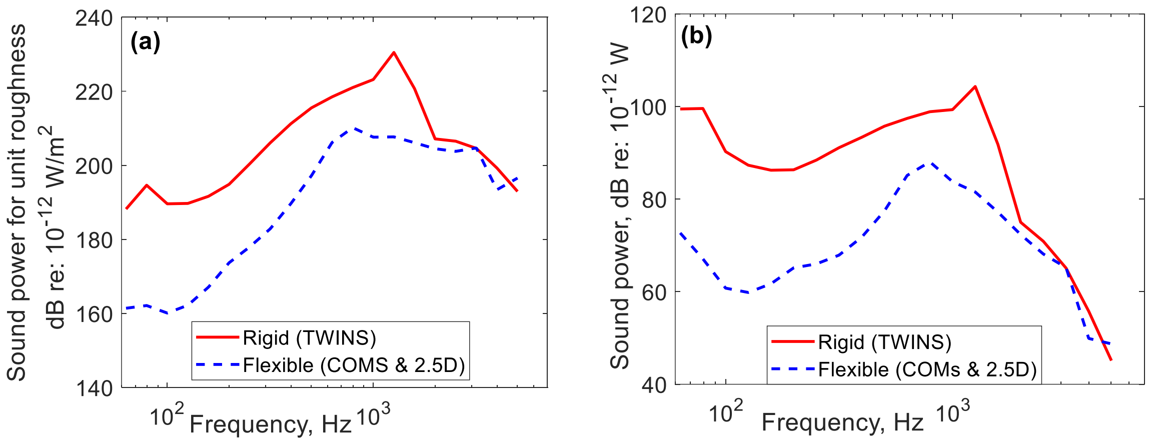

Figure 6-24 Comparison of sound power from the baseplate obtained from the bi-block model and the combined 2.5D FE and COMSOL model for railpad No.1, **(a)** for unit roughness, **(b)** for actual roughness spectrum.

Figure 6-25 and **Figure 6-26** present the sound power contributions of the rail, wheel and baseplate and the total. **Figure 6-25** gives the results obtained from the bi-block TWINS model where the baseplate is modelled as rigid mass. The results show that baseplate is the dominant contributor to the noise at low frequencies and remains important up to 1.6 kHz. **Figure 6-26** presents the corresponding results when the baseplate contribution is calculated using the combined 2.5D FE and COMSOL model. Comparing the results from these two figures, the noise from the flexible baseplate is 15 dB lower than when it modelled as a rigid mass, and the total noise is 3 dB lower. The noise from the flexible baseplate is much lower than the rigid one at low frequencies.

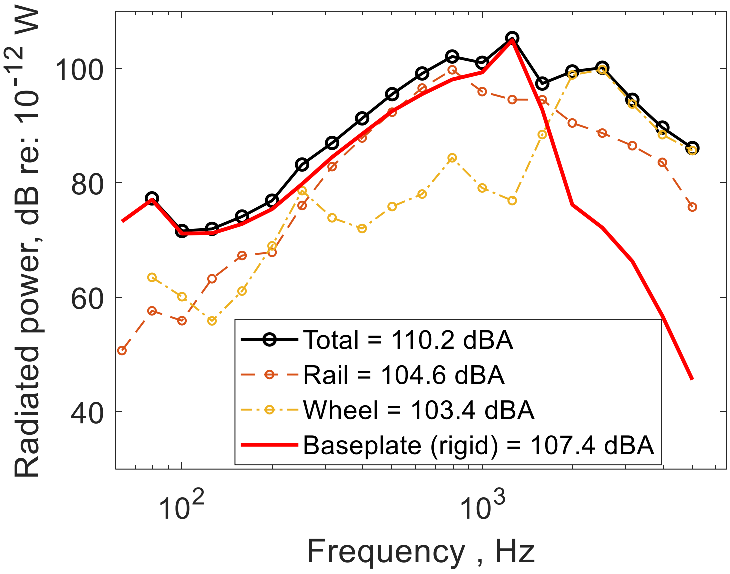

Figure 6-25 A-weighted sound power for the rail, wheel and baseplates for railpad No.1 using the bi-block model.

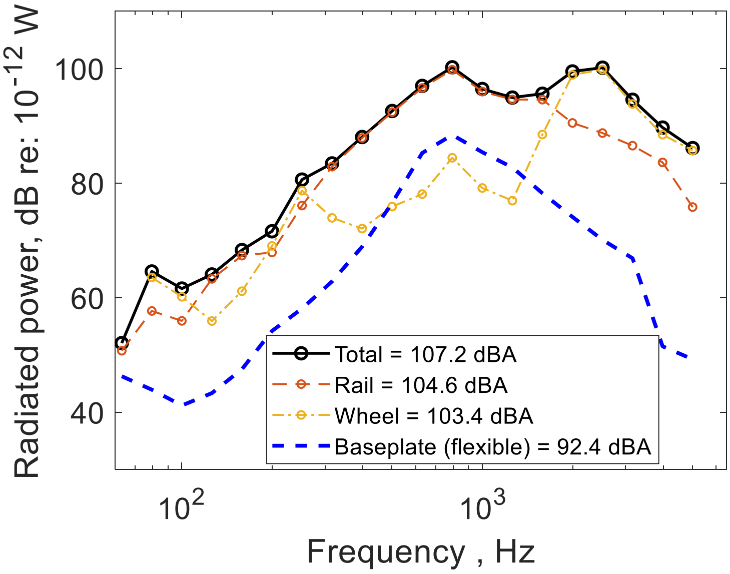

Figure 6-26 A-weighted sound power for the rail, wheel and baseplates for railpad No.1 using the bi-block model for the rail and the combined 2.5D FE and COMSOL model for the baseplate.

6.3 Measurements of sound radiation for the two-stage baseplate

A sample of half-width slab track including the baseplates, railpad No.1, and lower pad No.6 type A was supplied by Pandrol Ltd. It was fitted with a 6 m length of rail and installed in the ISVR reverberation chamber at the University of Southampton. Noise and vibration measurements have been conducted on the baseplates and the rail to determine their sound radiation. A schematic view of the test section of the slab track is shown in **Figure 6-27**. It has half the actual slab width and includes only one rail. It is assembled from four half-slab units, each with a length of 1.5 m and a thickness of 0.2 m. The slab units were laid directly on the floor of the reverberation chamber. On each slab unit, two rail fasteners (two-stage baseplates) were fitted with a spacing of 0.65 m, as shown in **Figure 6-28**. A detailed view of the measurement setup is shown in **Figure 6-29**, where the noise source (loudspeaker), the rotating microphone boom and the sensors (accelerometers) can be seen. A full schematic view of the measurement setup is shown in **Figure 6-30**.

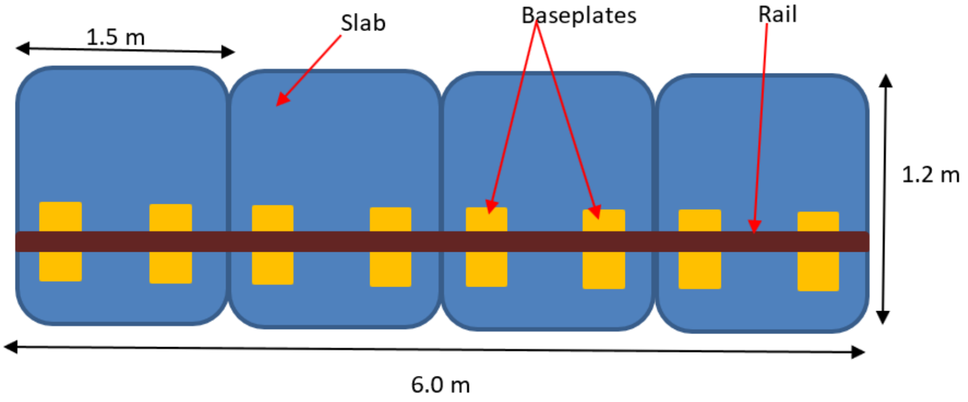

Figure 6-27 Schematic view of the half-width slab track.

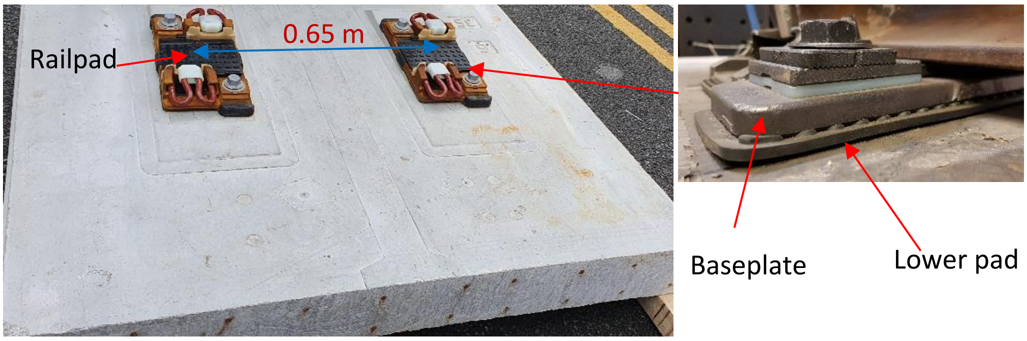

Figure 6-28 View of a single slab unit with two sets of the two-stage baseplate installed.

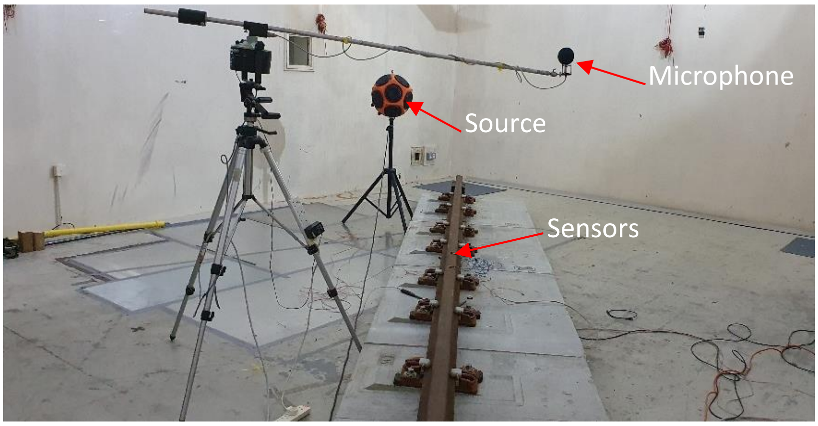

Figure 6-29 View of the 6 m half-width slab track assembled in the reverberation chamber for the measurements.

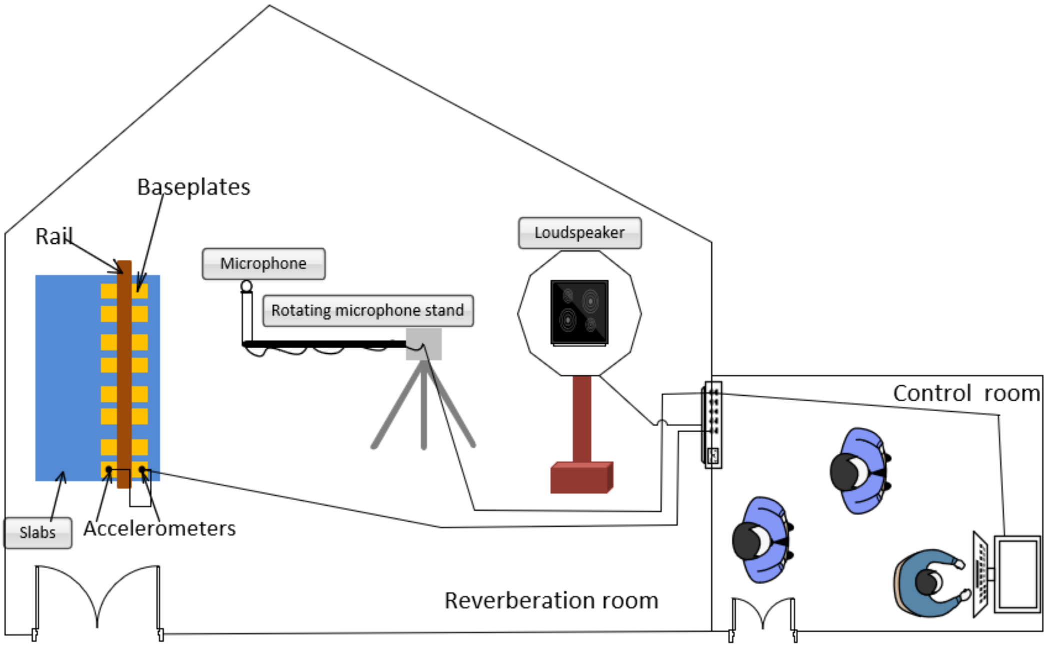

Figure 6-30 Full schematic view of the measurement setup.

6.3.1 Baseplate mobilities

Mobility measurements were first conducted on a single baseplate attached to the track slab. A PCB instrumented impact hammer (150 g) was used to excite the baseplate at seventeen locations on its surface (red dots shown in **Figure 6-31** (**a**)), and two accelerometers (with sensitivities 500 mV/g and 100 mV/g) were attached at the centre of the baseplate, as shown in **Figure 6-31** (**b**). The two accelerometers were of different types and were used for the benefit of comparison.

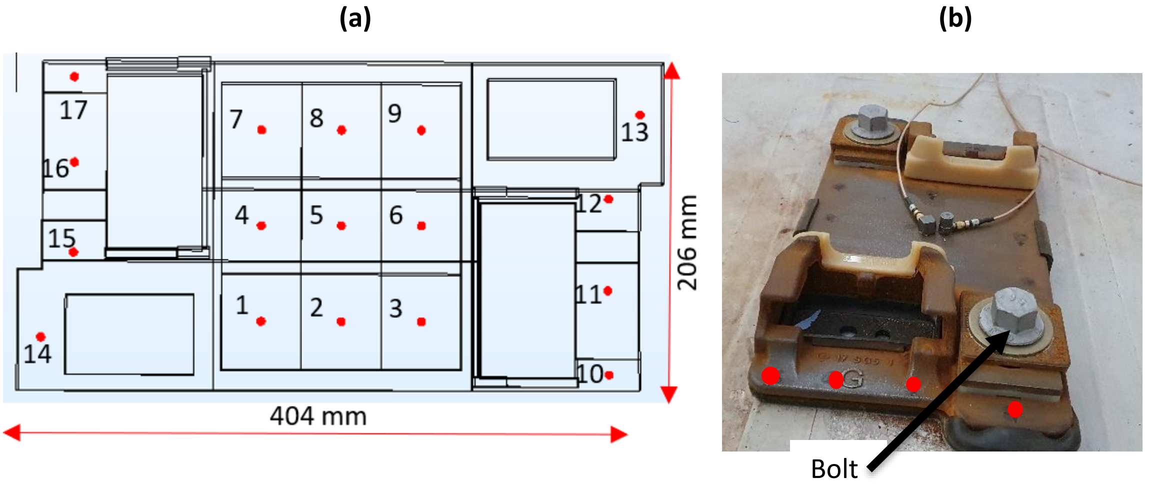

Figure 6-31 Schematic view of FEM nodes location **(a)**, and **(b)** picture of the baseplate showing some of the measured points (red dots).

The measured mobilities are compared with the ones predicted from the 3D FE model of the baseplate. The FE model uses a stiffness of 80 MN/m the lower pad No.6, Type A (uniform spatial distribution).

Figure 6-32 shows the magnitude and phase of the driving point mobility at the centre of the baseplate (location No. 5 in **Figure 6-31** (a)) which shows good agreement between measurements and predictions.

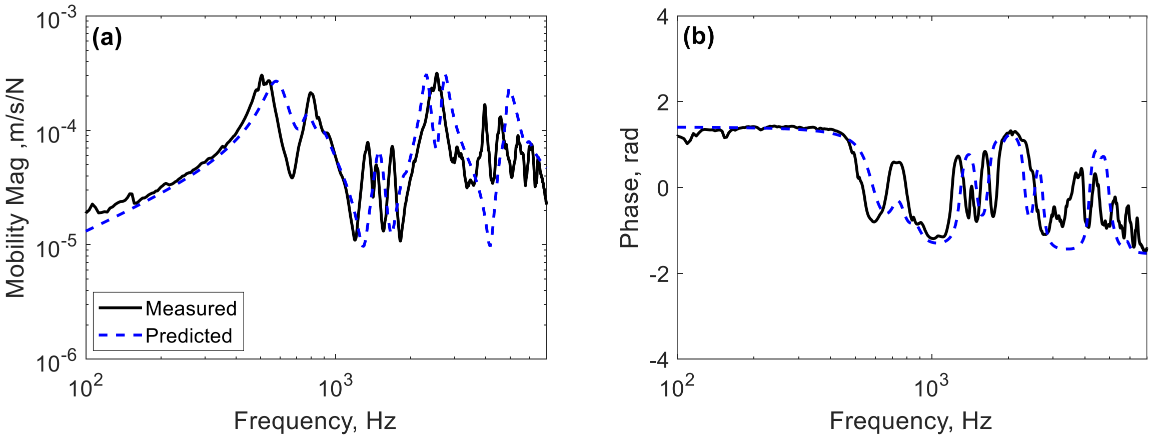

Figure 6-32 Comparison of the measured and the predicted driving point mobility of the baseplate with the impact at the centre of the baseplate **(a)** magnitude and **(b)** phase.

The average squared magnitude of the measured and predicted mobilities over all 17 points $\langle|Y_{\mathrm{t}}|^2\rangle$ is calculated, taking into account the baseplate's surface area, as indicated in Equation (**6-11**), and is shown in **Figure 6-33**. This value will be used in the next section for sound radiation ratio calculation.

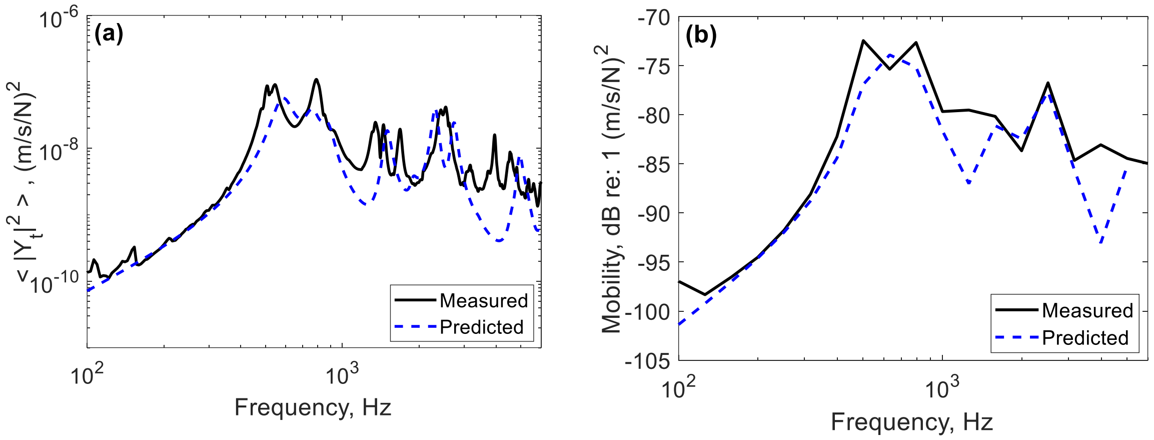

Figure 6-33 Spectrum of the measured and predicted mean squared mobility of the baseplate: **(a)** narrowband, **(b)** one-third octave band.

Figure 6-32 and **Figure 6-33** show that the agreement between the measured and the predicted baseplate vibration is generally good, both for the predicted level and trend. However, at high frequency, the predictions have a lower amplitude than the measurements. Moreover, some of the peaks shown in the measured data do not appear in the predictions. This might be due to the geometric simplifications used for the 3D FE baseplate model. It should be noted that the constraints of the baseplate in the FE model differ from the actual situation. The measured baseplate is secured with bolts on the slab (see **Figure 6-31**), while in the FE model, it is merely attached by the lower pad beneath the baseplate. Moreover, a rigid boundary condition is used below the pad whereas the slab will not be fully rigid.

To investigate the vibration transmission from the baseplate to the concrete slab, the baseplate is excited at its centre with the impact hammer, and the vibration is measured at the driving point and at two locations on the slab, one next to the baseplate (see **Figure 6-34**) and the other at the midspan between two fasteners (mid-way between two baseplates).

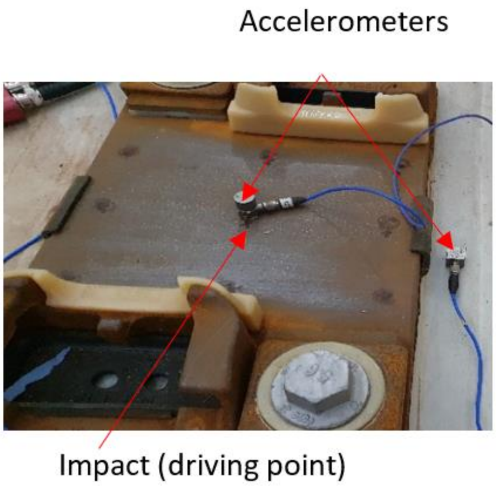

Figure 6-34 Photographic view of the measurement setup, showing the sensor next to the baseplate and at the centre of the baseplate next to the impact force location.

The measured mobility magnitude is presented in **Figure 6-35 (a)** and **(b)** as narrowband and one-third octave band spectra, respectively, for each measured point. The results show that the vibration levels measured on the slab next to the baseplate and at the slab midspan are similar. The vibration of the slab is attenuated by 10-20 dB compared with the driving point vibration on the baseplate because of the baseplate lower pad.

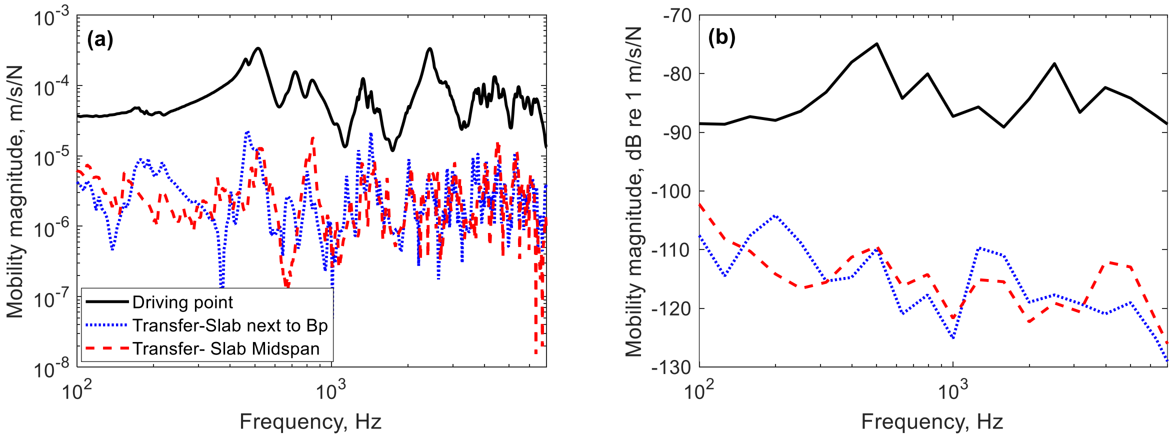

Figure 6-35 Measured mobility magnitude measured at the driving point on the baseplate and the slab in **(a)** narrowband and **(b)** one-third octave band.

6.3.2 Baseplate sound radiation

This section presents the radiation ratio of a single baseplate when the rail and the railpad are not attached to it. By normalising both the sound power and the squared velocity by the mean-square force (over time) acting on the structure in the frequency band, Equation (**6-5**) can be expressed as [86]:

$$\sigma_{\mathrm{rad}} = \frac{\mathrm{W}/\overline{\mathrm{F}^2}}{\rho_0 \mathrm{c}_0 S\langle|Y_{\mathrm{t}}|^2\rangle} \tag{6-12}$$

where $\langle|Y_{\mathrm{t}}|^2\rangle = \overline{v^2}/\overline{F^2}$ is the spatially averaged squared mobility, and $\overline{F^2}$ is the mean-square force acting on the structure.

To determine the radiation ratio, two measurements are required: an acoustic measurement, i.e. the radiated sound power, and a mechanical measurement, namely the spatially-averaged squared velocity. Equation (**6-12**) is used here, where the sound power per unit mean-square force and the spatially-averaged mobility were measured in the reverberation chamber. Spatially-averaged mobilities were measured by exciting the structure with an impact hammer at various locations, and its response was measured with an accelerometer. For the acoustic measurement, a reciprocity technique is used [86]. The structure is excited by acoustic excitation from an external sound source, and the resulting vibration of the structure is measured, as illustrated in **Figure 6-36**. A microphone is used to measure the sound pressure level (SPL) spectrum in the room during the acoustic excitation. It is also used to measure the background noise in the room.

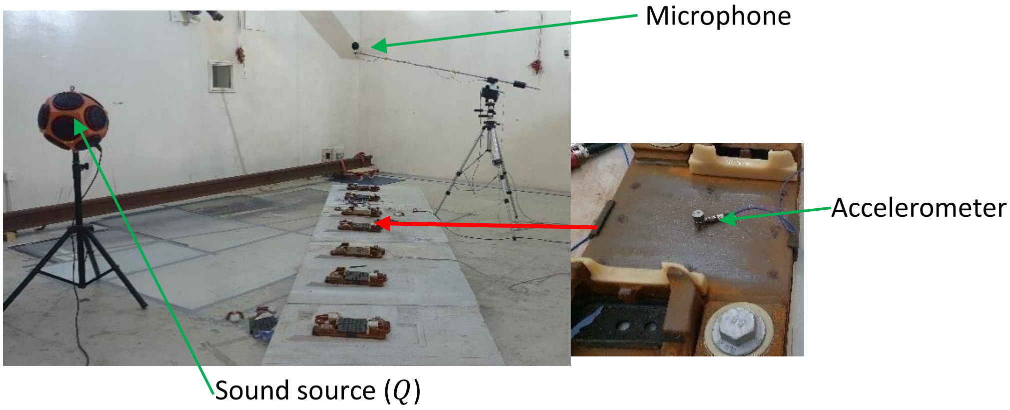

Figure 6-36 Setup for baseplate acoustic measurement.

The numerator in Equation (**6-12**) is measured indirectly from the reciprocity measurements in the reverberation chamber as follows [86]:

$$W/\overline{F^2} = \frac{\overline{a_{\mathrm{Q}}^2}}{\langle\overline{p_{\mathrm{Q}}^2}\rangle}\frac{\rho_0}{4\pi c_0} \tag{6-13}$$

where a_Q is the acceleration response of the structure and $\langle\overline{p_{\mathrm{Q}}^2}\rangle$ is the spatially-averaged mean-square acoustic pressure in the chamber due to the sound source Q. Excited by a loudspeaker, the accelerometer is attached to the structure at the position where the force is applied in the transfer mobility measurement, while a rotating microphone (the microphone is attached to a rotating boom on a tripod that can rotate through 360 degrees) in the chamber is used to measure the mean-square pressure $\langle\overline{p_{\mathrm{Q}}^2}\rangle$. All the data is collected using the Data Physics Corporation data analyser and processed using Matlab software.

Figure 6-37 shows the measured sound pressure and the background noise (when all the doors are closed and any mechanical noise is stopped) inside the reverberation chamber obtained using the rotating microphone boom. **Figure 6-38** shows the measured acceleration in the one-third octave bands when the sound source is on and off. These results demonstrate that the background levels will not affect the measured results in either case. **Figure 6-37** shows a peak at 50 Hz in background noise signal caused by electrical interference. Nonetheless, this peak does not affect the measured data, as the noise emitted from the source is higher at this frequency. For these measurements, the sensor was placed at the centre of one baseplate (the middle baseplate of the track section, 4th baseplate) and the measurements were repeated for the 5th baseplate.

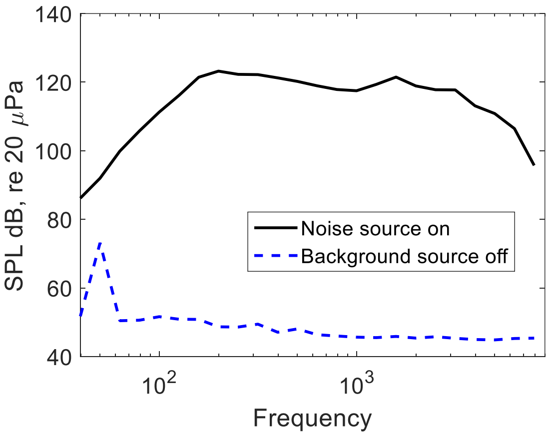

Figure 6-37 Measured sound pressure level and background noise inside the reverberation chamber.

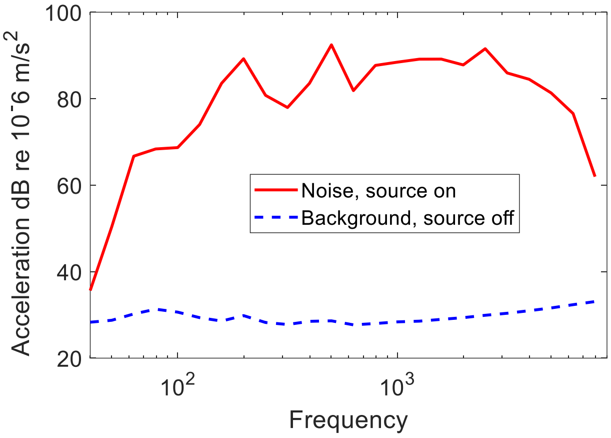

Figure 6-38 Measured acceleration with the accelerometer at the centre of the baseplate. Also shown is the background signal.

From these results, the measured radiation ratio and sound power from the middle baseplate are determined and shown in **Figure 6-39**. Predicted results from the combination of the FE model of the baseplate and the Rayleigh integral model for single baseplates are also shown for comparison. The measured results apparently show high levels of radiation ratio below 300 Hz. This is due to the radiation contribution of the slabs and possibly the room floor. **Figure 6-35** demonstrates the difference between baseplate and slab vibration at low frequencies is about 10 dB. In addition, the area of one slab is 1.8 m^2 (see **Figure 6-27**) while for the baseplate it is 0.08 m^2 (see **Figure 6-31**). This is sufficient to explain the higher values of radiated power at lower frequencies. The vibration of the floor may also contribute but was not measured. A reasonable agreement is found between the measured and the predicted results for higher frequencies (above 1 kHz).

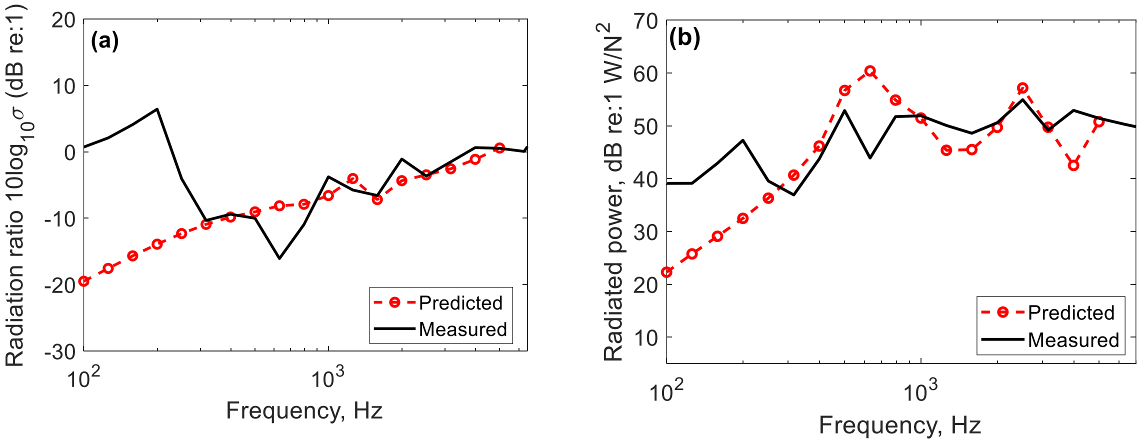

Figure 6-39 Comparison between the measured and predicted **(a)** radiation ratio, **(b)** radiated power per unit mean square force for a single baseplate.

6.3.3 Rail vibration measured in the reverberation chamber

As a step towards measuring the rail radiation, the rail vibration is measured for the track section in the reverberation chamber using the same method as for the baseplate described in section **6.3.2**. The rail-baseplate transmissibility (for impact at the railhead, the ratio of the response of the baseplate next to railpad area to that of the rail) is measured for four different conditions. These four conditions are considered to understand the influence on the vibration transmission between the rail and baseplate: (i) the rail is unclipped and resting on the railpads and baseplates with the plastic isolators present (see **Figure 6-40** or **Figure 1-7**); (ii) the rail is unclipped and resting on the railpads and baseplate with the isolators removed; (iii) the rail is unclipped and lifted by 60 mm at each end, resting on a stack of 10 softer pads, ('free-free' case); and (iv) the rail is clipped on the baseplates with isolators present as in the operational condition. No.1 railpads were fitted. In all cases, one pair of commercial 'Silent Track' rail dampers was attached to each end of the rail (see **Figure 6-41**). These contain steel masses embedded in an elastomer to form a damped tuned absorber with a broadband frequency response. These were used in an attempt to reduce wave reflections at the rail ends. The transmissibilities for all four cases are presented in **Figure 6-42**.

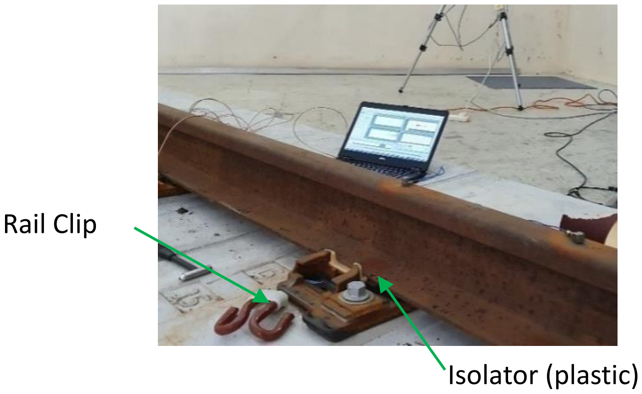

Figure 6-40 View of the setup showing the rail clip and isolator.

Figure 6-41 View of the 'Silent Track' rail dampers attached to the end of the rail.

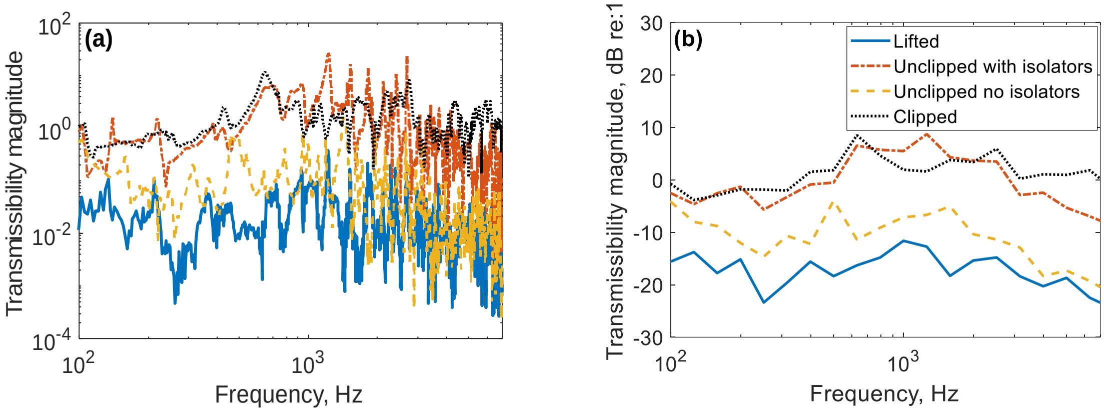

Figure 6-42 Transmissibility ratio between the baseplate and the rail **(a)** in narrowband, **(b)** in one-third octave band.

The measured results demonstrate that by having the rail unclipped but the isolators present, the rail vibration is still transmitted to the baseplate. Around 1 kHz the vibration being transmitted to the baseplate is even higher than when it is clipped. This suggests that the isolators maintain the preload applied to railpads. However, when the rail is unclipped and the isolators removed, or when the rail is lifted, much lower levels of vibration are transmitted to the baseplate. When the rail is resting on the pads, the studs are not compressed and the stiffness is much lowered than when a preload is applied.

To measure the mean-square mobility of the rail, required to derive its radiation ratio, it was excited with the impact hammer at 64 locations along the railhead (32, black circles) and one side of the rail foot (32, red circles) as seen in **Figure 6-43**. The measurements were conducted for the same four cases: unclipped with no isolators, unclipped with isolators, lifted, and clipped. Two accelerometers were used for this measurement: one placed on the rail above the 4th baseplate and the other on the rail at the middle of the 6 m section between the 4th and 5th baseplate, as shown in **Figure 6-44**.

Figure 6-43 Impact locations: **black** circles along the railhead (32) and **red** circles along the railfoot (32).

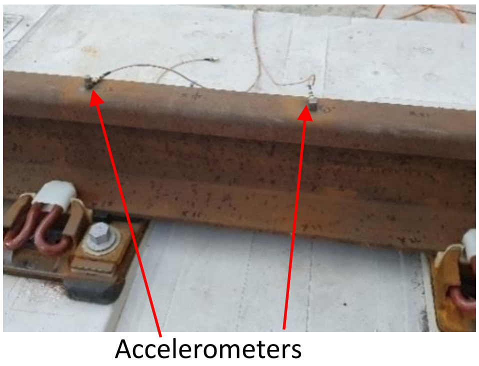

Figure 6-44 Rail vibration measurements setup showing two attached accelerometers.

Figure 6-45 shows the driving point mobility, magnitude and phase, measured at the railhead of the clipped rail with railpad No.1 in the reverberation chamber and on the track at Doncaster. Both were measured directly above the baseplate. These results are consistent, although in the current case the rail exhibits a series of resonances due to its short length. The peak at 5 kHz in both results corresponds to the rail 'foot flapping' mode [1].

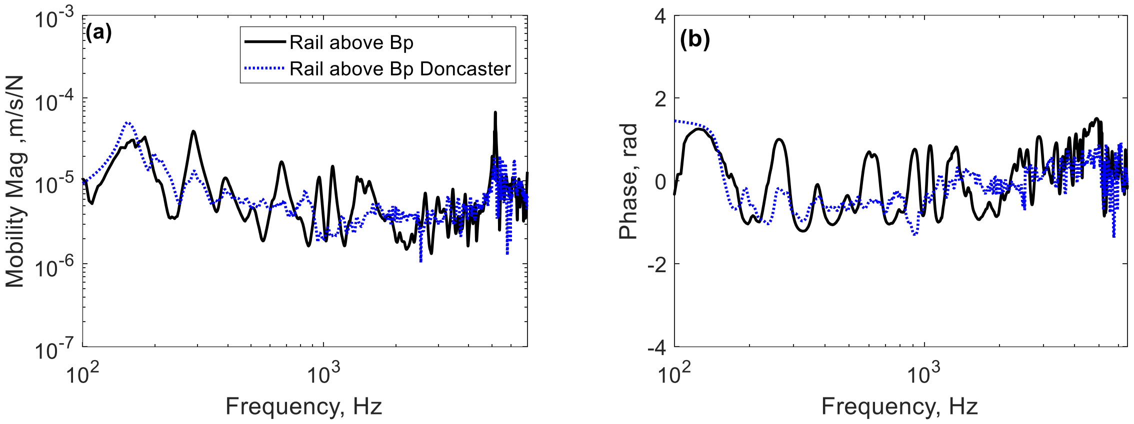

Figure 6-45 Measured driving point mobility of the clipped rail with railpad No.1**:** **(a)** magnitude and **(b)** phase.

Figure 6-46 shows the overall mean square rail mobility obtained from the two accelerometers. In each case, it is the average over the results for the 64 excitation positions on the railhead and the rail foot. The results are shown in narrowband and one-third octave bands.

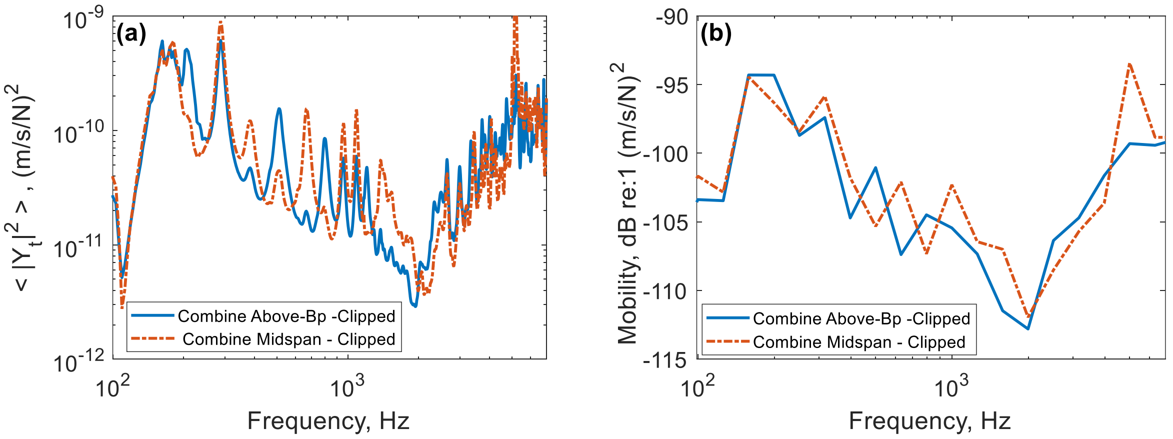

Figure 6-46 Measured mean squared rail mobility for the clipped case showing results for the two sensors: **(a)** narrowband and **(b)** one-third octave band.

Figure 6-47 compares the mean square rail mobility for the case where the rail is lifted with the clipped case. The results are presented in narrowband and one-third octave bands. In the lifted case, a series of lightly damped resonances are seen, especially at frequencies above 600 Hz. Consequently, higher average vibration levels are found for this case. For the clipped rail, these modes are still visible as peaks but the damping introduced by the rail pads reduces their height. The foot flapping mode at 5 kHz is seen particularly strongly in the results for the lifted rail.

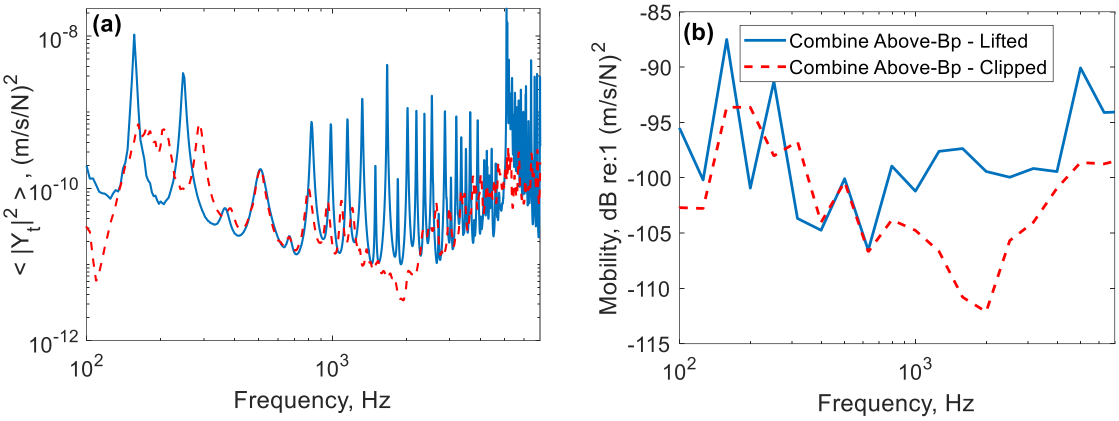

Figure 6-47 Measured mean square mobility for the lifted and clipped cases, measured above baseplate. **(a)** In narrowband; **(b)** in one-third octave band.

6.3.4 Rail sound radiation

The radiation ratio of the rail is obtained using the same method as for the baseplate (see Section **6.3.2**). The rail is excited by the external sound source, and its vibration is measured by the two sensors attached at the railhead (above the baseplate and at the midspan), although only the results above the baseplate are shown here. The radiation ratio is calculated using equation (**6-12**) for three measured cases: rail clipped; rail unclipped and resting on the pads, without isolators; and rail lifted by about 60 mm. The results are presented in **Figure 6-48** in narrowband and in one-third octave band form.

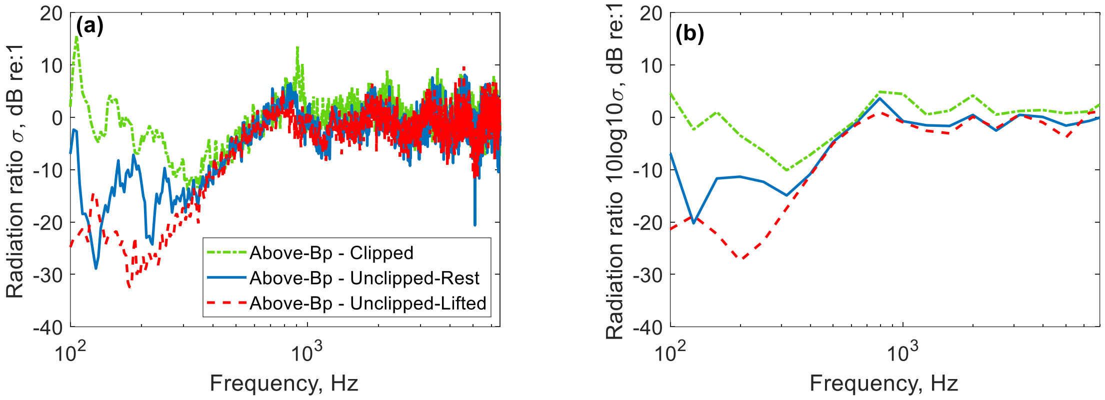

Figure 6-48 Measured radiation ratio for the rail: **(a)** in narrowband and **(b)** in one-third octave bands.

Above 300 Hz the results for the lifted and resting cases are very similar. However, the results for the clipped rail case are slightly higher than the other two cases. This is likely to be due to a contribution to the sound power from the baseplates, not taken into account in the radiation ratio. For frequencies below 300 Hz, coupling to the slab and the floor of the chamber may again be the reason for the apparently high radiation ratios.

In [36], Zhang *et al*. developed a numerical model based on the 2D BE method to predict the sound radiation from a rail in close proximity to the ground. This model was also verified by comparison with a 3D BE model in [36]. Results from this model are compared with the measured radiation ratios in **Figure 6-49**. In **Figure 6-49** (**a**) the measured result for the lifted rail is compared with the predicted result above a rigid ground, whereas in **Figure 6-49** (**b**) the measured result for the rail resting on the pads is compared with the predicted result based on a combination of cases in which the rail is partially attached to the ground and partially above the ground, which is used to represent a rail in situ [36].

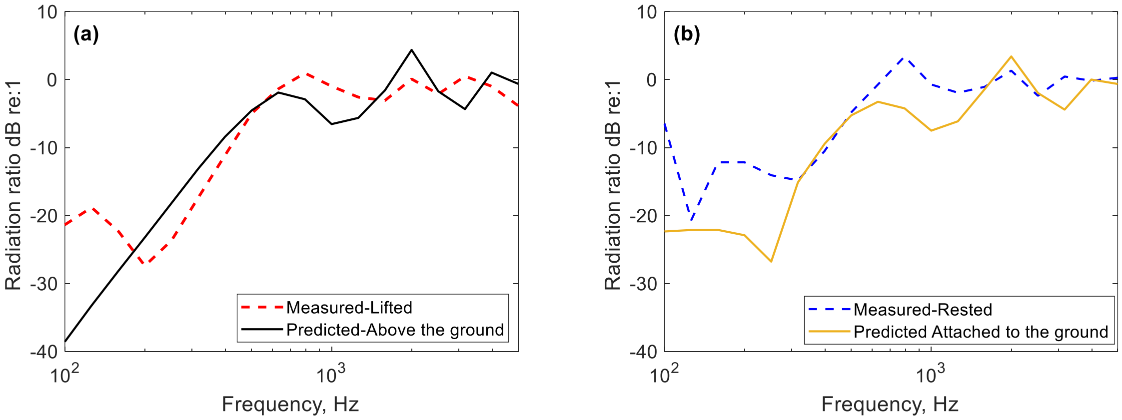

Figure 6-49 Comparison of rail radiation ratio between the measurements and predictions from the 2D model for the same rail properties. **(a)** Measured result for lifted rail, predicted result above the ground and **(b)** measured result for rail resting on the pads, predicted result partially attached to the ground and partially above the ground.

From the comparisons in **Figure 6-49** it can be seen that a good agreement is found between the measured and predicted radiation ratios. For the case of the lifted rail the model tends to over-predict by up to 5 dB between 200 Hz and 500 Hz and under-predict by a similar amount (up to 5 dB) between 630 Hz and 1600 Hz. For the case of the rail resting on the pads, the model tends to under-predict by up to 7 dB between 630 Hz and 1600 Hz, which may in part be due to the contribution from the baseplates. In the measured data for frequencies below 300 Hz, higher levels are seen which are due to the contribution from the slabs and the floor vibration as explained in Section **6.3.2**.

6.3.5 Track radiated power

In this Section, the sound power radiated by the whole track for a unit mean-square force on the railhead is predicted using the various models presented above and compared with the measurements. In the predictions, a superposition approach is followed, assuming that the radiated sound power from the rail and the baseplates can be treated as uncorrelated. The sound power radiated by the rail is determined from the spatially averaged vibration calculated using the 2.5D FE rail model combined with the radiation ratio from Zhang *et al.* [96]. The sound power radiated by the baseplates is calculated by determining the spatially averaged vibration of eight baseplates from the coupled track model and combining this with the radiation ratio calculated using the Rayleigh integral for three baseplates coupled through the rail. The contribution of only three baseplates to the radiation ratio is sufficient, as explained in Section **6.2.2**. These results are combined to determine the total sound power radiated by the track. This is then compared with the sound power for a unit force measured in the reverberation chamber.

The predicted sound power of the rail W_{r} and of the eight baseplates W_{bp} are obtained for a unit mean-square force acting on the rail. They are given by the following expressions:

$$W_{\mathrm{r}} = \sigma_{\mathrm{r}}\rho_0 c_0 S_{\mathrm{r}}\langle|Y_{\mathrm{r}}|^2\rangle \tag{6-14}$$

$$W_{\mathrm{bp}} = \sigma_{\mathrm{bp}}\rho_0 c_0 S_{\mathrm{bp}}\left\langle\left|Y_{\mathrm{bp}}\right|^2\right\rangle \tag{6-15}$$

where σ_r is the rail radiation ratio predicted using the 2D model in [96], σ_{bp} is the baseplate radiation ratio predicted using the Rayleigh integral method in Section **6.2.2**, S_{r} is the surface area of the rail, S_{bp} is the surface area of the eight baseplates and $\rho_0 c_0$ is characteristic acoustic impedance of sound in air (density of sound in air 1.2 kg/m^3 and speed of sound in air 343 m/s).

For the rail, only the vibration of the surfaces facing in the vertical direction is taken into account. The corresponding surface area is therefore the area projected in the vertical direction. The length of the measured rail is $L = 6$ m, and its perimeter length (projected in the vertical direction) is 0.4 m. Therefore, the total rail area is taken as $S_{\mathrm{r}} = 0.4 \times 6 = 2.4$ m^2. The spatially-averaged squared transfer mobility $\langle|Y_{\mathrm{r}}|^2\rangle$ is given as

$$\langle|Y_{\mathrm{r}}|^2\rangle = \frac{1}{L}\int_{-L/2}^{L/2}|Y_{\mathrm{r}}(x)|^2\mathrm{d}x = \frac{1}{L}\sum_{k=1}^{N_p}\Delta x\left|Y_{\mathrm{r},k}\right|^2 \tag{6-16}$$

where $Y_{\mathrm{r},k}$ is the rail mobility (this is the average of the railhead and the railfoot points) predicted by the coupled 2.5D-FE model spatially discretised in N_p positions along the rail with a spacing of 0.065 m. According to this approach, reflections from the ends of the 6 m length of rail are neglected. Although some reflections are present in the measurements, the comparison of point mobilities shown in **Figure 6-45** suggests the effect is rather limited.

The number of baseplates N used on the laboratory half slab track is eight. A single baseplate has a radiating area of $S_1 = 0.0247$ m^2, thus for all eight baseplates the surface area is $S_{\mathrm{bp}} = NS_1 = 8 \cdot 0.0247 = 0.1976$ m^2. The spatially-averaged squared transfer mobility $\left|Y_{\mathrm{bp}}\right|^2$ of the eight baseplates is given as:

$$\langle\left|Y_{\mathrm{bp}}\right|^2\rangle = \frac{1}{NS_1}\sum_{m=1}^{N_n} \Delta s\left|Y_{\mathrm{bp},m}\right|^2 \tag{6-17}$$

where $Y_{\mathrm{bp},m}$ is the baseplate velocity predicted by the 3D FE baseplate model by applying the railpad spring forces estimated by the coupled 2.5D FE track model. It, therefore, corresponds to a unit force on the rail. The area associated with each response position on the baseplate is $\Delta s = \Delta x \Delta y = 0.01 \cdot 0.01 = 10^{-4}$ m^2 and N_n is the total number of radiating nodes for the eight baseplates. The radiation radio for three baseplates calculated using the Rayleigh integral method (shown in **Figure 6-22 (a)**) was used for calculating the radiated power for the length of the measured half slab track.

The spatially-averaged squared transfer mobilities $\langle\left|Y_{\mathrm{bp}}\right|^2\rangle$ and $\langle|Y_{\mathrm{r}}|^2\rangle$ for the eight baseplates and the 6 m length of the rail obtained from the model are shown in **Figure 6-50** in both narrowband and one-third octave bands. From these values, the ratio of the baseplate response to the rail response $\langle\left|Y_{\mathrm{bp}}\right|^2\rangle/\langle|Y_{\mathrm{r}}|^2\rangle$ is calculated and shown in **Figure 6-51** in narrowband and in one-third octave band forms. The fact that the baseplate vibration is much smaller than that of the rail at low frequencies is consistent with the measured transmissibilities in **Chapter 5**.

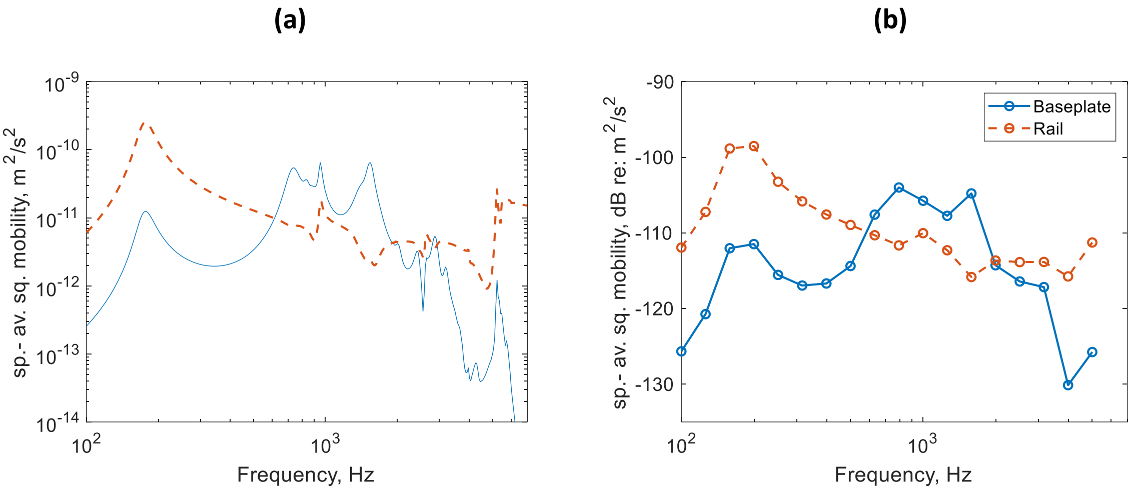

Figure 6-50 The predicted spatially averaged squared transfer mobilities for eight baseplates and the 6 m section of the rail, **(a)** in narrowband, **(b)** in one-third octave bands.

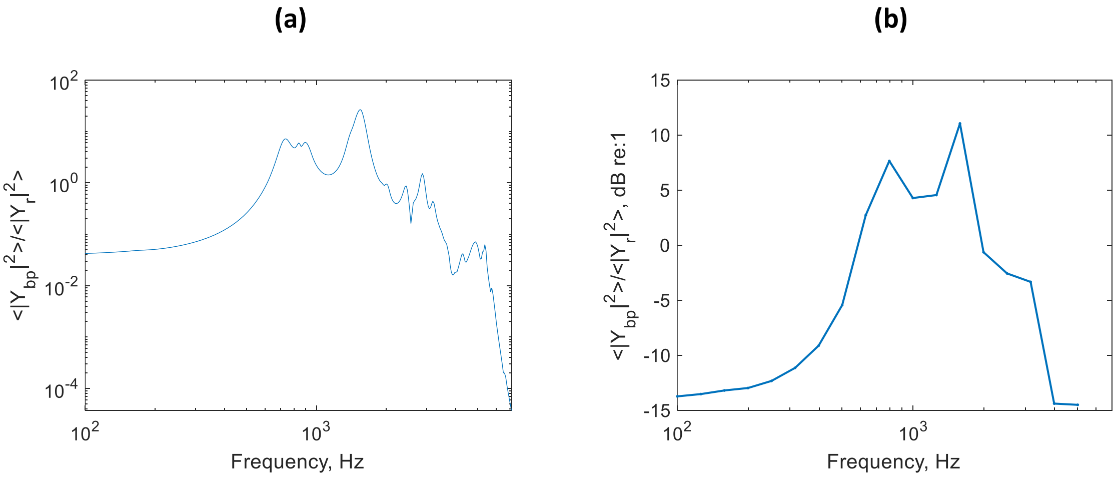

Figure 6-51 The ratio of spatially averaged squared transfer mobilities for eight baseplates and 6 m of rail: **(a)** in narrowband and **(b)** in one-third octave bands.

Figure 6-52 shows the comparison of the measured spatially-averaged squared transfer mobility of the rail $\langle |Y_{\mathrm{r}}|^2 \rangle$ measured from the slab track model in the reverberation chamber and that predicted by the coupled COMSOL and 2.5D FE model. A good agreement is seen between the measured and predicted results in terms of the overall trend. However, the model does not contain some of the peaks found in the measured data, and the measured data show levels slightly higher than the predicted ones. This is probably due to the finite length of the rail used in the measurements.

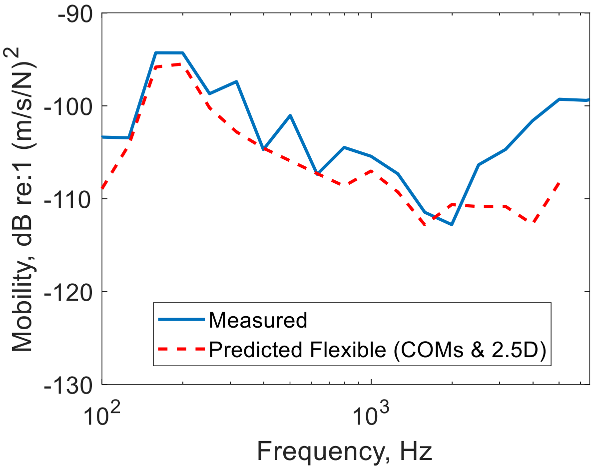

Figure 6-52 Comparison between the measured and predicted spatially-averaged squared transfer for eight baseplates and 6 m of rail in one-third octave.

Figure 6-53 shows the comparison between the measured and predicted average transmissibility of the baseplates relative to the 6 m rail. The results show good agreement between 160 Hz and 2500 Hz. For frequencies below 160 Hz and above 2500 Hz the measured values are higher than predicted ones.

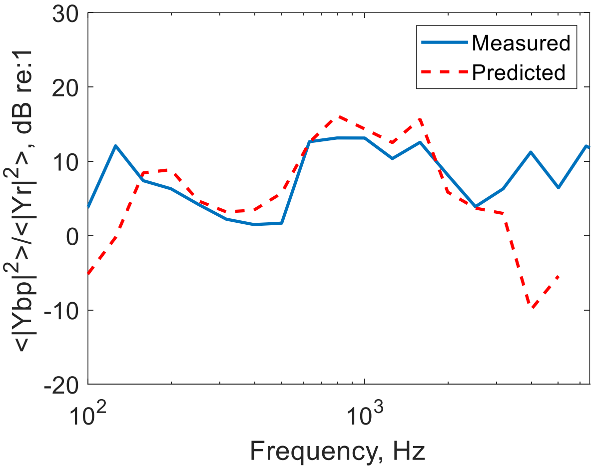

Figure 6-53 Comparison ratio of spatially averaged squared transfer mobilities for eight baseplates and 6 m of rail in one-third octave bands.

The model developed for the sound power of the baseplates (the Rayleigh integral model that uses the output from the 2.5D coupled vibration model) is based on an odd number of baseplates as it uses symmetry. However, the measured results here correspond to eight baseplates. Therefore, the sound power for eight baseplates is obtained as the mean of the sound power predicted for seven and nine baseplates. **Figure 6-54** shows the comparison for the radiated sound power predicted for eight baseplates calculated for a unit force on the railhead and of the rail calculated using the radiation ratio from the Timoshenko beam model [96]. Note for the baseplate radiated power the radiation ratio corresponds to three baseplates.

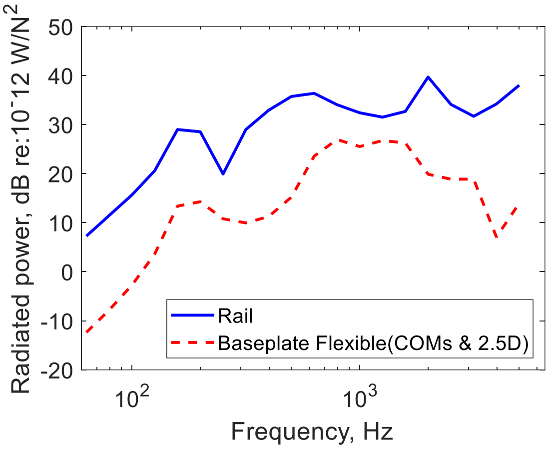

Figure 6-54 Radiated sound power predicted for a unit force on the rail using the radiation ratio of the rail from [96] and new developed model of the flexible baseplates.

The comparison of predicted sound power from the rail and the rail with the addition of the baseplate contribution is presented in **Figure 6-55**. The results indicate that the sound power of the baseplate has a negligible contribution to the total noise. In the measurements in **Figure 6-48** the baseplate noise has increased the combined noise by around 1 dB between 600 and 1600 Hz, suggesting that its contribution is 5-10 dB lower than the rail. **Figure 6-56** shows a comparison of the measured sound power for the 6 m rail clipped and the prediction of the combined rail and baseplate contribution.

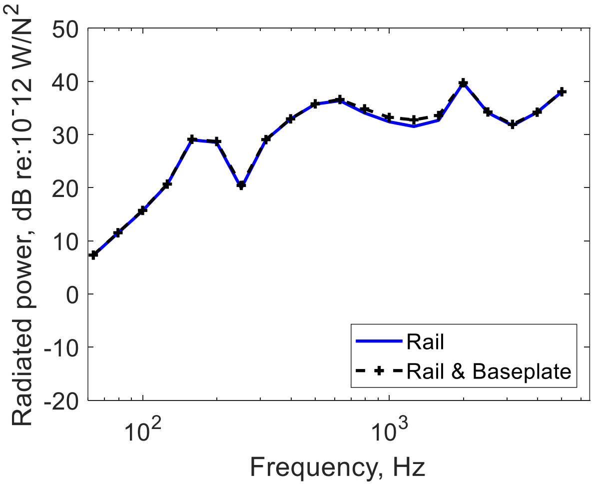

Figure 6-55 Comparison of predicted sound power from the rail and the rail with addition of the baseplate contribution.

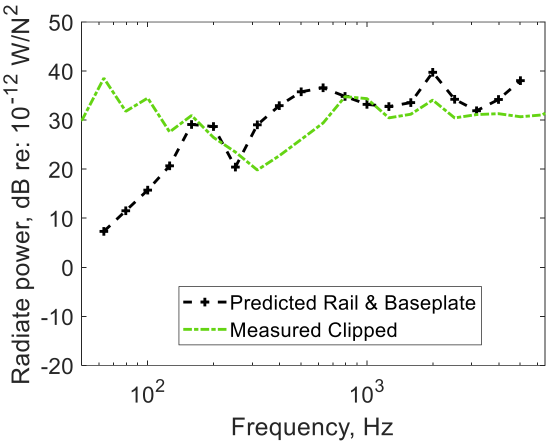

Figure 6-56 Comparison sound power of measured rail clipped and predicted from the total of the baseplate contribution for a unit force above the railhead.

6.4 Summary

The noise radiation from the baseplate has been modelled using a Rayleigh integral approach. It was found that the holes in the baseplate cause a reduction in the radiation ratio compared with a solid plate of the same size. The presence of the rail does not significantly affect the radiation ratio of the baseplate. The model is then used with the vibration obtained from the coupled 2.5D rail and 3D baseplate model developed in **Chapter 5**. It is shown that to obtain the radiation ratio, it is sufficient to consider three baseplates. The sound power from the baseplates is found to be smaller than predicted using a simple rigid mass model.

Measurements have been carried out in the reverberation chamber of a half-width section of slab track fitted with a 6 m section of rail and eight baseplates. The radiation ratio of an individual baseplate showed reasonable agreement with the prediction model. For the rail, good agreement was found with a previous 2D BE model. For the assembled track, the baseplate has been shown to have a minimal contribution to the total noise from the track for the configuration tested.

As shown in the previous chapters, using a stiff rail pad on a two-stage baseplate system will increase the rail decay rate, while selecting a soft lower pad will reduce the vibration transmission to the slab and the surrounding environment. Such a selection of pad stiffness will increase the vibration of the baseplate, but the findings of the current chapter show that this will not result in a significant increase in the total track noise.

In the next chapter, the effect of changing the parameters of the baseplate will be considered in terms of their effect on the total rolling noise.

Chapter 7 Noise sensitivity analysis for the two-stage baseplate fastening system

This chapter presents a study into the sensitivity of the predicted noise to changes in the two-stage baseplate fastening system. To minimise vibration transmission to the slab and the ground the overall stiffness should be kept as low as possible. This is mainly governed by the stiffness of the lower pad which is kept at 80 MN/m in the results of this Chapter. On the other hand, the stiffness of the rail pad and the mass of the baseplate affect the track decay rates and thereby the rolling noise. The study, therefore, focuses on the influence of those two parameters. The TWINS model is used here for the noise prediction and the overall assessment of the rolling noise but with the baseplate radiation introduced using the models developed in previous chapters.

First, however, the influence of the upper surface area of the baseplate is revisited. In **Chapter 6**, the radiated power from the baseplate was predicted using a model accounting for the holes in the baseplate, and it was shown that introducing these holes lowered the radiation ratio. However, when the baseplate is installed in the track, the holes are partially filled by the bolts and the rail clips. Therefore, the baseplate surface areas are modified to test the sensitivity to the size of these holes.

7.1 The effect of the surface areas of the baseplate

The effect of the vibrating surface areas of the baseplate that are taken into account is studied by modifying the size of the holes in the Rayleigh integral model of the baseplate used in the previous chapter. The baseplate is illustrated in **Figure 7-1 (a)**. **Figure 7-1** (**b**) represents the source area in the original Rayleigh integral model of the baseplate used in **Chapter 6**. Two modified configurations are considered here. In the case shown in **Figure 7-1** (**c**) the full surface area of the baseplate is considered with no holes, whereas in the case shown in **Figure 7-1** (**d**) the holes are partially filled. This is intended to account for some of the areas that were not previously included such as a clipping ear and other small parts around the bolting and clipping area. The corresponding surface areas of the three models are 0.0194, 0.0283 and 0.0372 m^2; compared with the original model in **Figure 6-1** the modified cases represent an increase in area of 46% and 92%.

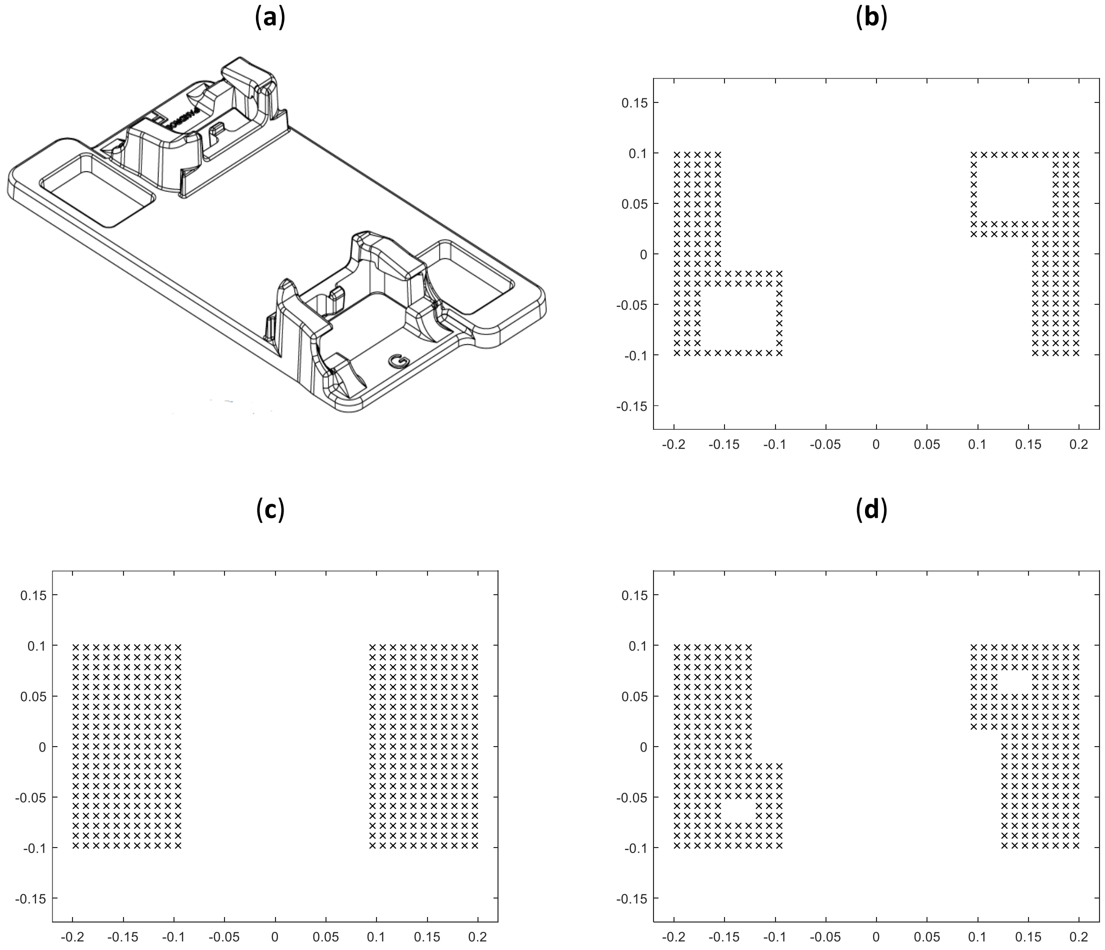

Figure 7-1 View of the two-stage baseplate showing (**a**) the actual baseplate, (**b**) the nodes of the simplified model used in **Chapter 6**, (**c**) full vibrating surface, (**d**) vibrating surface with reduced sized holes.

The radiation ratio and radiated power are calculated for these three cases. Only the Rayleigh integral model is modified; the vibration amplitudes of the various regions are allocated according to the FE model of the baseplate developed in **Chapter 5**. The Rayleigh integral models are based on three baseplates in each case; as shown in the previous chapter, it is sufficient to include three baseplates in determining the radiation ratio. The sound power is also calculated for three baseplates. The results are shown in **Figure 7-2**, which indicates that by increasing the baseplate surface areas by 46% the radiated ratio has increased by 2 dB at low frequency and the radiated power by 4 dB. When the surface areas are increased by 92%, the radiated ratio has increased by 3 dB and the radiated power by 6 dB (these increases correspond to $10\log_{10}(\text{surface area})$ and $20\log_{10}(\text{surface area})$).

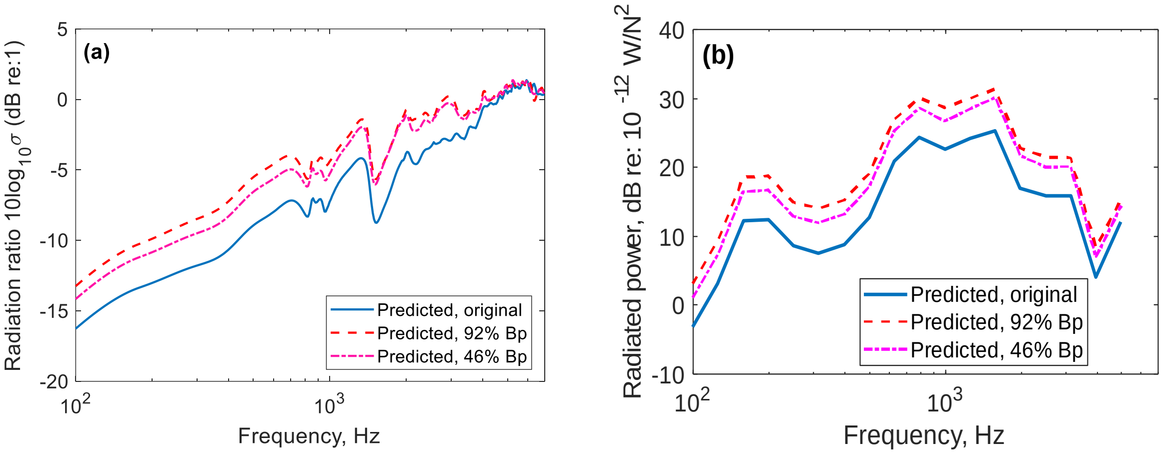

Figure 7-2 Effect of changing baseplate surface area; results shown for three baseplates: (**a**) radiation ratio and (**b**) radiated power for a unit mean-square force on the rail.

7.1.1 Rolling noise predictions

To understand the effect of the baseplate design on railway rolling noise, a Matlab implementation of the TWINS prediction model [1, 18, 19] is used. In the TWINS model, the track noise is predicted using either measured or predicted TDRs as an input. Here, the baseplate noise contribution is assessed using both measured TDRs from the Doncaster test tack (reported in **Chapter 4**) and predicted TDRs from the 2.5D FE model of the rail coupled to the FE model of the baseplate (presented in **Chapter 5**). **Table 7-1** reports the parameters used in TWINS and the 2.5D model for the track. Other parameters used in the TWINS model are reported in **Table 7-2**. All three baseplate models are used here for the assessment.

Table 7-1 Track properties used in the models that represent the measured track in Doncaster

Rail type	UIC60E1
Rail Young's modulus (E)	210 GPa
Rail Poisson's ratio (v)	0.3
Rail density (ρ)	7850 kg/m^3
Rail mass per unit length	60 kg/m
Rail vertical bending stiffness	6.42 MN·m^2
Rail lateral bending stiffness	1.07 MN·m^2
Vertical Timoshenko shear coefficient	0.4
Lateral Timoshenko shear coefficient	0.4
Rail vertical loss factor	0.02
Rail lateral loss factor	0.02
Pad	
Railpad vertical stiffness (measured)	310 MN/m
Railpad lateral stiffness (estimated)	62 MN/m
Railpad vertical damping loss factor (measured)	0.1
Railpad lateral damping loss factor (estimated)	0.1
Lower pad vertical stiffness (measured)	80 MN/m
Lower pad lateral stiffness (estimated)	80 MN/m
Lower pad vertical damping loss factor (measured)	0.2
Lower pad lateral damping loss factor (estimated)	0.2
Baseplate	
Baseplate mass	6.2 kg
Baseplate spacing	0.65 m
Baseplate length	0.404 m
Baseplate width	0.206 m
Baseplate height	0.015 m

Table 7-2 Typical parameters used in TWINS

Parameter	Value and units
Ground height below railhead	1.0 m
Ground flow resistivity	3 x 10^3 Pa.s/m^2
Microphone height above the railhead	1.5 m
Microphone distance from rail	7.5 m
Vehicle speed	120 km/h
Vehicle length	20 m
Wheelset mass	1100 kg
Wheel class	378

The rail mobility obtained from TWINS and that obtained from the 2.5D FE model are compared in **Figure 7-3**, **(a)** magnitude and **(b)** phase for excitation at the railhead above the baseplate. The results are slightly higher at lower frequencies for the 2.5D FE model.

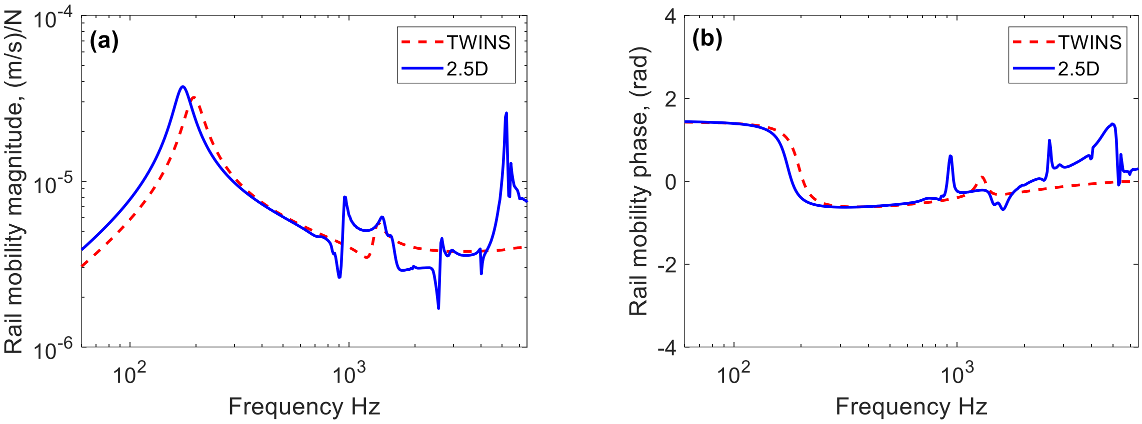

Figure 7-3 Comparison of the rail mobilities between Timoshenko beam model and coupled 2.5D-FE model: (**a**) mobility magnitude (**b**) phase of the mobility.

The rolling noise components from the train passage obtained from TWINS are presented as sound power per unit roughness for the rail and the wheel. However, for the contribution of the baseplate, the sound power is first obtained per unit force from the coupled 2.5D/3D FE model and the Rayleigh integral calculation for the baseplate. The baseplate sound power obtained from these models is converted to power per unit roughness by multiplying it by the vertical contact force obtained from the TWINS model (Timoshenko beam model), which is shown in **Figure 7-4**. The lateral force is not used as it is much smaller than the vertical one and therefore has a negligible effect. The various steps are as follows:

$$Y_{\mathrm{bp1}} = \left[Y_{\mathrm{bp(FE)}}\right][F_{2.5\mathrm{D}}] \tag{7-1}$$

$$V_{\mathrm{bp2}} = \left[Y_{\mathrm{bp1}}\right][F_{\mathrm{ct}}] \tag{7-2}$$

$$W_{\mathrm{bp(8)}} = \sigma_{\mathrm{bp(3)}}\rho_0 c_0 S_{\mathrm{bp(8)}} \left\langle \left|Y_{\mathrm{bp2(8)}}\right|^2 \right\rangle \tag{7-3}$$

where $Y_{\mathrm{bp(FE)}}$ is the spatially-averaged mobility of the baseplate due to a unit force at the centre of the baseplate, Y_{bp1} is spatially-averaged baseplate velocity for a unit force at the railhead, $[F_{2.5\mathrm{D}}]$ is the set of interaction forces from the 2.5D model acting on the baseplate calculated for a unit force at the railhead, F_{ct} is the wheel/rail contact force per unit roughness at the railhead (obtained from TWINS), V_{bp2} is the spatially-averaged velocity of the baseplate for a unit roughness. $\sigma_{\mathrm{bp(3)}}$ is the radiation ratio for three baseplates, $S_{\mathrm{bp(8)}}$ is the surface area of eight baseplates, $\rho_0 c_0$ is the acoustic impedance of air, and $W_{\mathrm{bp(8)}}$ is radiated sound power of the eight baseplates per unit roughness.

The calculated baseplate radiated power is added to the wheel and rail powers to give the total radiated power, as follows:

$$W_{\mathrm{Tot}} = W_{\mathrm{r}} + W_{\mathrm{wh}} + W_{\mathrm{bp(8)}} \tag{7-4}$$

where W_{Tot} is the total radiated power per unit roughness, W_{r} is the rail radiated power per unit roughness, and W_{wh} is the wheel radiated power per unit roughness. All sound powers correspond to a single wheel and the associated track vibration and are expressed in dB for a unit roughness. Finally, a roughness spectrum in dB from Fishbourne, UK, measured in 2013 (renewed track) is added to these results.

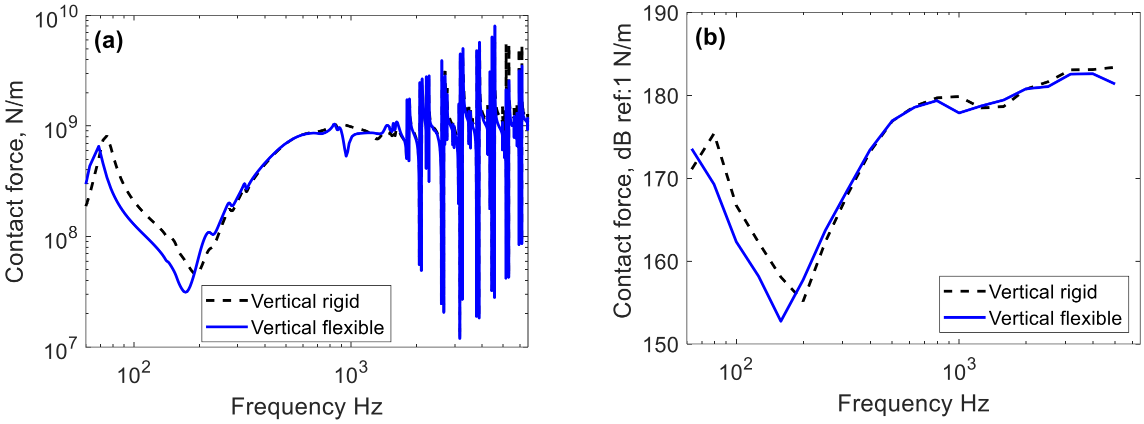

Figure 7-4 Contact force for the interaction between rail and wheel for a unit roughness (a) narrowband and (b) third octave band.

The radiation ratios obtained after increasing the surface areas of the baseplate are then used to calculate the sound power for a unit force at the railhead (above the baseplate) for the 121 baseplates. These are then implemented in the TWINS model for predicting the radiated power for the baseplate and this is combined with the radiated power from the rail to find the total noise from the track. **Figure 7-5** shows the results, (**a**) using the original representation of the baseplate with large holes, (**b**) for the baseplate with reduced hole size (increasing the vibrating the surface area by 46%), (**c**) for the baseplate with no holes (increasing the vibrating surface area by 92%) and (**d**) comparison of baseplate power contribution with increase in area. In terms of overall A-weighted sound power level, these results indicate that the contribution of the baseplate sound power is 12 dB lower than that of the rail for the original case, 8 dB lower for increased surface area by 46% and 6 dB lower for increased surface area by 92%.

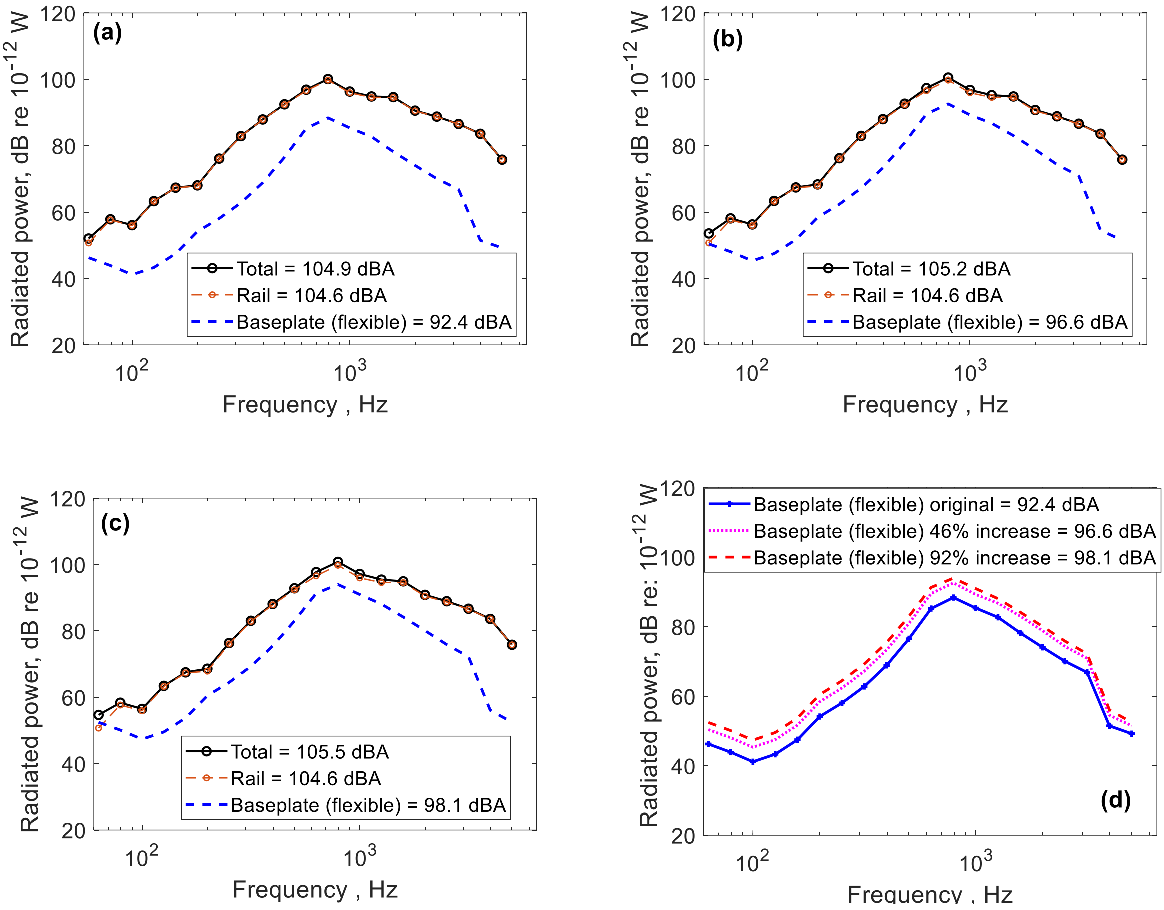

Figure 7-5 Comparison of total radiated power from the track: (**a**) using the original representation of the baseplate with bigger holes, (**b**) the holes size reduce by increasing the vibrating the surface area by 46%, (**c**) the holes reduced in size, increasing the vibrating surface area by 92% and (**d**) comparison for baseplate power contribution with increase in area.

The results show that by increasing the baseplate surface area by 46% to account for some of the areas that were not previously included, a higher radiated power is obtained. It can be considered that this is a closer representation of the actual surface areas that vibrate in the baseplate in an in-situ situation. Therefore, the baseplate with the holes partially filled shown in **Figure 6-1** (**b**) is used in the following sections in evaluating the rolling noise.

Figure 7-6 presents the predicted results for the rail, the wheel, the baseplate, and the total radiated power estimated using the properties in **Table 7-1** and **Table 7-2** along with the measured TDR from the Doncaster test track for railpad No.1. The results demonstrate that the flexible baseplate has a no significant contribution to the overall noise levels.

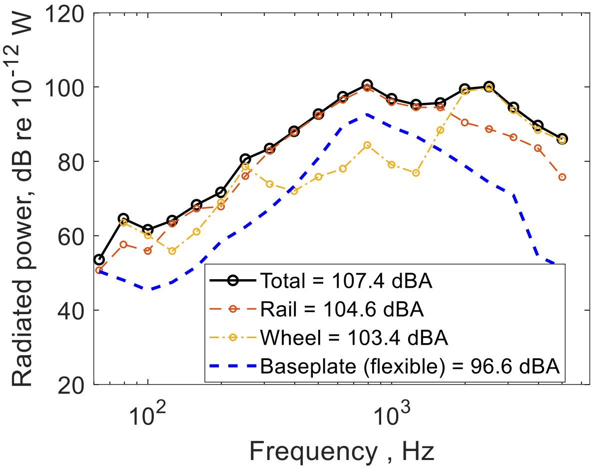

Figure 7-6 A-weighted sound power for the rail, the wheel, the baseplate and the total.

In the current configuration of the TWINS model, the baseplate can be represented as a rigid mass between two springs; for comparison with the above results, this is implemented here using the baseplate dimensions in **Table 7-1**. The predicted radiated power obtained is shown with the red line in **Figure 7-7**. This is compared with radiated power obtained from the newly developed baseplate model that accounts for the baseplate as a flexible body (2.5D/3D FE model). The results presented in **Figure 7-7** show that for the rigid mass model (TWINS model), the baseplate has higher levels of noise for frequencies up to 2 kHz whereas above this frequency the results from the two models are similar. The results for the flexible body correspond to the partially reduced hole size (see **Figure 7-1** (**d**)).

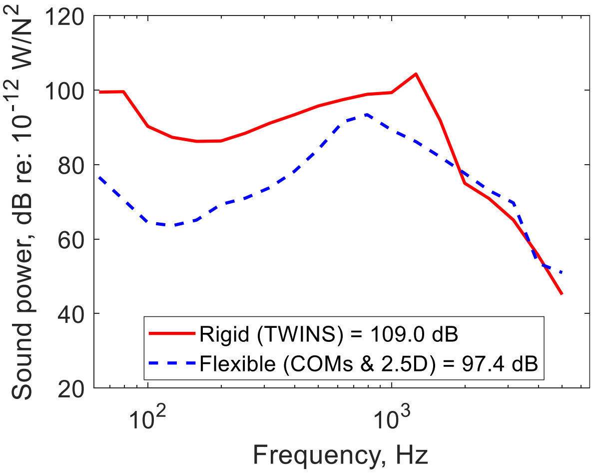

Figure 7-7 Comparison of the baseplate radiated power represented as a rigid mass and a flexible plate.

7.2 The effect of the baseplate thickness

The current design of Pandrol baseplate studied in this thesis has evolved from earlier designs that were considerably heavier. This has been done to minimise unit costs by reducing the mass. Nevertheless, the baseplate mass can act as a tuned absorber attached to the rail that increases the TDR. A lower mass may therefore have disadvantages. In this section, the influence of the baseplate mass is studied using the models developed in this thesis.

The effect of changing the thickness is studied using the FE model of the baseplate. The original model from **Chapter 5** shown in **Figure 7-8** (**a**) is modified simply by increasing its thickness by a factor of 2 (**Figure 7-8** (**b**)) and 4 (**Figure 7-8** (**c**)). The corresponding masses are 6.2 kg, 12.4 kg, and 24.8 kg. The new predicted mobilities from the FE models are then implemented in the coupled 2.5D/3D model. The radiated power, TDR and prediction noise levels are compared for each model.

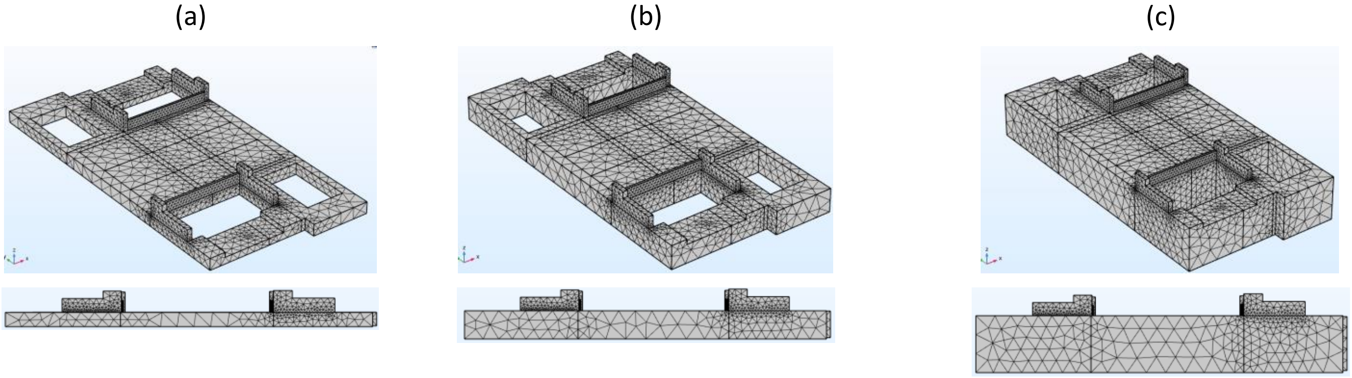

Figure 7-8 Baseplate FE model: (**a**) original baseplate, (**b**) thickness of the original baseplate is two times (2H) and (**c**) four times the original baseplate thickness (4H).

7.2.1 Vibration for different baseplate thickness

The magnitude and phase of the driving point mobility of the baseplate for different thicknesses with impact at the centre of the baseplate are presented in **Figure 7-9**. By increasing the thickness of the baseplate, both mass and stiffness increase, and the vibration response has decreased. Moreover, the fundamental mode of the baseplate has shifted to lower frequencies, whereas the bending modes shift to higher frequencies. **Figure 7-10** presents the spatially averaged mobility of the baseplate for a unit force at the railhead above the baseplate (**a**) narrowband and (**b**) third octave band. These are shown as the square root of the mean square mobilities. The result shows that as the thickness of the baseplate increases the vibration of the baseplate at frequencies below 600 Hz increases, whereas it decreases at frequencies above 600 Hz. The predicted mobilities are then used in the 2.5D/3D FE model to predict the TDR of the track for each baseplate case. The results are shown in **Figure 7-11**. It can be seen that, for the larger thicknesses, the TDR increases in the frequency range 500-800 Hz due to the increased influence of the dynamic absorber effect. This can be beneficial in reducing the noise from the rail. However, the TDRs reduce at frequencies above 1 kHz.

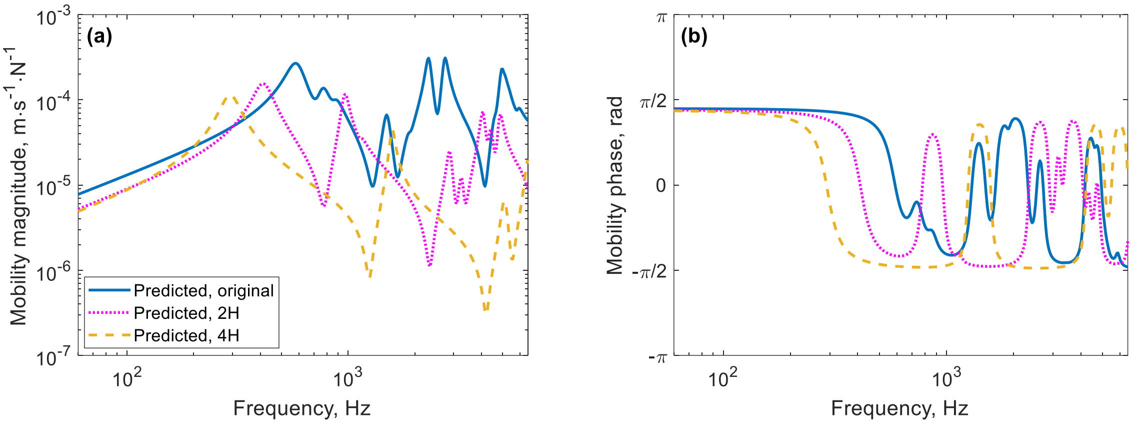

Figure 7-9 Comparison between the driving point mobilities predicted from 3D FEM of the baseplate for different thickness due to the impact at the centre of the baseplate: (**a**) magnitude and (**b**) phase: original, double (2H) and quadruple (4H).

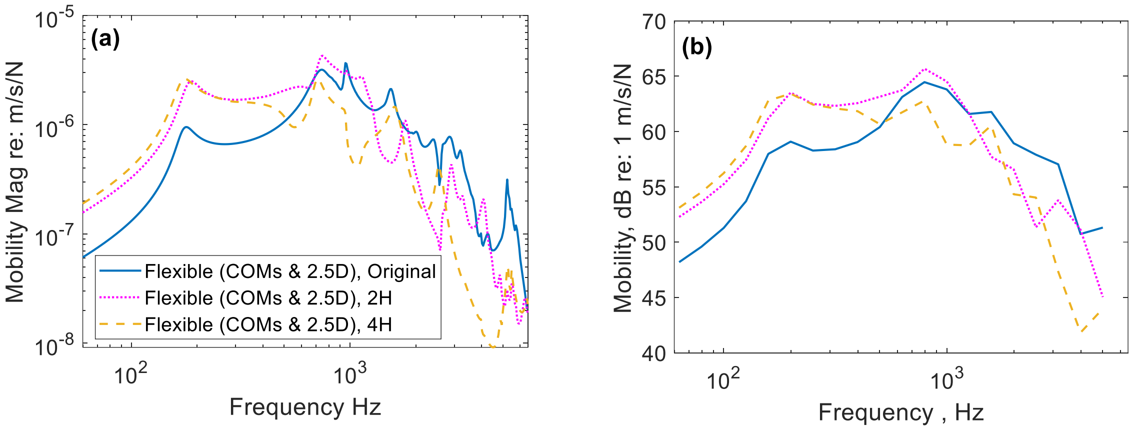

Figure 7-10 Comparison between the spatially averaged baseplate squared mobilities for a unit force at the railhead above the baseplate for different thickness of the baseplate: (**a**) in narrowband and (**b**) third octave band: original, double (2H) and quadruple (4H).

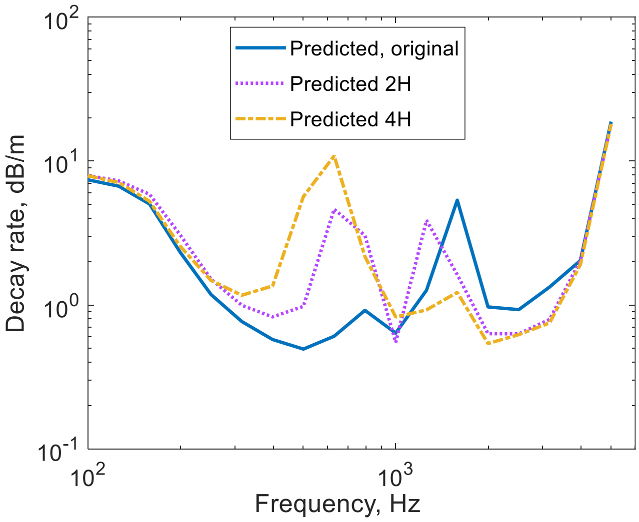

Figure 7-11 TDR predicted from the 2.5D/3D FE model for railpad No.1 with different baseplate thicknesses: original, double (2H) and quadruple (4H).

Figure 7-12 presents the ratio of the average squared velocity between the baseplate and the rail. These results show that by increasing the thickness of the baseplate, the vibration of the exposed parts of the baseplate has increased significantly at lower frequencies. This is because the thinner baseplate can flex allowing the central part to move more than the outer part, whereas for the thicker ones this is no longer the case. However, the vibration at higher frequencies is reduced by increasing the thickness.

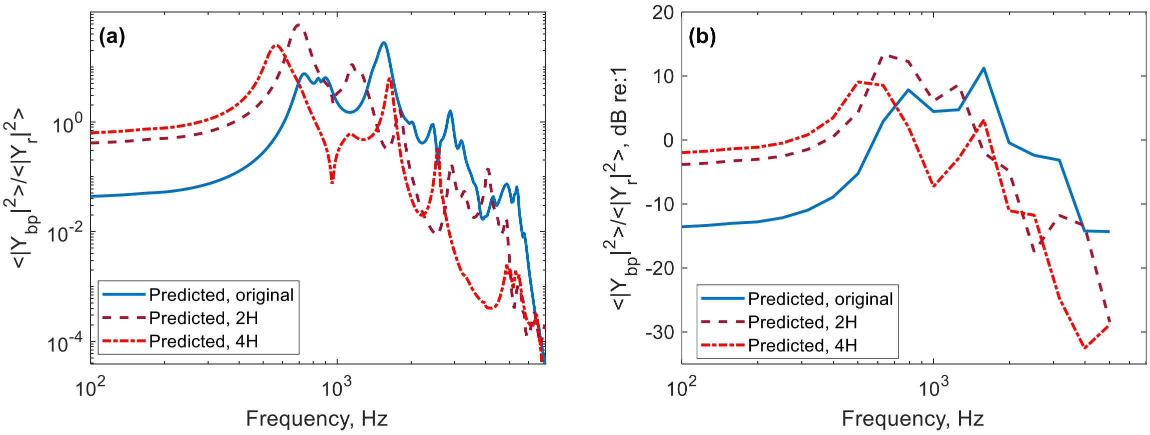

Figure 7-12 Comparison of the mobility ratio between the baseplate and the rail: (**a**) in narrowband and (**b**) in one third-octave band: original, double (2H) and quadruple (4H).

7.2.2 Radiated sound power comparisons for different baseplate thickness

The Rayleigh integral model shown in **Figure 7-1** (**d**) with the partially filled holes is used in the predictions of sound radiation ratio. The radiation ratios for the three thicknesses are presented in **Figure 7-13**. There is minimal influence at low frequencies, but between 700 Hz and 4000 Hz, the heavier baseplates have higher radiation ratios.

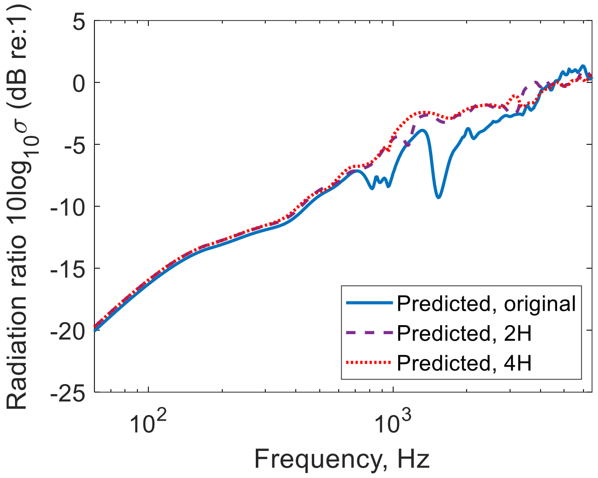

Figure 7-13 Comparison between the radiation ratios for the baseplate with different thickness: original, double (2H) and quadruple (4H).

The radiated sound power predicted for the different baseplate thickness is shown in **Figure 7-14** for a unit force on the rail. These results correspond to a track with eight baseplates as used in the measured results in **Section 6.3**. As the baseplate thickness is increased, a higher radiated power at the baseplate is obtained below 600 Hz and a lower radiated power is found above 600 Hz.

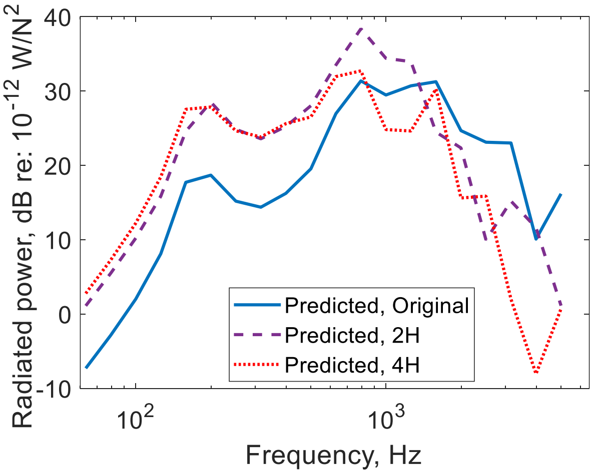

Figure 7-14 Comparison of the radiated power from 8 baseplates per unit mean square force on the rail for the baseplates with different thickness: original, double and quadruple.

7.2.3 Rolling noise predictions

The contribution of the noise from the baseplates to the total rolling noise is predicted following the procedure described in Section **7.1.1**. The results are presented in **Figure 7-15** for (**a**) the rail, (**b**) the baseplates and (**c**) the total sound power including the wheel. All results are given for railpad No.1 properties.

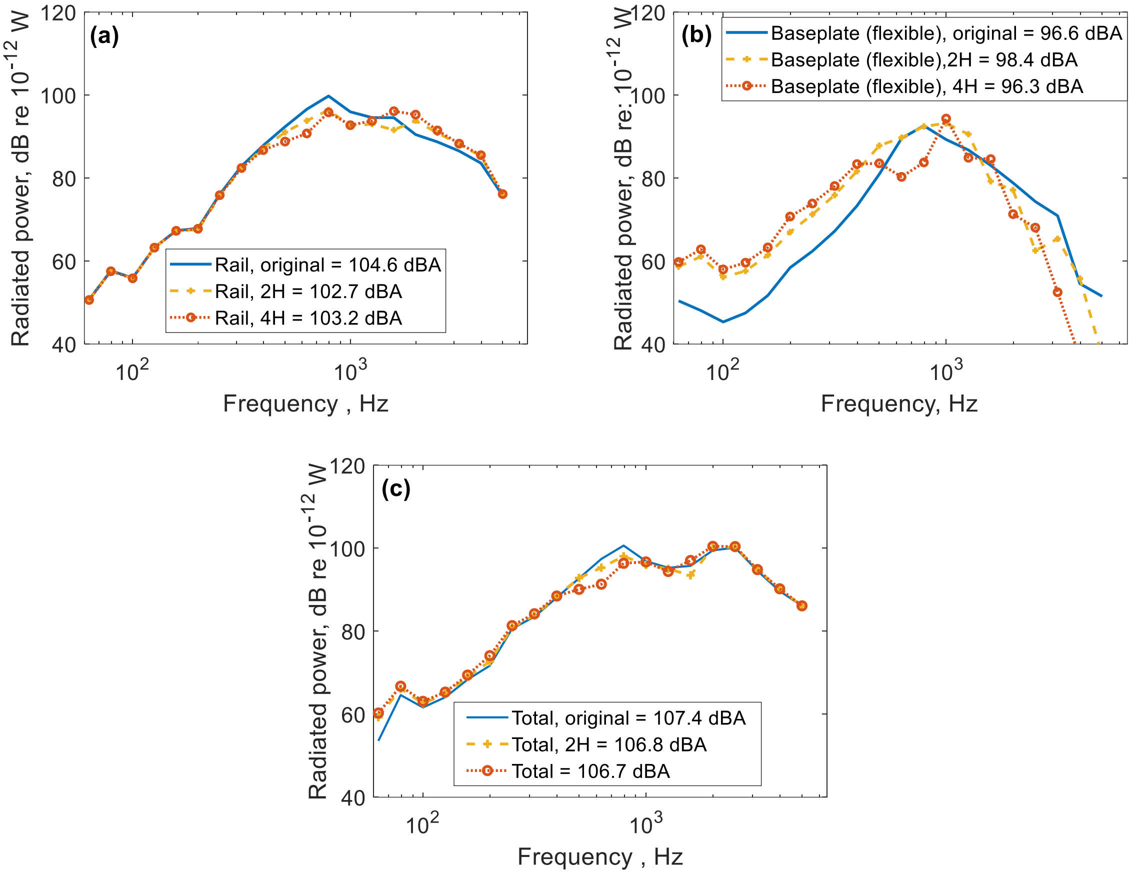

Figure 7-15 Comparison of the predicted radiated power using different thickness of the baseplate for railpad No1: (**a**) rail, (**b**) baseplate and (**c**) total.

The predictions show that by increasing the thickness of the baseplate, the rail noise is reduced by up to 2 dB at frequencies between 300 Hz and 1.25 kHz, due to the change in TDR. Conversely, the noise from the baseplate itself is increased with increasing thickness at frequencies below 500 Hz by up to 12 dB and reduced with increased thickness at frequencies above 500 Hz by up to 10 dB. The total noise is reduced by up to about 3 dB between 500 Hz and 1 kHz. The summary of the overall sound power levels is given in **Table 7-3**. Although thicker baseplates have some advantage in reducing the noise levels, the differences in overall noise level are quite small and would not justify the increase in materials and cost.

Table 7-3 Summary of predicted radiated power for the three thicknesses

Thickness	Rail dBA	Baseplate dBA	Wheel dBA	Total dBA
Original	104.6	96.6	103.4	107.4
Double (2H)	102.7	98.4	103.4	106.8
Quadruple (4H)	103.2	96.3	103.4	106.7

7.3 The effect of railpad stiffness

The impact of railpad stiffness is investigated in this section using the measured dynamic stiffness of the railpads presented in **Chapter 3**. In **Chapter 5** the rail mobilities and TDRs predicted with the coupled 2.5D FE model were compared with the measurements taken in Doncaster (presented in **Chapter 4**) for four different values of rail pad stiffness (1200, 528, 310 and 120 MN/m), showing good agreement. Here, the same values of pad stiffness are considered, together with a lower and a higher value (50 and 2500 MN/m); the stiffness of the lower pad is kept as 80 MN/m throughout. These results are used to assess the dependence of the noise contribution from the track components on pad stiffness.

7.3.1 The effect of railpad stiffness on track noise

Figure 7-16 shows the predicted driving point mobility from the 2.5D/3D coupled FE model for the six values of railpad stiffness. **Figure 7-17** shows the corresponding TDR results. The TDR comparison in **Figure 7-17** shows that by decreasing the railpad stiffness, a low TDR is obtained, which will result in higher rolling noise. Nevertheless, the low railpad stiffness will isolate the vibration transmitted to the track structure and the ground. On the other hand, by increasing the railpad stiffness, the TDR is increased at frequencies below 500 Hz and at higher frequencies, above 1.6 kHz.

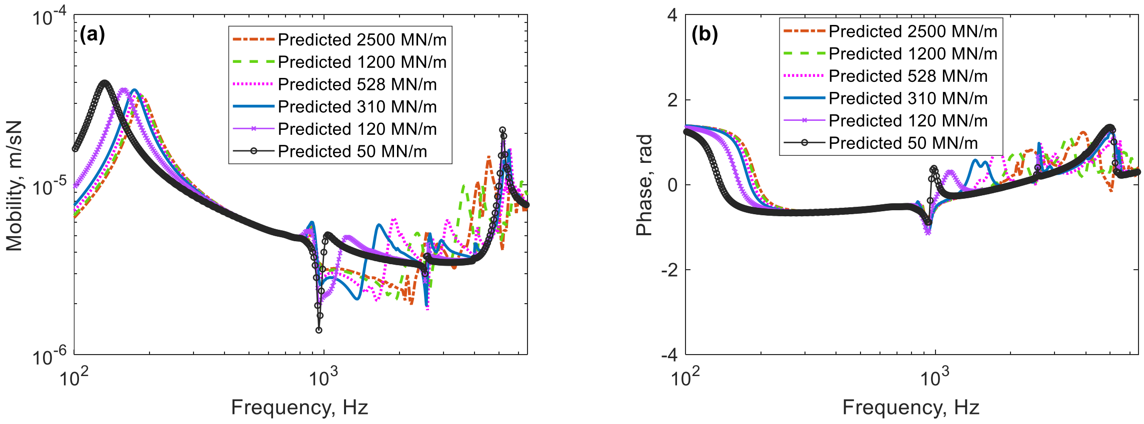

Figure 7-16 Comparison for the driving point mobilities from the coupled 2.5D-FE model for different railpad stiffness: (**a**) magnitude and (**b**) phase.

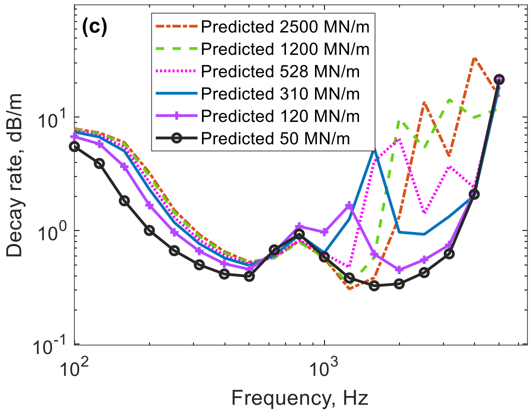

Figure 7-17 Comparison of the TDR predicted from the coupled 2.5D-FE model for different railpad stiffness.

7.3.2 Noise comparison

The noise radiated during a train passage is predicted using the approach described in Section **7.1.1** for the same six values of railpad stiffness. Results are presented as radiated sound power in **Figure 7-18** for (**a**) the rail (**b**) the baseplates and (**c**) the total (including the wheel). A summary of the sound power results for rail, baseplate, wheel and total for different values of railpad stiffness are presented in **Table 7-4**. The results show that by having a stiff railpad, the baseplate noise contribution is increased at frequencies below 300 Hz and high frequencies above 800 Hz. However, the railpad stiffness has the opposite effect on the rail noise contribution. Only a small increase is found for the total noise. From this assessment, based on a lower pad stiffness of 80 MN/m, a railpad stiffness of around 500 MN/m can be considered as the optimum value in terms of noise radiation from the track as shown in **Figure 7-19**.

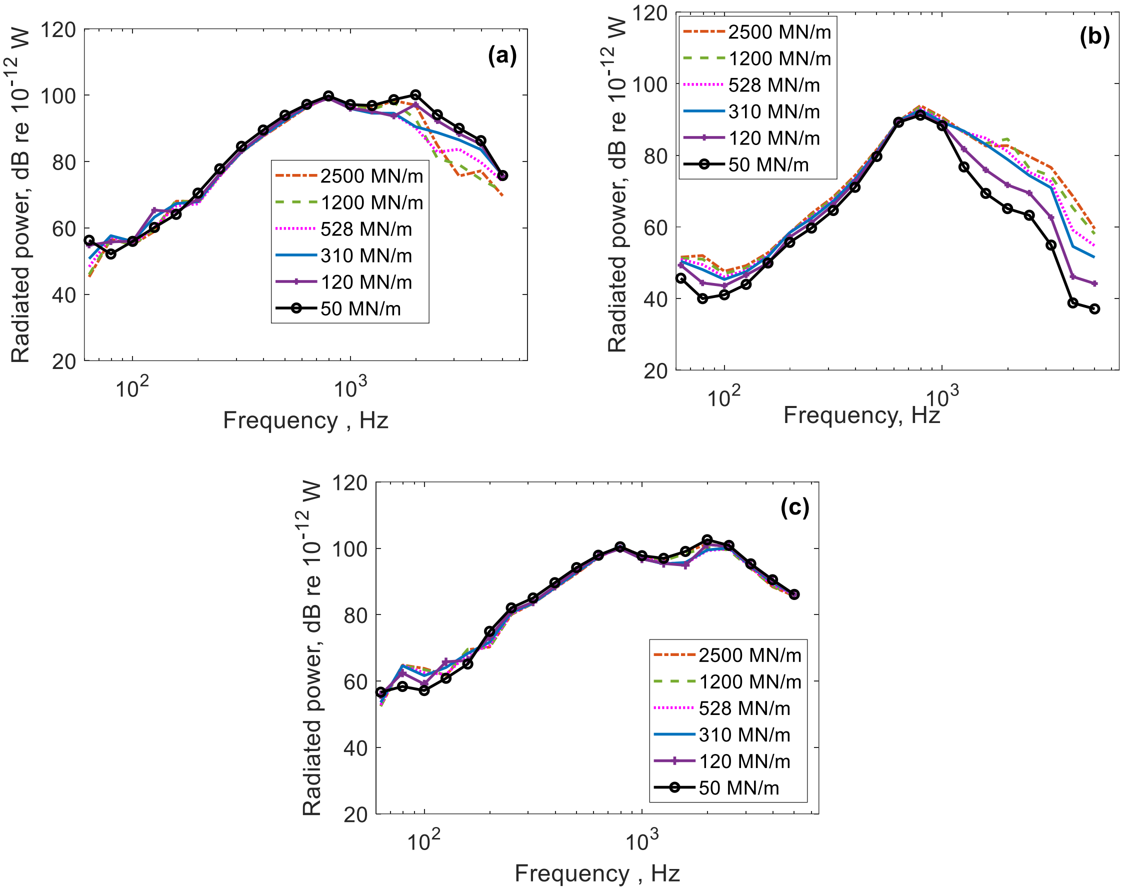

Figure 7-18 Comparison of the predicted radiated sound power using different stiffnesses of the railpad: (**a**) rail, (**b**) baseplate and (**c**) total.

Table 7-4 Summary of prediction radiated power for different stiffness

Stiffness (MN/m)	**Rail dBA**	**Baseplate dBA**	**Wheel dBA**	**Total dBA**
2500	105.6	97.5	103.7	108.1
1200	105.1	97.3	103.4	107.7
528	104.3	96.9	103.3	107.3
310	104.6	96.6	103.4	107.4
120	105.2	95.3	103.5	107.7
50	107.0	94.8	103.5	108.8

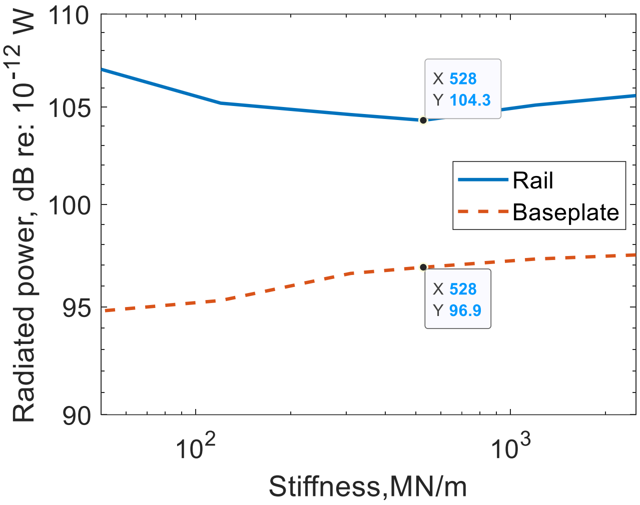

Figure 7-19 The overall predicted radiated power of the rail and baseplate against stiffness.

7.4 Summary

This chapter has focused on the sensitivity of the radiated noise to changes in the properties of the two-stage baseplate system.

If the thickness of the baseplate is increased, the rail noise is reduced between 200 Hz and 1 kHz due to changes in the TDR. Conversely, the noise from the baseplate itself is increased. The change in the total noise is quite small. As increased mass implies increased cost, the limited benefits of a larger baseplate are unlikely to justify a change in design.

It has been shown that for a stiff railpad, the baseplate noise is increased at low and high frequencies and with a softer railpad it is reduced. However, the railpad stiffness has the opposite effect on the rail noise contribution. Only a small effect is found for the total noise. From this assessment, based on a lower pad stiffness of 80 MN/m, it can be concluded that the optimum railpad stiffness should be around 500 MN/m.

Chapter 8 Conclusions and recommendations

8.1 Conclusions

The main aim in this thesis was to establish the influence of two-stage baseplate fastening systems on the overall railway rolling noise and to determine what are the key design parameters that affect the rolling noise. These aims were addressed by using laboratory and field measurements of vibration and noise as well as prediction models. This Chapter presents the main conclusions and outcomes of this research and suggests avenues for further study.

8.1.1 **Dynamic stiffness measurements**

An experimental setup for measuring the vertical dynamic stiffness of railpads and fastener systems based on the indirect method has been presented. The dynamic stiffness of several rail-fastening systems has been determined, including its dependence on frequency and preload. A mild dependence on frequency is found, whereas the preload leads to a marked increase in the stiffness. The loss factor is relatively unaffected by preload. Simple mass-spring models have been used to interpret the measured results and a good agreement is found between the measured data and these models. The effect of the rail clips has been shown to correspond an increase in preload of 20 kN which increases the dynamic stiffness of the railpad.

8.1.2 **Track vibration measurements**

Track vibration has been measured on a demonstration slab track with four different railpads fitted. The results have been presented as driving point mobilities, track decay rates and transfer mobilities at different baseplate locations. The results have shown that the stiffness of the railpad has a significant effect on the track decay rates. As the stiffness of the pad increases, higher TDR values are obtained at low frequencies (below about 500 Hz) and even greater values at high frequencies above 2 kHz. Conversely, for a softer railpad, the rail is better isolated from the fastener system. Therefore, it is more free to vibrate and radiate noise, while for a stiffer railpad the rail is more strongly coupled to the foundation and for this reason, it will have a higher TDR.

Higher values of TDR were measured in December than in July for low frequencies up to 500 Hz and high frequencies above 1 kHz. The reason for the differences is due to the changes in the railpad stiffness caused by temperature. The stiffness of the railpad is expected to have increased at low temperature [95] and the results from December are more consistent with those for a stiffer pad.

The vibration response of the baseplate has been investigated using in-situ and laboratory measurements. The results have shown that the baseplate is not vibrating uniformly, and a higher vibration response occurs near the railpad region compared with other peripheral locations of the baseplate.

8.1.3 Vibration modelling of baseplates

An FE model has been developed for the two-stage baseplate and tuned using laboratory measurements. For the unconstrained baseplate, a good agreement is found with the measured response apart from the frequency region around the second resonance.

The FE model is then considered on a distributed spring foundation, and measurements are used to determine the appropriate value of stiffness for the lower pad. The stiffness is found to depend strongly on the torque applied to the fixing bolts.

A published model of track vibration has been adapted to represent a slab track with two-stage baseplates. The rail is represented by a 2.5D FE model and is coupled to the 3D FE model of the baseplate using a receptance coupling method. Good agreement is found with measured mobilities and TDR, with most of the features in the measured data being well replicated by the newly developed model.

8.1.4 Noise radiation from the baseplate

To predict the noise radiation from the baseplates, a Rayleigh integral approach and a BE model are compared. Although more detail of the baseplate geometry can be included in the BE model, this has minimal effect on the results. It is more important to include the holes in the baseplate correctly as these reduce the radiation ratio and radiating area. The sound radiation from the bolt-heads and the baseplate clips has not been assessed but it is expected that these could contribute to a slight increase in total radiation ratio. When connected through the rail, the radiation ratio of the baseplates can be estimated reliably using just three baseplates.

Measurements in the reverberation chamber on a 6 m long half-width slab track section were used to assess the radiation of the baseplates and validate the numerical models. Overall, the baseplate has been shown to have a minimal contribution to the total noise from the track. Compared with the conventional model of the track in TWINS, that represents the baseplates as a rigid mass, improved predictions are obtained by including baseplate flexibility and modifying the radiation ratio to account for the holes. The rigid mass model considerably over-estimates the noise from the baseplates at frequencies up to 2 kHz.

The baseplate was shown not to contribute significantly to the total slab track noise radiation. Using a two-stage baseplate rail fastening system can therefore be effective for track noise reduction.

8.1.5 Noise sensitivity analysis for the two-stage baseplate

The effect of varying three different parameters of the baseplate system have been investigated: (i) modifying the vibrating surface area of the baseplate, (ii) modifying the mass and stiffness of the baseplate by increasing its thickness and (iii) varying the railpad stiffness. The effect on rolling noise levels has been studied using the TWINS model together with the newly developed models for the baseplate.

Increasing the thickness of the baseplate can lead to a reduction in the noise from the rail by up to 2 dB whereas the noise from the baseplate increases by a similar amount. However, the overall noise does not change significantly.

Using a stiff railpad, the noise from the baseplate is increased at low and high frequencies, whereas the stiffness of the railpad has the opposite effect on the noise from the rail. Nevertheless, the stiffness of the railpad has only a small effect on the total rolling noise. An optimum railpad stiffness is identified of around 500 MN/m, based on a lower pad stiffness value of 80 MN/m.

8.2 Recommendations for future research

The following recommendations are given for further research:

(i) Investigation of sound radiation from the bolt-heads and the baseplate clips should be carried out. Although these are very small areas they could contribute to an increase in total radiation ratio of the baseplate so it is required to be investigated and the model for sound calculation should be updated taking into account these areas.

(ii) It has been assumed that ground vibration is sufficiently attenuated by using a soft lower pad. It would be worthwhile to study ground vibration using the two-stage baseplate and to test the effect of varying upper and lower pad stiffnesses. If a softer lower pad is beneficial for ground vibration, its effect on rolling noise should be assessed.

(iii) The noise radiation from the track slab should be calculated and the effect of the baseplates on this noise should be evaluated.

(iv) The models for the baseplate developed here should be implemented in the TWINS software to allow further design studies to be carried out.

(v) The dependence of dynamic stiffness on preload and frequency could be introduced into the model and its effect on TDR and noise could be determined.

Appendix A Dynamic stiffness of additional specimens

A.1 Additional measured specimens

As described in **Chapter 3**, Section **3.6**, additional samples were available for testing as detailed in **Table A-1** below, and the results for dynamic stiffness and loss factor are also presented from **Figure A-2** to **Figure A-11**.

Table A-1 The details of extra the tested resilient elements

No.	Test specimen and material	Type (pad width)	Test details
A-1	NR Studded pad	Pandrol 13300 (150 mm)	On its own
A-2	EVA studded pad	Pandrol 13618 (150 mm)	On its own
A-3	EVA studded pad	Pandrol 7850 (150 mm)	On its own
A-4	NR Studded pad	Pandrol 6650 (150 mm)	On its own
A-5	NR Striped pad	Vossloh 139 (150 mm)	On its own
A-6	NR Striped pad	Vossloh 900 (150 mm)	On its own
A-7	NR plain pad	Unknown CDM-64 (150 mm)	On its own
A-8	EVA plain pad	SBB Sample 1 (180 mm)	On its own
A-9	NR striped pad	SBB Sample 2 (180 mm)	On its own
A-10	NR plain pad	SBB Sample 3 (160 mm)	On its own
A-11	NR plain pad	SBB Sample 4 (160 mm)	On its own
A-12	NR plain pad	SBB Sample 5 (180 mm)	On its own
A-13	NR grooved pad	Semperit pad (190 mm)	On its own
A-14	Single-stage baseplate	Pandrol 404 by 206 by 19.4 mm	A single-stage system with Pandrol pad No.3
A-15	Single-stage baseplate	Pandrol 404 by 206 by 19.4 mm	With plastic isolator beneath the baseplate no railpad fitted
A-16	Two-stage baseplate only	Pandrol 404 by 206 by 15 mm	With no lower pad or railpad

No.	Test specimen and material	Type (pad width)	Test details
A-17	NR Lower pad for two-stage	Type A This is a single stud pad with International Rubber Hardness Degree (IRHD) of 70	Two-stage system with no railpad
A-18	NR Lower pad for two-stage	Type B, This is a double stud pad with International Rubber Hardness Degree (IRHD) of 62	Two-stage system with no railpad
A-19	NR Lower pad for two-stage	Type C This is a single stud with International Rubber Hardness Degree (IRHD) of 75	Two-stage system with no railpad
A-20	NR Lower pad for two-stage	Type D This is a double stud with International Rubber Hardness Degree (IRHD) of 64	Two-stage system with no railpad
A-21	NR Lower pad for two-stage	Type E This is a single stud with International Rubber Hardness Degree (IRHD) of 65	Two-stage system with no railpad
A-22	NR Lower pad for two-stage	Type F This is a double stud with International Rubber Hardness Degree (IRHD) of 60	Two-stage system with no railpad
A-23	Steel plate sandwiched between two layers of rubber NR	Pandrol 3-in-1 system -FCA (see **Figure A-1** (**2**) (210×150×22.5 mm)	Whole assembly
A-24	NR Striped pad	China Baseplate Type-A railpad	On its own
A-25	NR Lower pad with China baseplate Type-A	China Baseplate Type-A with lower pad	
A-26	Whole assembly	China Baseplate Type-A with lower pad and railpad	
A-27	NR Striped pad	China Baseplate Type-B railpad	On its own
A-28	China baseplate Type-B	China Baseplate Type-B	On its own
A-29	Whole assembly	China Baseplate Type-B with railpad	

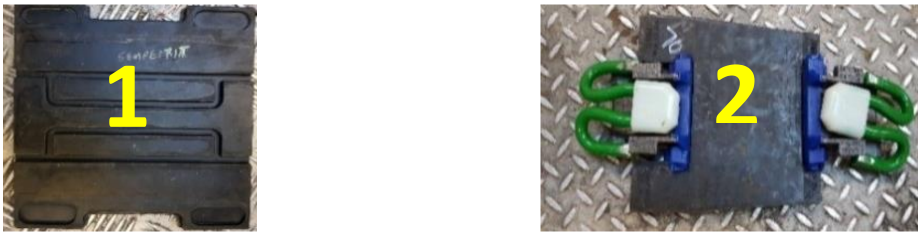

Figure A-1 (**1**) railpad specimens (No. A-13), (**2**) FCA fastener system No. A-23.

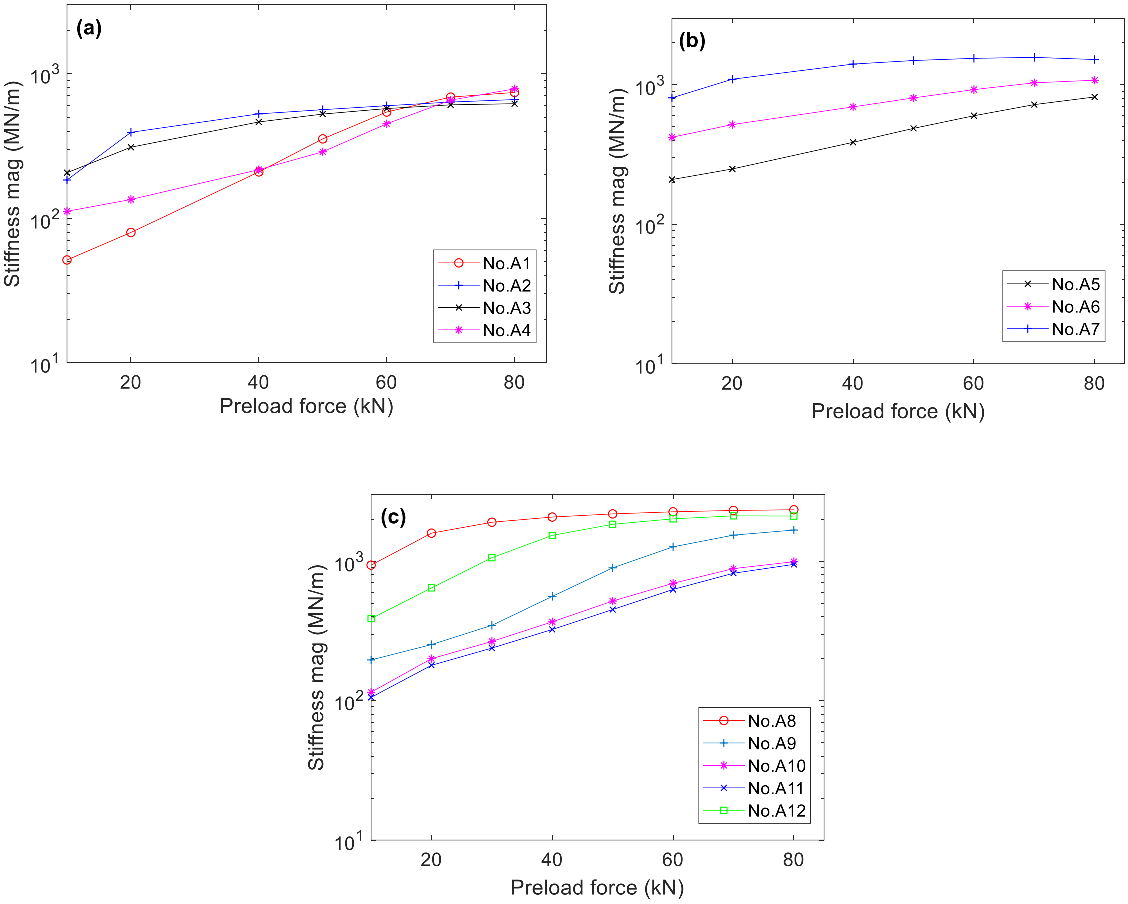

Figure A-2 Dynamic stiffness magnitude at 300 Hz plotted against static preload: (**a**) No.A1-A4 (Pandrol), (**b**) other available pads (No.A5-A7), (**c**) No. A8-A12 (SBB).

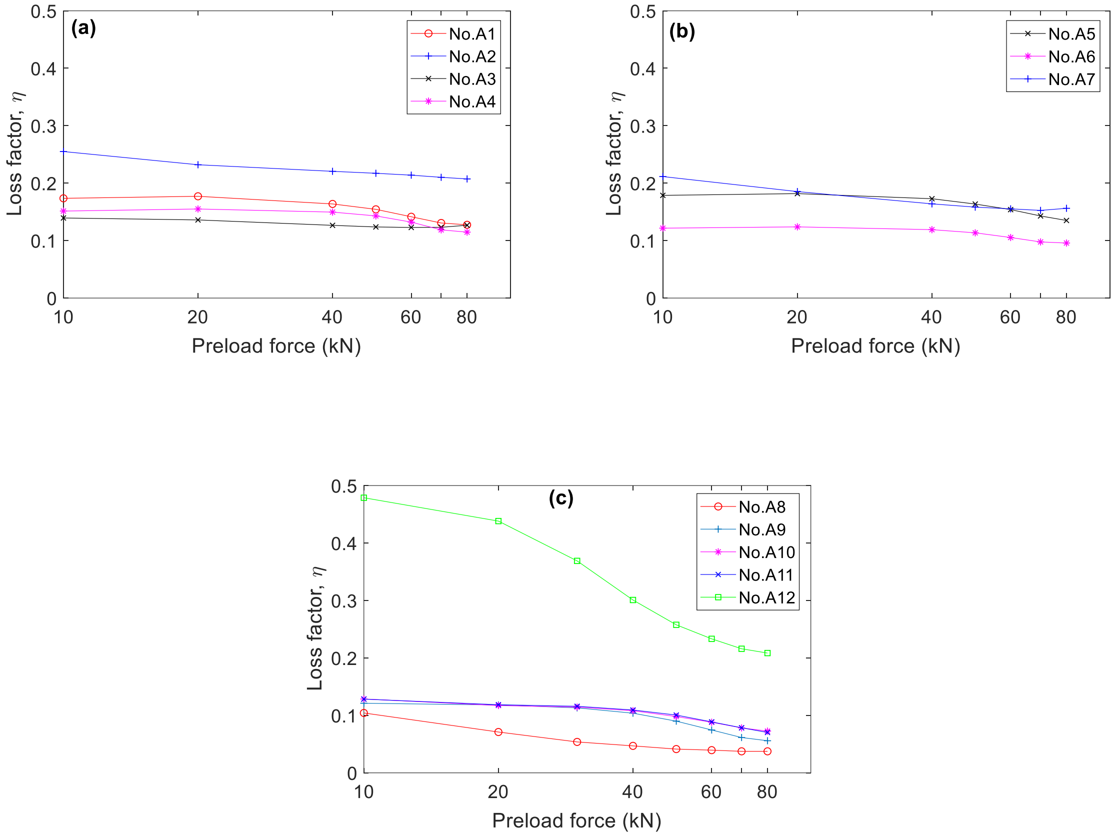

Figure A-3 Loss factor at 300 Hz plotted against static preload: (**a**) No.A1-A4 (Pandrol), (**b**) other available pads (No.A5-A7), (**c**) No. A8-A12 (SBB).

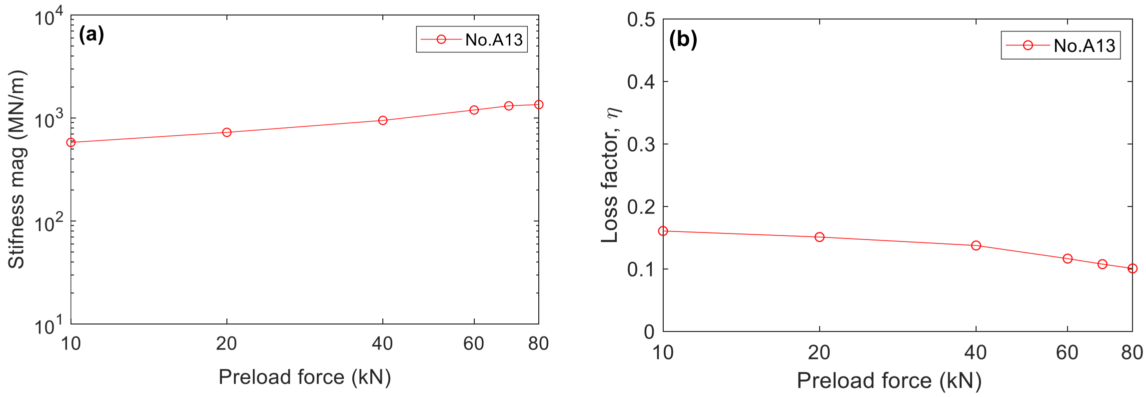

Figure A-4 (**a**) Dynamic stiffness magnitude and (**b**) loss factor at 300 Hz plotted against static preload for railpad No.A13.

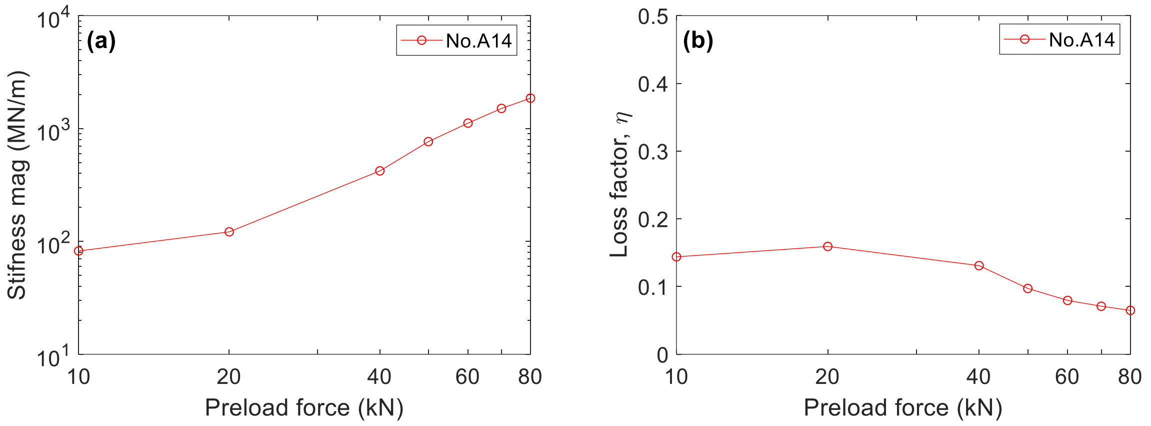

Figure A-5 (**a**) Dynamic stiffness magnitude and (**b**) loss factor at 300 Hz plotted against static preload for lower pad No.A14 with railpad No.A3.

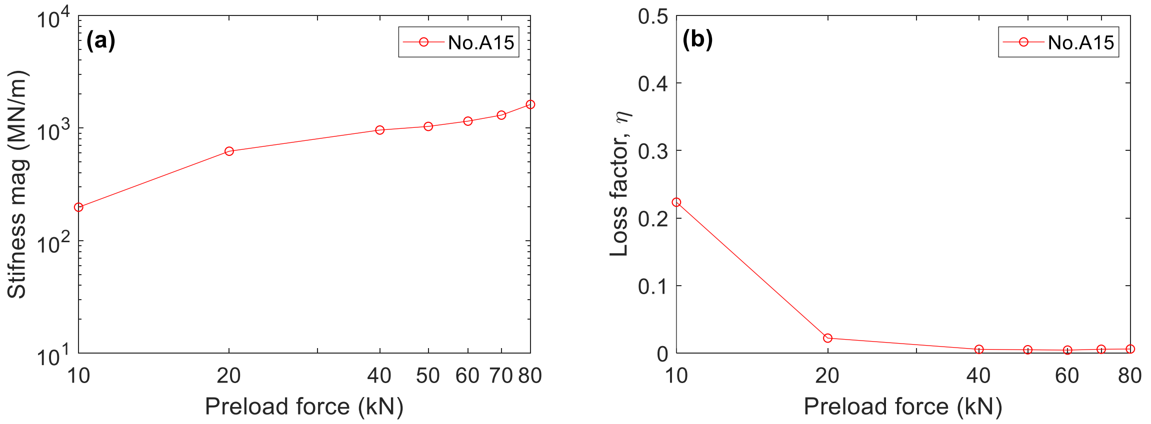

Figure A-6 (**a**) Dynamic stiffness magnitude and (**b**) loss factor at 300 Hz plotted against static preload for No.A15 single stage baseplate only.

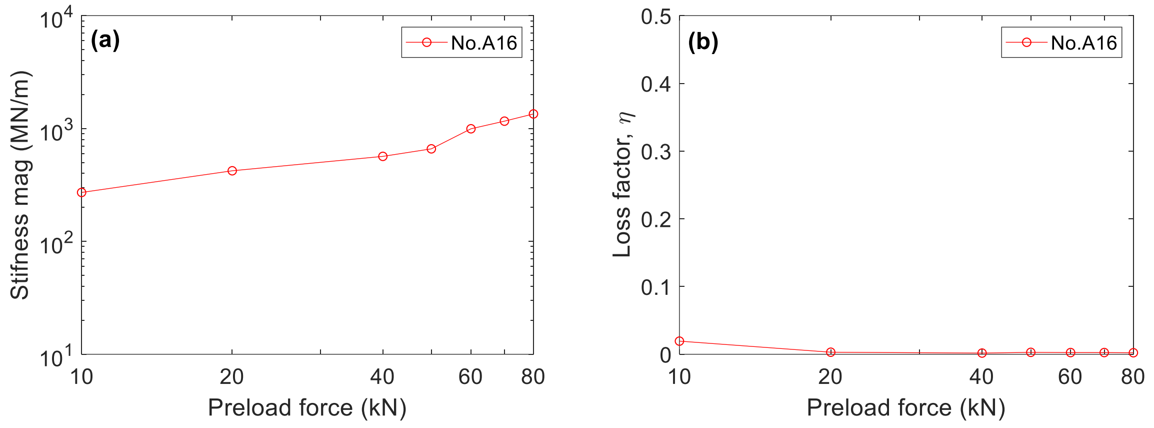

Figure A-7 (**a**) Dynamic stiffness magnitude and (**b**) loss factor at 300 Hz plotted against static preload for No.A16 two-stage baseplate only with no pads.

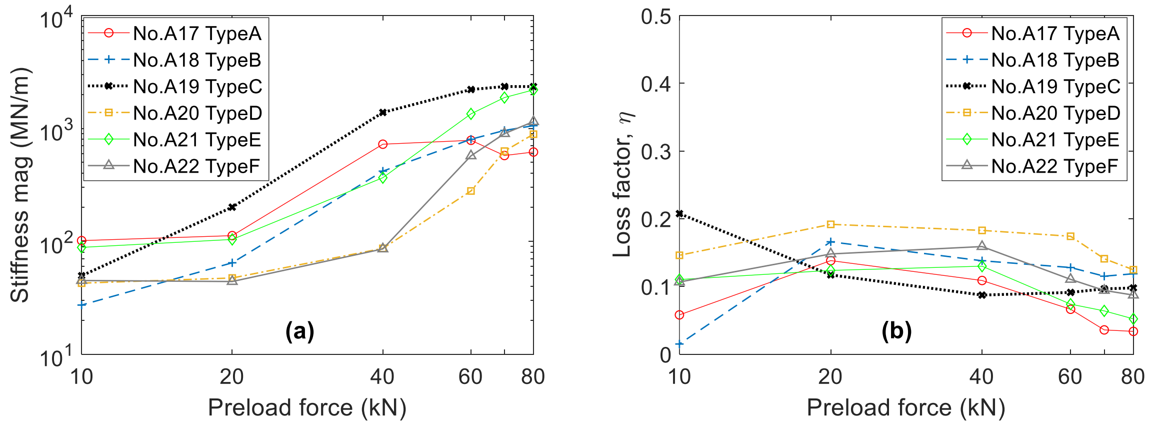

Figure A-8 (**a**) Dynamic stiffness magnitude and (**b**) loss factor at 300 Hz plotted against static preload for two-stage baseplate with different lower pads (No.A17 – No.A22).

A.2 Results from FCA fastening system

The FCA is a new type of fastening system manufactured by Pandrol. As shown in **Figure A-9**, it has a different design to a conventional rail fastening system. This rail fastener can be classified as a three-in-one system as it is built of a single pad (combined upper and lower pad) embedded with strips of steel located at each end. The system has a total mass of 2 kg. It has been designed so that it can provide good vibration isolation with a reduced manufacturing and installation cost. It is intended to be used on slab tracks.

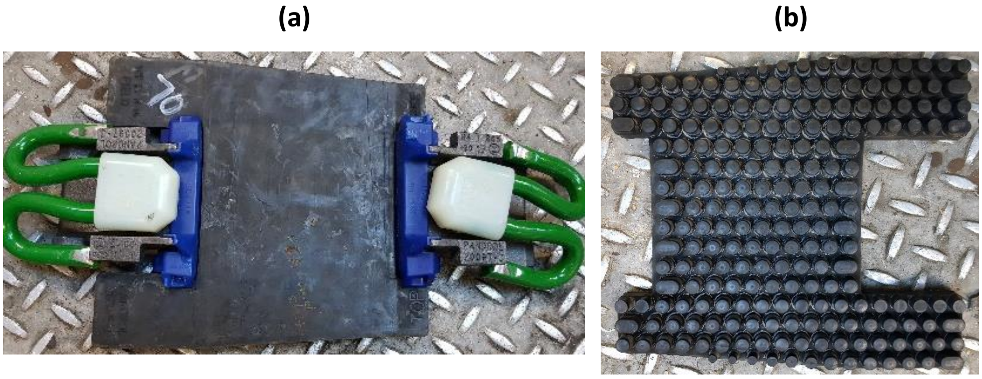

Figure A-9 FCA rail fastener system **(a)** top view, **(b)** bottom view No.A23.

Figure A-10 shows the frequency-dependent dynamic stiffness magnitude for different static preloads for the FCA fastener. No strong internal resonances are seen.

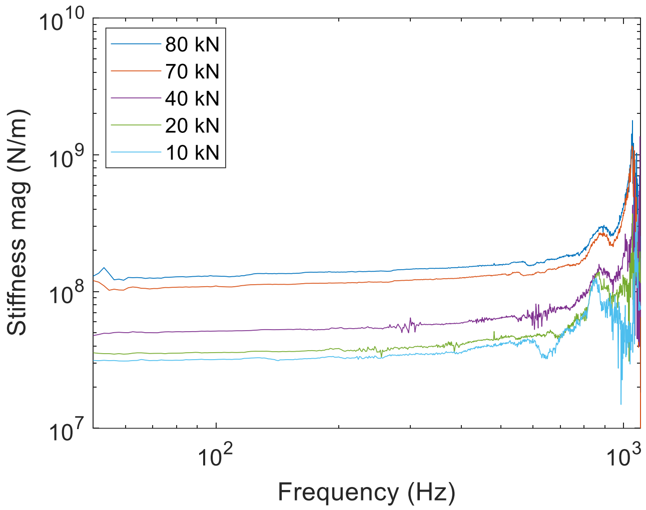

Figure A-10 Dynamic stiffness magnitude plotted against frequency for FCA fastener system No.A23.

Figure A-11 (a) and **(b)** show the dynamic stiffness magnitude and damping loss factor for the FCA rail fastener plotted against preload. It can be seen that similar to the results for the other fastening systems reported in the previous sections, the dynamic stiffness of this system increases when the preload increases, whereas the damping loss factor generally decreases as the preload increases. However, at lower preload up to 20 kN, the damping loss factor values seem to increase with the increase in preload.

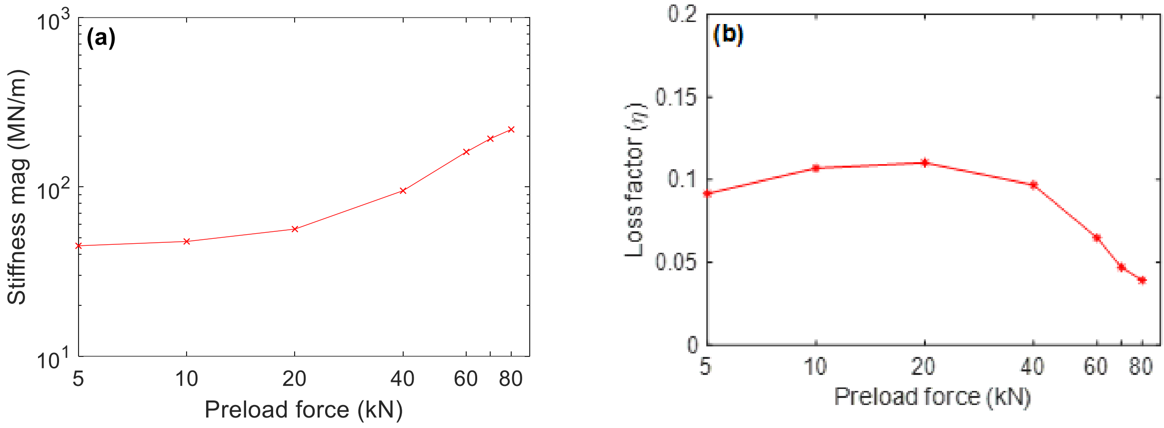

Figure A-11 **(a)** dynamic stiffness and **(b)** damping loss factor at 300 Hz plotted against static preload for FCA fastener system No.A23.

A.3 Results from China baseplate fastening system Type A

The China baseplate fastening system Type A was provided by Professor Li Qi from Tongji University in China. This is a two-stage baseplate system as seen in **Figure A-12** (**b**). The baseplate has a total mass of 10.05 kg. Results are presented for railpad only (**Figure A-13**), baseplate and lower pad only, bolted with a torque of 300 Nm (**Figure A-14**) and the full system containing baseplate, lower pad and railpad, bolted with a torque of 300 Nm and the clips bolted with a torque of 80 Nm (**Figure A-15**). The dynamic stiffness and loss factor values are selected from the fitted curves at the frequency of 160 Hz.

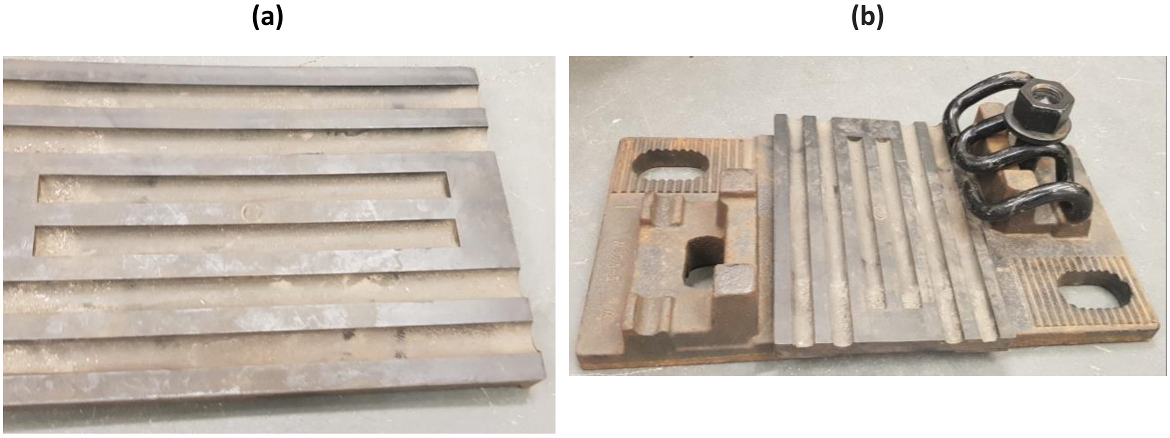

Figure A-12 China baseplate fastening system Type A **(a)** railpad only **(b)** Baseplate and railpad No. A-24.

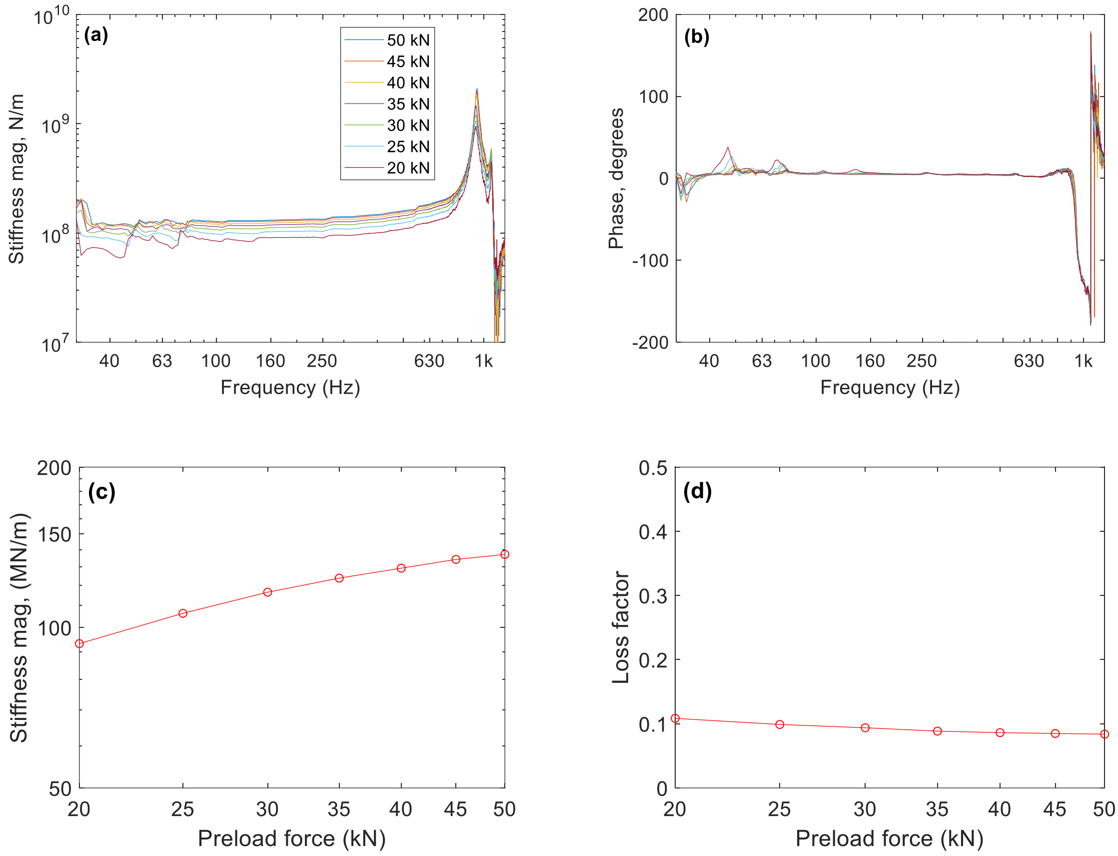

Figure A-13 **(a)** Dynamic stiffness magnitude and (**b**) phase of the dynamic stiffness plotted against frequency, (**c**) dynamic stiffness and **(d)** damping loss factor at 160 Hz plotted against static preload for railpad only No.A-24.

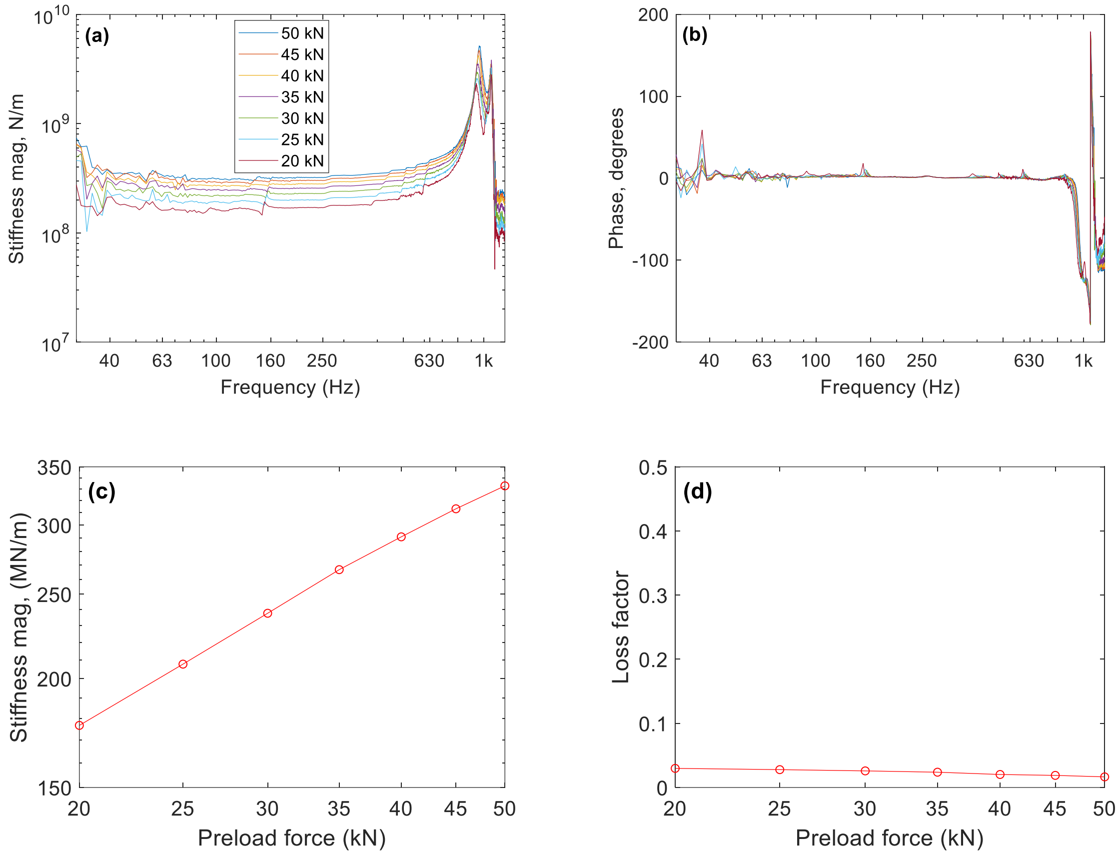

Figure A-14 **(a)** Dynamic stiffness magnitude and (**b**) phase of the dynamic stiffness plotted against frequency, (**c**) dynamic stiffness and **(d)** damping loss factor at 160 Hz plotted against static preload for the baseplate and lower pad only No.A-25.

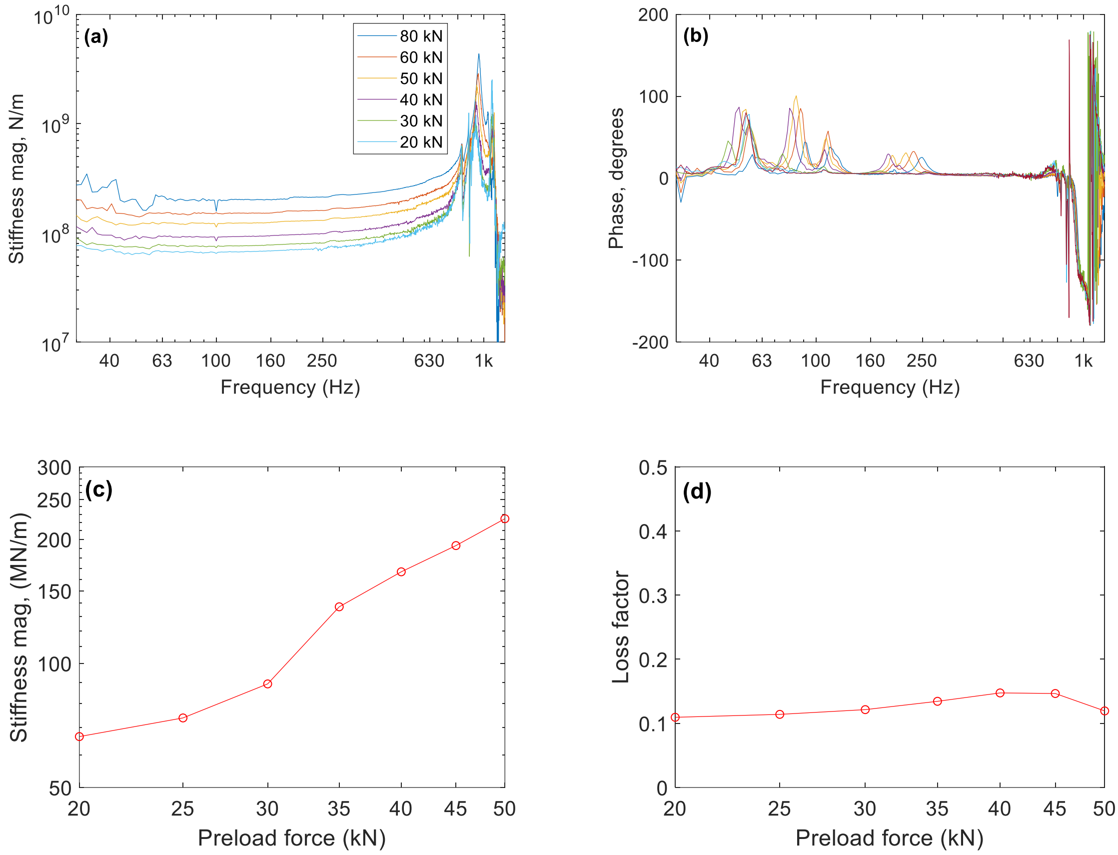

Figure A-15 **(a)** Dynamic stiffness magnitude and (**b**) phase of the dynamic stiffness plotted against frequency, (**c**) dynamic stiffness and **(d)** damping loss factor at 160 Hz plotted against static preload for the full system baseplate, lower pad and railpad No.A-26.

A.4 Results from China baseplate fastening system Type B

The China baseplate fastening system Type B was provided by Professor Li Qi from Tongji University in China. This is a three-stage baseplate system as seen in **Figure A-16** (**b**). The baseplate has a total mass of 16.35 kg contains two steel plates on either side of a rubber pad with double studs. Results are presented for the railpad only (**Figure A-17**), the baseplate only, bolted at a torque of 300 Nm (**Figure A-18**) and the full system containing the baseplate and railpad bolted at torque of 300 Nm and the clips bolted at a torque of 80 Nm (**Figure A-19**). The dynamic stiffness and loss factor values are selected from the fitted curves at the frequency of 160 Hz.

(a) **(b)**

Figure A-16 China baseplate fastening system Type B **(a)** railpad only **(b)** Baseplate and railpad No. A-27.

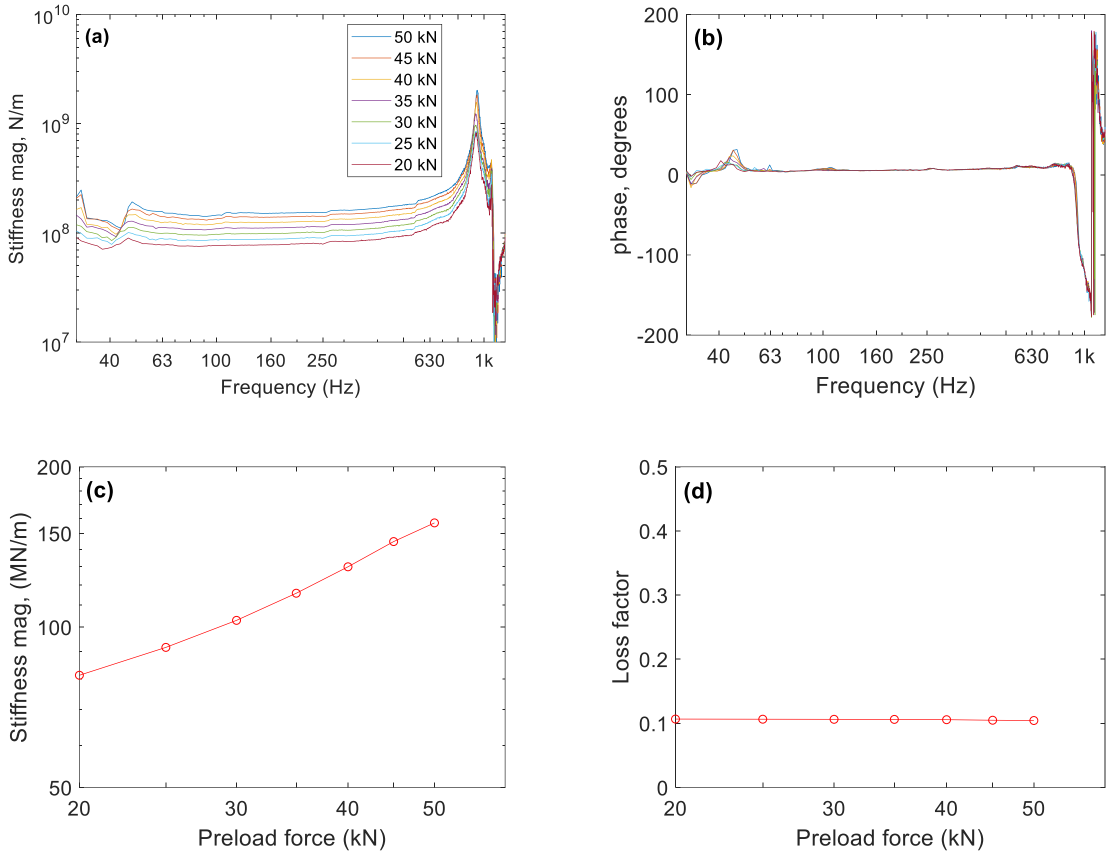

Figure A-17 **(a)** Dynamic stiffness magnitude and (**b**) phase of the dynamic stiffness plotted against frequency, (**c**) dynamic stiffness and **(d)** damping loss factor at 160 Hz plotted against static preload for railpad only No.A-27.

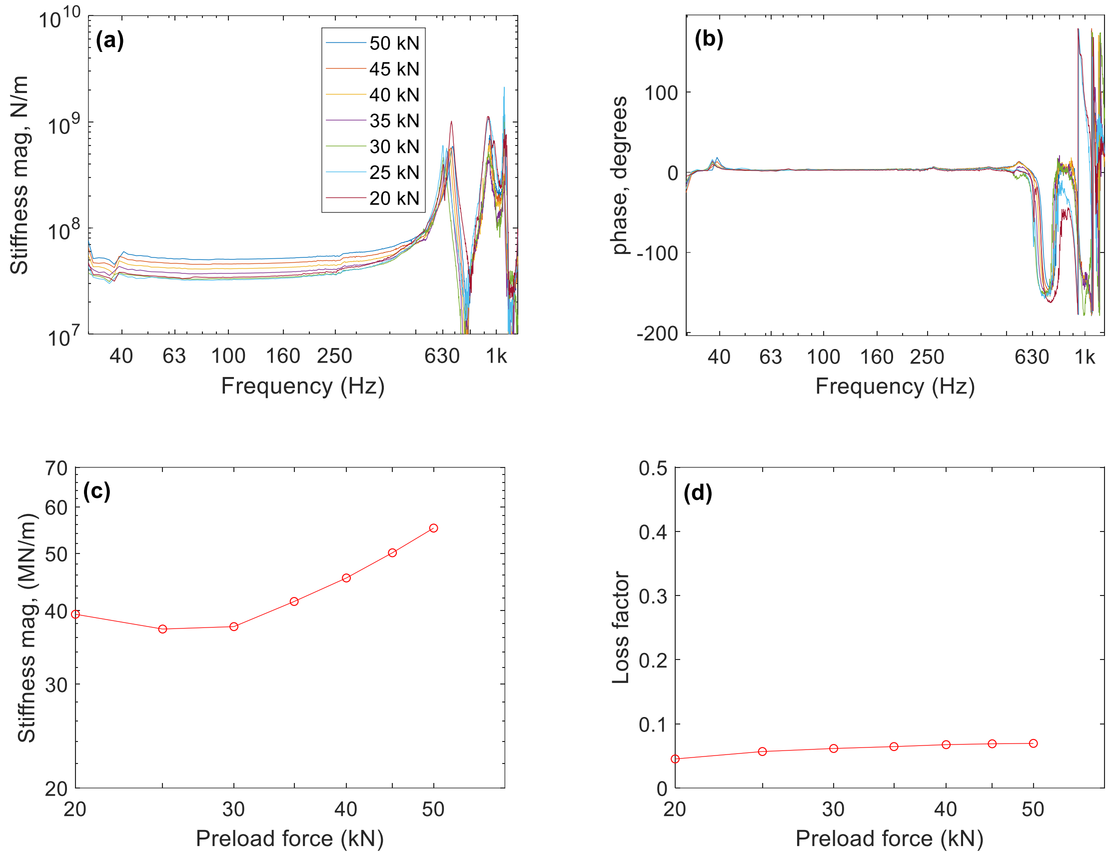

Figure A-18 **(a)** Dynamic stiffness magnitude and (**b**) phase of the dynamic stiffness plotted against frequency, (**c**) dynamic stiffness and **(d)** damping loss factor at 160 Hz plotted against static preload for baseplate only No.A-28.

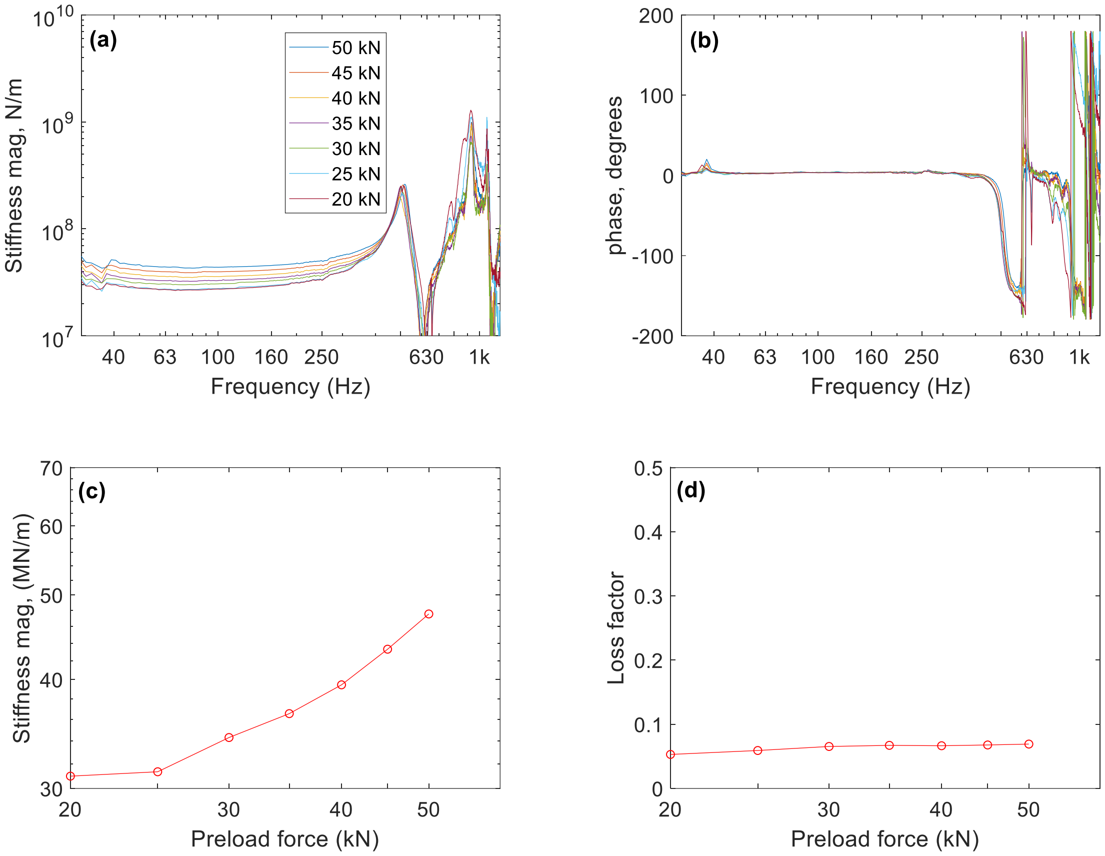

Figure A-19 **(a)** Dynamic stiffness magnitude and (**b**) phase of the dynamic stiffness plotted against frequency, (**c**) dynamic stiffness and **(d)** damping loss factor at 160 Hz plotted against static preload for the full system baseplate and railpad No.A-29.

Appendix B The Vanguard fastener system

B.1 The Vanguard fastener system

This section describes laboratory measurements for determining the vertical static stiffness and the vertical and lateral dynamic stiffness for the Vanguard fastening system. The Pandrol-manufactured Vanguard fastening system was shown in **Figure 1-9.** The measurements of the vertical static stiffness were carried out by applying the hydraulic preload to the test rig in increments of 2.5 kN over the range of 2.5 kN to 50 kN. The measurements for the dynamic stiffness were carried out using the indirect method [56] in the frequency range 40 Hz to 1 kHz and for preloads in the range 2.5 kN to 80 kN.

B.2 Description of the experimental rig

The experimental procedures for determining the vertical static stiffness as well as the lateral and vertical dynamic stiffness of the Vanguard fastening system have been conducted at the former University of Southampton (UoS) Heavy Structures Laboratory (HSL) using the same test rig with the 100 kN Instron Schenck servo-hydraulic actuator. For the static stiffness measurements, only the actuator force was used. For the vertical dynamic stiffness measurements, the inertial dynamic shaker was used, while for the lateral stiffness measurements, an impact hammer was used.

Figure B-20 shows a picture and a zoomed view of the measurement rig setup used for the dynamic stiffness measurements. A schematic view of the rig setup is shown in **Figure 2-4**. The details of the equipment used for assembling the rig and for the experimental procedure are given in **Table 3-1**.

Figure B-20 Laboratory dynamic stiffness setup for the Vanguard system at the UoS HSL.

B.3 Static stiffness measurement setup

To measure the static stiffness of the Vanguard fastening system, dial gauges were added to the rig as shown in **Figure B-21**. The hydraulic preload was applied in increments of 2.5 kN from 2.5 kN to 50 kN. The dial gauges were used for measuring the relative displacement of the rail and the steel block. Two dial gauges were used to eliminate the effect of any rotation that may occur due to the lack of perfect symmetry of the rig.

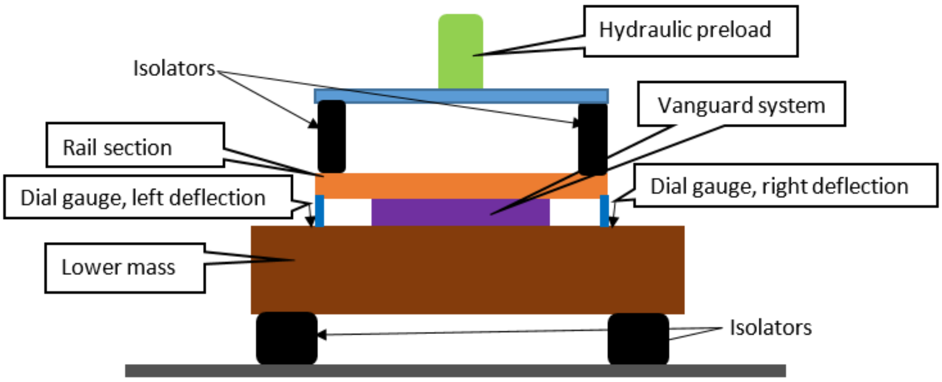

Figure B-21 Schematic view for measured static stiffness for Vanguard system.

B.3.1 Static stiffness results

Figure B-22 (a) shows the static load-deflection curve, while **Figure B-22 (b)** shows the static tangent stiffness as a function of preload. The static stiffness is obtained from the slope of the load-deflection curve:

$$\text{Static stiffness} = \frac{\Delta\text{Load}(\text{kN})}{\Delta\text{deflection (mm)}} \tag{B-1}$$

where Δ is the difference in the values of two adjacent points on the load-deflection curve.

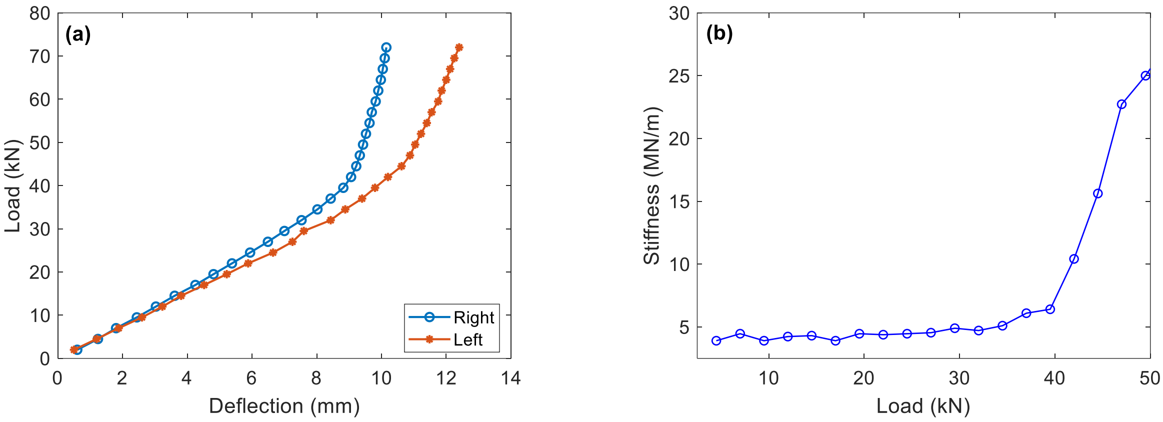

Figure B-22 (a) Load with left and right deflection, **(b)** static stiffness with preload.

The results indicate that the static stiffness is almost constant at 4 MN/m for preloads up to 40 kN. Above 40 kN, it increases significantly. This increase in stiffness is caused by the rail contacting and starting to compress the pad located beneath the rail (between the rail and the Vanguard baseplate). This pad is designed to act as a bump stop for the rail in real applications.

The measured load-deflection curve is compared with data provided by Pandrol in **Figure B-23**. It can be seen that the measured results show good agreement with the provided data.

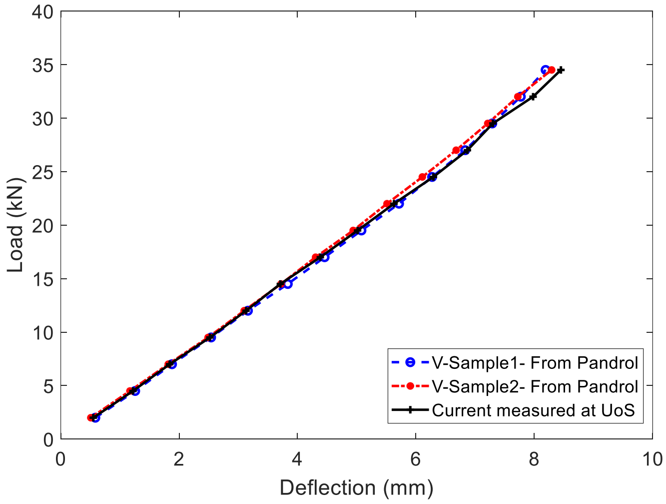

Figure B-23 Comparison of measured load-deflection curves with the data provided by Pandrol.

B.4 Dynamic stiffness measurements

The dynamic stiffness of the Vanguard system is obtained using the indirect method as described in Section 3.3. The transmissibility $H_{2,1}$ is obtained using the average of two input accelerations $\ddot{x}_1$ and $\ddot{x}_2$ at two symmetric positions on the rail (as close as possible to the dynamic shaker, as shown in **Figure B-20**, and the average of the accelerations $\ddot{x}_3$ and $\ddot{x}_4$ measured on the lower block. The average of the accelerations is used to cancel any rotation effects as it was discovered that the rail was prone to rotation which transmitted a moment to the lower block. **Figure B-24** presents a schematic view of the sensor locations for the upper and lower blocks. The lower sensors are placed anti-symmetrically at the nodal points of the first bending mode of the lower block (see Section **3.4**). The first bending mode of the lower block is around 1250 Hz, which constrains the upper-frequency limit that can be used for measuring the dynamic stiffness.

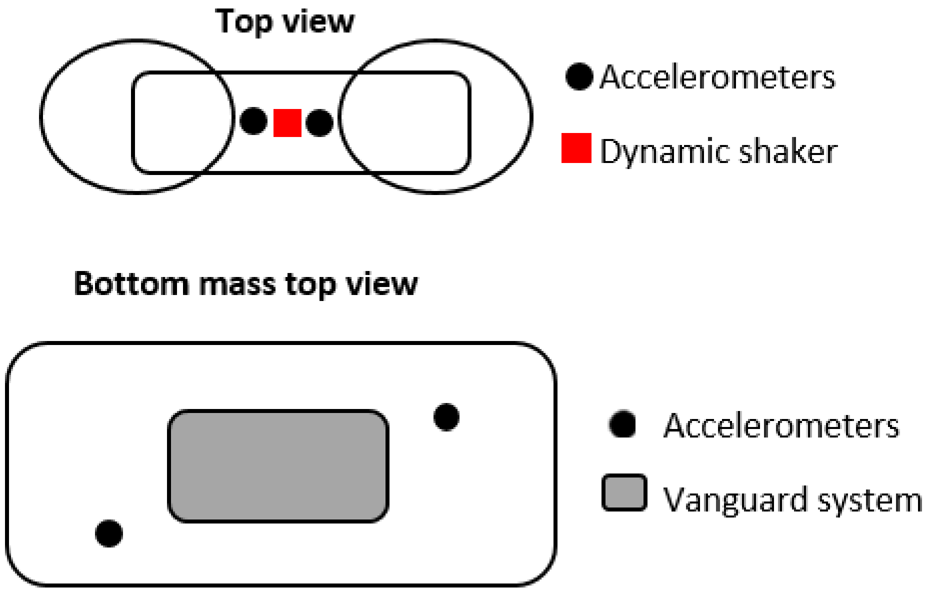

Figure B-24 Top view of accelerometer placement for vertical dynamic stiffness measurement of Vanguard system

B.4.1 Vertical dynamic stiffness results

In order to estimate a single value of dynamic stiffness and damping loss factor from the measured data, the procedure explained in Section **3.5** is followed.

Figure B-25 (a) and **(b)** show the magnitude and the phase of the vertical dynamic stiffness for different preloads below 35 kN. It is observed that the Vanguard system shows low stiffness at this preload range. However, for higher preloads, the stiffness is increased about ten times, as shown in **Figure B-26**. The stiffness starts to increase significantly above the preload of 35 KN, at which the rail starts to make contact with the bump-stop; this was also seen for the static stiffness test (see **Figure B-22**).

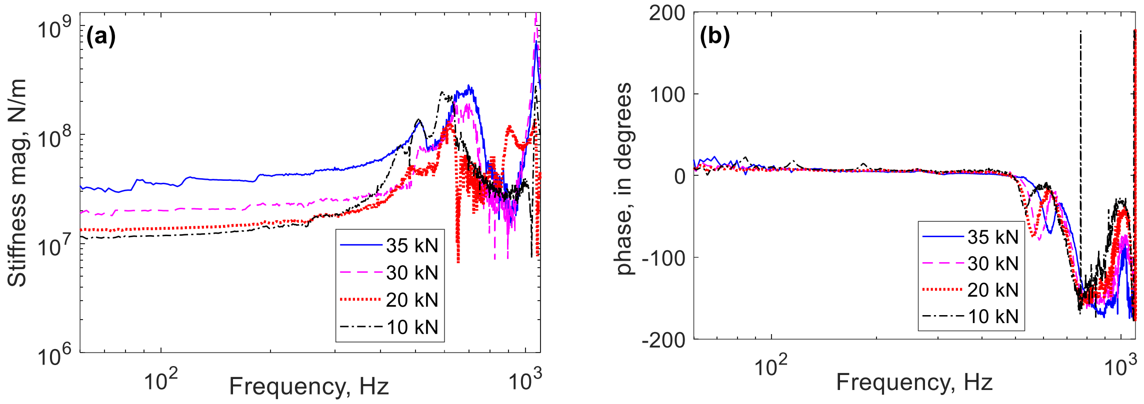

Figure B-25 **(a)** Magnitude and **(b)** phase of complex vertical stiffness with frequency for various preloads of the Vanguard system.

Figure B-26 **(a)** and **(b)** show the vertical dynamic stiffness and loss factor plotted against preload obtained by following the procedure described in Section **3.3**. It can be seen that for preloads below 30 kN the dynamic stiffness is almost constant at about 16 MN/m with a damping loss factor of about 0.08.

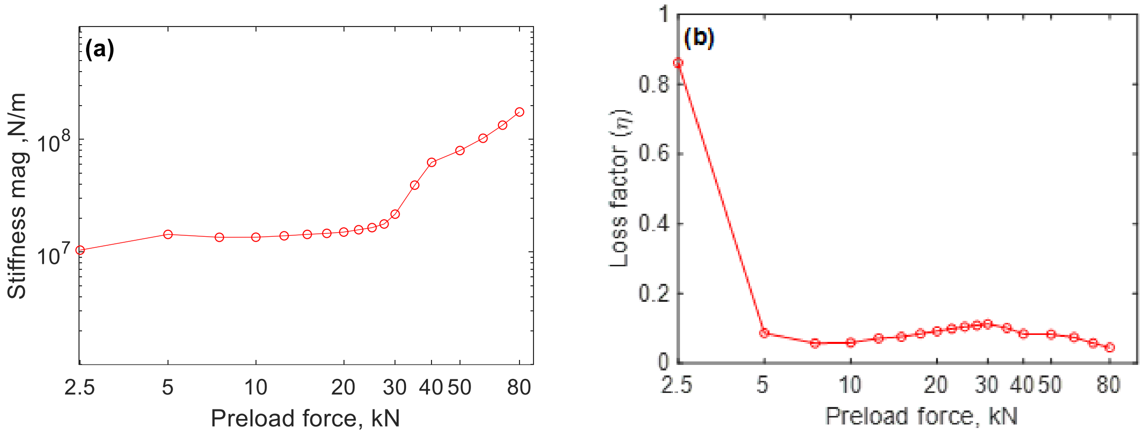

Figure B-26 Vertical stiffness **(a)** magnitude and **(b)** loss factor as a function of preload for the Vanguard system.

B.5 Measurement setup for lateral dynamic stiffness

The same rig setup was used for lateral dynamic stiffness measurements. This time, the excitation was provided by an impact hammer that gives better control of the location of excitation. The rail was excited by a number of impacts at the centre of the railhead. Two accelerometers were attached to the railhead symmetrically and a third accelerometer was attached to the centre of the lower block, as can be seen in **Figure B-27**.

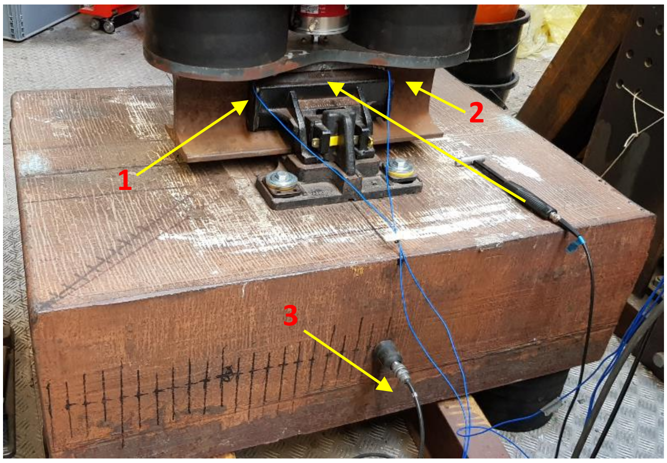

Figure B-27 View of the experimental setup for the lateral dynamic stiffness for the Vanguard system.

The rotation of the rail is investigated by studying the difference between the two signals. The lateral vibration of the lower block is measured by an accelerometer placed in the centre of side, from which the lateral stiffness is obtained using the following equation:

$$K = -m\omega^2 \left(\frac{1}{\frac{\ddot{x}_1 + \ddot{x}_2}{2\ddot{x}_3} - 1} \right) \qquad \text{(B-2)}$$

where K is the transfer stiffness, m is the mass of the lower block, $\ddot{x}_1$ and $\ddot{x}_2$ are the accelerations of the upper mass, $\ddot{x}_3$ is the acceleration of the lower mass and ω is the frequency in rad/s.

B.5.1 Lateral dynamic stiffness results

Using the setup shown in **Figure B-28**, excitation is applied using an impact hammer at the railhead. Preloads are applied in the range of 2.5 to 30 KN with 2.5 KN increments. The data is collected using the Data Physics acquisition system and then processed using Matlab. The vibration ratio between the railhead sensors and the lower block sensor is analysed, using the following equations:

$$\mathrm{Vb}_1 = \frac{\frac{\ddot{u}_3}{F}}{\frac{\ddot{u}_1}{F}} = \frac{H_{3,\mathrm{ref}}}{H_{1,\mathrm{ref}}} \qquad \text{(B-3)}$$

$$\mathrm{Vb}_2 = \frac{\frac{\ddot{u}_3}{F}}{\frac{\ddot{u}_2}{F}} = \frac{H_{3,\mathrm{ref}}}{H_{2,\mathrm{ref}}} \tag{B-4}$$

$$\mathrm{Vb}_3 = \frac{2\frac{\ddot{u}_3}{F}}{\frac{\ddot{u}_1}{F} + \frac{\ddot{u}_2}{F}} = \frac{2H_{3,\mathrm{ref}}}{H_{1,\mathrm{ref}} + H_{2,\mathrm{ref}}} \tag{B-5}$$

where $H_{i,ref}$ are the accelerance transfer functions for sensor i.

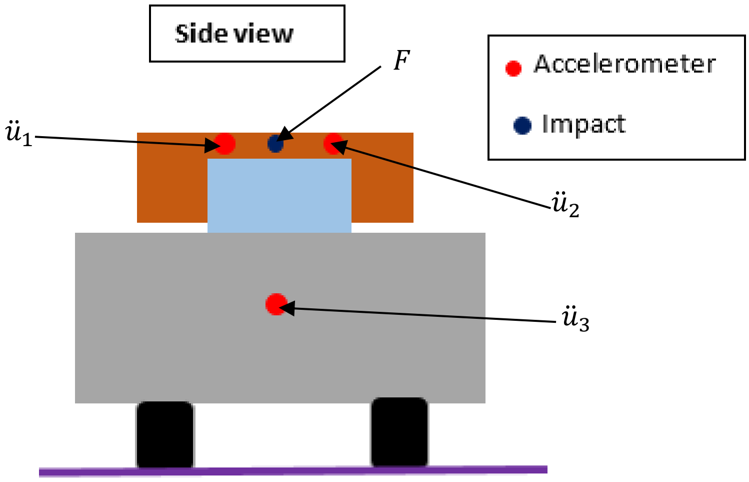

Figure B-28 Schematic view of the measurements for the lateral stiffness of the Vanguard system showing sensors and impact location.

Figure B-29 (a) and **(b)** show the magnitude and the phase of the vibration ratio for the preload of 10 kN. Three vibration ratios are compared: using one of each of the two accelerances on each side of the railhead (Vb_1 and Vb_2) and the case where the signal of the two sensors on the railhead are summed together to cancel any rotation from the rail (Vb_3). The results show that the vibration ratios are similar for all sensor combinations. Three peaks can be seen below 200 Hz (at around 65, 100 and 145 Hz). These peaks are assumed to be the translational and rotational rigid body modes of the rail and the attached dog-bone plate and they are further investigated below.

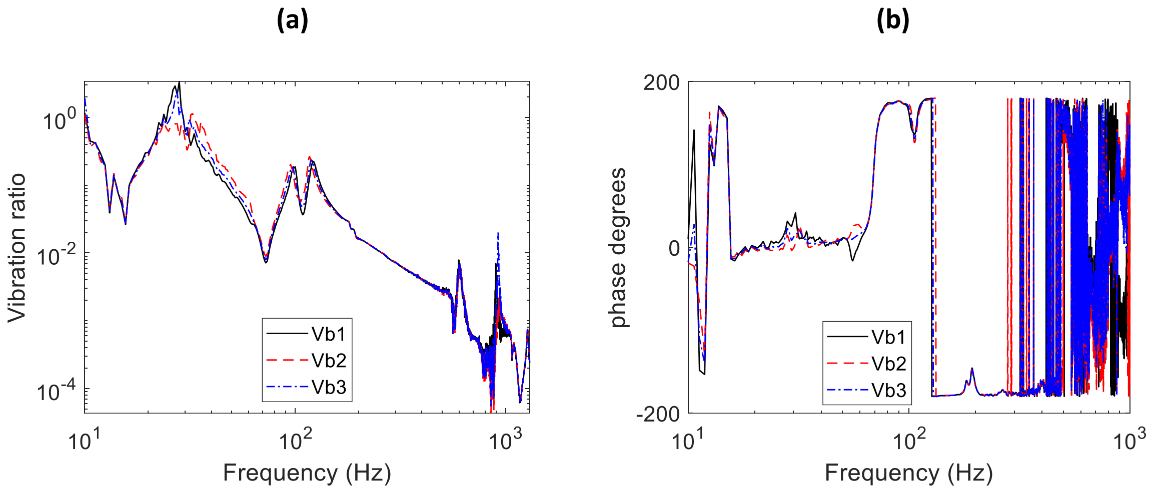

Figure B-29 Vibration ratio with frequency between the railhead and lower block for the preload of 10 kN: **(a)** magnitude and **(b)** phase.

By using the indirect method, the lateral dynamic stiffness magnitude and the phase are obtained and shown in **Figure B-30 (a)** and **(b)** for the preload of 10 kN. Both the stiffness magnitude and phase are presented for three combinations of the sensor data using the equations:

$$k_1 = -\omega^2 m_2 \left(\frac{1}{\left({}^{1}/_{\mathrm{Vb}_1} \right) - 1} \right) \tag{B-6}$$

$$k_2 = -\omega^2 m_2 \left(\frac{1}{\left({}^{1}/_{\mathrm{Vb}_2} \right) - 1} \right) \tag{B-7}$$

$$k_3 = -\omega^2 m_2 \left(\frac{1}{\left({}^{1}/_{\mathrm{Vb}_3} \right) - 1} \right) \tag{B-8}$$

The estimated values of the stiffnesses are shown in **Figure B-30** for the three sensor configurations. It can be seen that regardless of the position of the sensors on the railhead, the stiffness values are similar.

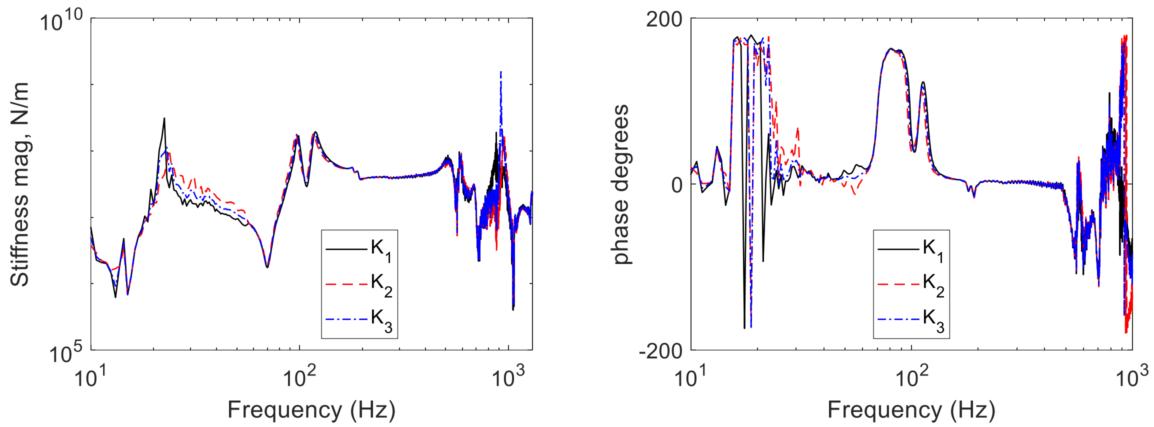
(a)

(b)

Figure B-30 Magnitude **(a)** and **(b)** phase of the lateral dynamic stiffnesses with frequency.

Figure B-31, shows the lateral dynamic stiffness and damping loss factor as a function of preload. The results show that as the preload increases, the stiffness increases. The damping loss factor decreases for preloads up to 17.5 kN. Above 17.5 kN it increases with the preload.

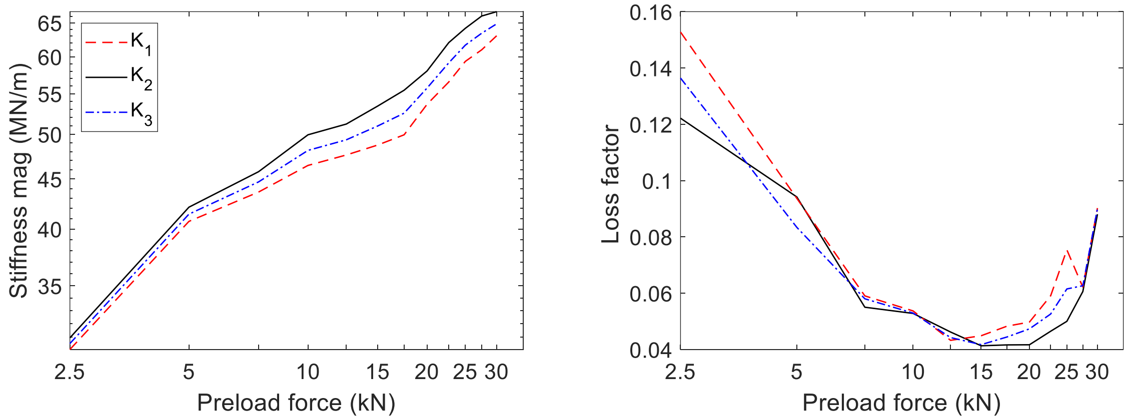
(a)

(b)

Figure B-31 **(a)** Magnitude and **(b)** damping loss factor of the lateral dynamic stiffness with preload.

Next, the sensors at the rail are moved from the railhead and placed to the rail foot, as shown in **Figure B-32**. The measurements are repeated to confirm if the peaks appearing in the previous data (with sensors on the railhead) can be eliminated. The result shows no elimination of the peaks. Therefore, further investigations were conducted. However, the stiffness has increased, and the loss factor reduced as shown in **Figure B-33**.

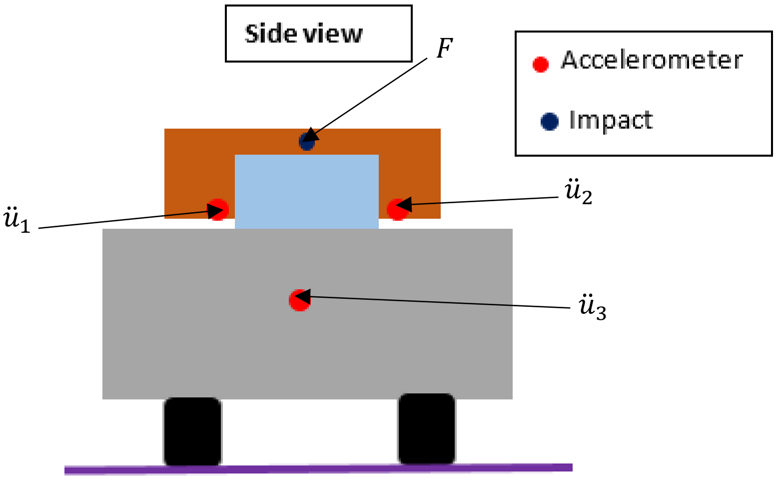

Figure B-32 Schematic view of the measurements of the lateral stiffness with sensors at the rail foot of the Vanguard system.

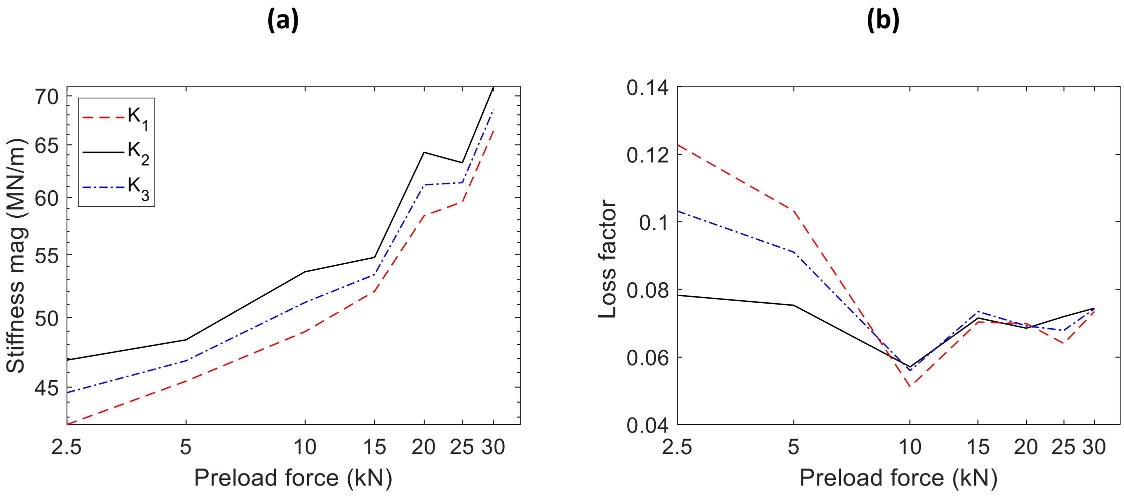

Figure B-33 **(a)** Magnitude lateral dynamic stiffness and **(b)** loss factor with preload.

B.5.2 Peak Identification

In this section, the peaks in the vibration ratio and lateral dynamic stiffness magnitude below 200 Hz are further investigated. The mobility magnitude and phase measured at the railhead and the rail foot are shown in **Figure B-34 (a)** and **(b)**. In **Figure B-34** (**b**), can be seen that the phase between the rail foot and the railhead shows a 180-degree difference at the first peak frequency and 0 degrees at the second peak frequency. This indicates that the first peak at 63 Hz is the rotation mode of the rail while the second peak at 108 Hz is the bouncing mode of the rail and the Vanguard system on the block. The third peak of 146 Hz should be related to the lateral stiffness of the Vanguard system.

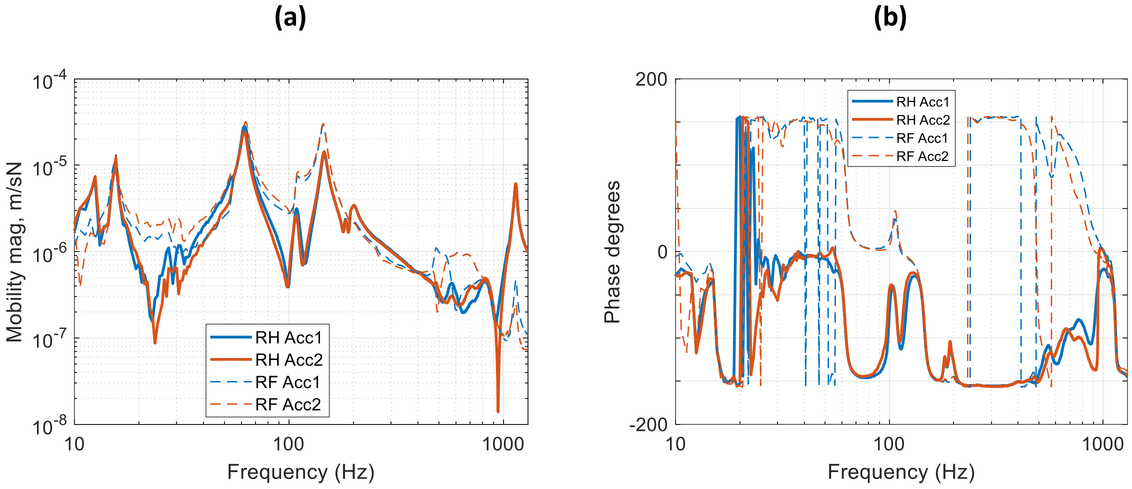

Figure B-34 Mobility **(a)** magnitude and **(b)** phase with frequency (RH= railhead), (RF =rail foot).

A SolidWorks model of the rail and the attached dog-bone shaped plate was developed, as shown in **Figure B-35**. The model is used to extract more accurately the total mass and moments of inertia, which are reported in **Table B-2**. These values are then used to calculate the rotation and lateral stiffness using the peak frequency from the mobility magnitude data shown in **Table B-3**, and then compared with the measured dynamic lateral stiffness of the Vanguard system.

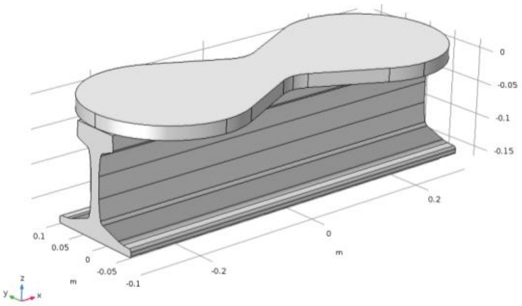

Figure B-35 SolidWorks model of the rail and dog bone plate.

Table B-2 Moments of inertia and total mass

L_{xx}	0.297 kgm^2
L_{yy}	1.695 kgm^2
L_{zz}	1.557 kgm^2
mass	49 kg

Table B-3 Peak frequencies obtained from mobility magnitude data

Peak frequency Hz	
1. 63	f_R (rotation)
2. 108	f_u
3. 146	f_L (lateral)

The rotational stiffness is estimated using the natural frequency of a 1-dof rigid body on a rotational spring:

$$\begin{aligned} k_{\mathrm{R}} &= (2\pi f_{\mathrm{R}})^2 I \\ &= 0.046\ \mathrm{MNm/rad} \end{aligned} \tag{B-9}$$

where f_{R} is the frequency at the peak (63 Hz) and I is the moment of inertia around z-z axis of the coordinate system shown in **Figure B-37**

The lateral stiffness is estimated using the natural frequency of a 1-dof rigid body on a spring:

$$\begin{aligned} k_{\mathrm{L}} &= (2\pi f_{\mathrm{L}})^2 m \\ &= 41\ \mathrm{MN/m} \end{aligned} \tag{B-10}$$

where f_{L} is the lateral natural frequency (146 Hz) and m is the total mass of the rail and the attached plate.

The lateral dynamic stiffness obtained from the simplified 1-dof systems using the values from the SolidWorks model is compared with the measured lateral dynamic stiffness obtained with the sensors at the railhead (RH) and rail foot (RF), and a good match is found for the frequency range of 180-450 Hz as shown in **Figure B-36**. Therefore, the peak at 146 Hz of the mobility is due to the lateral stiffness of the Vanguard system.

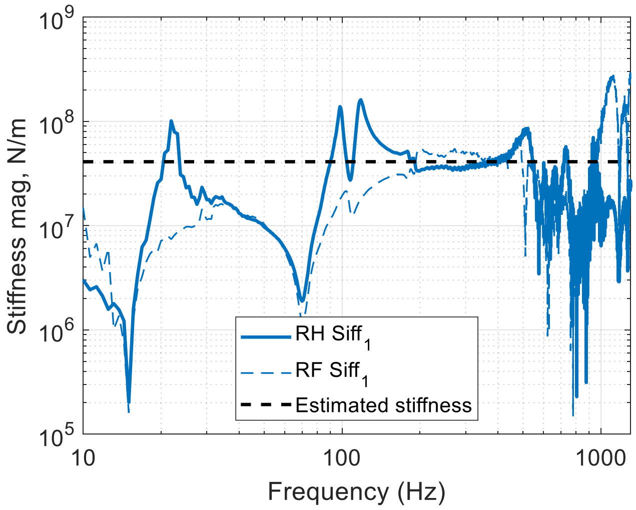

Figure B-36 Lateral stiffness for the Vanguard system; measured at the railhead (RH), measured at rail foot (RF) and predicted by the model.

The stiffness with a peak at 108 Hz is investigated,

$$\begin{aligned} k_\mathrm{u} &= (2\pi f_\mathrm{u})^2 m \\ &= 23\ \mathrm{MN/m} \end{aligned} \tag{B-11}$$

where f_u is the vertical natural frequency (108 Hz) and m is the combined mass of the rail and the attached plate.

This stiffness is similar to the measured vertical dynamic stiffness of the Vanguard system for preload of 30 kN, which is 22 MN/m. The average measured vertical dynamic stiffness for the Vanguard system between the preload of 5 kN and 30 kN is around 16 MN/m. Therefore, this peak might not be directly related to the vertical dynamic stiffness of the Vanguard system.

Figure B-37 shows a summary of the corresponding modes identified from the peaks of the mobility magnitude of the Vanguard system.

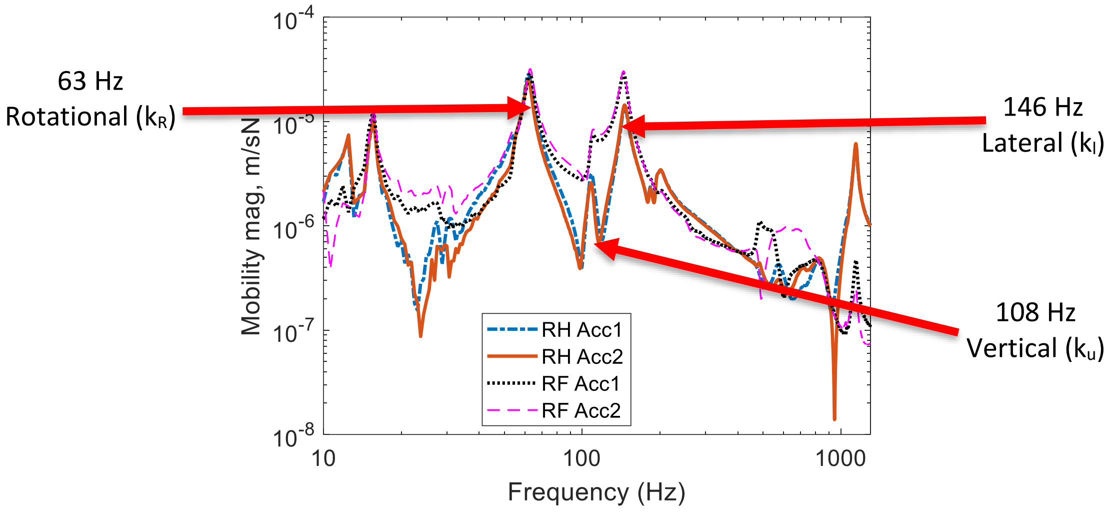

Figure B-37 Mobility magnitude with frequency showing the mode identification.

Appendix C Receptance coupling method

A 2.5D FE model of an infinite free rail is used to obtain transfer receptances of the rail. The response of the track to an external force can then be obtained by using the superposition principle. **Figure C-38** illustrates the concept of two coupled structures, in this case representing an infinite rail and a finite number of baseplates [36].

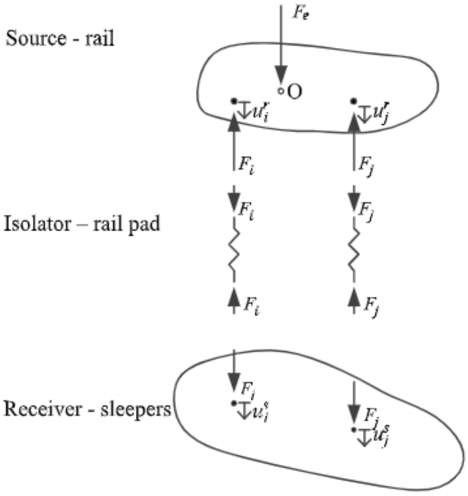

Figure C-38 Source and receiver structures coupled at multiple connection points through resilient elements [36].

It is assumed that a harmonic force of amplitude $F_e = 1$ at circular frequency ω is acting on the rail. A damped spring is introduced at each of the connection points j between the rail and the baseplates. These are assumed to exert a force of amplitude $-F_j$ on the rail. By applying the superposition principle, the displacement amplitude of the rail at position i is given by

$$u_i^r = \alpha_{ie}^r F_e - \sum_j \alpha_{ij}^r F_j \tag{C-1}$$

where α_{ie}^r is the transfer receptance of the free rail giving the response at the connection point i due to a unit force at the excitation point, α_{ij}^r is the transfer receptance giving the response on the rail at the connection point i due to a unit force acting at the point j.

The relative displacement of the i^{th} spring connecting the rail and baseplates is given by

$$u_i^r - u_i^s = \sum_j \alpha_{ij}^p F_j \tag{C-2}$$

where u_i^s is the displacement of the baseplate at point i, α_{ij}^p is the receptance of the spring connection giving the relative displacement at point i due to the force acting at the attachment point j, F_j is the interaction force at point j. In practice $\alpha_{ij}^p = 0$ for $i \neq j$.

For the baseplates, the displacement at the connection point is given by

$$u_i^s = \sum_j \alpha_{ij}^s F_j \tag{C-3}$$

For the connection points on different baseplates, which are assumed to be uncoupled, $\alpha_{ij}^s = 0$,but multiple connection points on one baseplate are allowed in which case it would be non-zero. Considering all the connection points, the equation of motion can be written in matrix form for the three structures:

$$\boldsymbol{u}_r = \alpha_e^r F_e - \alpha^r \mathbf{F} \tag{C-4}$$

$$\boldsymbol{u}_r - \boldsymbol{u}_s = \alpha^p \mathbf{F} \tag{C-5}$$

$$\boldsymbol{u}_s = \alpha^s \mathbf{F} \tag{C-6}$$

where $\boldsymbol{u}_r$ are the displacements on the rail foot at the positions of every spring, $\boldsymbol{u}_s$ are the displacements on the top surface of the baseplates at the corresponding points, α^r, α^p and α^s are matrices of the receptances at every connection point of the rail, railpad and the baseplates respectively due to the force at the spring positions. α_e^r is the vector of receptances of the rail at the connection points due to the external force F_e.

The addition of equations **C-5** and **C-6** gives.

$$\boldsymbol{u}_r = \alpha^p \mathbf{F} + \alpha^s \mathbf{F} \tag{C-7}$$

Substituting Equation **C-7** into Equation **C-4** and rearranging gives

$$\mathbf{I} + \alpha^r(\alpha^p + \alpha^s)^{-1})\boldsymbol{u}_r = \alpha_e^r \mathbf{F}_e \tag{C-8}$$

where $\mathbf{I}$ is a unit matrix. This allows $\boldsymbol{u}_r$ to be obtained as

$$\boldsymbol{u}_r = (\mathbf{I} + \alpha^r(\alpha^p + \alpha^s)^{-1})^{-1} \alpha_e^r \mathbf{F}_e \tag{C-9}$$

The displacement at an arbitrary point k on the rail can be finally calculated as

$$u_k^r = \alpha_{ke}^r \mathbf{F}_e - \alpha_k^{rT} \mathbf{F} \tag{C-10}$$

where α_k^r is the vector of receptances of the free rail giving the response at point k on the rail to a unit force at each spring location on the rail foot. α_{ke}^r is the transfer receptance of the free rail from the external force $\mathbf{F}_e$ to the response point k. Note that the spacing between baseplates is not specified in the above formulation; this implies that the coupled track system could have discrete supports with arbitrary spacing.

List of References

1. Thompson, D., *Railway Noise and Vibration mechanisms, modelling and means of Control*. 2009, Oxford: Elsevier Ltd.

2. Commission, E., *Future noise policy*, C.o.t.E. communities, Editor. 1996, European Commission Green Paper: Brussels.

3. World Health Organization, *Night Noise Guidelines for Europe*. 2009: World Health Organization,.

4. She, W., et al., *Influence of coarse fly ash on the performance of foam concrete and its application in high-speed railway roadbeds.* Construction and Building Materials, 2018. **170**: p. 153-166.

5. UIC, *High-speed database & maps*, I.H. Committee, Editor. 2018, The worldwide railway organisation: France.

6. Xia, W., K. Wang, and A. Zhang, *Air Transport and High-speed Rail Interactions in China: Review on Impacts of Low-cost Carriers, Rail Speed, and Modal Integration*, in *Airline Economics in Asia*. 2018, Emerald Publishing Limited.

7. Harassek, A., *European Railway Agency and development of the TSIs for European High Speed Railway System.* Technika Transportu Szynowego, 2015(6).

8. *Commission Regulation (EU)-No 1304/2014 of 26 November 2014 on the technical specification for interoperability relating to the subsystem ‘rolling stock — noise’ amending Decision 2008/232/EC and repealing Decision 2011/229/EU,Official Journal of the European Union.* 2014.

9. Thompson, D. and P. Gautier, *Review of research into wheel/rail rolling noise reduction.* Proceedings of the Institution of Mechanical Engineers, Part F: Journal of Rail and Rapid Transit, 2006. **220**(4): p. 385-408.

10. Thompson, D. and C. Jones, *Low noise track meets environmental concerns.* Railway Gazette International, 2002. **158**(7).

11. Ntotsios, E., D. Thompson, and M. Hussein, *The effect of track load correlation on ground-borne vibration from railways.* Journal of Sound and Vibration, 2017. **402**: p. 142-163.

12. Lombaert, G., et al., *Ground-borne vibration due to railway traffic: a review of excitation mechanisms, prediction methods and mitigation measures*, in *Noise and vibration mitigation for rail transportation systems*. 2015, Springer. p. 253-287.

13. Thompson, D.J., G. Kouroussis, and E. Ntotsios, *Modelling, simulation and evaluation of ground vibration caused by rail vehicles.* Vehicle System Dynamics, 2019. **57**(7): p. 936-983.

14. Remington, P.J., *Wheel/rail noise—Part I: Characterization of the wheel/rail dynamic system.* Journal of Sound and Vibration, 1976. **46**(3): p. 359-379.

15. Remington, P.J., *Wheel/rail rolling noise, II: Validation of the theory.* The Journal of the Acoustical Society of America, 1987. **81**(6): p. 1824-1832.

16. Remington, P.J., *Wheel/rail rolling noise, I: Theoretical analysis.* The journal of the Acoustical Society of America, 1987. **81**(6): p. 1805-1823.

17. Remington, P.J., *Wheel/rail noise—Part IV: Rolling noise.* Journal of Sound and Vibration, 1976. **46**(3): p. 419-436.

18. Thompson, D., P. Fodiman, and H. Mahé, *Experimental validation of the TWINS prediction program for rolling noise, part 2: results.* Journal of sound and vibration, 1996. **193**(1): p. 137-147.

19. Thompson, D., B. Hemsworth, and N. Vincent, *Experimental validation of the TWINS prediction program for rolling noise, part 1: description of the model and method.* Journal of sound and vibration, 1996. **193**(1): p. 123-135.

20. Kitagawa, T. and D.J. Thompson, *The horizontal directivity of noise radiated by a rail and implications for the use of microphone arrays.* Journal of sound and vibration, 2010. **329**(2): p. 202-220.

21. Zea, E., et al., *Wavenumber–domain separation of rail contribution to pass-by noise.* Journal of Sound and Vibration, 2017. **409**: p. 24-42.

22. Thompson, D., et al., *Assessment of measurement-based methods for separating wheel and track contributions to railway rolling noise.* Applied Acoustics, 2018. **140**: p. 48-62.

23. Indraratna, B., W. Salim, and C. Rujikiatkamjorn, *Advanced rail geotechnology-ballasted track*. 2011: CRC press.

24. Steenbergen, M., A. Metrikine, and C. Esveld, *Assessment of design parameters of a slab track railway system from a dynamic viewpoint.* Journal of Sound and Vibration, 2007. **306**(1-2): p. 361-371.

25. Pandrol, *Vanguard rail fastening system*. 2015: Pandrol Ltd.

26. Herron, D., et al., *Development of a Test Procedure for Stiffness Measurements Appropriate to Ground-Borne Noise Modelling*, in *Noise and Vibration Mitigation for Rail Transportation Systems*. 2018, Springer. p. 619-631.

27. Andersen, L. and S.R. Nielsen, *Reduction of ground vibration by means of barriers or soil improvement along a railway track.* Soil Dynamics and Earthquake Engineering, 2005. **25**(7): p. 701-716.

28. Bewes, O.G., *The calculation of noise from railway bridges and viaducts EngD thesis*. 2005, University of Southampton.

29. 13481-2, E.B., *Railway applications–track–performance requirements for fastening systems. Fastening systems for concrete sleepers.* British-Adopted European Standard, 2012.

30. Bewes, O., et al., *Calculation of noise from railway bridges and viaducts: Experimental validation of a rapid calculation model.* Journal of Sound and Vibration, 2006. **293**(3-5): p. 933-943.

31. 13146-9:2009+A1, E., *Railway applications-Track-Test method for fastening systems. Part 9: Determination of stiffness* British-Adopted European standard 2011.

32. standardization, E.C.f., *Railway applications-Noise emission-Characterisation of the dynamic properties of track sections for pass by noise measurements*, in *EN 15461:2008, European Committee for standardization*. 2008: Brussels.

33. Institution, B.S., *BS EN 15461:2008+A1:2010 -Railway applications. Noise emission. Characterisation of the dynamic properties of track selections for pass by noise measurements*. 2010, British Standard Institution.

34. Thompson, D., *Railway Noise and Vibration mechanisms,modelling and means of Control* 2009, Oxford: Elsevier Ltd.

35. Jones, C., D. Thompson, and R. Diehl, *The use of decay rates to analyse the performance of railway track in rolling noise generation.* Journal of Sound and Vibration, 2006. **293**(3): p. 485-495.

36. Zhang, X., et al., *A model of a discretely supported railway track based on a 2.5 D finite element approach.* Journal of Sound and Vibration, 2019. **438**: p. 153-174.

37. Thompson, D., et al., *The influence of the non-linear stiffness behaviour of rail pads on the track component of rolling noise.* Proceedings of the Institution of Mechanical Engineers, Part F: Journal of rail and rapid transit, 1999. **213**(4): p. 233-241.

38. Vincent, N., et al., *Theoretical optimization of track components to reduce rolling noise.* Journal of Sound and Vibration, 1996. **193**(1): p. 161-171.

39. C.J.C Jones and J.W. Edwards, *Development of wheels and track components for reduced rolling noise from freight trains.* Proceedings of Inter Noise, Liverpool, 1996: p. 403-408.

40. Talotte, C., et al., *Identification, modelling and reduction potential of railway noise sources: a critical survey.* Journal of Sound and Vibration, 2003. **267**(3): p. 447-468.

41. Oscarsson, J., *Dynamic train-track interaction: linear and non-linear track models with property scatter PhD Thesis*. 2001: Chalmers University of Technology.

42. Hemsworth, B., P.-E. Gautier, and R. Jones. *Silent freight and silent track projects*. in *Proceedings of Internoise*. 2000.

43. Wang, A., et al., *Railway bridge noise control with resilient baseplates.* Journal of sound and vibration, 2000. **231**(3): p. 907-911.

44. Odebrant, T., *Noise from steel railway bridges: a systematic investigation on methods for sound reduction.* Journal of sound and vibration, 1996. **193**(1): p. 227-233.

45. Wettschureck, R.G. and R.J. Diehl, *The dynamic stiffness as an indicator of the effectiveness of a resilient rail fastening system applied as a noise mitigation measure: laboratory tests and field application.* Rail Engineering International, 2000. **4**: p. 7-10.

46. Wettschureck, R. and M. Heim. *Reduction of the noise emission of a steel railway bridge by means of resilient rail fastenings with dynamically soft baseplate pads*. in *Proceedings Euro-Noise*. 1998.

47. Zhang, X., et al., *The noise radiated by ballasted and slab tracks.* Applied Acoustics, 2019. **151**: p. 193-205.

48. Zhu, S., et al., *Low-frequency vibration control of floating slab tracks using dynamic vibration absorbers.* Vehicle System Dynamics, 2015. **53**(9): p. 1296-1314.

49. Ando, K., et al., *Development of slab tracks for Hokuriku Shinkansen line.* Quarterly Report of RTRI, 2001. **42**(1): p. 35-41.

50. Ryue, J. and S. Jang, *Characteristics of vibration and sound radiated from rails of concrete slab tracks for domestic high speed trains.* Transactions of the Korean Society for Noise and Vibration Engineering, 2013. **23**(7): p. 605-616.

51. Brinckerhoff, P., *Track design handbook for light rail transit.* National Academy of Sciences, Washington, DC, 2012: p. 4-7.

52. Van Lier, S., *The vibro-acoustic modelling of slab track with embedded rails.* Journal of sound and vibration, 2000. **231**(3): p. 805-817.

53. Ntotsios, E., D.J. Thompson, and M.F. Hussein, *A comparison of ground vibration due to ballasted and slab tracks.* Transportation Geotechnics, 2019. **21**: p. 100256.

54. Sheng, T., et al., *Experimental study on a geosynthetics isolator for the base vibration isolation of buildings neighboring metro transportation.* Geotextiles and Geomembranes, 2021.

55. Thompson, D. and J. Verheij, *The dynamic behaviour of rail fasteners at high frequencies.* Applied Acoustics, 1997. **52**(1): p. 1-17.

56. Thompson, D., W. Van Vliet, and J. Verheij, *Developments of the indirect method for measuring the high frequency dynamic stiffness of resilient elements.* Journal of Sound and Vibration, 1998. **213**(1): p. 169-188.

57. ISO 10846-3, B.E.I., *Acoustics and vibration-Laboratory measurement of vibro-acoustics transfer properties of resilient elements Part 3: Indirect method for determination of the dynamic stiffness of resilient supports for translatory motion.* 2002.

58. Thompson, D.J. and N. Vincent, *Track dynamic behaviour at high frequencies. Part 1: theoretical models and laboratory measurements.* Vehicle system dynamics, 1995. **24**(sup1): p. 86-99.

59. Kari, L., *Dynamic transfer stiffness measurements of vibration isolators in the audible frequency range.* Noise Control Engineering Journal, 2001. **49**(2): p. 88-102.

60. Fenander, Å., *Frequency dependent stiffness and damping of railpads.* Proceedings of the Institution of Mechanical Engineers, Part F: Journal of rail and rapid transit, 1997. **211**(1): p. 51-62.

61. Maes, J., H. Sol, and P. Guillaume, *Measurements of the dynamic railpad properties.* Journal of Sound and Vibration, 2006. **293**(3): p. 557-565.

62. Morison, C., A. Wang, and O. Bewes, *Methods for measuring the dynamic stiffness of resilient rail fastenings for low frequency vibration isolation of railways, their problems and possible solutions.* Journal of low frequency noise, vibration and active control, 2005. **24**(2): p. 107-115.

63. ISO, *ISO 10846-5, Acoustics and vibration — Laboratory measurement of vibro-acoustic transfer properties of resilient elements — Part 5: Driving point method for determination of the low-frequency transfer stiffness of resilient supports for translatory motion*. 2008.

64. Thompson, D., *Experimental analysis of wave propagation in railway tracks.* Journal of sound and vibration, 1997. **203**(5): p. 867-888.

65. Zhao, Y., et al., *Measuring, modelling and optimising an embedded rail track.* Applied Acoustics, 2017. **116**: p. 70-81.

66. Ryue, J., et al., *Investigations of propagating wave types in railway tracks at high frequencies.* Journal of Sound and Vibration, 2008. **315**(1): p. 157-175.

67. Ryue, J., et al., *Decay rates of propagating waves in railway tracks at high frequencies.* Journal of Sound and Vibration, 2009. **320**(4-5): p. 955-976.

68. Wu, T. and D. Thompson, *A double Timoshenko beam model for vertical vibration analysis of railway track at high frequencies.* Journal of Sound and Vibration, 1999. **224**(2): p. 329-348.

69. Knothe, K. and S. Grassie, *Modelling of railway track and vehicle/track interaction at high frequencies.* Vehicle system dynamics, 1993. **22**(3-4): p. 209-262.

70. Graff, K.F., *Wave motion in elastic solids*. 2012: Courier Corporation.

71. Grassie, S., et al., *The dynamic response of railway track to high frequency vertical excitation.* Journal of Mechanical Engineering Science, 1982. **24**(2): p. 77-90.

72. Clark, R., et al., *An investigation into the dynamic effects of railway vehicles running on corrugated rails.* Journal of Mechanical Engineering Science, 1982. **24**(2): p. 65-76.

73. Thompson, D., *Wheel-rail noise generation, part III: rail vibration.* Journal of sound and vibration, 1993. **161**(3): p. 421-446.

74. Vincent, N. and D.J. Thompson, *Track dynamic behaviour at high frequencies. Part 2: experimental results and comparisons with theory.* Vehicle System Dynamics, 1995. **24**(sup1): p. 100-114.

75. Nilsson, C.-M., *Waveguide finite elements applied on a car tyre*. 2004, PhD thesis, KTH, Stockholm ,Farkost och flyg.

76. Fahy, F. and D. Thompson, *Fundamentals of Sound and Vibration*. Second ed. 2015, London: Taylor & Francis Group.

77. Bender, E. and P. Remington, *The influence of rails on train noise.* Journal of Sound and Vibration, 1974. **37**(3): p. 321-334.

78. Thompson, D., *Wheel-rail noise generation, part I: introduction and interaction model.* Journal of sound and vibration, 1993. **161**(3): p. 387-400.

79. Thompson, D., C. Jones, and N. Turner, *Comparison of 2D and 3D rail radiation models.* ISVR Contract Report, 1999. **99**.

80. Thompson, D.J., C.J.C. Jones, and N. Turner, *Investigation into the validity of two-dimensional models for sound radiation from waves in rails.* Journal of the Acoustical Society of America, 2003. **113**(4): p. 1965-1974.

81. Grassie, S., *Dynamic modelling of concrete railway sleepers.* Journal of Sound and Vibration, 1995. **187**(5): p. 799-813.

82. Grassie, S. and S. Cox, *The dynamic response of railway track with flexible sleepers to high frequency vertical excitation.* Proceedings of the Institution of Mechanical Engineers, Part D: Transport Engineering, 1984. **198**(2): p. 117-124.

83. Thompson, D. and M. Janssens, *TWINS–Track-wheel interaction noise software. Theoretical manual, version 2.4.* TNO Institute of Applied Physics Report TPD-HAG-RPT, 1997: p. 93-0214.

84. David, A.M. and D.J.Thompson, *Measurement of the vibration and sound radiation of a concrete railway sleeper.* ISVR contract report 98/22, September, 1998.

85. Nielsen, J., *Acoustic optimization of railway sleepers.* Journal of Sound and Vibration, 2000. **231**(3): p. 753-764.

86. Squicciarini, G., et al., *Use of a reciprocity technique to measure the radiation efficiency of a vibrating structure.* Applied Acoustics, 2015. **89**: p. 107-121.

87. ISO 3745, *Acoustics—Determination of Sound Power Levels and Sound Energy Levels of Noise Sources Using Sound Pressure—Precision Methods for Anechoic Rooms and Hemi-Anechoic Rooms*. 2012, International Organization of Standards Geneva, Switzerland.

88. Fahy, F.J. and P. Gardonio, *Sound and structural vibration: radiation, transmission and response*. 2007: Elsevier.

89. Wright, J. and G. Skingle. *On the direct or indirect measurement of force in vibration testing*. in *SPIE*. 1997.

90. Zheng, J., F.J. Fahy, and D. Anderton, *Application of a vibro-acoustic reciprocity technique to the prediction of sound radiated by a motored IC engine.* Applied Acoustics, 1994. **42**(4): p. 333-346.

91. *Hawley, S.W., 1997. Anomalies in ISO 48, hardness of rubber.Polymer testing, 16(4), pp.327-333.*

92. Herrmann, K., *Hardness testing: principles and applications*. 2011: ASM international.

93. Ziegenhain, G. and H. M. Urbassek, *Effect of material stiffness on hardness: a computational study based on model potentials.* Philosophical Magazine, 2009. **89**(26): p. 2225-2238.

94. Institution, B.S., *BS EN 15461:2008+A1:2010 -Railway applications. Noise emission. Characterization of the dynamic properties of track selections for pass by noise measurements*. 2010, British Standard Institution.

95. Squicciarini, G., et al., *The effect of temperature on railway rolling noise.* Proceedings of the Institution of Mechanical Engineers, Part F: Journal of Rail and Rapid Transit, 2016. **230**(8): p. 1777-1789.

96. Zhang, X., et al., *An engineering model for the prediction of the sound radiation from a railway track.* Journal of Sound and Vibration, 2019. **461**: p. 114921.

97. Ntotsios, E., *Experimental modal analysis using ambient and earthquake vibrations: Theory, Software and Applications*. 2008, MS Thesis Report No. SDL-08-1, Department of Mechanical and Industrial ….

98. Zhang, X., D.J. Thompson, and G. Squicciarini, *Sound radiation from railway sleepers.* Journal of Sound and Vibration, 2016. **369**: p. 178-194.